Title

Computational Studies of Molecular Motion and Chemical Reactivity Across Crystalline and Solution-Phase Environments

ISBN

9798189297052

Author

Shan, Jing-Ran

Publication Date

2026-08-31

Peer reviewed|Thesis/dissertation

UNIVERSITY OF CALIFORNIA

Los Angeles

Computational Studies of Molecular Motion and Chemical Reactivity Across Crystalline and Solution-Phase Environments

A dissertation submitted in partial satisfaction of the

requirements for the degree Doctor of Philosophy in Chemistry

by

Jing-Ran Shan

2026

ABSTRACT OF THE DISSERTATION

Computational Studies of Molecular Motion and Chemical Reactivity Across Crystalline and Solution-Phase Environments

by

Jing-Ran Shan

Doctor of Philosophy in Chemistry

University of California, Los Angeles, 2026

Professor Miguel A. Garcia-Garibay, Co-Chair

Professor Kendall N. Houk, Co-Chair

Molecular motion and chemical reactivity are two fundamental manifestations of molecular behavior, both of which are strongly influenced by their environments. In crystalline solids, carefully designed architectures can combine long-range structural order with substantial molecular freedom, giving rise to unusual dynamics and reactivity. In solution, interactions among substrates, catalysts, and solvents shape reaction pathways and selectivity. Computational chemistry provides a molecular-level framework for investigating these phenomena across distinct

chemical environments. This dissertation presents a series of computational studies of molecular motion and chemical reactivity in crystalline and solution-phase systems.

The first part of this dissertation, Chapters 1–4, examines the distinctive molecular dynamics and chemical reactivity that emerge in crystalline environments. Chapter 1 combines quantum mechanical calculations, molecular dynamics simulations, and NMR measurements to demonstrate gas-phase-like inertial rotation of cubane units in CUB-5, characterized by a nearly negligible rotational barrier and ultrafast gigahertz-scale dynamics. Chapter 2 extends this investigation to a series of cage-like rotors in isoreticular MOF-5 homologues, establishing a quantitative description of their rotational behavior, including inertia-dominated unidirectional motion, long-time Brownian diffusion, and differences in rotor–lattice coupling through a Langevin framework. Chapter 3 explores ground-state destabilization and dipole–dipole interactions in pillared paddle-wheel MOFs, showing how steric and electronic effects can tune rotational barriers and collective dipolar ordering. Chapter 4 turns from molecular motion to chemical reactivity in crystals, where calculations and experiments support a photochemically triggered thermal chain mechanism that amplifies the solid-state conversion of 2-azidobiphenyl derivatives relative to solution.

The second part of the dissertation, Chapters 5–7, presents computational studies of catalytic organic reactions in solution. Chapter 5 investigates the N-heterocyclic carbene (NHC)-catalyzed radical acylfluoroalkylation of bicyclobutanes, where computational studies elucidate the formation of an NHC-derived ketyl radical and the origin of stereoselective radical–radical coupling. Chapter 6 describes a nickel-catalyzed, base-free Suzuki–Miyaura cross-coupling of organoboron reagents with aryl (pseudo)halides, where computational studies identify a cationic nickel(II) intermediate and reveal an electrophilic substitution pathway for the transmetalation step.

Chapter 7 explores cobaloxime-catalyzed hydrogen atom transfer in the regiodivergent carbamoylation of branched alkenes, where computational studies reveal the steric origin of ligand-controlled regioselectivity.

The dissertation of Jing-Ran Shan is approved.

Matthew J. Nava

Soumitra Athavale

Stuart Brown

Miguel A. Garcia-Garibay, Committee Co-Chair

Kendall N. Houk, Committee Co-Chair

University of California, Los Angeles

2026

CONTENTS

LIST OF FIGURES

LIST OF TABLES

LIST OF SCHEMES

ACKNOWLEDGEMENTS

As my doctoral journey draws to a close, I find myself reflecting with deep gratitude on the years I have spent here. Before acknowledging the individuals who shaped this journey, I wish to express my gratitude to UCLA, the institution that made it all possible. Its intellectual freedom, academic community, and research environment gave me the opportunity to pursue the questions that inspired me and to grow, both as a chemist and as a person.

I wish to express my deepest gratitude to my advisors, Miguel and Ken. To me, they embody the fullest meaning of the Chinese word 大师 — *"Great Masters"*: *Great* in the breadth and depth of their learning, and *Masters* whose teaching and example are worthy of emulation. In *The Analects*, Zi Gong, one of Confucius's disciples, once described the learning of Confucius through the image of enclosing walls: *"To take the walls of a residence as an analogy, my wall reaches only to the shoulder, so that one may look over it and glimpse the beauty of the house within. The Master's wall rises many fathoms high; unless one finds the gate and enters, one cannot behold the magnificence of the ancestral temple or the richness of all that lies within"* (譬之宫墙，赐之墙也及肩，窥见室家之好。夫子之墙数仞，不得其门而入，不见宗庙之美，百官之富). I count myself profoundly fortunate to have entered through their gates and learned under their guidance. What I have been able to glimpse may be only a small fraction of all that lies within, yet what I have received from them will remain with me for a lifetime.

I would like to thank my committee members, Prof. Matthew Nava, Prof. Soumitra Athavale, and Prof. Stuart Brown, for their continued guidance, thoughtful advice, and generous support throughout my doctoral studies. I am sincerely grateful for the time and care they have given me over the years.

I am also grateful to my collaborators at UCLA, including Prof. Matthew Nava, Prof. Stuart Brown, and Prof. Alexander Spokoyny, as well as the members of their groups with whom I had the pleasure of working: Dr. Martin-Louis Riu, Kevin Liu, Dr. Riku Yamamoto, Sara Saib, and Dr. Varun Tej Raviprolu. I also thank my collaborators at other institutions in the United States, China, and Europe for their expertise and insight, and for the opportunity to work together.

I would also like to thank my labmates and colleagues for their help, support, and companionship throughout my doctoral studies.

Finally, and most importantly, I wish to express my deepest gratitude to my family, who have always been my surest fortress and my unwavering source of support.

Chapter 1 is an adapted version of the following published work: Jing-Ran Shan, Qingyang Zhou, Riku Yamamoto, Sara M. Saib, Roberto Chavez, Stuart E. Brown, K. N. Houk, Miguel A. Garcia-Garibay, "Gas-Phase-like Inertial Rotation of a Platonic Solid in Reticular Amphidynamic Crystals of CUB-5: Molecular Dynamics and Experiment," *J. Am. Chem. Soc.* **2025**, *147*, 41809−41818.

Chapter 2 is an adapted version of the following published work: Jing-Ran Shan, Qingyang Zhou, K. N. Houk, and Miguel A. Garcia-Garibay, "Computational Insight into Free Molecular Rotors in Crystalline Solids: Inertial Rotational and Langevin Dynamics," *J. Am. Chem. Soc.* **2026**, *148*, 26373−26382.

Chapter 3 is an adapted version of the following published work: Ieva Liepuoniute, Jing-Ran Shan, K. N. Houk, and Miguel A. Garcia-Garibay, "Computational Study of Ground-State Destabilization Effects and Dipole−Dipole Interaction Energies in Amphidynamic Crystals," *J. Org. Chem.* **2024**, *89*, 9−15.

Chapter 4 is an adapted version of the following unpublished manuscript: Indrajit Paul, Sahil Kapila, Rishika Rai, Jing-Ran Shan, Krzysztof A. Konieczny, K. N. Houk, and Miguel A. Garcia-Garibay, "Evidence for a Photochemically Triggered Thermal Chain Reaction of Nanocrystalline 2-Azidobiphenyl to Carbazole Enabled by Energy Release in the Time Scales of Intramolecular Vibrational Redistribution and Vibrational Energy Transfer," **2026**, *submitted*.

Chapter 5 is an adapted version of the following published work: Chuyu Xiao, Jing-Ran Shan, Wen-Deng Liu, Xingyuan Gao, Jingwei Dai, Zuwei Wang, Wentao Wang, K. N. Houk, and Jiannan Zhao, "Stereoselective Radical Acylfluoroalkylation of Bicyclobutanes via N-Heterocyclic Carbene Catalysis," *Angew. Chem. Int. Ed.* **2025**, *64*, e202416781.

Chapter 6 is an adapted version of the following published work: Meng Zhang, Jing-Ran Shan, Yuke Xie, Lannen Wei, Haigen Xiong, Ge-Ning Xie, Ting Qi, Qinqin Shi, K. N. Houk, and Hui Huang, "General Base-Free Suzuki-Miyaura Cross-Coupling Reaction via Electrophilic Substitution Transmetalation," *Angew. Chem. Int. Ed.* **2025**, *64*, e202512496.

Chapter 7 is an adapted version of the following published work: Ziyu Jiang, Jing-Ran Shan, Junqi Su, Jia-Nan Mo, Fangyuan Zhang, K. N. Houk, and Jiannan Zhao, "Cobaloxime-Catalysed Regiodivergent Hydrogen Atom Transfer for Alkenyl and Allylic Carbamoylation with Branched Alkenes," *Nat. Commun.* **2026**, *17*, 7764.

VITA

Education:

University of California, Los Angeles Los Angeles, CA
Candidate in Philosophy, Chemistry, 2024
Master of Science in Chemistry, 2024

University of California, Berkeley Berkeley, CA
Visiting Undergraduate (Non-degree), 2020

Dalian University of Technology – Dalian Institute of Chemical Physics Dalian, China
Bachelor of Science in Applied Chemistry (Zhang Dayu Program), 2021

Honors and Awards:

Saul Winstein Fellowship Fund, 2026
Herbert Newby McCoy Commencement Award, 2026
John Stauffer Excellence in Second Year Academics and Research Award, 2025

PUBLICATIONS (As of August 28, 2026)

‡ These authors contributed equally * Corresponding authors

1. "Adamantyl-BOX Ligand Enabling Stereoselective Synthesis of Axially Chiral Aldehydes Bearing Vicinal Stereogenic Centers", Hao, E.-J.‡,*; Ding, X.-B.‡; **Shan, J.-R.‡**; Wu, Z.; Wang, X.; Cao, R.; Jin, F.; Houk, K. N.*; Shi, L.*, *ACS Cent. Sci.* **2026**, *accepted*.

2. "Cobaloxime-Catalysed Regiodivergent Hydrogen Atom Transfer for Alkenyl and Allylic Carbamoylation with Branched Alkenes", Jiang, Z.‡; **Shan, J.-R.‡**; Su, J.*; Mo, J.-N.; Zhang, F.; Houk, K. N.*; Zhao, J.*, *Nat. Commun.* **2026**, *17*, 7764.

3. "Computational Insight into Free Molecular Rotors in Crystalline Solids: Inertial Rotation and Langevin Dynamics", **Shan, J.-R.‡**; Zhou, Q.‡; Houk, K. N.*; Garcia-Garibay, M. A.*, *J. Am. Chem. Soc.* **2026**, *148*, 26373-26382.

4. "Diastereoselective Synthesis of β-Hydroxy Allylic Tertiary Sulfides via Nickel/Photoredox Cooperative Catalysis", Xu, H.‡; Wu, Z.‡; **Shan, J.-R.***; Shi, L.*, *Chem. Commun.* **2026**, *62*, 9927-9931.

5. "Reversible Room Temperature Heterolytic Activation of Vinylic sp^2 C–H Bonds at a Gallium Center", Liu, K.; Riu, M.-L. Y.; **Shan, J.-R.**; Zarnitsa, L. M.; Houk, K. N.*; Nava, M.*, *J. Am. Chem. Soc.* **2025**, *147*, 42441-42451.

6. "Gas-Phase-like Inertial Rotation of a Platonic Solid in Reticular Amphidynamic Crystals of CUB-5: Molecular Dynamics and Experiment", **Shan, J.-R.‡**; Zhou, Q.‡; Yamamoto, R.‡; Saib, S. M.; Chavez, R.; Brown, S. E.*; Houk, K. N.*; Garcia-Garibay, M. A.*, *J. Am. Chem. Soc.* **2025**, *147*, 41809-41818.

7. "Hydroaminoalkylation of 1,3-Dienes by Dual Photoredox and Nickel Catalysis", Jin, F.; Chen, Y.*; Xu, H.; Zhou, E.; Qiu, L.; **Shan, J.-R.**; Shi, L.*, *Chem. Commun.* **2025**, *61*, 13723-13726.

8. “General Base-Free Suzuki-Miyaura Cross-Coupling Reaction via Electrophilic Substitution Transmetalation”, Zhang, M.‡; **Shan, J.-R.‡**; Xie, Y.; Wei, L.; Xiong, H.; Xie, G.-N.; Qi, T.; Shi, Q.*; Houk, K. N.*; Huang, H.*, *Angew. Chem. Int. Ed.* **2025**, e202512496.

9. “Rapid Access to Azetidines via Allylation of Azabicyclo[1.1.0]butanes by Dual Copper/Photoredox Catalysis”, Shi, L.*; Liu, Y.‡; Qi, X.‡; Cao, R.; Zhu, Y.; **Shan, J.-R.**; Hao, E.-J.*; Jin, Y.; Feng, X.*, *Chem. Commun.* **2025**, *61*, 6352-6355.

10. “Dual Photoredox- and Titanium Catalysis-Enabled Three-Component Radical Propargylation of Aldehydes with 1,3-Enynes”, Qi, X.; Cao, R.; Wu, Z.; **Shan, J.-R.**; Li, F.; Hao, E.-J.; Feng, X.*; Shi, L.*, *Org. Lett.* **2025**, *27*, 3332-3337.

11. “Chemoselective Functionalization of Tertiary C–H Bonds of Allylic Ethers: Enantioconvergent Access to sec,tert-Vicinal Diols”, Chen, Y.‡; Wang, X.‡; **Shan, J.-R.‡**; Wu, Z.; Cao, R.; Liu, Y.; Jin, Y.; Hao, E.*; Houk, K. N.*; Shi, L.*, *Angew. Chem. Int. Ed.* **2025**, *64*, e202501924.

12. “Stereoselective Radical Acylfluoroalkylation of Bicyclobutanes via N-Heterocyclic Carbene Catalysis”, Xiao, C.‡; **Shan, J.-R.‡**; Liu, W.-D.; Gao, X.; Dai, J.; Wang, Z.; Wang, W.; Houk, K. N.*; Zhao, J.*, *Angew. Chem. Int. Ed.* **2025**, *64*, e202416781.

13. “Metal-Ligand Cooperativity Enables Zero-Valent Metal Transfer”, Riu, M.-L. Y.; **Shan, J.-R.**; Houk, K. N.*; Nava, M.*, *Chem. Sci.* **2025**, *16*, 3888-3894.

14. “Cascade Photoreaction in Crystals: A Phase Change Caused by a Dewar Benzene Quantum Chain Triggers a Topochemical [2 + 2] Photodimerization”, Paul, I.; Konieczny, K. A.; Chavez, R.; **Shan, J.-R.**; Houk, K. N.; Garcia-Garibay, M. A.*, *J. Am. Chem. Soc.* **2024**, *146*, 27988-27992.

15. “Titanium Catalyzed [2σ + 2π] Cycloaddition of Bicyclo[1.1.0]butanes with 1,3-Dienes: Expedient Access to Stilbene Bioisosteres”, Liu, Y.‡; Wu, Z.‡; **Shan, J.-R.***; Yan, H.; Hao, E.*; Shi, L.*, *Nat. Commun.* **2024**, *15*, 4374.

16. “Computational Study of Ground-State Destabilization Effects and Dipole−Dipole Interaction Energies in Amphidynamic Crystals”, Liepuoniute, I.; **Shan, J.-R.**; Houk, K. N.*; Garcia-Garibay, M. A.*, *J. Org. Chem.* **2024**, *89*, 9-15.

17. “Photoredox Chromium and Cobalt Dual Catalysis for Carbonyl Allylation with Butadiene via Allyl Radical Intermediates”, Yan, H.‡; Zhang, D.‡; Liu, Y.; Wang, X.; Wu, Z.; Jin, Y.; Ding, X.; **Shan, J.-R.**; Hao, E.*; Shi, L.*, *Org. Chem. Front.* **2024**, *11*, 684-689.

18. “Photochemical Metal-Hydride Hydrogen Atom Transfer Mediated Radical Hydrofunctionalization of Dienes and Allenes”, Yan, H.‡; **Shan, J.-R.‡**; Shi, L.*, *ChemCatChem* **2024**, *16*, e202301344.

19. “Radical Crotylation of Aldehydes with 1,3-Butadiene by Photoredox Cobalt and Titanium Dual Catalysis”, Yan, H.‡; **Shan, J.-R.‡**; Zhang, F.; Chen, Y.; Zhang, X.; Liao, Q.; Hao, E.*; Shi, L.*, *Org. Lett.* **2023**, *25*, 7694-7699.

20. “Enhancing Substrate–Metal Catalyst Affinity via Hydrogen Bonding: Pd(II)-Catalyzed β-C(sp^3)–H Bromination of Free Carboxylic Acids”, Hu, L.‡; Meng, G.‡; Chen, X.; Yoon, J. S.; **Shan, J.-R.**; Chekshin, N.; Strassfeld, D. A.; Sheng, T.; Zhuang, Z.; Jazzar, R.*; Bertrand, G.*; Houk, K. N.*; Yu, J.-Q.*, *J. Am. Chem. Soc.* **2023**, *145*, 16297-16304.

Chapter 1: Gas-Phase-like Inertial Rotation of a Platonic Solid in Reticular Amphidynamic Crystals of CUB-5: Molecular Dynamics and Experiment

1.1 Contributions

This chapter is based on the following published article: Jing-Ran Shan, Qingyang Zhou, Riku Yamamoto, Sara M. Saib, Roberto Chavez, Stuart E. Brown, K. N. Houk, Miguel A. Garcia-Garibay, "Gas-Phase-like Inertial Rotation of a Platonic Solid in Reticular Amphidynamic Crystals of CUB-5: Molecular Dynamics and Experiment," *J. Am. Chem. Soc.* **2025**, *147*, 41809−41818. This work was carried out through an interdepartmental collaboration with Prof. Stuart E. Brown and his group in the Department of Physics and Astronomy at UCLA. Qingyang Zhou, Riku Yamamoto and I contributed equally to this work and are listed as co-first authors. I designed and carried out most of the computational studies presented in this work. The two-dimensional free-energy surface (2D-FES) calculations were performed by Qingyang Zhou, who also developed RadVCalc, the in-house program used for trajectory analysis. I prepared and characterized the samples used in this study, while the cross-polarization magic-angle-spinning (CP-MAS) ^{13}C NMR spectra were acquired by Roberto Chavez. The solid-state ^{1}H spin-lattice relaxation (T_1) measurements and analyses were performed by Riku Yamamoto and Sara M. Saib. I also contributed to writing the main text of the manuscript.

1.2 Abstract

Amphidynamic crystals are a type of condensed matter that blends two extremes of the dynamic spectrum: rigid components forming a static lattice and rapidly moving parts. Among

them, ordered rotor arrays within metal−organic frameworks (MOFs) constitute a promising platform to explore uncharted territories, such as gas phase-like dynamics in the crystalline state. Through quantum mechanical (QM) calculations and molecular dynamics (MD) simulations we verified that nearly barrierless cubane rotators in CUB-5 display rotational dynamics that transitions from continuous or inertial at high temperature, to chaotic behavior, and ultimately to discrete jumps, as the temperature decreases from room temperature down to cryogenic conditions. ^{1}H NMR spin−lattice (T_1) relaxation measurements corroborate our theoretical predictions, with experimental rotational activation energy of 0.17 kcal/mol and an attempt frequency of 1.03×10^{12} s^{-1} that compare well with calculated values of 0.15 kcal/mol and 0.38×10^{12} s^{-1}, respectively.

1.3 Introduction

Recent advances in the field of molecular rotors have taken advantage of amphidynamic crystals with stator-rotator-stator architectures where bulky stators (**Figure 1a**) would ideally create sufficient free space for the rotator to undergo unhindered rotation (**Figure 1b**).[1] However, while this structural design enables ordered rotation, close-packed molecular crystals have high energy barriers as the result of steric interactions with interdigitated neighbors (**Figure 1c**). Their motion falls in the regime of diffusion-controlled dynamics.[1d] In contrast, reticular amphidynamic crystals based on metal−organic frameworks (MOFs)[2] are constructed with metal nodes and organic linkers to form extended, long-range ordered crystals through coordination interactions are able to support low density structures with free volume for unhindered rotation to take place (**Figure 1d**). Our early work demonstrated the potential of MOFs as reticular amphidynamic crystals using MOF-5 as a model system (**Figure 1e**).[3] MOF-5 adopts a cubic crystal lattice, where Zn_4O clusters occupy the eight corners of the unit cell while 1,4-benzene dicarboxylate (BDC)

linkers span the 12 edges. Upon solvent removal, the activated MOF-5 exhibits large internal voids, making it a natural amphidynamic crystal. However, solid-state NMR studies revealed that the phenylene unit in BDC linkers undergoes rotational motion with an energy barrier of 11.3 kcal/mol, which originates almost entirely from the electronic conjugation between the benzene ring and the carboxylate groups. This result demonstrated that rotational dynamics under free volume fall in the regime of activation control,[1d] and that replacing the conjugated phenylene with a similar, isosteric aliphatic rotator could eliminate both steric and electronic barriers, potentially enabling completely unhindered rotation within the framework.

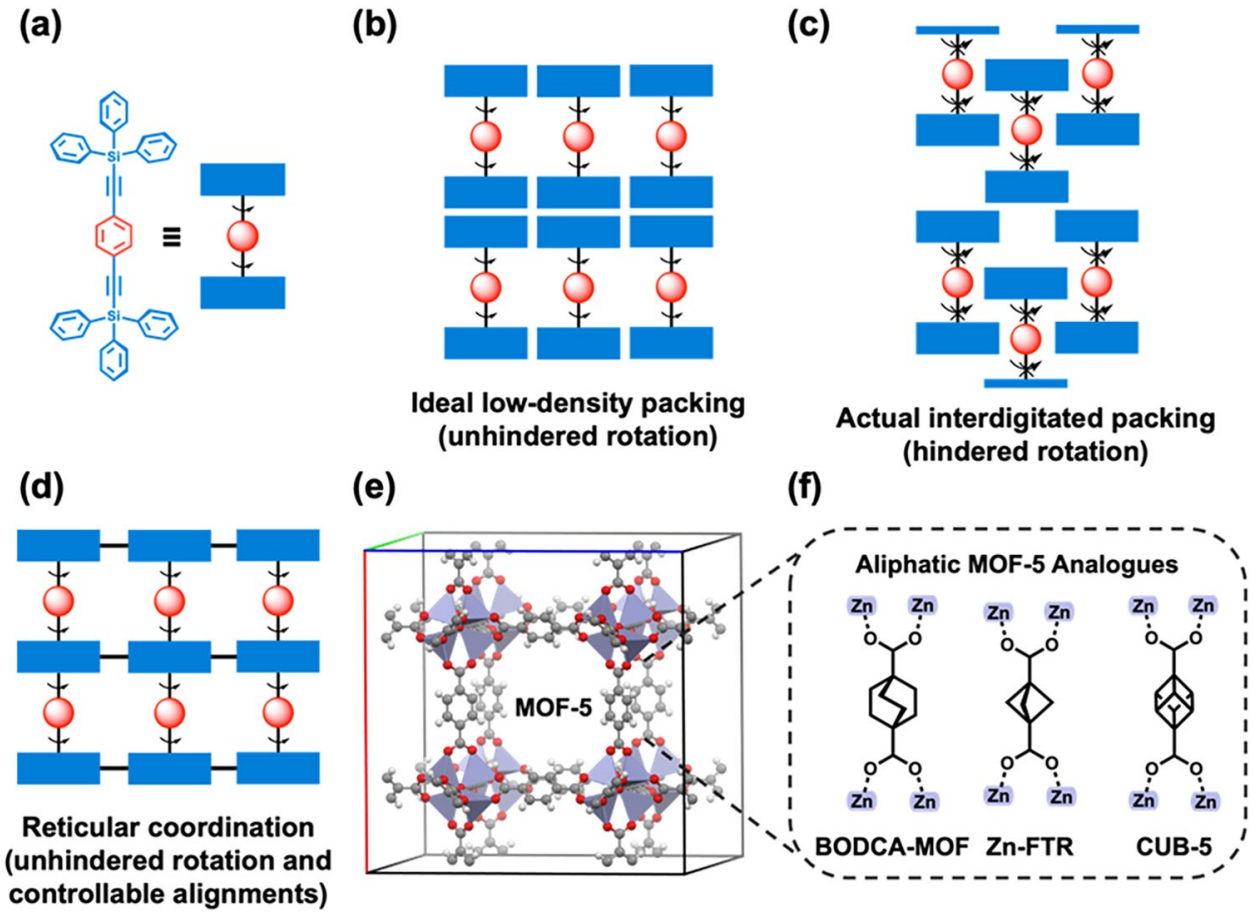

Figure 1. (a) Representation of molecular rotors based on dumbbell shaped structures and their tendency to form close-packed amphidynamic crystals rather than low density solids. (b−d) Different packing arrangements of molecular rotors. (e−f) Structure of MOF-5 along with its three aliphatic isostructural analogues.

In our subsequent work, we explored bicyclo[2.2.2]octane 1,4-dicarboxylic acid (BODCA) as ligand to synthesize BODCA-MOF (**Figure 1f**),[2a] and confirmed that an isosteric aliphatic replacement for the phenylene unit, bicyclo[2.2.2]octane, exhibits a remarkably low activation energy for rotation of only 0.185 kcal/mol, a value that is well below thermal energies at ambient temperature (0.596 kcal/mol). Subsequently, the group of Comotti and Sozzani synthesized the MOF-5 analogue, Zn-FTR, with bicyclo[1.1.1]pentane as the rotator and showed that it possesses

an exceptionally low rotational barrier of 0.0062 kcal/mol.[2b] These findings underscore the remarkable potential of MOFs as amphidynamic crystals, where low structural barriers make it possible to explore gas-phase-like dynamics and emergent properties when dipolar rotors are installed in the framework.

Similar to bicyclo[1.1.1]pentane and bicyclo[2.2.2]octane, cubane can be seen as a saturated isosteric analogue of benzene. Due to its highly symmetric structure and unique chemical properties, cubane has long been a subject of significant research interest. In 2019, Macreadie et al. first reported the MOFs structure, CUB-5, using cubane 1,4-dicarboxylic acid and zinc nitrate hexahydrate as the components for MOF synthesis.[4] Notably, CUB-5 crystallizes in a cubic system with a cubyl rotor in each of its 12 edges and a pore volume that is comparable to that of MOF-5.

In this work, we report the rotational energy barrier of the cubane unit in an isolated single rotor system using highly accurate quantum mechanical (QM) calculations, which yielded an electronic barrier of 0.15 kcal/mol. Then we constructed a 192-rotor supercell model of CUB-5 and performed systematic molecular dynamics (MD) simulations across a range of temperatures. The MD simulations revealed that cubane units undergo ultrafast and frequent continuous rotations, and even at low temperatures, closely resembling their expected gas phase behavior despite being in a crystalline solid. In the absence of steric hindrance, the rotors can continuously overcome the energy barrier, achieving full 360° rotations at GHz frequencies with an activation energy of 0.17 kcal/mol and an attempt frequency of 169.0 GHz.[5] To experimentally support these findings, we conducted spin−lattice (T_1) ^{1}H NMR relaxation time measurements from 4 to 100 K across a range of frequencies. The experimental results confirmed an activation energy of 0.17 kcal/mol and a pre-exponential factor of 1.03×10^{12} s^{-1}.

1.4 Computational Details

A one-dimensional potential energy surface (PES) scan for an isolated cubane rotor in the gas phase was performed using Gaussian 16 program (Revision C.02).[6] We used the M06−2X hybrid functional with superfine integration grid, along with the def2-TZVP basis set and Grimme's D3 dispersion correction.[7,8,9a] Constrained optimizations were performed at 1° increments for a total of 180 steps. Throughout the relaxed scan, the dihedral angle between the two carboxylate groups was fixed at 0°. Structures near the maxima and minima of the PES were then extracted, and their single-point energies were calculated using the high-accuracy DLPNO−CCSD(T) method with the def2-QZVPP basis set using ORCA 5.0.3 program to estimate the electronic barrier for cubane rotation.[8,10,11] The RIJK approximation was applied for Hartree−Fock exchange. The def2-QZVPP/C auxiliary basis set was used for correlation calculations, and the def2/JK auxiliary basis set was employed for Coulomb and exchange fitting.[12,13] TightPNO and TightSCF convergence criteria were applied during calculations.

For molecular dynamics (MD) simulations, the initial crystal structure was obtained from reports by Macreadie et al.[4a] A 2 × 2 × 2 supercell containing 24 rotors (520 atoms) was constructed and optimized using CP2K v2024.1 program with the PBE functional and the DZVP-MOLOPT-SR-GTH basis set, including Grimme's D3 dispersion correction (with Becke−Johnson damping), while keeping the unit cell constrained to a cubic system.[9,14−16] Periodic boundary conditions were also applied during optimization. Atomic charges were calculated using the Charge Model 5 (CM5) method in Multiwfn program at the same level of theory and were subsequently used for MD simulations.[17,18] The force field parameters for C, H, and O atoms were obtained from the General Amber Force Field (GAFF).[19] For the force field parameters related to Zn atoms, which are absent in GAFF, Lennard−Jones (LJ) parameters were first adopted from the Universal Force

Field (UFF).[20] A Zn_4O cluster, coordinated by six acetate ligands, was then constructed and subjected to geometry optimization and vibrational frequency analysis at the B3LYP-D3(BJ)/6−31G(d) level of theory using Gaussian 16 program.[6,8,9,21] The missing bond stretching, angle bending, torsional dihedral and improper dihedral parameters were obtained by fitting harmonic force constants using the Sobtop program.[22] Specifically, for the torsional dihedral parameters associated with Zn_4O cluster (e.g., os-Zn-os-c2 and Zn-os-Zn-os), the generated harmonic potential was imposed at three minima (0°, 120° and −120°) to approximate a 3-fold periodic torsional potential. Other missing torsional dihedral or improper dihedral terms were described using generic parameters or set to zero. A detailed description of the parametrization procedures can be found in the Supporting Information of our published work.[29]

MD simulations were performed using GROMACS v2021 program by constructing a 4 × 4 × 4 supercell that contains 192 rotors (4160 atoms).[23] The Velocity−Verlet integration algorithm was used for both equilibrium phase and production phase, with periodic boundary conditions applied. Long-range electrostatic interactions were considered using the particle-mesh Ewald (PME) method, while van der Waals interactions were truncated at 1 nm with long-range energy and pressure correction applied.[24] The integration time step was set to 1 fs, and the structure was saved every 50 fs. For equilibrium phase, an NPT ensemble was applied for 2 ns using the velocity rescaling thermostat (time constant: τ_t = 0.2 ps) and the Berendsen barostat (isotropic pressure control at 1 atm, time constant: τ_p = 0.5 ps).[25,26] The production phase was conducted under an NVT ensemble for another 2 ns using the Nosé-Hoover thermostat (time constant: τ_c = 0.5 ps, chain length: 10).[27] For the construction of the two-dimensional free energy surface (2D-FES), a 2 ns equilibrium phase and another 500 ns production phase were performed at 100 K, where the position coordinates were saved every 100 fs while all other settings remained unchanged. Unless

otherwise specified, all other parameters were set as default in the programs used. The implementation details of the 2D-FES construction can be found in the Supporting Information of our published work.[29]

1.5 Results and Discussion

1.5.1 Rotational Dynamics of Cubane in Isolated Rotor System

Among the three isosteres of benzene in **Figure 2a**, cubane exhibits the largest axial length at 2.70 Å. When fixed along a rotational axis, the 12 C−C single bonds of cubane adopt a staggered projection with D_{3d} symmetry, in contrast to the D_{3h} symmetry of bicyclo[1.1.1]pentane. By comparison, bicyclo[2.2.2]octane, adopts a twisted D_3-symmetric ground-state, with two enantiomers rapidly interconverting via a D_{3h}-symmetric transition state. Notably, despite having the largest rotational diameter, cubane possesses a lower rotational mass and moment of inertia compared to bicyclo[2.2.2]octane due to its fewer hydrogen atoms. Consequently, cubane is expected to exhibit faster rotational dynamics than bicyclo[2.2.2]octane at any given temperature despite having comparable molecular sizes. As shown in **Figure 1.2b**, we investigated the rotational potential of a single cubane dicarboxylic acid molecule coordinated with lithium atoms keeping the dihedral angle between the two carboxylate groups fixed at 0°. Dihedral angle between the carboxylate group and the cubane unit ($\Phi_{O-C-C-C}$) was scanned from 0° to 180° at the M06−2X-D3/def2-TZVP level with constrained optimizations performed at 1° intervals. The resulting potential energy scan confirmed the expected 6-fold periodicity with maxima and minima occurring every 60° along the rotational pathway, consistent with the 3-fold rotational symmetry of the cubane rotator multiplied by the 2-fold rotational symmetry of the carboxylate groups. Vibrational frequency analysis within the harmonic approximation identified a torsional mode with

a frequency of 12.74 cm^{-1} (~381.9 GHz) for the equilibrium structure, which may be viewed as the attempt frequency corresponding the pre-exponential A-factor of the Arrhenius equation. High-accuracy single-point energy calculations at the DLPNO−CCSD(T)/def2-QZVPP level were performed to estimate the electronic energy difference between the maxima and minima, which was determined to be 0.15 kcal/mol. It should be noted that the highest precision achievable in quantum mechanical calculations (chemical accuracy) is approximately 1 kcal/mol. However, to facilitate comparison with subsequent molecular dynamics simulation and experimental results, here we report the electronic barrier with two decimal places.

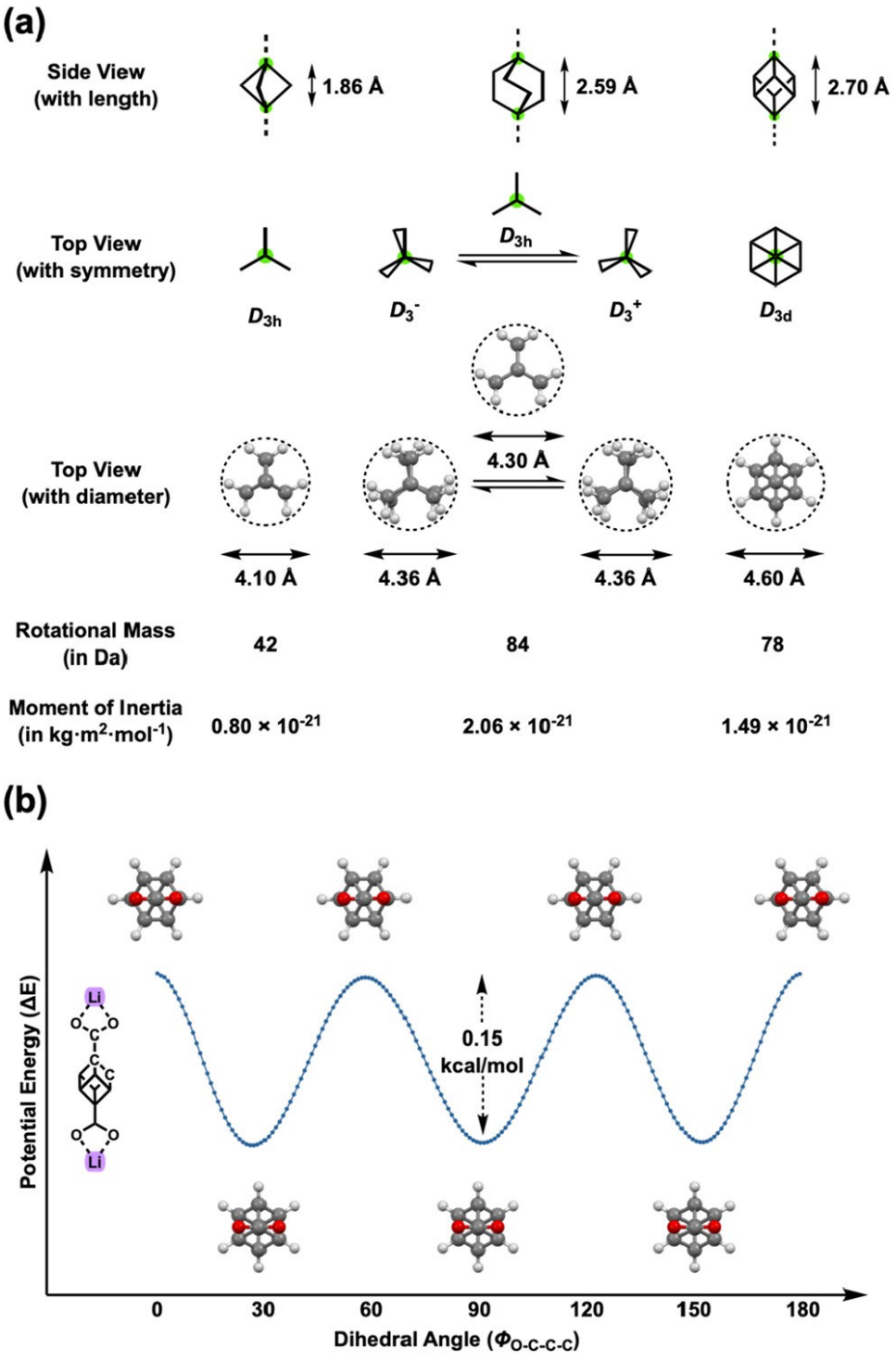

Figure 2. (a) Comparison of the geometries of three isosteres of benzene and (b) rotational potential energy profile of cubane rotator in an isolated rotor system. Lithium atoms are omitted in the top-view representations for clarity.

1.5.2 Rotational Dynamics of Cubane in CUB-5

We next investigated the dynamic behavior of the cubane unit in the CUB-5 crystal. We first optimized a 2 × 2 × 2 supercell of CUB-5, which contains 24 rotors, at the PBE-D3(BJ)/DZVP-MOLOPT-SR-GTH level with periodic boundary conditions. The optimized unit cell parameter was found to be 25.895 Å, which is in close agreement with the reported experimental value of 25.470 Å.[4a] To ensure a more comprehensive thermodynamic sampling and better reproduce the vibrational modes present in real crystal environments, we further constructed a 4 × 4 × 4 supercell containing 192 rotors (**Figure 3a**) and performed MD simulations under periodic boundary conditions. A representative animation of the dynamics of the supercell at 100 K can be found in the Supporting Information Video of our published work.[29] As shown in **Figure 3b**, in analogy to the isolated rotor system (**Figure 2b**), the rotational behavior of each cubane unit within the crystal was examined by tracking the dihedral angle $\Phi_{O–C–C–C}$ between the plane of the carboxylate group and one of the planes of the cubane moieties (labeled in green) as a function of simulation time.

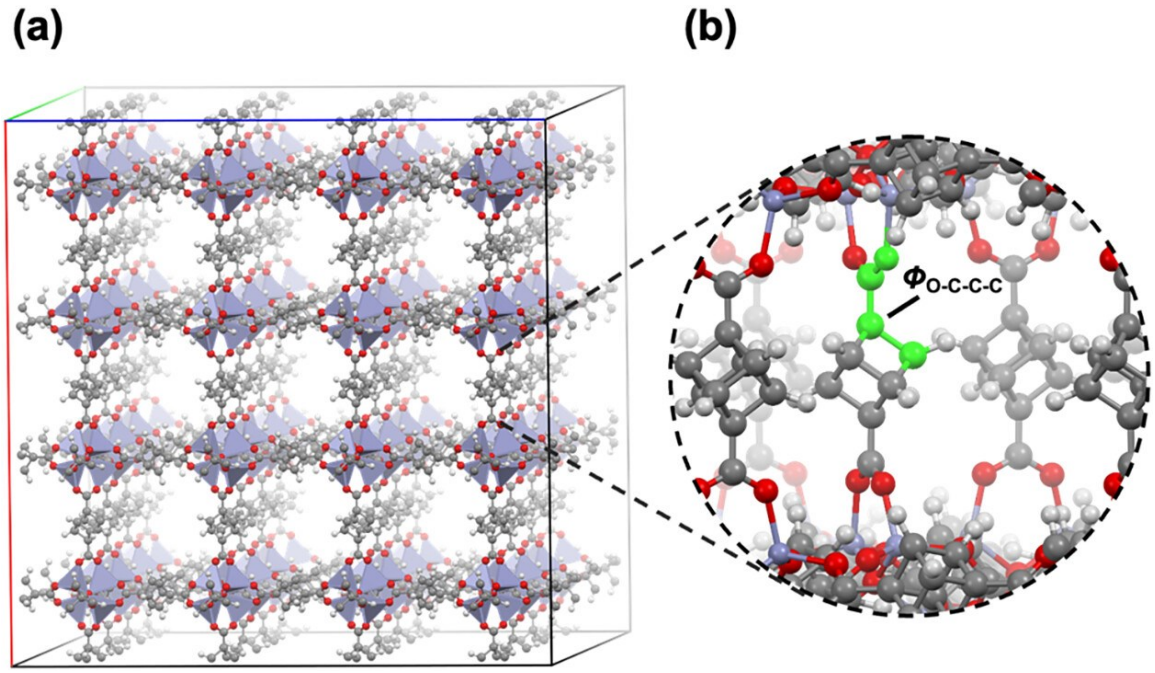

Figure 3. (a) 192-rotor supercell of CUB-5 and (b) enlarged view of a single cubane rotator. The dihedral angle $\Phi_{O-C-C-C}$ between the cubane moiety and the carboxylate group (labeled in green) is used to characterize the rotational motion of the rotor.

Figure 4 shows the time evolution of the dihedral angle for a representative cubane rotator in the supercell during a 2 ns (2000 ps) simulation at 298 K. The results reveal that at 298 K, the cubane unit undergoes barrierless and continuous rotation within the crystal lattice for most of the time. The dihedral angle exhibits a periodic change from +180° to −180°, which is equivalent to +180° when rotation occurs in one direction, or from −180° to +180° and then −180°, if rotation occurs in the opposite direction. Continuous rotation under this representation is observed as a series of nearly parallel straight lines where the slope of each line indicates the angular velocity.

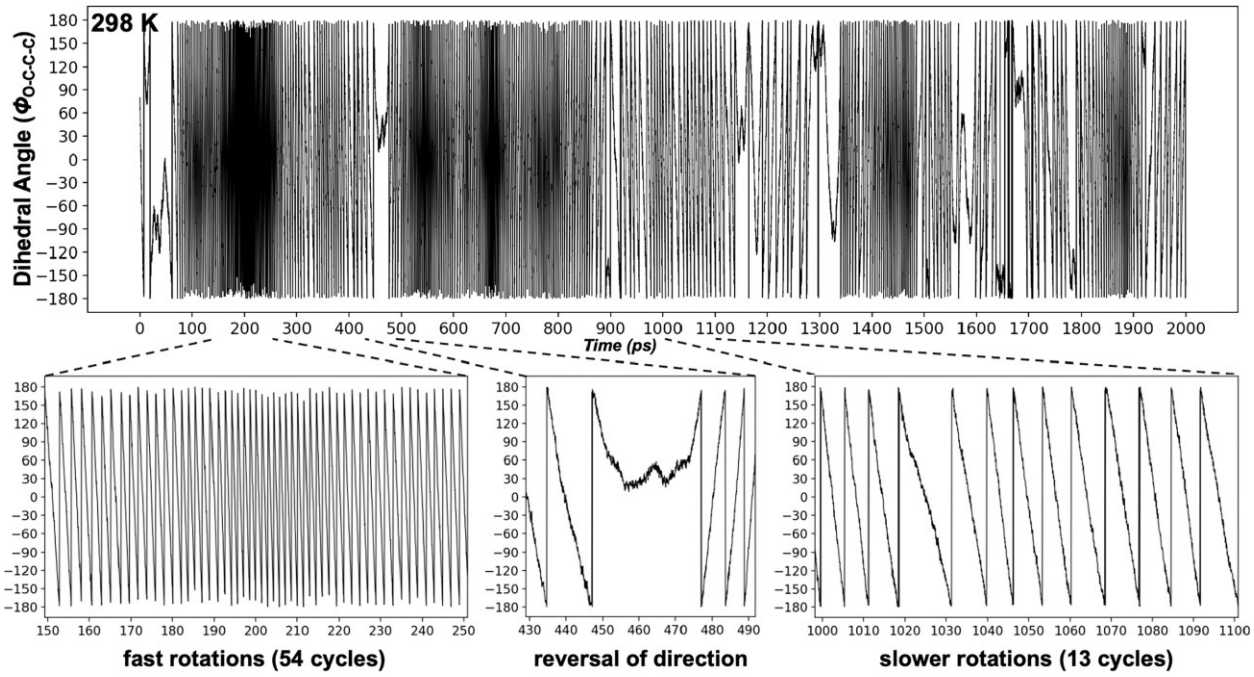

Figure 4. Rotational dynamics of a representative cubane rotator at 298 K over 2 ns. The y-axis represents the dihedral angle between the cubane moiety and the carboxylate group (deg). The x-axis represents the simulation time (ps). The second row presents zoomed-in views of three selected time intervals from the MD simulation: 150 to 250 ps (left), 430 to 490 ps (center), and 1000 to 1100 ps (right).

The MD results in **Figure 4** indicate that the cubane unit exhibits ultrafast unidirectional rotations over certain time intervals. For example, between 150 and 250 ps (bottom left), the cubane rotates approximately 54 full cycles, corresponding to a temporary rotational frequency of 540 GHz. By contrast, the rotational speed between 1000 and 1100 ps is relatively slower (bottom right), completing 13 full cycles, which corresponds to a local frequency of 130 GHz. Occasionally, at specific moments (bottom center), the rotation slows down and halts before reversing its direction, which is presumably due to the coupling between the cubane rotation and lattice vibrations. Nevertheless, the overall rotational behavior of the cubane rotor at 298 K closely

resembles the dynamics that may be observed in a gas phase system, which exhibits minimal constraints from the surrounding environments.

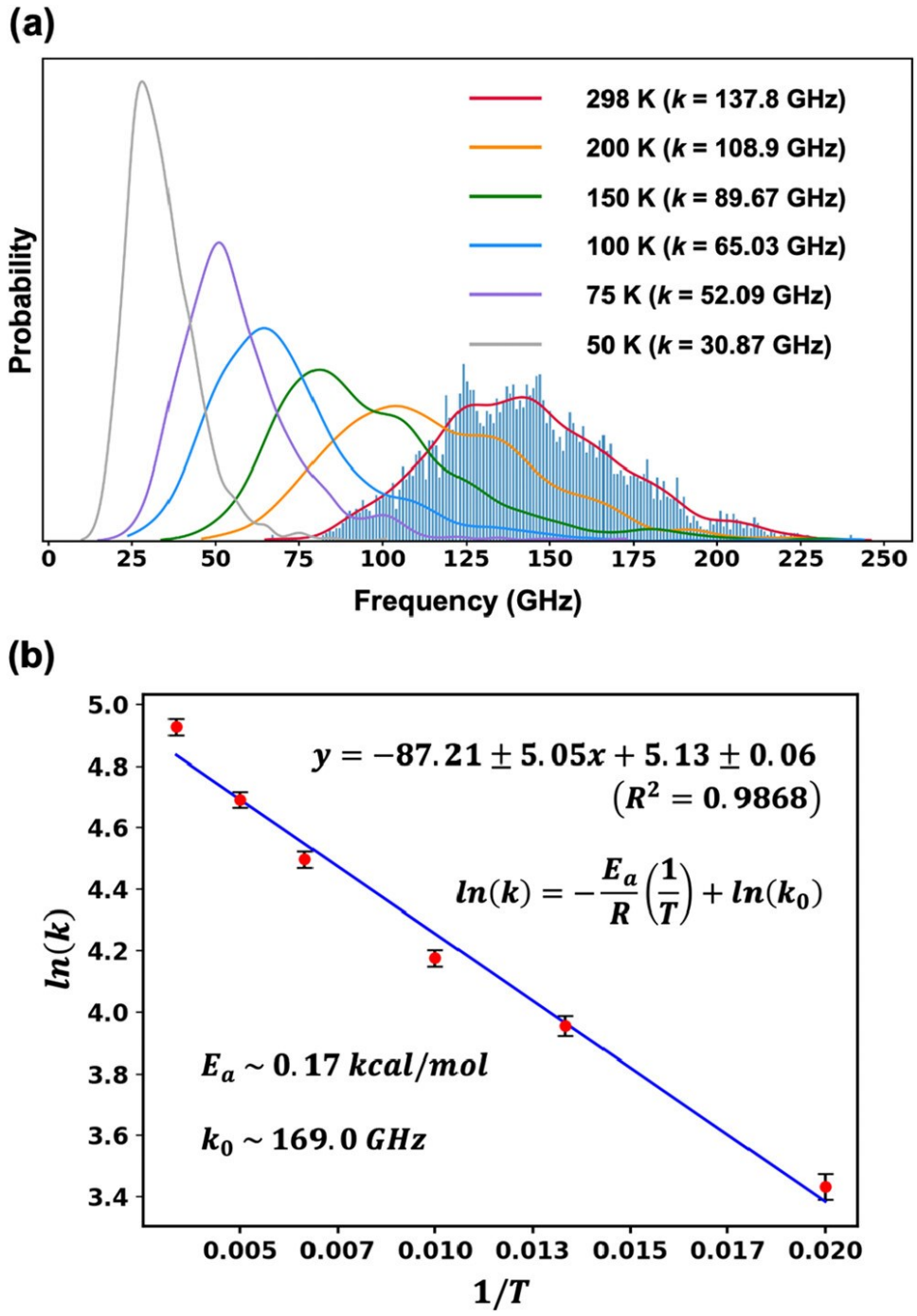

Figure 5. 360° full rotations of cubane rotators. (a) Distribution of 360° full rotational frequencies for all 192 rotors in the supercell from 298 to 50 K. Simulation at each temperature was conducted for 2 ns with 5 replicas. For clarity, the frequency bars (in blue) are only shown for 298 K. The frequency distributions at other temperatures are represented by kernel density estimation (KDE) fitted outline curves. *k* represents

the average frequencies. (b) Plot of ln(k) versus 1/T, with a corresponding fit to the Arrhenius equation. The error bars represent the standard deviation.

Building on these observations, we aimed to quantify the rotational dynamics of the cubane rotors by measuring the frequency of complete 360° rotations within the simulation time frame. To achieve this, we conducted MD simulations across a range of temperatures, from 298 K down to 50 K. The total number of 360° rotations for each rotor within the 192-rotor supercell was then statistically analyzed using the Automatic Multiscale-based Peak Detection (AMPD) algorithm (details on the implementation of this analysis is provided in the Supporting Information of our published work).[29] To ensure sufficient sampling, each simulation was performed for 2 ns with five independent replicas, and the results were aggregated. The blue bars in the histograms in **Figure 5a** represent the distribution of 360° rotational frequencies for all cubane rotors at 298 K. For clarity, rotational distributions at lower temperatures are presented as curves with frequency bars omitted. At 298 K, the rotational frequency spans a broad range from 65 to 245 GHz, with an average rotational frequency of approximately 137.8 GHz. As the temperature decreases, the mean rotational frequency k gradually shifts toward lower values, and the distribution narrows. A statistical analysis of k at each temperature revealed a linear correlation between ln$k$ and 1/T, consistent with an Arrhenius-like dependence. Fitting the data to the Arrhenius equation yielded an activation energy E_a of 0.17 kcal/mol and an attempt frequency k_0 of 169.0 GHz, which corresponds to the frequency at an infinite temperature or in the limit of zero energy barrier (**Figure 1.5b**). However, the Eyring equation did not provide a satisfactory description of this process.[29] This outcome aligns with our expectations, as a complete 360° rotation requires overcoming six consecutive energy barriers, rather than being governed by a single transition state as assumed in

the transition state theory. Similarly, the time required for each complete 360° rotation was analyzed. The duration of individual rotations is mostly distributed between 2 and 10 ps.[29] Summing the rotation times across all rotors at 298 K reveals that cubane rotators spend approximately 78.0% of the total simulation time in full 360° rotations. An Arrhenius-like dependence was also observed by analyzing the percentage of rotation time (P) at different temperatures, in which an activation energy E_a of 0.12 kcal/mol and a pre-exponential factor P_0 of 100.5% were determined.[29]

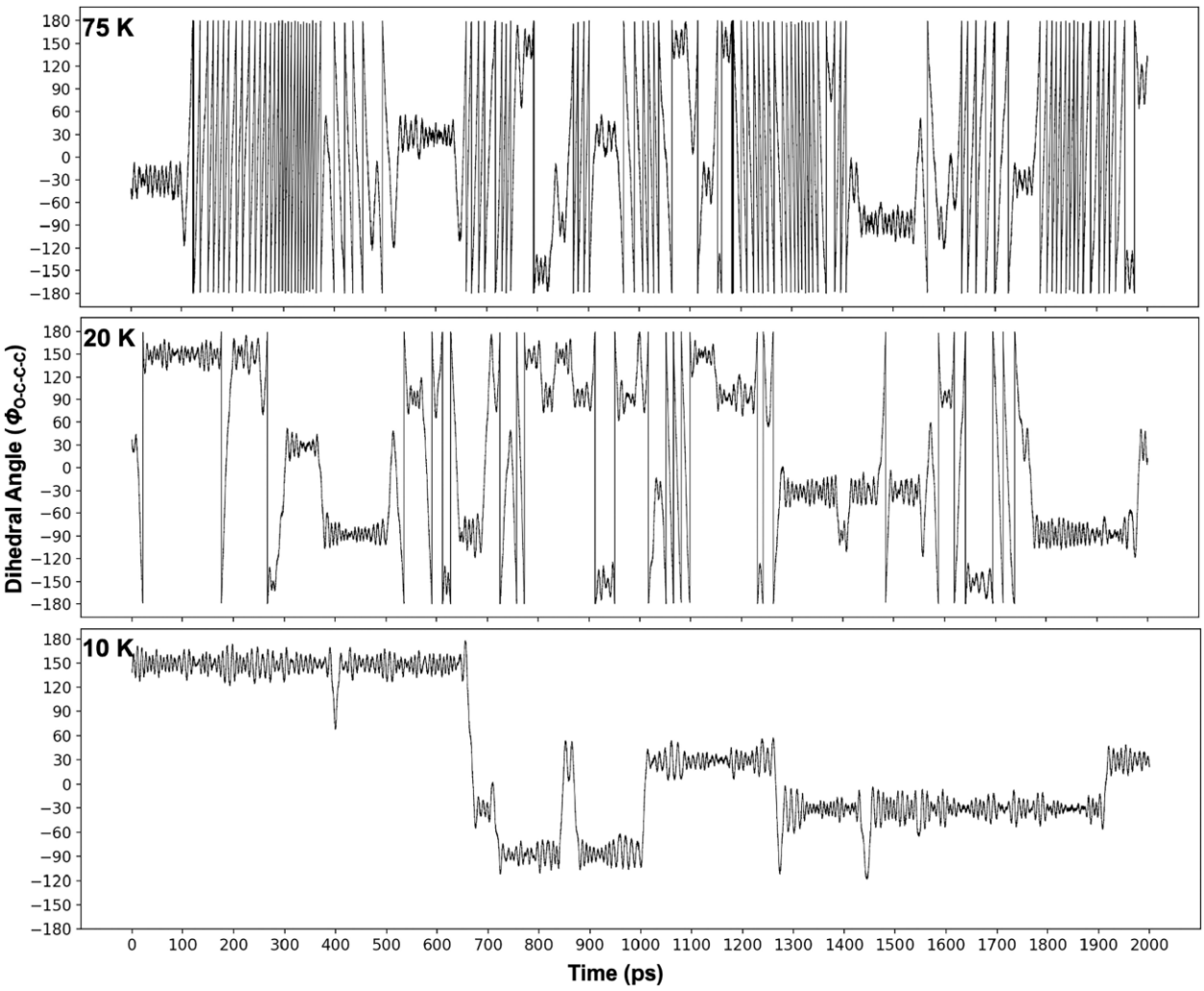

Figure 6. Rotational dynamics of a representative cubane rotator at 75, 20, and 10 K over 2 ns. The y-axis represents the dihedral angle between the cubane moiety and the carboxylate group (deg). The x-axis represents the simulation time (ps).

While the cubane rotator exhibits near-barrierless motion at ambient to moderately low temperatures, any potential energy barrier becomes increasingly significant as the temperature drops to extremely low regimes. **Figure 6** shows the time evolution of the dihedral angle for cubane rotation in a temperature range of 75 to 10 K. Starting our analysis at 75 K, one can see that the cubane rotator continues to undergo continuous rotations, but distinct jumping behavior

starts to emerge. The rotator experiences intermittent trapping at local energy minima where it undergoes localized oscillations before resuming continuous rotational motion. As the temperature is further decreased to 20 K, the fraction of time spent in active rotation decreases significantly while inter-well hopping between different local minima becomes more pronounced. The retention time at individual minima also increases. Ultimately, at 10 K, the complete 360° rotation of the cubane rotator is nearly eliminated and replaced entirely by discrete hopping between potential energy wells. This indicates a transition from free rotation to a thermally activated hopping regime where the system's kinetic energy is no longer sufficient to consecutively overcome the energy barriers.

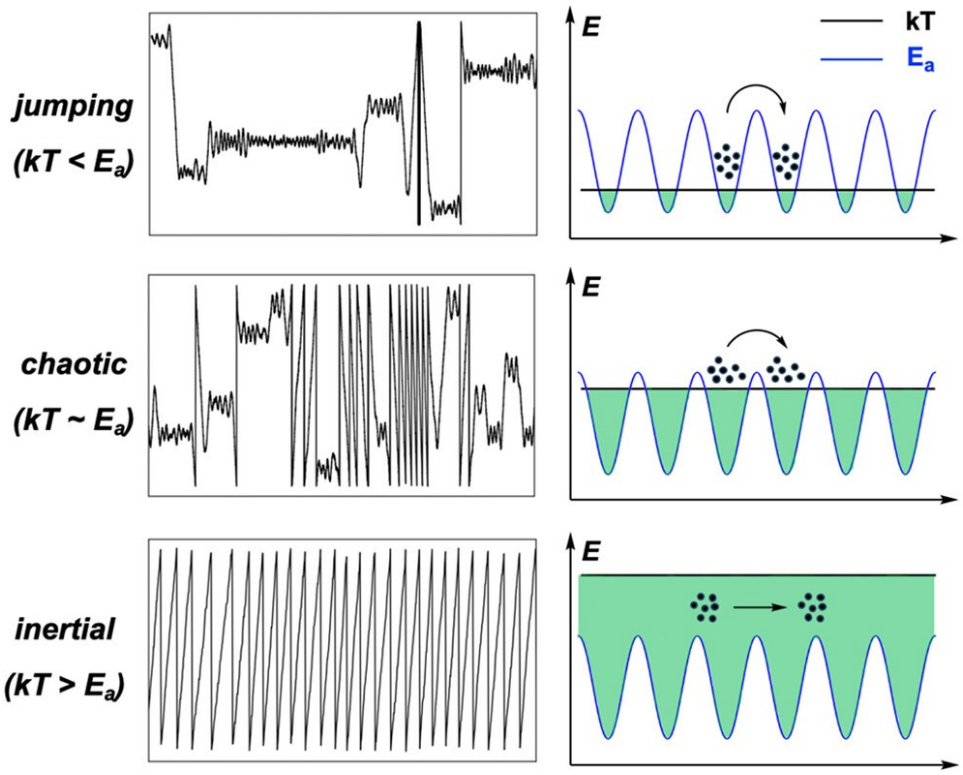

Figure 7. Schematic representation of rotational dynamic behaviors at varying temperatures.

The dynamic behavior of an individual cubane rotor at different temperature regimes can be illustrated in **Figure 7**. When $kT < E_a$, the rotator remains trapped within discrete potential wells, oscillating around local energy minima and undergoing thermally activated hopping motions at a characteristic frequency. In this regime, consecutive rotation is effectively hindered. Conversely, when $kT >> E_a$, the rotator possesses sufficient energy to continuously overcome energy barriers, preventing trapping in any potential well. In this regime, the rotator exhibits unhindered rotational dynamics, which is analogous to that in the gas phase. At intermediate temperature regimes, where $kT \approx E_a$, the system is characterized by a mixture of hopping and inertial behaviors, which we refer to as the chaotic motions. The rotor intermittently undergoes barrier crossings while still experiencing transient localization within potential wells, leading to an irregular rotational trajectory.

1.5.3 Inter-Rotor Coupling Between Neighboring Cubanes in CUB-5

After investigating the rotational behavior of individual rotors within the crystal, we sought to determine whether any weak couplings exist between two neighboring cubane units. **Figure 8a** and **Figure 8b** illustrate two distinct arrangements of neighboring cubane rotators within a unit cell cross-section: one in which the two cubane rotators are positioned on opposite edges of the square and the other in which they are positioned on adjacent edges. The H···H distance between rotator pairs in the opposite-configuration is approximately 9.3 Å, whereas in the adjacent-configuration, the distance is approximately 4.7 Å. In both cases, the inter-rotor distance exceeds the van der Waals radius of the cubane units. Nevertheless, we aimed to explore whether any weak inter-rotor coupling could exist. To probe this, we conducted a 500 ns MD simulation at 100 K using the 192-rotor supercell. For each frame in the trajectory, we extracted the dihedral angles of

every pair of neighboring cubane rotators with opposite- or adjacent-configuration, constructing a two-dimensional histogram. The corresponding two-dimensional free-energy surface (2D-FES) was then reconstructed based on Boltzmann distribution.

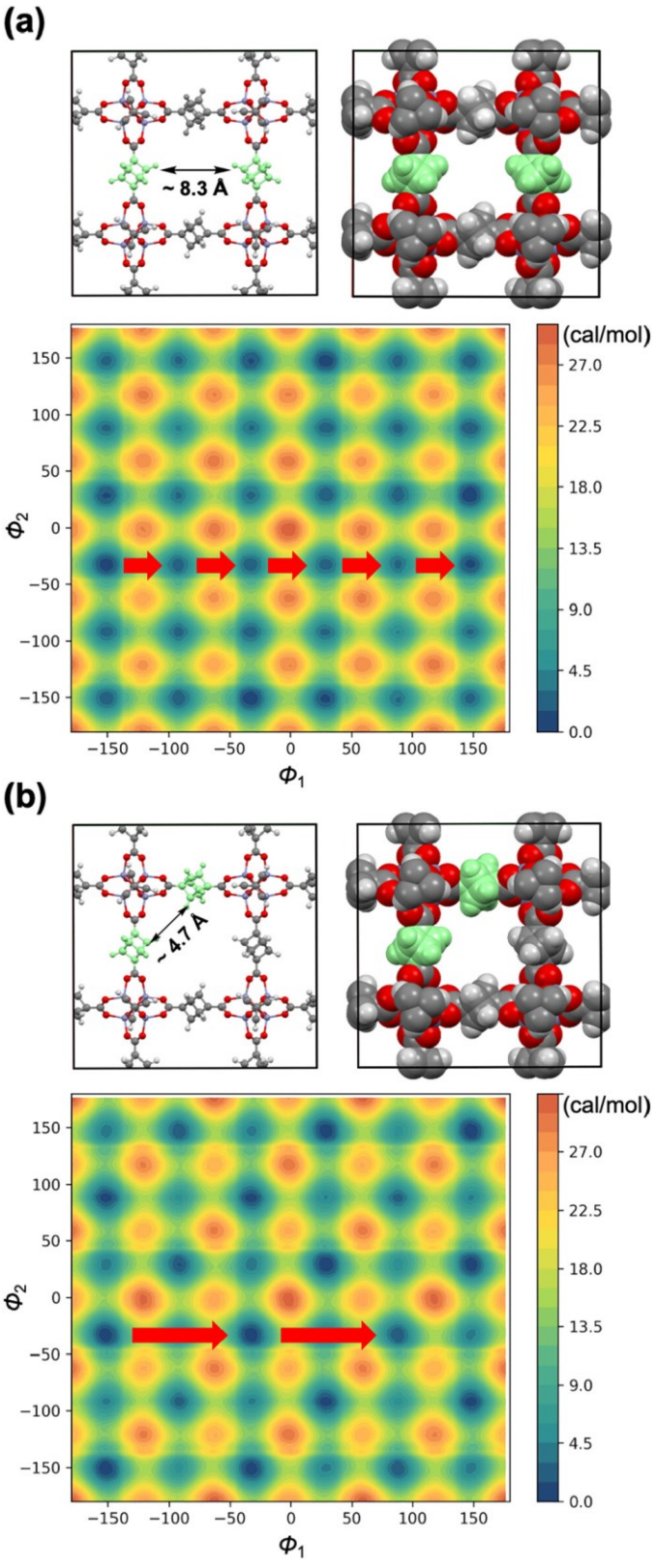
(a)
~ 8.3 Å
(cal/mol)
27.0
22.5
18.0
13.5
9.0
4.5
0.0
150
100
50
0
−50
−100
−150
Φ2
−150 −100 −50 0 50 100 150
Φ1
(b)
~ 4.7 Å
(cal/mol)
27.0
22.5
18.0
13.5
9.0
4.5
0.0
150
100
50
0
−50
−100
−150
Φ2
−150 −100 −50 0 50 100 150
Φ1

Figure 8. Inter-rotor interactions between two neighboring cubane rotators in (a) opposite and (b) adjacent configurations. The first row shows ball-and-stick and space-filling representations of two neighboring rotors (labeled in green). The second row shows the two-dimensional free energy surface (2D-FES) for the respective configurations. The x- and y-axes correspond to the dihedral angles (Φ_1 and Φ_2) between each cubane rotator and its respective carboxylate group. Free energies are reported in cal/mol.

Figure 8a presents the 2D-FES for rotators with an opposite-configuration. The energy minima (dark blue) and maxima (orange red) are arranged in an alternating fashion, forming a symmetric 6 × 6 grid. Each minimum displays a similar color depth. The results indicate that, similar to an isolated rotor system (**Figure 2b**), each cubane rotator exhibits a characteristic 6-fold periodic free energy barrier. Along the minimum energy pathway (MEP) of any given rotator (indicated by the red arrows), the dihedral angle changes through a series of minima separated by 60° intervals, with each free energy barrier being approximately 20 cal/mol. This behavior is fully consistent with the dynamics of two independent, non-interacting rotor systems, suggesting minimal couplings in this configuration.

In contrast, as shown in **Figure 8b**, the 2D-FES for rotators with an adjacent-configuration deviates from the ideal 6-fold symmetry, with the minima displaying a pronounced alternation in color depth. Instead of a global minimum occurring every 60°, the rotator now exhibits global minimum every 120°, while the former 60° global minima are reduced to local minima. Consequently, as indicated by the arrows in the figure, the most favorable rotational trajectory requires 120° jumps instead of 60°. This result suggests that the adjacent rotor systems may exhibit a coupled rotational behavior reminiscent of a bevel gear mechanism at extremely low temperatures, which is presumably mediated by the through-space coupling via the weak

dispersive and electrostatic interactions, or the through-bond coupling via the connecting Zn_4O cluster.

To further probe the influence of lattice vibrations on rotor dynamics, we performed an additional simulation at 298 K in which the lattice was frozen by constraining all Zn and O atoms, while only the C and H atoms of the cubane moiety were allowed to evolve during the 2 ns simulation time. Interestingly, when the lattice is frozen, and thus the through-bond coupling between rotors is eliminated, the dynamics of each rotor becomes remarkably less susceptible to perturbations. A rotor that started with a large initial velocity continues to rotate unidirectionally (**Figure 9a**), whereas one with a small initial velocity remains trapped and oscillating at the bottom of its shallow potential well (**Figure 9c**). Occasional changes of motion observed in other rotors may be ascribed to the weak through-space coupling between neighboring rotors or to sporadic perturbations from the thermostat (**Figure 9b**). While a quantitative assessment is beyond the scope of the present work, these conditions differ substantially from the those obtained with a fully relaxed lattice and suggest the complex role of lattice vibrations on rotor dynamics and the effects of through-bond interactions between rotors.

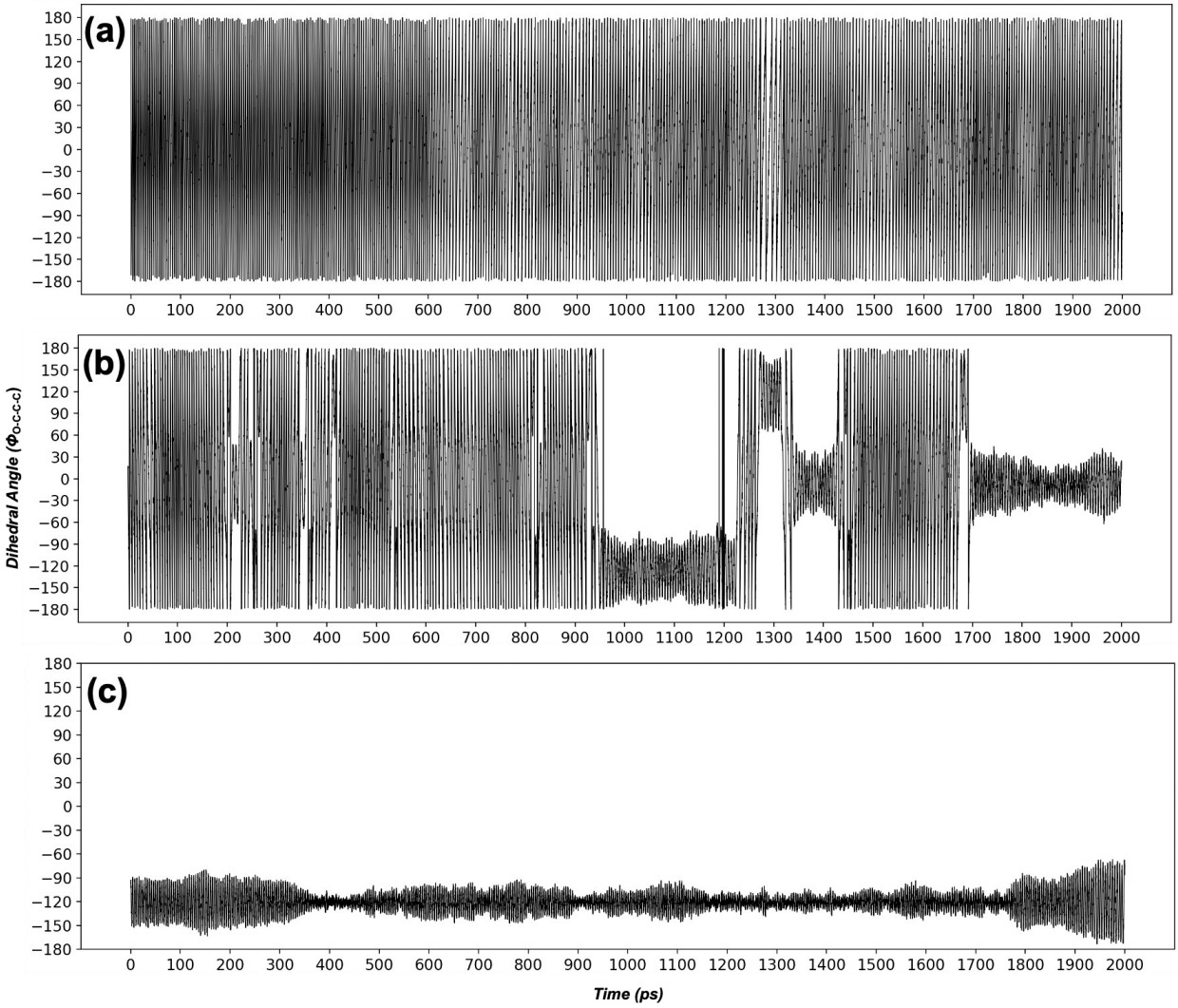

Figure 9. Rotational dynamics of three representative cubane rotator with frozen lattice (with Zn and O atoms frozen) at 298 K over 2 ns. The y-axis represents the dihedral angle between the cubane moiety and the carboxylate group (°). The x-axis represents the simulation time (ps).

1.5.4 Experimental Observation of Cubane Rotation via Solid-State NMR

Following our QM calculations and MD simulations, we synthesized CUB-5 following a slightly modified procedure from the literature by Macreadie et al.[4a] To improve the homogeneity of MOF crystals, multiple small batches were prepared under identical conditions and combined

for activation. For the activated sample, the cross-polarization magic-angle spinning (CP-MAS) ^{13}C NMR was performed to confirm the complete removal of the solvent molecules and the homogeneity of the sample. As shown in **Figure 10**, three distinct peaks appear at δ 181.20, δ 57.89 and δ 45.95 ppm, corresponding to the carbonyl carbon (red), bridgehead carbon (blue), and tertiary carbon (green), respectively. The increasing peak intensities follow the expected trend based on decreasing distances between the carbon nuclei and hydrogen atoms, which enhances cross-polarization effects. Notably, the peaks corresponding to the bridgehead carbon (blue) and tertiary carbon (green) are exceptionally sharp, indicating that the carbon atoms in the crystalline environment exhibit ultrafast dynamic behaviors.

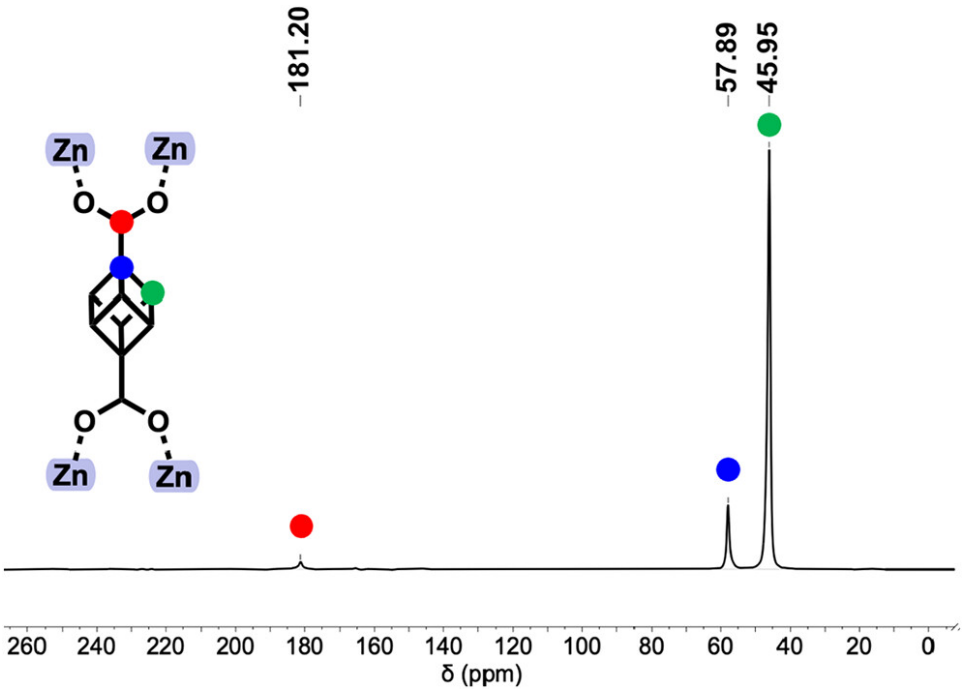

Figure 10. CP-MAS ^{13}C NMR spectrum of activated CUB-5.

Subsequently, we measured the temperature-dependent spin−lattice (T_1) relaxation time of ^{1}H in solid-state NMR between 4 and 100 K over a range of frequencies (38.256 MHz, 61.769 MHz, 191.378 and 361.678 MHz). The sample was loaded into a homemade cryoprobe under ultrahigh-purity helium and T_1 relaxation times were acquired using the saturation-recovery method. For a typical thermally activated dynamic process, the T_1 relaxation time can be described by the Kubo−Tomita equation (**eq 1**), where ω_0 represents the Larmor precession frequency, τ_c is the correlation time which is assumed to follow a temperature-dependent Arrhenius behavior (**eq 2**) characterized by an activation energy (E_a) and an attempt frequency (τ_0^{-1}). C is a constant that represents the strength of the sum of dipolar fields involved in the relaxation process and can be expressed as **eq 3**, where μ_0 is the permeability of free space, γ denotes the gyromagnetic ratio, $\hbar$ is the reduced Planck's constant, and r represents the internuclear distance. At the condition where the inverse of the correlation time (τ_c^{-1}) matches the proton Larmor precession frequency (ω_0), the relaxation process reaches its maximum efficiency.

$$\frac{1}{T_1} = C\left[\frac{\tau_c}{1+\omega_0^2\tau_c^2} + \frac{4\tau_c}{1+4\omega_0^2\tau_c^2}\right] \quad \textbf{(eq 1)}$$

$$\tau_c^{-1} = \tau_0^{-1}\exp\left(-\frac{E_a}{RT}\right) \quad \textbf{(eq 2)}$$

$$C = \sum_i \frac{2}{3}\gamma^2 B_{\mathrm{nuc},i}^2 = \sum_i \frac{2}{3}\left(\frac{\mu_0}{4\pi}\right)^2 \frac{\gamma^4\hbar^2}{\gamma_i^6} \quad \textbf{(eq 3)}$$

Figure 11 presents the semilogarithmic plot of $1/T_1$ as a function of inverse temperature $1/T$. In CUB-5, all hydrogen atoms are chemically equivalent, with only a single type of hydrogen present on the cubane rotators. As a result, these hydrogen atoms are solely responsible for contributing to the T_1 relaxation. The data between 8.5 and 25 K can be well fitted using the Kubo−Tomita equation, yielding an activation energy of $E_a = 0.17 \pm 0.01$ kcal/mol and an attempt frequency of $\tau_0^{-1} = (1.03 \pm 0.01) \times 10^{12}$ s^{-1}, which corresponds to a rotational frequency of ~1.03 THz and a 360° full-cycle rotational frequency of ~164 GHz.[28] These results are highly consistent with our QM calculations and MD simulations, providing strong experimental validations for our theoretical predictions.

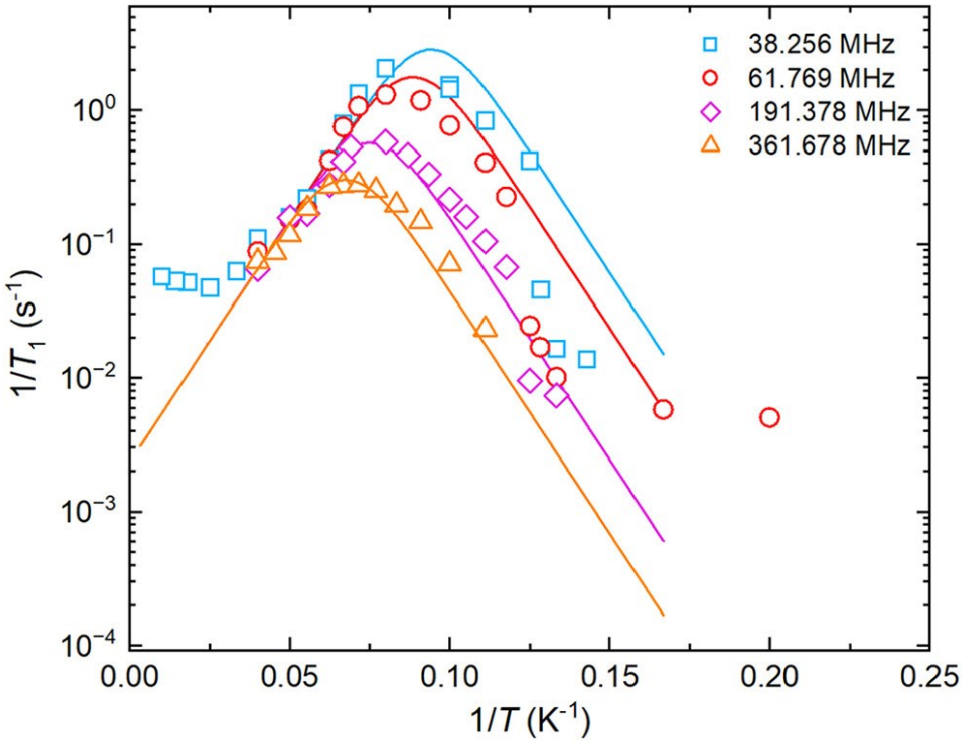

Figure 11. Semilogarithmic plot of $1/T_1$ versus $1/T$ at different frequencies, with a corresponding fit to the Kubo−Tomita equation.

However, it should be noted that at temperatures below 8.5 K, a sudden drop in $1/T_1$ was observed, indicating an abrupt change in the rotational dynamics associated with a phase transition. Additionally, at temperatures above 25 K, the Kubo−Tomita equation fails to describe the correlation between $1/T_1$ and $1/T$. In this regime, the temperature dependence of $1/T_1$ becomes significantly weaker, indicating that a different mechanism dominates the relaxation at these higher temperatures. Additional measurements and further discussion are provided in the Supporting Information of our published work.[29]

1.6 Conclusion

Comprehensive QM calculations and MD simulations have theoretically predicted that CUB-5 features cubane rotators with negligible (< 0.2 kcal/mol) rotational energy barriers. Cubane units exhibit ultrafast rotational dynamics with frequencies in GHz regime from moderate to extremely low temperatures. Experimental validation through T_1 relaxation time measurements further confirmed our theoretical predictions, revealing an activation energy of 0.17 kcal/mol and an attempt frequency of 1.03×10^{12} s^{-1}. These findings demonstrate that CUB-5 is an ideal reticular amphidynamic crystal with internal rotational dynamics that can be as fast as they are in the gas phase. Notably, there are conditions where rotations occur inertially and in a given (random) direction for long periods of time, suggesting future experiments where a given direction can be controlled by interfacing dipolar rotors with electric AC quadrupoles, polarized microwaves, or terahertz spectroscopy. We anticipate that this work will also provide a foundation for future exploration of correlated molecular motions by taking advantage of dipole−dipole interactions across the framework.

1.7 Experimental Details

1.7.1 General Information

Unless otherwise noted, all solvents or reagents were used as received without further purification. Dichloromethane (DCM, extra dry, 99.9%) and N,N-dimethylformamide (DMF, anhydrous, 99.8%) were purchased from ThermoFisher Scientific. Dimethyl 1,4-cubane dicarboxylate (98%) was purchased from A2B Chem. ^{1}H and ^{13}C spectra for ligands and precursors were recorded on a Bruker Avance 400 MHz spectrometer using deuterated solvent as the lock and residual protiated solvent as internal reference (CD_3OD: δ H 3.31 ppm, δ C 49.00 ppm). Solid-state Cross-Polarization Magic Angle Spinning (CP-MAS) ^{13}C NMR spectra for activated CUB-5 were recorded on a Bruker Avance 600 MHz spectrometer. Experimental parameters were set to an 18 kHz spinning rate, 2048 scans, 5 ms contact time (P15), 3s recycle delay (D1) and a 203 receiver gain value (RG). The Powder X-Ray Diffraction (PXRD) patterns were collected with Cu–Kα_1 radiation (1.5406 Å). Samples were placed on a zero–background plate at a fixed stage. Data was collected from 2 theta (2θ) angles of 5 to 50 degrees at 298 K.

1.7.2 Preparation of CUB-5

Synthesis of 1,4-cubane dicarboxylic acid: Dimethyl 1,4-cubane dicarboxylate (200 mg, 0.9 mmol, 1 equiv.) was dissolved in a 1:1 (v/v) mixture of THF (12 mL) and EtOH (12 mL), followed by the addition of 2 M aqueous NaOH (12 mL, 24 mmol, 27 equiv.). The mixture was refluxed at 90°C for 4 h. After completion, organic solvents were removed under reduced pressure. The resulting aqueous phase was acidified with concentrated HCl dropwise to pH ≈ 1 and then allowed to stand for 10 min. The white precipitate was collected by centrifugation, washed 3 times

with aqueous HCl (pH ≈ 3) and dried to afford the product as a white powder (140 mg, 80% yield). ^{1}H NMR (400 MHz, CD_3OD): δ = 4.19 (s, 6H). ^{13}C NMR (101 MHz, CD_3OD): δ = 175.4 (C=O), δ = 57.7 (cubyl), δ = 48.1 (cubyl).

Synthesis of MOFs: CUB-5 was prepared using a slightly modified procedure from the literature by Macreadie et al.[4a] In a 20 mL glass scintillation vial 1,4-cubane dicarboxylic acid (29 mg, 0.15 mmol, 1 equiv.) and zinc nitrate hexahydrate (134 mg, 0.45 mmol, 3 equiv.) were dissolved in anhydrous DMF (10 mL) and sonicated. The vial was then placed in a forced circulation oven and heated at 100°C for 24 h. After slowly cooling to room temperature, crystalline product was collected. This procedure corresponds to a single small batch, and the samples used for subsequent measurements were obtained by combining multiple small batches prepared with the same conditions. We believe that this will ensure a more uniform growth of the MOF crystals.

1.7.3 Activation and Characterization of CUB-5

The as-synthesized CUB-5 crystals were washed with anhydrous DMF and soaked in fresh DMF for 24 h. The sample was then subjected to solvent exchange with extra dry DCM over 72 h, during which the solvent was replaced every 12 h. Finally, the sample was evacuated under high vacuum at room temperature to 40°C for 24 h to afford a crystalline white powder as activated CUB-5. The CP-MAS ^{13}C NMR spectrum and PXRD pattern of the activated sample are shown in **Figure 12**.

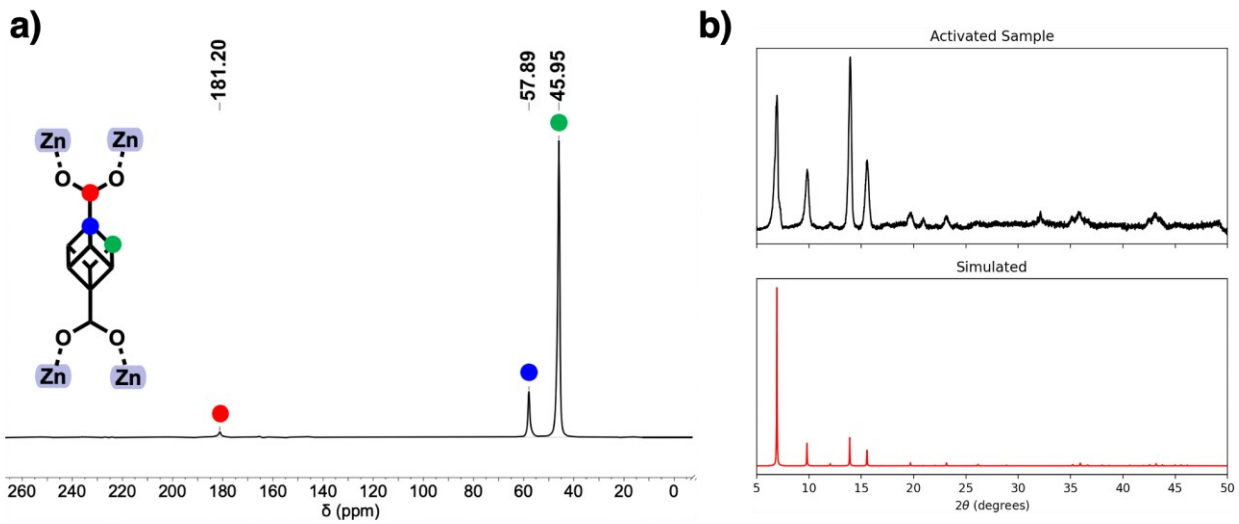

Figure 12. (a) Solid-state CP-MAS ^{13}C NMR spectrum (150 MHz, 298 K) and (b) PXRD pattern of activated CUB-5.

1.7.4 Spin-Lattice (T_1) Relaxation Time Measurements of CUB-5

Sample preparation: To thoroughly eliminate any potential influence of trace residual solvent molecules on the T_1 measurements, the CUB-5 sample was further activated at 120°C under high vacuum for 12 h. The activated sample was then loaded into a Pyrex NMR tube of around 2 cm in length, which was cut from a standard one. Both ends of the tube were sealed with Teflon tape, with small pinholes introduced to allow gas exchange between the inside and outside. The tube was then wrapped with copper coils and placed in an ultrahigh-purity helium atmosphere within a variable temperature insert (VTI) with a homemade cryoprobe.

T_1 measurements and Kubo-Tomita fitting: ^1H NMR measurements were conducted with the solid-echo pulse technique and the spin-lattice relaxation times (T_1) were acquired using the saturation-recovery method. The nuclear spin relaxation process follows from the modulation of nuclear dipolar magnetic fields at the proton Larmor frequency ($\omega_0 = 2\pi\nu_0$) and the thermally

activated dynamics are modeled by the Kubo-Tomita equation (**eq 1** and **eq 2**). The fitting of the model using **eq 3** yields $C = (4.8 \pm 0.4) \times 10^8\ s^{-2}$, $E_a = 0.17 \pm 0.01$ kcal/mol and $\tau_0^{-1} = (1.03 \pm 0.01) \times 10^{12}\ s^{-1}$ (**Figure 11**).

1.7.5 ^{1}H and ^{13}C NMR Spectra of 1,4-Cubane Dicarboxylic Acid

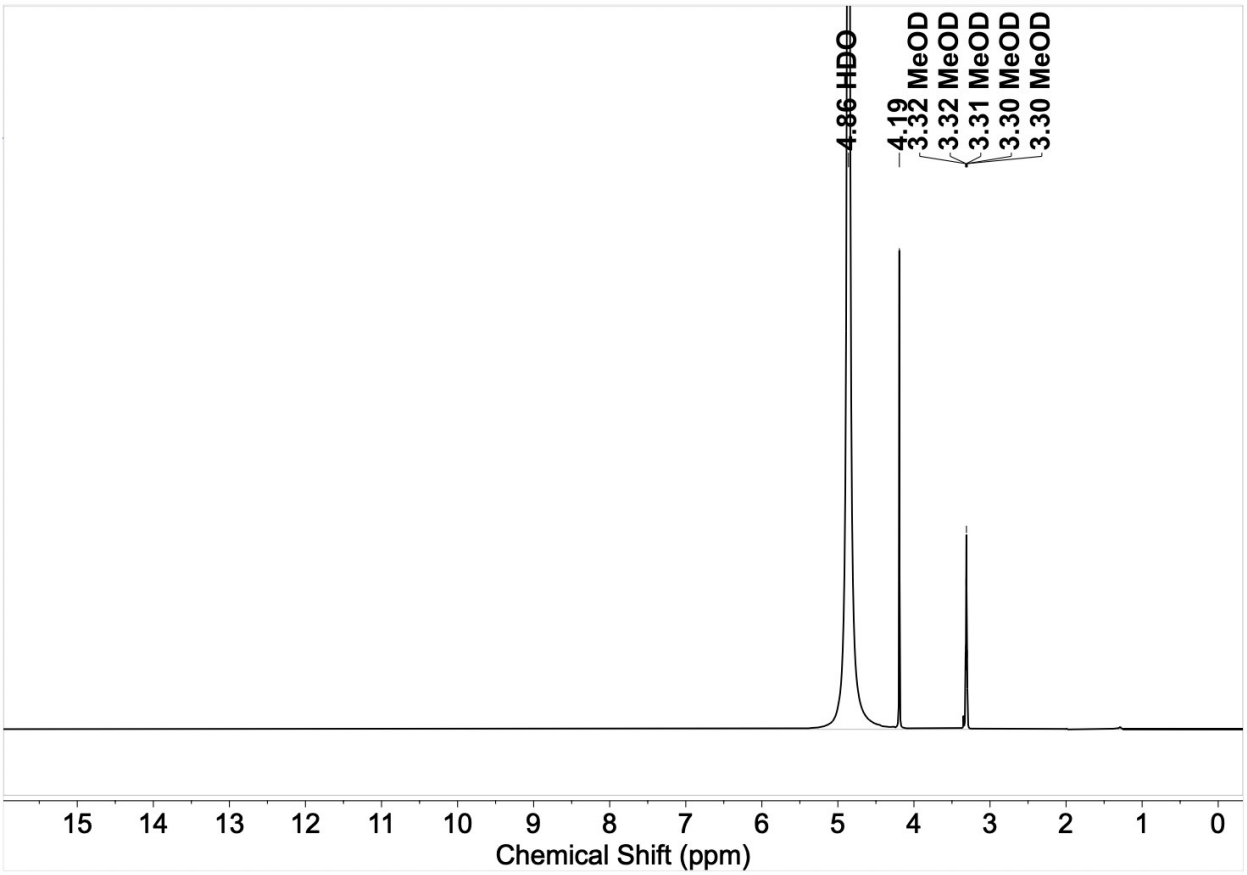

Figure 13. ^{1}H NMR spectrum of 1,4-cubane dicarboxylic acid (400 MHz, CD_3OD).

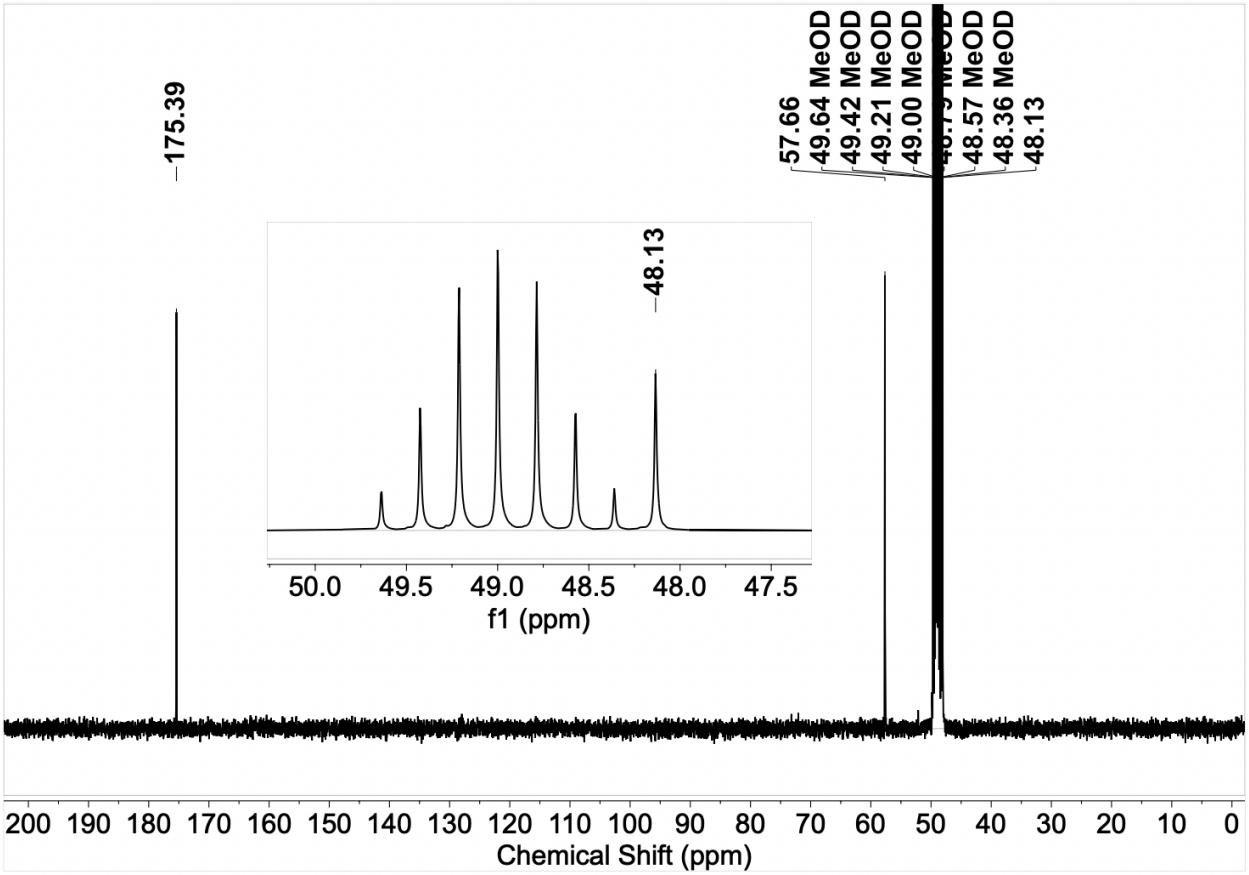

Figure 14. ^{13}C NMR spectrum of 1,4-cubane dicarboxylic acid (101 MHz, CD_3OD).

1.8 References

(1) (a) Dominguez, Z.; Dang, H.; Strouse, M. J.; Garcia-Garibay, M. A. Molecular "Compasses" and "Gyroscopes". I. Expedient Synthesis and Solid State Dynamics of an Open Rotor with a Bis(triarylmethyl) Frame. *J. Am. Chem. Soc.* **2002**, *124* (11), 2398−2399. (b) Khuong, T.-A. V.; Dang, H.; Jarowski, P. D.; Maverick, E. F.; Garcia-Garibay, M. A. Rotational Dynamics in a Crystalline Molecular Gyroscope by Variable-Temperature ^{13}C NMR, ^{2}H NMR, X-ray Diffraction, and Force Field Calculations. *J. Am. Chem. Soc.* **2007**, *129* (4), 839−845. (c) Khuong, T.-A. V.; Zepeda, G.; Ruiz, R.; Khan, S. I.; Garcia-Garibay, M. A. Molecular Compasses and

Gyroscopes: Engineering Molecular Crystals with Fast Internal Rotation. *Cryst. Growth Des.* **2004**, *4* (1), 15−18. (d) Howe, M. E.; Garcia-Garibay, M. A. The Roles of Intrinsic Barriers and Crystal Fluidity in Determining the Dynamics of Crystalline Molecular Rotors and Molecular Machines. *J. Org. Chem.* **2019**, *84*, 9835−9849.

(2) (a) Vogelsberg, C. S.; Uribe-Romo, F. J.; Lipton, A. S.; Yang, S.; Houk, K. N.; Brown, S.; Garcia-Garibay, M. A. Ultrafast Rotation in an Amphidynamic Crystalline Metal Organic Framework. *Proc. Natl. Acad. Sci. U.S.A.* **2017**, *114* (52), 13613−13618. (b) Perego, J.; Bracco, S.; Negroni, M.; Bezuidenhout, C. X.; Prando, G.; Carretta, P.; Comotti, A.; Sozzani, P. Fast Motion of Molecular Rotors in Metal−Organic Framework Struts at Very Low Temperatures. *Nat. Chem.* **2020**, *12* (9), 845−851. (c) Danowski, W.; van Leeuwen, T.; Abdolahzadeh, S.; Roke, D.; Browne, W. R.; Wezenberg, S. J.; Feringa, B. L. Unidirectional Rotary Motion in a Metal−Organic Framework. *Nat. Nanotechnol.* **2019**, *14*, 488−494. (d) Su, Y.-S.; Lamb, E. S.; Liepuoniute, I.; Chronister, A.; Stanton, A. L.; Guzman, P.; Pérez-Estrada, S.; Chang, T. Y.; Houk, K. N.; Garcia-Garibay, M. A.; Brown, S. E. Dipolar Order in an Amphidynamic Crystalline Metal−Organic Framework through Reorienting Linkers. *Nat. Chem.* **2021**, *13*, 278−283. (e) Perego, J.; Bezuidenhout, C. X.; Bracco, S.; Prando, G.; Marchio,` L.; Negroni, M.; Carretta, P.; Sozzani, P.; Comotti, A. Cascade Dynamics of Multiple Molecular Rotors in a MOF: Benchmark Mobility at a Few Kelvins and Dynamics Control by CO_2. *J. Am. Chem. Soc.* **2021**, *143*, 13082−13090. (f) Perego, J.; Bezuidenhout, C. X.; Bracco, S.; Piva, S.; Prando, G.; Aloisi, C.; Carretta, P.; Kaleta, J.; Le, T. P.; Sozzani, P.; Daolio, A.; Comotti, A. Benchmark Dynamics of Dipolar Molecular Rotors in Fluorinated Metal-Organic Frameworks. *Angew. Chem., Int. Ed.* **2023**, *62*, No. e202215893. (g) Liu, Z.; Wang, Y.; Garcia-Garibay, M. A. Rotational Dynamics of an Amphidynamic Zirconium Metal−Organic Framework Determined by Dielectric Spectroscopy. *J.*

Phys. Chem. Lett. **2021**, *12*, 5644−5648. (h) Liepuoniute, I.; Huynh, C. M.; Perez-Estrada, S.; Wang, Y.; Khan, S.; Houk, K. N.; Garcia-Garibay, M. A. Enhanced Rotation by Ground State Destabilization in Amphidynamic Crystals of a Dipolar 2,3-Difluorophenylene Rotator as Established by Solid State ^{2}H NMR and Dielectric Spectroscopy. *J. Phys. Chem. C* **2020**, *124*, 15391−15398. (i) Perego, J.; Daolio, A.; Bezuidenhout, C. X.; Piva, S.; Prando, G.; Costarella, B.; Carretta, P.; Marchio,` L.; Kubicki, D.; Sozzani, P.; Bracco, S.; Comotti, A. Solid State Machinery of Multiple Dynamic Elements in a Metal−Organic Framework. *Angew. Chem., Int. Ed.* **2024**, *63*, No. e202317094. (j) Liepuoniute, I.; Shan, J.-R.; Houk, K. N.; Garcia-Garibay, M. A. Computational Study of Ground-State Destabilization Effects and Dipole−Dipole Interaction Energies in Amphidynamic Crystals. *J. Org. Chem.* **2024**, *89*, 9−15. (k) Torres-Huerta, A.; Galicia-Badillo, D.; Aguilar-Granda, A.; Bryant, J. T.; Uribe-Romo, F. J.; Rodríguez-Molina, B. Multiple Rotational Rates in a Guest-Loaded, Amphidynamic Zirconia Metal−Organic Framework. *Chem. Sci.* **2020**, *11*, 11579−11583.

(3) Gould, S. L.; Tranchemontagne, D.; Yaghi, O. M.; Garcia-Garibay, M. A. Amphidynamic Character of Crystalline MOF-5: Rotational Dynamics of Terephthalate Phenylenes in a Free-Volume, Sterically Unhindered Environment. *J. Am. Chem. Soc.* **2008**, *130*, 3246−3247.

(4) (a) Macreadie, L. K.; Mensforth, E. J.; Babarao, R.; Konstas, K.; Telfer, S. G.; Doherty, C. M.; Tsanaktsidis, J.; Batten, S. R.; Hill, M. R. CUB-5: A Contoured Aliphatic Pore Environment in a Cubic Framework with Potential for Benzene Separation Applications. *J. Am. Chem. Soc.* **2019**, *141*, 3828−3832. (b) Macreadie, L. K.; Qazvini, O. T.; Babarao, R. Reversing Benzene/Cyclohexane Selectivity through Varying Supramolecular Interactions Using Aliphatic, Isoreticular MOFs. *ACS Appl. Mater. Interfaces* **2021**, *13*, 30885−30890. (c) Chen, C.; Maynard-Casely, H. E.; Duyker, S. G.; Babarao, R.; Kepert, C. J.; Evans, J. D.; Macreadie, L. K. Lowering

the Energetic Landscape for Negative Thermal Expansion in 3D-Linker Metal−Organic Frameworks. *Chem. Mater.* **2023**, *35*, 9945−9951.

(5) In this work, both the activation energy and attempt frequency obtained from MD simulations refer specifically to full 360° rotational events of the cubane rotor.

(6) Frisch, M. J.; Trucks, G. W.; Schlegel, H. B.; Scuseria, G. E.; Robb, M. A.; Cheeseman, J. R.; Scalmani, G.; Barone, V.; Petersson, G. A.; Nakatsuji, H.; Li, X.; Caricato, M.; Marenich, A. V.; Bloino, J.; Janesko, B. G.; Gomperts, R.; Mennucci, B.; Hratchian, H. P.; Ortiz, J. V.; Izmaylov, A. F.; Sonnenberg, J. L.; Williams-Young, D.; Ding, F.; Lipparini, F.; Egidi, F.; Goings, J.; Peng, B.; Petrone, A.; Henderson, T.; Ranasinghe, D.; Zakrzewski, V. G.; Gao, J.; Rega, N.; Zheng, G.; Liang, W.; Hada, M.; Ehara, M.; Toyota, K.; Fukuda, R.; Hasegawa, J.; Ishida, M.; Nakajima, T.; Honda, Y.; Kitao, O.; Nakai, H.; Vreven, T.; Throssell, K.; Montgomery, J. A., Jr.; Peralta, J. E.; Ogliaro, F.; Bearpark, M. J.; Heyd, J. J.; Brothers, E. N.; Kudin, K. N.; Staroverov, V. N.; Keith, T. A.; Kobayashi, R.; Normand, J.; Raghavachari, K.; Rendell, A. P.; Burant, J. C.; Iyengar, S. S.; Tomasi, J.; Cossi, M.; Millam, J. M.; Klene, M.; Adamo, C.; Cammi, R.; Ochterski, J. W.; Martin, R. L.; Morokuma, K.; Farkas, O.; Foresman, J. B.; Fox, D. J. Gaussian 16, Revision 02C; Gaussian, Inc.: Wallingford CT, 2019.

(7) Zhao, Y.; Truhlar, D. G. The M06 Suite of Density Functionals for Main Group Thermochemistry, Thermochemical Kinetics, Noncovalent Interactions, Excited States, and Transition Elements: Two New Functionals and Systematic Testing of Four M06-Class Functionals and 12 Other Functionals. *Theor. Chem. Acc.* **2008**, *120*, 215−241.

(8) (a) Ditchfield, R.; Hehre, W. J.; Pople, J. A. Self-consistent molecular-orbital methods. IX. An extended Gaussian-type basis for molecular-orbital studies of organic molecules. *J. Chem. Phys.* **1971**, *54*, 724−728. (b) Hariharan, P. C.; Pople, J. A. The influence of polarization functions on

molecular orbital hydrogenation energies. *Theor. Chim. Acta* **1973**, *28*, 213−222. (c) Hehre, W. J.; Ditchfield, R.; Pople, J. A. Self−consistent molecular orbital methods. XII. Further extensions of Gaussian−type basis sets for use in molecular orbital studies of organic molecules. *J. Chem. Phys.* **1972**, *56*, 2257−2261. (d) Rassolov, V. A.; Pople, J. A.; Ratner, M. A.; Windus, T. L. 6−31G* basis set for atoms K through Zn. *J. Chem. Phys.* **1998**, *109*, 1223−1229.

(9) (a) Grimme, S.; Antony, J.; Ehrlich, S.; Krieg, H. A Consistent and Accurate Ab Initio Parametrization of Density Functional Dispersion Correction (DFT-D) for the 94 Elements H-Pu. *J. Chem. Phys.* **2010**, *132*, No. 154104. (b) Grimme, S.; Ehrlich, S.; Goerigk, L. Effect of the damping function in dispersion corrected density functional theory. *J. Comput. Chem.* **2011**, *32*, 1456−1465.

(10) Riplinger, C.; Neese, F. An Efficient and near Linear Scaling Pair Natural Orbital Based Local Coupled Cluster Method. *J. Chem. Phys.* **2013**, *138*, No. 034106.

(11) Neese, F.; Wennmohs, F.; Becker, U.; Riplinger, C. The ORCA Quantum Chemistry Program Package. *J. Chem. Phys.* **2020**, *152*, No. 224108.

(12) Weigend, F. Accurate Coulomb-Fitting Basis Sets for H to Rn. *Phys. Chem. Chem. Phys.* **2006**, *8*, 1057−1065.

(13) Weigend, F.; Häser, M.; Patzelt, H.; Ahlrichs, R. RI-MP2: Optimized Auxiliary Basis Sets and Demonstration of Efficiency. *Chem. Phys. Lett.* **1998**, *294*, 143−152.

(14) Kühne, T. D.; Iannuzzi, M.; Del Ben, M.; Rybkin, V. V.; Seewald, P.; Stein, F.; Laino, T.; Khaliullin, R. Z.; Schütt, O.; Schiffmann, F.; Golze, D.; Wilhelm, J.; Chulkov, S.; Bani-Hashemian, M. H.; Weber, V.; Borstnik, U.; Taillefumier, M.; Jakobovits, A. S.; Lazzaro, A.; Pabst, H.; Müller, T.; Schade, R.; Guidon, M.; Andermatt, S.; Holmberg, N.; Schenter, G. K.;

Hehn, A.; Bussy, A.; Belleflamme, F.; Tabacchi, G.; et al. CP2K: An Electronic Structure and Molecular Dynamics Software Package - Quickstep: Efficient and Accurate Electronic Structure Calculations. *J. Chem. Phys.* **2020**, *152*, No. 194103.

(15) Perdew, J. P.; Burke, K.; Ernzerhof, M. Generalized gradient approximation made simple. *Phys. Rev. Lett.* **1996**, *77*, 3865−3868.

(16) VandeVondele, J.; Hutter, J. Gaussian Basis Sets for Accurate Calculations on Molecular Systems in Gas and Condensed Phases. *J. Chem. Phys.* **2007**, *127*, No. 114105.

(17) Marenich, A. V.; Jerome, S. V.; Cramer, C. J.; Truhlar, D. G. Charge Model 5: An Extension of Hirshfeld Population Analysis for the Accurate Description of Molecular Interactions in Condensed Phases. *J. Chem. Theory Comput.* **2012**, *8*, 527−541.

(18) (a) Lu, T.; Chen, F. Multiwfn: A Multifunctional Wavefunction Analyzer. *J. Comput. Chem.* **2012**, *33*, 580−592. (b) Lu, T. A comprehensive electron wavefunction analysis toolbox for chemists Multiwfn. *J. Chem. Phys.* **2024**, *161*, No. 082503.

(19) Wang, J.; Wolf, R. M.; Caldwell, J. W.; Kollman, P. A.; Case, D. A. Development and Testing of a General Amber Force Field. *J. Comput. Chem.* **2004**, *25*, 1157−1174.

(20) Rappe, A. K.; Casewit, C. J.; Colwell, K. S.; Goddard, W. A., III; Skiff, W. M. UFF, a Full Periodic Table Force Field for Molecular Mechanics and Molecular Dynamics Simulations. *J. Am. Chem. Soc.* **1992**, *114*, 10024−10035.

(21) Stephens, P. J.; Devlin, F. J.; Chabalowski, C. F.; Frisch, M. J. Ab Initio Calculation of Vibrational Absorption and Circular Dichroism Spectra Using Density Functional Force Fields. *J. Phys. Chem. A* **1994**, *98*, No. 11623.

(22) Lu, T. Sobtop, Version 1.0 (dev4), **2025**. http://sobereva.com/soft/Sobtop. (accessed on March 01, 2025).

(23) Abraham, M. J.; Murtola, T.; Schulz, R.; Páll, S.; Smith, J. C.; Hess, B.; Lindahl, E. GROMACS: High Performance Molecular Simulations through Multi-Level Parallelism from Laptops to Supercomputers. *SoftwareX* **2015**, *1−2*, 19−25.

(24) Darden, T.; York, D.; Pedersen, L. Particle Mesh Ewald: An Nlog(N) Method for Ewald Sums in Large Systems. *J. Chem. Phys.* **1993**, *98*, 10089−10092.

(25) Bussi, G.; Donadio, D.; Parrinello, M. Canonical Sampling through Velocity Rescaling. *J. Chem. Phys.* **2007**, *126*, No. 014101.

(26) Berendsen, H. J. C.; Postma, J. P. M.; van Gunsteren, W. F.; DiNola, A.; Haak, J. R. Molecular Dynamics with Coupling to an External Bath. *J. Chem. Phys.* **1984**, *81*, 3684−3690.

(27) Martyna, G. J.; Klein, M. L.; Tuckerman, M. Nosé-Hoover Chains: A New Approach to Constant Temperature Molecular Dynamics. *J. Chem. Phys.* **1992**, *97*, 2635−2643.

(28) Here, we approximately convert the fitted attempt angular frequency (in rad/s) into a 360° rotational frequency (in turns/s) by dividing by 2π.

(29) Shan, J.-R.; Zhou, Q.; Yamamoto, R.; Saib, S. M.; Chavez, R.; Brown S. E.; Houk, K. N.; Garcia-Garibay, M. A. Gas-Phase-like Inertial Rotation of a Platonic Solid in Reticular Amphidynamic Crystals of CUB-5: Molecular Dynamics and Experiment. *J. Am. Chem. Soc.* **2025**, *147*, 41809−41818.

Chapter 2: Computational Insight into Free Molecular Rotors in Crystalline Solids: Inertial Rotational and Langevin Dynamics

2.1 Contributions

This chapter is based on the following published article: Jing-Ran Shan, Qingyang Zhou, K. N. Houk, and Miguel A. Garcia-Garibay, "Computational Insight into Free Molecular Rotors in Crystalline Solids: Inertial Rotational and Langevin Dynamics," *J. Am. Chem. Soc.* **2026**, *148*, 26373−26382. Qingyang Zhou and I contributed equally to this work and are listed as co-first authors. I designed and carried out most of the computational studies presented in this work. Qingyang Zhou developed RadVCalc, the in-house program used for trajectory analysis, and performed the machine-learning-potential molecular dynamics (MLP-MD) simulations. I also contributed to the writing of the main text of the manuscript.

2.2 Abstract

Recent studies have shown that metal−organic frameworks (MOFs) can enable ultralow rotational barriers for molecular rotors in the solid state. In this near-free-rotor regime, elucidating how molecules behave within an ordered lattice becomes central to both a fundamental understanding and the design of crystalline molecular machines. Here, using a series of structurally simple, isoreticular MOF-5 homologues as a common platform, we present a systematic computational investigation of the rotational dynamics of five highly symmetric, rigid cage-like hydrocarbon rotators − bicyclo[1.1.1]pentane (BCP), cubane (CUB), bicyclo[2.2.2]octane (BCO), barrelene (BAR), and diamantane (DIA) − over a broad temperature range of 30−300 K. We show

that under nearly barrierless conditions, these molecular rotators can exhibit inertia-dominated, continuous unidirectional rotations, which we quantify by the frequency of 360° turnover events. Temperature dependence of the 360° turnover frequency reveals clear differences among the rotors in how their dominant dynamical mechanisms transition with temperature. Furthermore, we introduce a Langevin description to quantitatively analyze the time evolution of the mean squared net angular displacement of the rotors in their rotational coordinate. We show that on long time scales all rotors enter the Brownian diffusion regime. The extracted rotational damping coefficients η reveal pronounced differences among the five rotors in both the strength of rotor−lattice coupling and its temperature dependence.

2.3 Introduction

How fast can molecules rotate within a crystal? Intuitively, a rigid macroscopic object constructed with ordered building blocks may be expected to contain rigid molecular units. Yet, with appropriate molecular design and crystal engineering strategies, certain molecular units can undergo rapid rotation around defined axes or anchoring points, even when embedded in rigid lattices. Some of them are able to achieve rotational motion comparable to the one observed for molecules in liquids, sometimes reaching gas-phase-like rotational frequencies. Crystalline systems that retain such pronounced internal molecular motion despite long-range structural order are known as amphidynamic crystals.[1]

Molecular rotors are an essential component in the realm of artificial molecular machines, often as a part of molecular gears, switches, and motors,[2] designed respectively to transfer rotational motion, change between states, or transduce excess energy into directional mechanical output.[3−5] We adopt here the nomenclature proposed by Michl et al.,[2] with the terms rotor, rotator,

stator, and axle referring respectively to the ensemble, the rotating unit, the static elements that provide a frame of reference for motion, and the linker that pins the rotator to the stator. In this article we address fundamental questions related to free, or quasi-free rotational motion in confined environments. Over the past two and a half decades, advances in molecular design and crystal engineering have enabled rotational barriers in the solid state to be reduced to fractions of a kcal/mol, in which rotational dynamics are often governed by weak interactions with the surrounding environments.[6] More recently, the use of metal−organic frameworks (MOFs) as structural platforms to design molecular rotors has further accelerated this progress. Owing to their highly ordered and tunable porous crystalline environments, rotational barriers can be reduced to extremely low values. Reports from our group and work from Sozzani and Comotti have shown that, even at cryogenic temperatures, molecular rotators embedded in MOFs can sustain rotational frequencies in the gigahertz (GHz) regime, with ultralow barriers in the range of 0.2 and 0.01 kcal/mol,[7] effectively approaching the limit of free molecules in the gas phase.

The concept of vanishing rotational barriers elicits a compelling question: how should the rotational performance of a molecular rotor be described? Or, more simply, what constitutes an ideal rotor? Intriguingly, the three representative examples of the above-mentioned reticular amphidynamic crystals, Zn-FTR (referred to as BCP-5 in this work), CUB-5, and BODCA-MOF (referred to as BCO-5 in this work), display striking structural similarities.[7a,b,8] First, their rotators are all highly symmetric and rigid, cage-like hydrocarbons: bicyclo[1.1.1]pentane (BCP), cubane (CUB), and bicyclo[2.2.2]octane (BCO). Second, all three systems share isostructural MOF-5 frameworks that adopt remarkably simple and highly isotropic crystal structures.[9] Such convergence in both molecular and framework structure thus provides an exceptional platform for probing the intrinsic rotational dynamics among various rotors and rotor candidates.

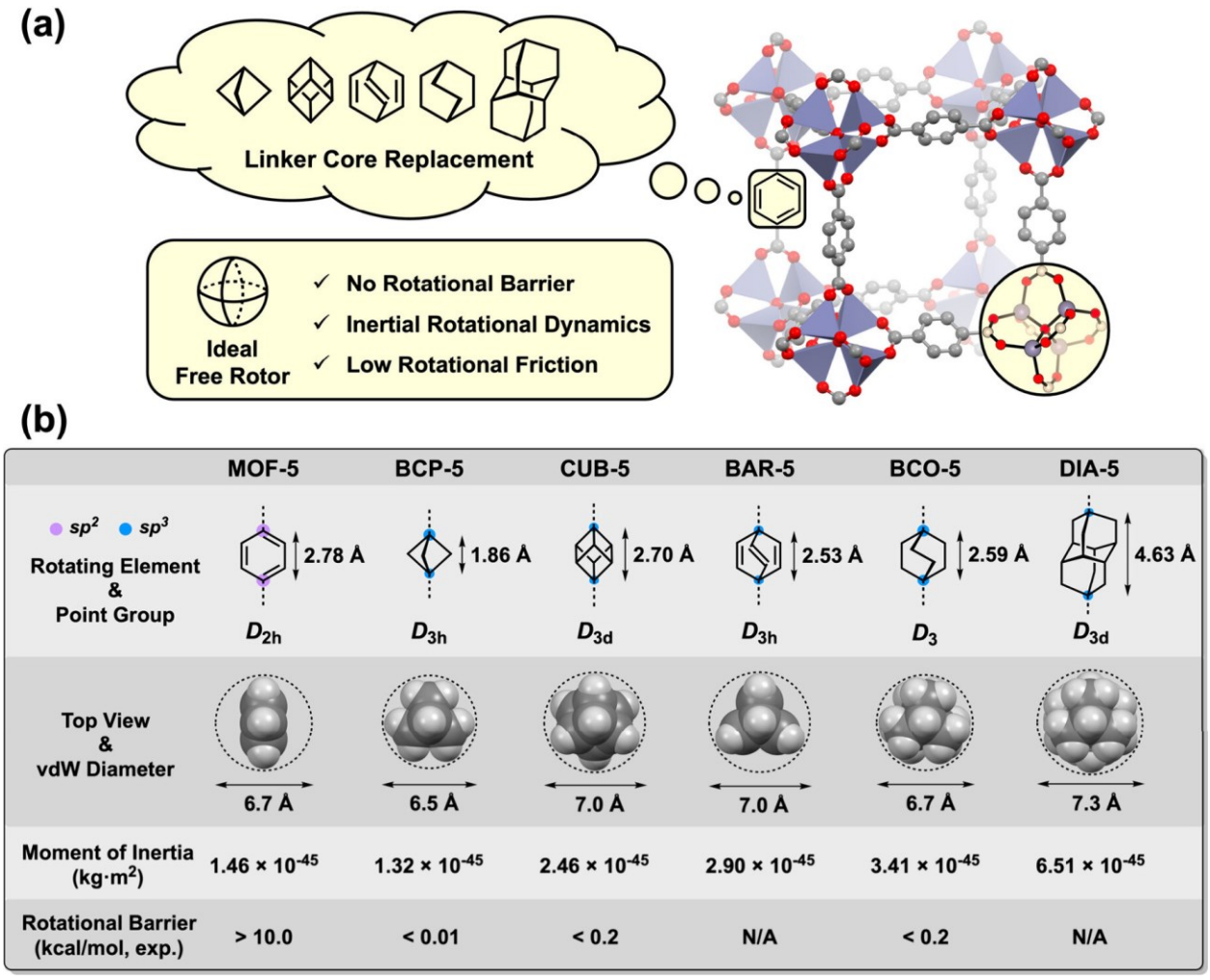

Figure 15. (a) Schematic representation of the MOF-5 structure and its nonaromatic isoreticular homologues. Hydrogen atoms are omitted for clarity. (b) Structural features of the rotating units in MOF-5 and its five isoreticular homologues investigated in this work. The last row shows the experimentally measured flipping or rotational barriers for MOF-5,[26] BCP-5,[7b] CUB-5,[7d] and BCO-5.[7a] In the actual crystal structure of BCP-5, the bicyclo[1.1.1]pentane dicarboxylate linker predominantly adopts an orthogonal conformation.

In this work, we combine quantum mechanical (QM) calculations and molecular dynamic (MD) simulations, employing the Langevin rotor model and Brownian motion theory, to systematically investigate the rotational dynamics of a series of highly symmetric and rigid cage-

like hydrocarbon rotators embedded in the isoreticular MOF-5 homologues. The rotator set studied in this work includes the previously mentioned bicyclo[1.1.1]pentane (BCP), cubane (CUB), and bicyclo[2.2.2]octane (BCO), as well as two additional rigid hydrocarbon rotor candidates: barrelene (BAR) and diamantane (DIA), as shown in **Figure 15a**. Their corresponding MOF-5 homologues are denoted with the "-5" suffix, i.e., BCP-5, CUB-5, BCO-5, BAR-5, and DIA-5. Crystal structures of the latter two have not yet been experimentally reported and are therefore treated as two hypothetical but theoretically valuable models in this work. For all five MOF systems, the rotor structures are anticipated to approach that of an ideal molecular rotor − which can be viewed as a spherical rigid body rotating freely about a fixed axis with no rotational barrier, while exhibiting inertial rotational dynamics and low rotational friction (**Figure 15a**). In this picture, their high rotational symmetry may give rise to a nearly flat rotational potential energy surface, while the rigid cage-like structure and minimal orientational interactions with the framework allow their motion to remain predominantly inertia-driven. Guided by this idealized picture, we quantitatively investigate (1) the intrinsic rotational barrier, (2) the frequency of sustained unidirectional rotation, and (3) the degree of rotor−lattice coupling of the five rotor systems. Our results elucidate how, within the regime of ultralow rotational barriers, these factors act in concert to determine the actual rotational behavior of molecular rotors in the solid state, thereby providing deeper insight into the understanding and design of molecular rotors operating under ultralow barrier regime.

2.4 Computational Methods

All quantum mechanical (QM) calculations were carried out using the Gaussian 16 program.[10] Structural information for all rotors in **Figure 15b** was obtained from geometry

optimizations performed in the gas phase at the M06−2X/def2-TZVP level of theory (with superfine integration grid).[11,12] For the MOF linkers, one-dimensional (1D) potential energy surface (PES) scans along the rotational coordinate of the rotor units were conducted at the same level. During the relaxed scans, the dihedral angle between the two carboxylate groups in the linker was fixed at 0°, ensuring a planar configuration. The dihedral angle $\theta_{O-C-C-C}$ between the carboxylate group and the rotor core was incrementally scanned in steps of 1°.

For each MOF-5 homologue containing a given rotator, geometry optimization of a 2 × 2 × 2 supercell containing 24 rotators was first performed using the CP2K program (version 2024.1) at the PBEsol/DZVP-MOLOPT-SR-GTH level of theory with periodic boundary conditions applied.[13−15] Single-point energies were then computed at the PBEsol/TZVP-MOLOPT-GTH level (with Zn atoms described using the TZVP-MOLOPT-SR-GTH basis set). Atomic charges were thus obtained using the Multiwfn program (version 3.8) with Truhlar and Cramer's Charge Model 5 (CM5) in order to reproduce the electrostatic potential on the molecular van der Waals surface during MD simulations.[16,17] Molecular force field parameters were generated using the General Amber Force Field (GAFF).[18] The missing parameters in GAFF were derived by constructing cluster models and fitting harmonic force constants based on density functional theory (DFT) calculations. Details of the parametrization procedure are provided in the Supporting Information of our published work,[30] where the Sobtop program was used.[19]

All MD simulations were performed using the GROMACS program (version 2021) with periodic boundary conditions applied.[20] A 4 × 4 × 4 supercell containing 192 rotators was first constructed, and an initial 2 ns equilibration simulation was carried out in the NPT ensemble using a velocity rescaling thermostat (time constant: τ_t = 0.2 ps) and a Berendsen barostat (isotropic pressure control at 1 atm, time constant: τ_p = 0.5 ps).[21,22] This allowed the system to relax to the

target temperature and yielded the average cell parameters, which were fixed for subsequent production simulations. The ensemble was then switched to NVT, and the production simulation was carried out using a Nosé-Hoover-chain thermostat (chain length = 10) with an extended time constant τ_t of 5.0 ps to minimize external perturbations to the intrinsic rotor dynamics.[23] In both equilibration and production phases, electrostatic interactions were treated using the particle-mesh Ewald (PME) method, and van der Waals interactions were treated by employing a cutoff of 1 nm.[24] The velocity Verlet algorithm was used for integration, and the simulation time step was set to 1 fs. For normal analyses discussed in the main text, a 10 ns production trajectory was collected at each temperature for each rotor.

Statistics of the unidirectional 360° rotations and the net angular displacements of the rotors were realized using our in-house program RadVCalc.[25] Details of the implementation of this analysis are provided in the Supporting Information of our published work.[30]

2.5 Results and Discussion

2.5.1 Rotor Structures and Intrinsic Rotational Barriers

We started by examining the molecular structure, symmetry, and intrinsic rotational barriers of the five rotors in the absence of lattice and environmental interactions. **Figure 15b** presents the structural features of the rotating units in the five MOF-5 homologues studied here. In contrast to the phenylene rotator in MOF-5, all five rotors possess bridgehead carbon atoms that are sp^3 hybridized, forming tetrahedral geometries with respect to their rotational axes. As a result, each rotor exhibits an effective 3-fold rotational symmetry during axial rotation. Compared to the 2-fold symmetry of the phenylene rotator, this renders their rotational profile closer to that of an

ideal sphere. Moreover, owing to their nonaromatic nature, these rotors do not experience conjugative interactions between the rotor core and the terminal carboxylate groups which must be overcome during the rotation in MOF-5. This absence of conjugation drastically reduces their intrinsic rotational barriers from approximately 11 kcal/mol for the benzene dicarboxylate rotator in MOF-5 to nearly negligible values (last row, **Figure 15b**).[26]

We first constructed single-molecule rotor models consistent with the actual MOF linker structures to obtain the one-dimensional (1D) rotational potential energy surfaces for each rotor. According to the geometry of MOF-5, the dicarboxylate MOF linker can in principle adopt two conformations upon coordination to the Zn_4O cluster: one where the two carboxylate groups are coplanar, and the second one with the two carboxylate groups being orthogonal to one another. In MOF-5, strong conjugation between the phenylene rotator and the carboxylate groups exclusively enforces the coplanar conformation in the crystal structure.[9a] In contrast, for the nonaromatic MOF-5 homologues, the absence of conjugation permits both conformations to coexist in the crystal: In the case of BCP-5, the relatively short axial length of bicyclo[1.1.1]pentane (~1.86 Å; **Figure 15b**) leads to stronger electrostatic repulsion between two coplanar carboxylates compared to its orthogonal conformation. As a result, the orthogonal conformation accounts for a more significant portion of the reported crystal structure.[7b] For CUB-5 and BCO-5, the longer axial lengths of cubane and bicyclo[2.2.2]octane (~2.70 Å and ~2.59 Å, respectively; **Figure 15b**) reduce such repulsion, making the two conformations nearly identical in energy. Therefore, the planar and orthogonal orientations of the dicarboxylate MOF linkers are experimentally indistinguishable in their crystal structures.[7a,8a] However, it should be noted that two orthogonal carboxylates (4-fold) combined with a 3-fold rotator would produce a 12-fold rotational symmetry with an extremely flat potential energy surface, which is challenging to describe reliably with

current computational approaches. For that reason, we decided to adopt the planar linker conformation throughout both the single-molecule model calculations and the subsequent molecular dynamic simulations. This modeling strategy also ensures structural and computational consistency across different rotors and facilitates meaningful comparison of their dynamical behaviors.

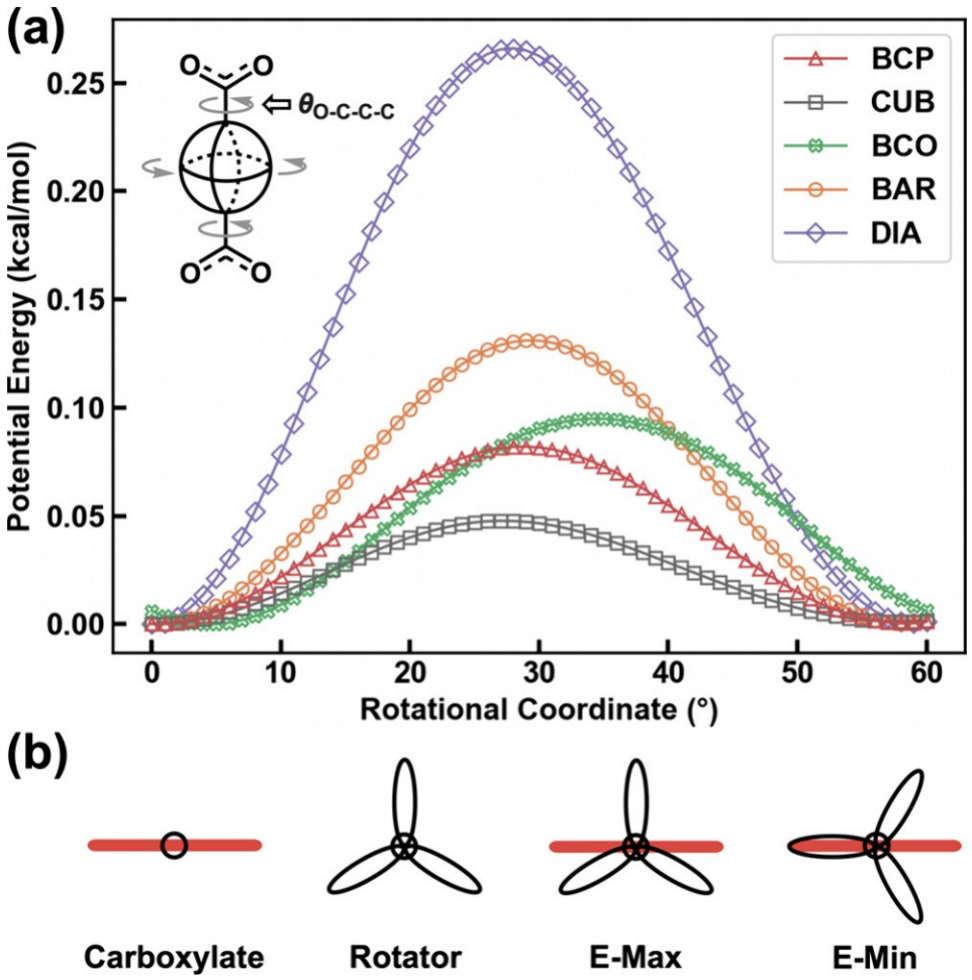

Figure 16. (a) 1D rotational potential energy surfaces of the five rotating units obtained from single-molecule rotor models. (b) Schematic illustration (top view) of the 2-fold carboxylate group, actual 3-fold rotator, maximum energy conformer, and minimum energy conformer during the scan.

As shown in **Figure 16**, for the single-molecule rotor models, the dihedral angle between the two carboxylate groups was fixed, while the dihedral angle $\theta_{O–C–C-C}$ between one carboxylate group and the rotor core was scanned from 0° to 60° in 1° increments. At each step, a constrained geometry optimization was performed at the M06−2X/def2-TZVP level of theory. The resulting potential energy curves exhibit regular periodicity, with energy minima and maxima alternately appearing every 30°, consistent with the expected 6-fold periodicity of the planar linker model (2-fold from the two coplanar carboxylates and 3-fold from the rotator). For bicyclo[1.1.1]pentane (BCP), cubane (CUB), barrelene (BAR), and diamantane (DIA), the energy minima and maxima occur near 0° (60°) and 30°, respectively. Bicyclo[2.2.2]octane (BCO, green cross), however, shows a ~5° shift due to the slight torsional distortion in its ground state structure. As seen from **Figure 15b** (middle row), the three carbon atoms in the upper half of bicyclo[2.2.2]octane are slightly staggered relative to those in the lower half (~9.5°), resulting in a D_3 symmetry slightly lower than the other rotors (D_{3h} and D_{3d}). In reality, bicyclo[2.2.2]octane exists in two enantiomeric ground states which rapidly interconvert through a barrier around 0.3 kcal/mol.[30] This feature endows it with additional degree of flexibility and conformational freedom compared to the other more rigid rotors.

The computed barrier heights reveal that bicyclo[1.1.1]pentane (BCP) and cubane (CUB) exhibit rotational barriers below 0.1 kcal/mol, followed by bicyclo[2.2.2]octane (BCO). Barrelene (BAR) presents a barrier of approximately 0.13 kcal/ mol, likely due to stronger electrostatic interactions between its more acidic C(sp^2)−H bonds and the carboxylate groups. Diamantane (DIA) shows the highest barrier of around 0.25 kcal/mol, possibly reflecting the subtle structural and electronic effects arising from its diamondoid framework. It is important to note that, however, given the inherent uncertainties of quantum chemical calculations in this low-energy regime, we

refrain from overinterpreting the absolute barrier heights, particularly for the bicyclo[1.1.1]pentane (BCP) and cubane (CUB) whose rotational barriers are well below 0.1 kcal/mol. Nevertheless, the overall conclusion is unambiguous: all five investigated rotors possess substantially lower rotational barriers than conventional molecular rotors. Their MOF-5 homologues should therefore display pronounced amphidynamic characteristics. On a thermal scale, even at 100 K ($k_BT \approx 0.2$ kcal/mol), these barriers can be readily overcome by thermal fluctuations.

2.5.2 Sustained Unidirectional Rotations

Before we proceed, it is useful to introduce a simple dimensionless parameter, $\Lambda = V_{barrier}/k_BT$, defined as the ratio between the rotational barrier and the thermal energy in the lattice environment. For an ideal free rotor, $\Lambda \sim 0$, whereas for real molecular rotors with finite barriers, Λ varies with temperature and provides a convenient measure of the extent to which the rotational dynamics deviate from the free-rotor limit.

To investigate the rotational behavior of the rotors within actual crystalline environments, we incorporated each rotor into a 4 × 4 × 4 MOF-5 supercell and performed molecular dynamic (MD) simulations. Each supercell contains 192 rotors, such that a single MD trajectory can provide 192 statistically equivalent samples for computing ensemble-averaged dynamical quantities. Periodic boundary conditions were applied in all three dimensions to eliminate finite-size effects.

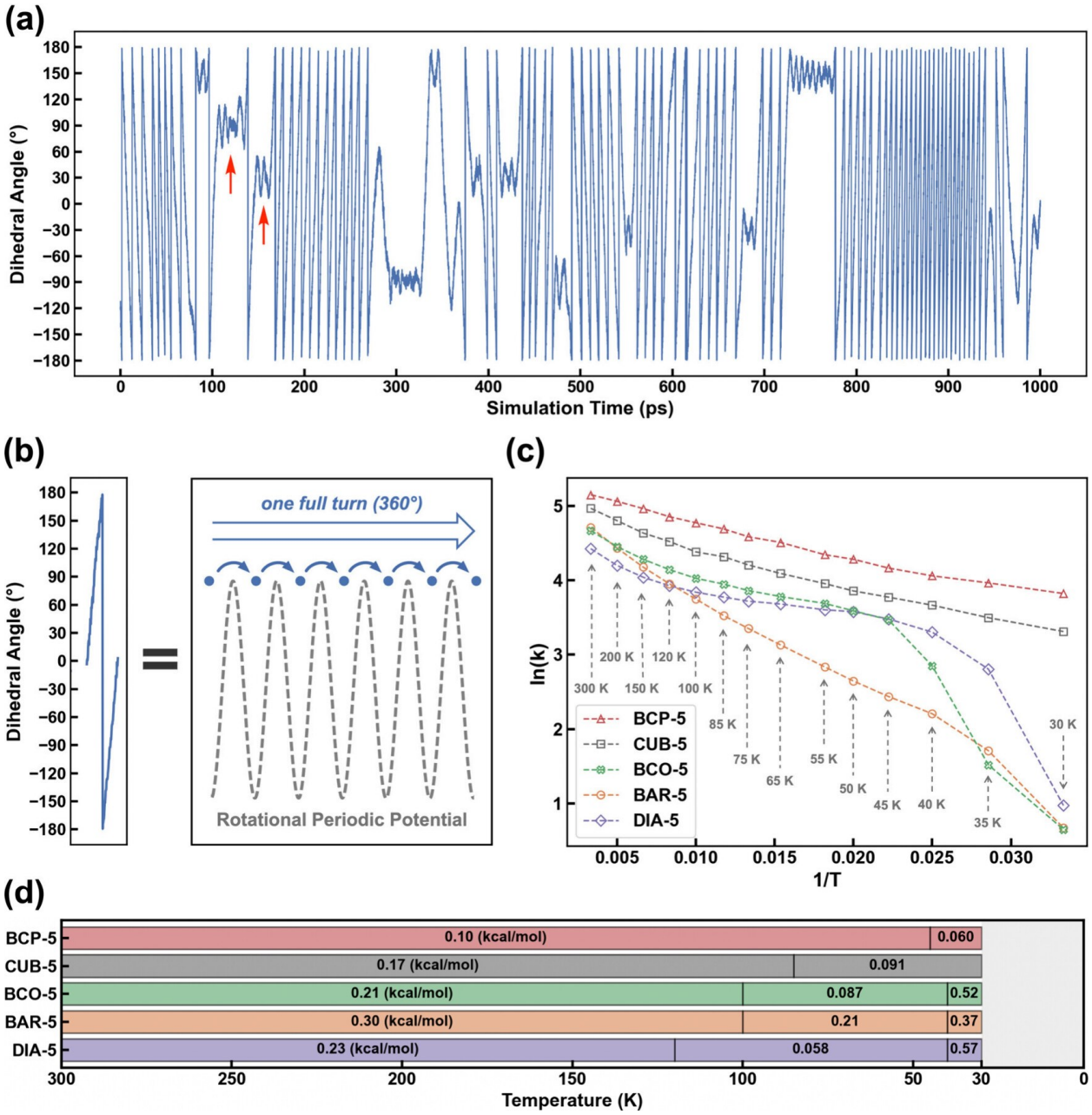

Figure 17. (a) Representative rotational trajectory of a single rotor in CUB-5 supercell at 100 K over 1000 ps (1 ns). The red arrows indicate several hopping events and residence between energy minima. (b) Schematic illustration of the mechanism of a 360° turnover event. (c) Temperature dependence of the averaged 360° turnover frequency k for the five rotors, shown as ln(k) versus 1/T over the range of 300−30 K. (d) Identification of distinct dynamical regimes from the ln(k)−1/T plots for the five rotors and their corresponding apparent activation energies E_a (kcal/mol) obtained from Arrhenius fits within each

temperature interval. The segmentation was determined using the Bayesian Information Criterion (BIC) to minimize potential fitting artifacts.

For each rotor, we monitored the dihedral angle $\theta_{O–C–C–C}$ between the carboxylate group and the rotating unit during the MD simulations, thereby obtaining the rotational coordinate as a function of the simulation time. **Figure 17a** illustrates a representative 1000 ps (1 ns) trajectory of one rotor in CUB-5 at 100 K. Within this short time scale, rich dynamical features are observed, such as stochastic hopping events between energy minima (examples are indicated by red arrows). These hopping events become more pronounced upon lowering the temperature, and the residence time following each jump increases substantially (**Figure 18**). As shown in **Figure 17a**, the rotor visits angular positions such as +150°, +90°, +30°, −30°, and −90°, consistent with the 6-fold periodicity predicted by the single-molecular rotor model. A second, particularly striking feature of the rotational trajectories in **Figure 17a** is the presence of numerous parallel lines with varying densities. As illustrated schematically in **Figure 17b**, each individual line corresponds to a unidirectional 360° turnover event: The rotor begins at 0° in the middle of the graph, rotates continuously upward to +180°, which is equivalent to −180°, so that it starts at the bottom and proceeds further in the same direction, ultimately returning to 0°, completing a full revolution (**Figure 17b**, left). In contrast to the intermittent hopping events between energy minima, such events represent rapid, continuous, unidirectional motion in which the rotor surmounts six energy maxima without being trapped in any potential well (**Figure 17b**, right). When these events occur consecutively, they are represented as parallel streaks in the rotational trajectory. The slope of each line indicates the direction of rotation, while the density of the lines reflects the 360° rotational frequency.

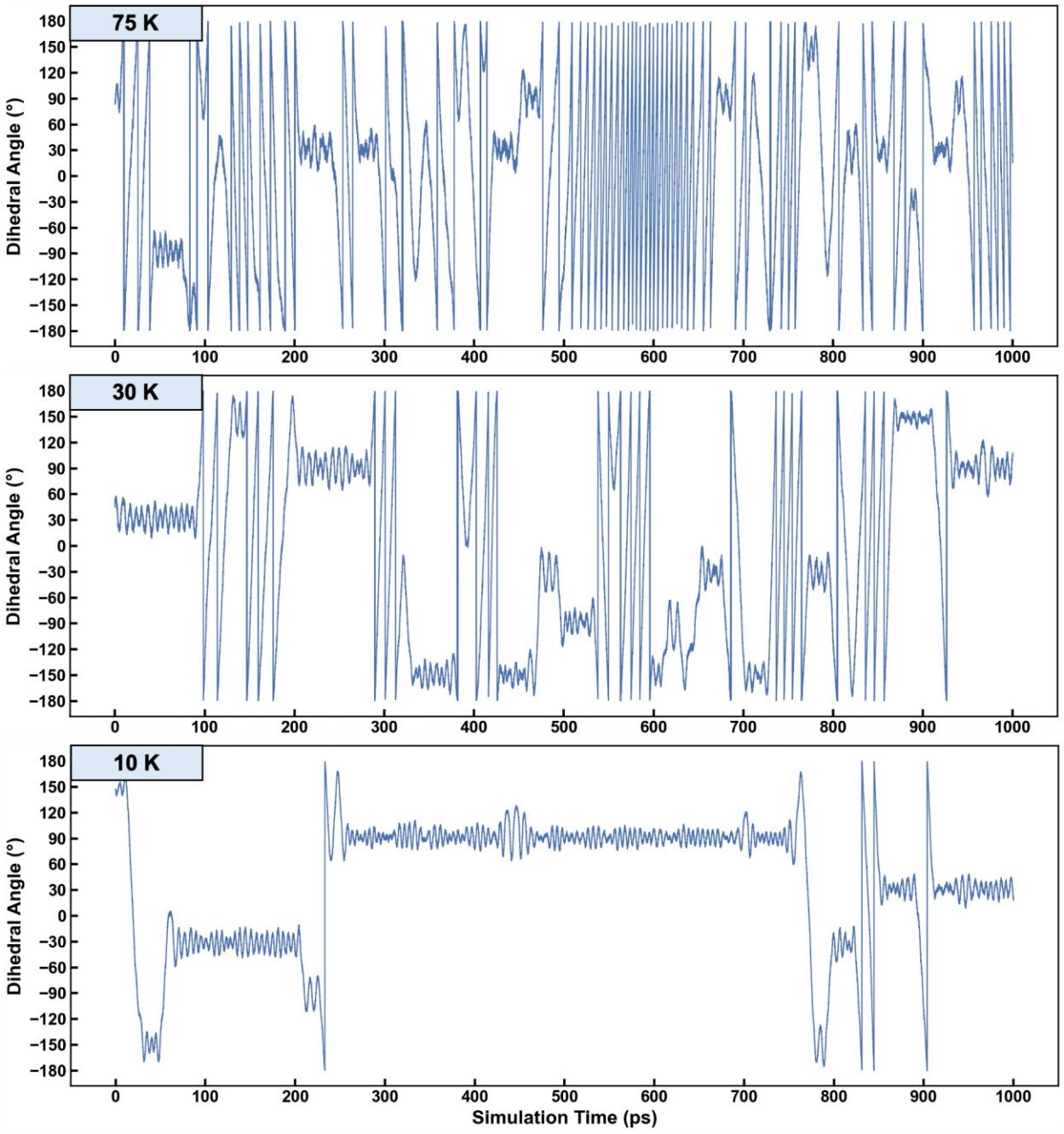

Figure 18. Rotational trajectory of a single rotor in CUB-5 supercell at 75 K, 30 K, and 10 K. It should be noted that the behavior of an individual rotor is not statistically representative compared to the averaged behavior of all 192 rotors.

This behavior is particularly intriguing, because completing a 360° turnover event requires not only overcoming six rotational barriers in succession, but also requires maintaining the directionality of angular momentum long enough to avoid randomization by system−environment coupling. We therefore regard the frequency of these 360° turnover events as a meaningful descriptor of a rotor's capability to sustain angular momentum and maintain dynamical stability over finite time scales at a given temperature. To analyze this, we performed MD simulations across a broad temperature range over 300−30 K. At each temperature, a 10 ns production trajectory was collected, and the 360° turnover frequency of each of the 192 rotors in the supercell was calculated to obtain an average frequency k (in GHz). It should be noted that random jumps by this metric result in slower full turn rotational frequencies. The temperature dependence of $\ln(k)$ recorded in this manner for all five rotors is presented in **Figure 17c**.

As shown in **Figure 17c**, differences in the 360° turnover capability among the five rotators are clearly manifested, each with varying degrees of deviations from linearity. At 300 K, BCP-5 exhibits the highest average rotational frequency of 172.24 GHz ($\ln(k) \approx 5.15$), whereas DIA-5 shows the lowest, with a value of 83.43 GHz ($\ln(k) \approx 4.42$), which is about half as large. As the temperature decreases toward 30 K, BCP-5 and CUB-5 display modest deviations from linearity and a relatively small slope to maintain relatively high average rotational frequencies of 45.68 and 27.43 GHz ($\ln(k) \approx 3.82$ and 3.31), respectively. In contrast, BCO-5, BAR-5, and DIA-5 display different regimes with varying slopes, reaching average frequencies below 3 GHz ($\ln(k) \approx 1.10$) at 30 K.

Deviations from linearity in the $\ln(k)$ versus $1/T$ plots reveal that these rotors do not follow a simple Arrhenius behavior over this broad temperature range of 300−30 K (**Figure 17c**). We suggest that the slope, and apparent activation energy variations reflect changes in rotator-lattice

dynamic interactions that affect their corresponding rotational dynamics as captured by the model. Taking the more complex behavior of BCO-5 as a reference, we identify three different regimes. The ln(k) vs 1/T shows the greatest slope in the 30−40 K range with an activation energy value of 0.52 kcal/mol (green cross, **Figure 17c**). A plateau region emerges between 40−120 K, with a much smaller activation energy of 0.087 kcal/mol. Further heating in the range of 120−300 K results in an upward temperature dependence with an activation energy that increases up to ca. 0.21 kcal/mol. A similar behavior with three analogous regimes can be observed for DIA-5 and BAR-5 with distinct low, medium, and high temperature regions. In contrast, BCP-5 and CUB-5 may be viewed as displaying only two dynamical regimes across the same temperature range of 300−30 K − in fact, a third regime characterized by a rapid decrease in slope would only emerge at extremely low temperatures. However, for these two systems, such a regime would occur near absolute zero and thus lies outside the scope of the present study.[30]

The estimated temperature regimes and activation energies for all five rotors are collected in the horizontal bar graphs displayed in **Figure 17d**, which span from 300 K to the left to 30 K to the right. Shown with a red horizontal bar, the suggested high and low temperature regimes for BCP-5 extend from 300 to 45 K, and from 45 to 30 K, respectively, with a modest change in slope from 0.10 to 0.060 kcal/mol. Similar information is encoded in different color bars for the other four molecular rotors. We suggest that this information reflects temperature-dependent transitions among different dominant dynamics mechanisms. At very low temperatures, even tiny energy barriers become significant, and rotors are more likely to remain trapped within individual potential wells. Turnover events in this region are governed primarily by multiple random thermally activated barrier crossings, primarily controlled by the intrinsic potential of the rotator. As the temperature increases, barrier crossings become facile, and inertia allows the rotor to

traverse multiple energy maxima consecutively. Lattice thermal fluctuations in this temperature range are not yet sufficient to randomize angular momentum. At still higher temperatures, stronger thermal fluctuations randomize angular momentum efficiently, thereby reducing the directional correlation required for sustained unidirectional motion. As a result, a stronger temperature dependence of 360° turnover events emerges, leading to an increase in the apparent activation energy.

This observation is particularly interesting, as it can be rationalized by a rough estimate using the above-mentioned parameter Λ. Taking BCO-5, BAR-5, and DIA-5 as examples, their rotational barriers obtained from MD simulations are on the order of ~ 0.2 kcal/mol.[30] The onset of their barrier-dominated regime around ~ 40 K ($k_BT \approx 0.08$ kcal/ mol) therefore corresponds to Λ values of approximately 2−3, at which point the rotors can be regarded as hindered. In contrast, for BCP-5 and CUB-5 whose effective barriers are below ~ 0.05 kcal/mol,[30] Λ values remains in the range of ca. 0.05−0.8 over the temperature range of 300−30 K. Comparable Λ values of 2−3 for BCP-5 and CUB-5 would only be reached at much lower temperatures, well beyond the $1/T$ window explored here, consistent with the absence of a distinct thermally activated regime in our analysis.

2.5.3 Langevin Dynamics and Rotational Damping Coefficients

We now return to the idealized picture of a molecular rotor depicted in **Figure 15a**. For a rotor undergoing rotation about a fixed axis, its motion is described by a single torsional degree of freedom, θ. In the present systems, this fixed axis is imposed by the MOF-5 framework geometry, which constrains the rotor to effectively one-dimensional rotation. This can therefore be treated as a one-dimensional rotor system.[2] The generalized coordinate $\theta(t)$ represents the angular position

of the rotator, while its first- and second-time derivatives correspond to its angular velocity and angular acceleration, respectively. In the absence of external driving torques (such as an electric field acting on a rotating dipole in the case of rotary dipolar arrays), the total torque acting on a rotator consists of three contributions: The conservative torque arising from the intrinsic periodic potential; the dissipative torque due to environmental coupling; and the stochastic torque resulting from thermal fluctuations. The rotor dynamics thus follow the Langevin equation (**eq 4**):[27]

$$I\frac{d^2\theta}{dt^2} = \frac{-\partial V_{\text{net}}}{\partial\theta} - \eta\frac{d\theta}{dt} + \xi(T,t) \quad \textbf{(eq 4)}$$

where I is the moment of inertia, V_{net} is the intrinsic periodic potential, η is the friction constant, and $\xi(T,t)$ represents the stochastic torque induced by thermal fluctuations. In the ideal limit of a completely isolated system, where intrinsic barrier, friction, and thermal noise are all absent, the total torque vanishes, and the rotator would rotate at a constant angular velocity.

Under the approximation of a vanishing barrier but finite thermal coupling, however, the system reduces to a free rotor interacting with a thermostat. In this case, the Langevin equation can be solved analytically under the fluctuation−dissipation relation, and the mean squared net angular displacement of a rotor evolves with time as **eq 5**:[28]

$$\langle\theta_{\text{net}}^2\rangle = \frac{2k_BT}{\eta}\left[t - \frac{I}{\eta}\left(1 - e^{-\frac{\eta t}{I}}\right)\right] \quad \textbf{(eq 5)}$$

where k_B is the Boltzmann's constant, T is the absolute temperature, t is the evolution time, and η is the rotational damping coefficient. This equation contains both a linear term and an exponentially decaying term. At longer times when $t >> I/\eta$, the exponential term vanishes and **eq 5** reduces to **eq 6**:

$$\langle \theta_{\text{net}}^2 \rangle = \frac{2k_B T}{\eta} t \quad \textbf{(eq 6)}$$

where the mean squared net angular displacement increases linearly with time, indicating a diffusive Brownian behavior, which is also referred to as random walk. The characteristic time scale I/η serves as the relaxation time, marking the crossover from the inertia-dominated ballistic regime ($t < I/\eta$) to the diffusive regime ($t >> I/\eta$).

Given the extremely low intrinsic barriers of the five rotators examined in this work and the pronounced amphidynamic character of their MOF-5 homologues, their dynamical behaviors are expected to approach the barrierless free rotor limit to some extent. We therefore analyzed the evolution of the mean squared net angular displacement of each rotator from the MD trajectories.

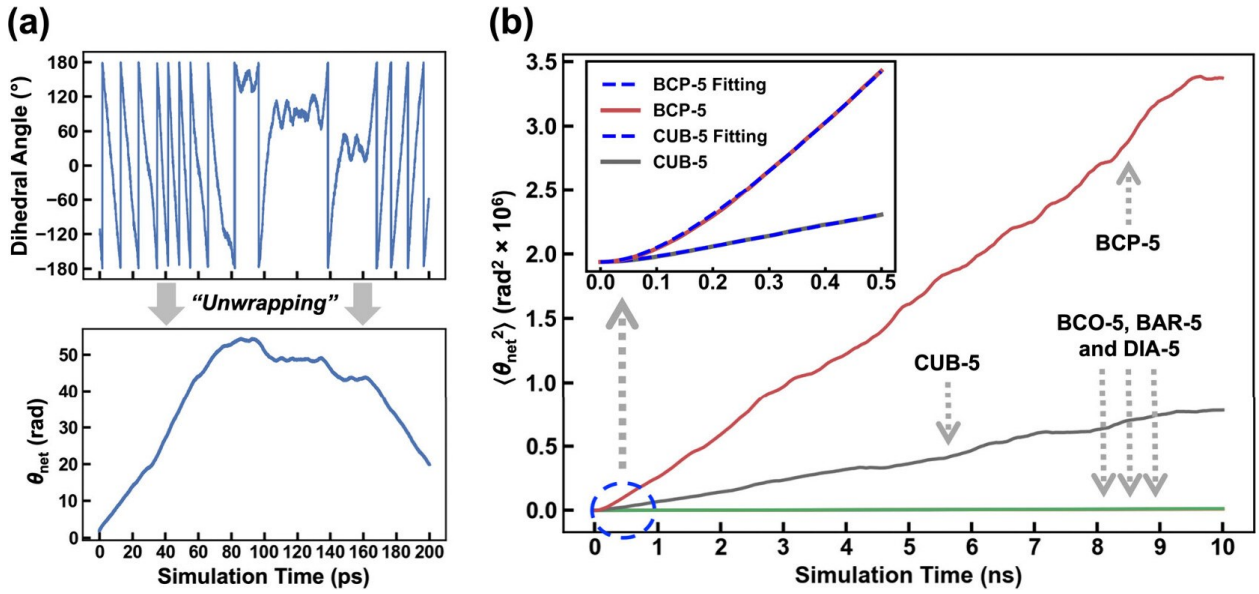

Figure 19. (a) Example of trajectory unwrapping for a rotor over 200 ps. Extraction of the net angular displacement from the raw rotational trajectory is illustrated. (b) Time evolution of the mean squared net angular displacement for the five rotors at 100 K over a 10 ns trajectory. The inset highlights the 0−0.5 ns region for BCP-5 and CUB-5, and their corresponding fits.

To obtain the net angular displacement, the rotational trajectories discussed previously were first unwrapped. **Figure 19a** shows an example from a 200 ps segment. From 0 to 80 ps, the rotator undergoes multiple consecutive 360° turnover events in a single direction, albeit with a nonconstant instantaneous velocity, yielding a monotonically increasing net angular displacement. Between 80 and 160 ps, the rotator undergoes stochastic hopping between energy minima, and resides within individual wells, leading to a stepwise evolution of the net angular displacement. From 160 to 200 ps, continuous rotation resumes but in the opposite direction, thus producing a monotonic decrease in net angular displacement, all of which can be used to obtain the desired mean squared net angular displacement $<\theta_{net}^2>$ values.

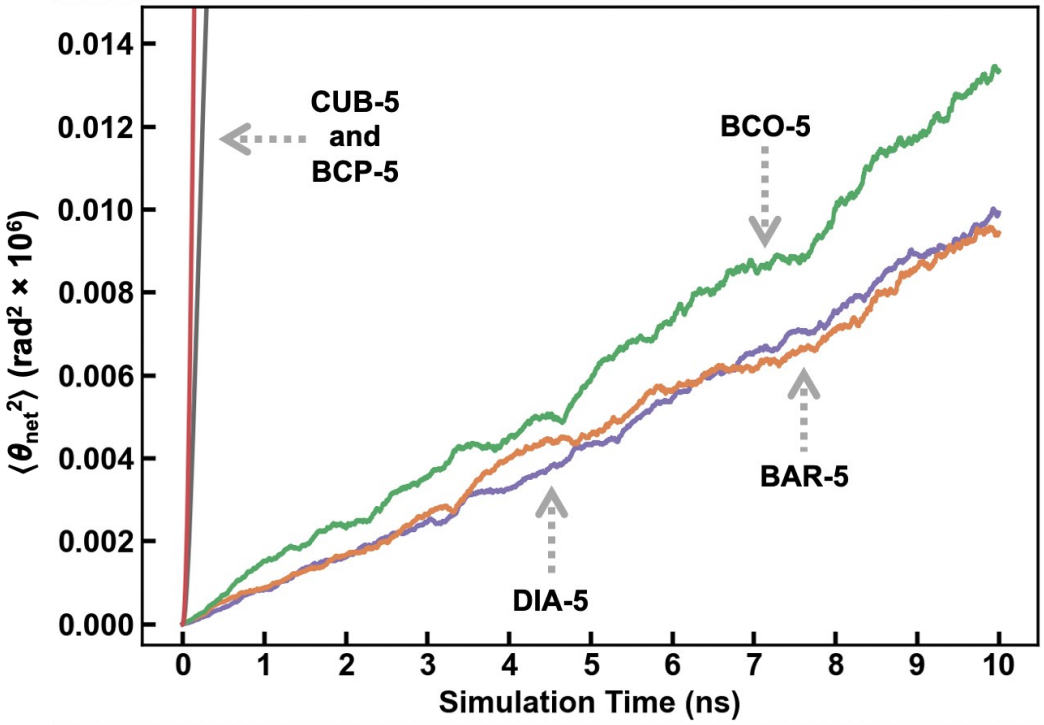

Figure 20. Time evolution of the mean squared net angular displacement for the five rotors at 100 K over a 10 ns trajectory. The region of BCO-5 (green), BAR-5 (orange), and DIA-5 (purple) are enlarged for clarity.

As in the previous analyses, the mean squared net angular displacement was averaged over all 192 rotors within each supercell. **Figure 19b** shows the results at 100 K as an example. For all five systems, the mean squared net angular displacement of rotors increases approximately linearly with time. BCP-5 exhibits the largest slope, followed by CUB-5. By contrast, BCO-5, BAR-5, and DIA-5 have much smaller slopes and therefore nearly overlap on this time scale (**Figure 19b**, green line; see **Figure 20** for an enlarged view of this region). Notably, BCP-5 and CUB-5 show a gradually increasing slope within the initial 0−0.5 ns window (**Figure 19b**, inset), reflecting the influence of the exponential term in **eq 5** at short times. This regime can be fitted in a reasonable manner using **eq 5**, yielding relaxation times (I/η) of approximately 153 and 56 ps for BCP-5 and

CUB-5, respectively. These results indicate substantially longer inertia-dominated regimes of BCP-5 and CUB-5 compared to the other systems. For BCO-5, BAR-5, and DIA-5, the relaxation times are well below 1 ps and nearly indistinguishable, implying that these rotors enter the diffusive regime almost instantaneously.

Table 1. Fitted rotational damping coefficients for the five rotors in the range of 300−30 K.

Rotational Damping Coefficient η ($kg{\cdot}m^2{\cdot}s^{-1} \times 10^{-35}$)					
	BCP-5	CUB-5	BCO-5	BAR-5	DIA-5
300 K	1.88	4.39	99.52	139.06	128.41
200 K	1.28	3.81	113.72	139.93	150.25
150 K	1.02	3.64	140.18	211.84	219.58
120 K	1.01	3.49	153.98	217.65	240.07
100 K	0.81	3.42	219.19	298.08	294.82
85 K	0.83	3.52	261.39	391.09	475.26
75 K	0.84	3.68	380.73	504.91	512.72
65 K	0.79	4.22	561.83	788.61	726.30
55 K	0.95	4.85	1020.27	1202.84	1530.05
50 K	1.05	5.77	1570.94	1396.35	1742.53
45 K	1.48	9.68	2334.62	2104.82	2678.48
40 K	1.47	9.89	3587.80	3404.06	5431.55
35 K	1.70	9.13	9211.29	9244.58	6723.12
30 K	1.82	17.11	20934.77	18110.87	22641.34

Fitting the full 10 ns trajectories allows quantitative extraction of the rotational damping coefficients η. As shown in the Supporting Information of our published work,[30] all fits display satisfactory linearity across the examined temperatures. The η values obtained between 300 and 30 K are summarized in **Table 1**. BCP-5 and CUB-5 consistently exhibit significantly smaller

damping coefficients than BCO-5, BAR-5, and DIA-5 across the entire temperature range, and their curves also display a clear exponential growth regime at early times (see the Supporting Information of our published work).[30] Moreover, their η values display much weaker temperature dependence, suggesting closer adherence to the simple Langevin model where the rotational damping coefficient is approximately constant. Plotting the data in **Table 1** on a logarithmic scale further highlights the differences in both magnitude and temperature dependence of η for the five rotor systems (**Figure 21**). For BCO-5, BAR-5, and DIA-5, the increase in η remains relatively modest between 300 and 100 K. Below 100 K − which corresponds approximately to Λ of 1 − the η begins to increase rapidly in an exponential manner, exhibiting an apparent thermally activated behavior. Although the Langevin model still provides satisfactory linear fits, the extracted damping coefficients in this regime are no longer purely reflective of rotor−lattice coupling, but instead incorporate substantial contributions from the rotational barrier term $V(\theta)$, which is formally absent in the underlying assumptions of **eq 5** and **eq 6**. In this sense, the extracted η here can be regarded as an effective quantity, η_{eff}, and its physical interpretation becomes less well-defined in regimes where $\Lambda > 1$. By contrast, between 300 and 100 K when $\Lambda < 1$, the temperature dependence of η is significantly reduced, and the extracted η values may be approximately regarded as the intrinsic (real) damping coefficient η_{real}. For BCP-5 and CUB-5, their η can be treated as η_{real} over nearly the entire range of 300−30 K as a reasonable estimate of the degree of intrinsic rotor−lattice coupling, and their $\Lambda > 1$ would only be reached at much lower temperatures (ca. 10−20 K).

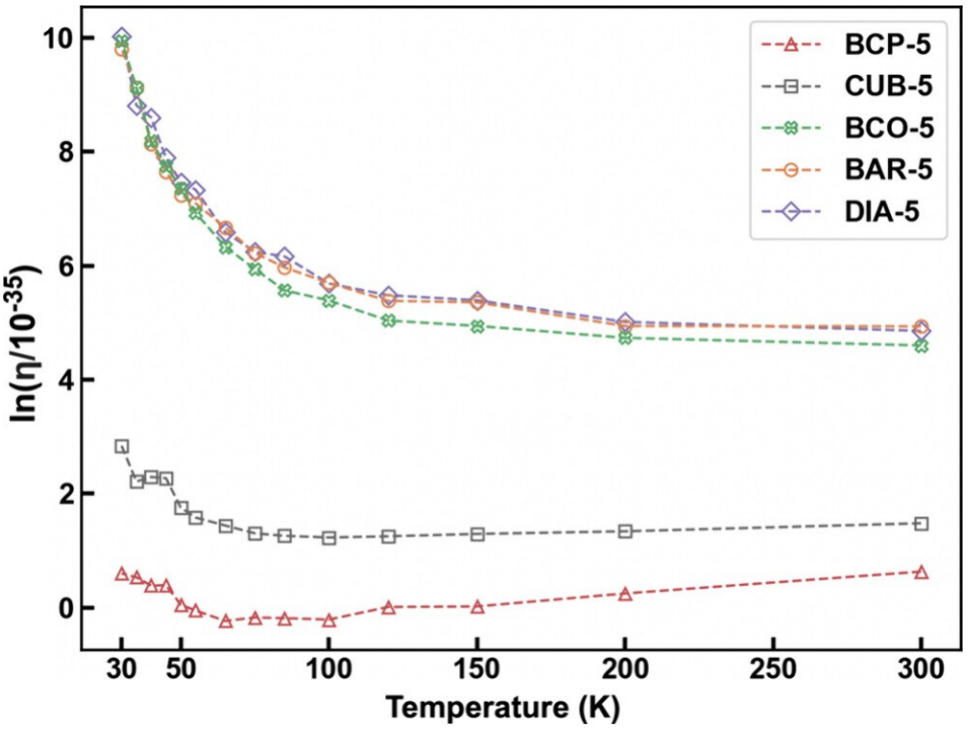

Figure 21. Logarithmic plot of rotational damping coefficients η for the five rotors as a function of temperature.

Based on the above analysis, the intrinsic rotational damping coefficients ηreal that reflect rotor−lattice coupling can be qualitatively ranked as BCP-5 < CUB-5 << BCO-5 ≈ BAR-5 ≈ DIA-5. Beyond the influence of the rotational barrier, we speculate that this trend may originate from differences in the coupling efficiency between the low-frequency (< 100 cm^{-1}) torsional modes of the rotor and lattice phonons. In particular, for BCO-5, BAR-5, and DIA-5, stronger coupling in this low-frequency range may introduce more efficient dissipative pathways, leading to enhanced energy dissipation than BCP-5 and CUB-5. In the case of BCO-5, this effect may be further amplified by its partial conformational flexibility, where fluctuating center of mass can provide additional channels for dissipation, which similarly increase the η.[29]

Furthermore, an interesting observation is that, for BCO-5, BAR-5, and DIA-5, the damping coefficient decreases monotonically with increasing temperature. In contrast, both BCP-5 and CUB-5 exhibit a minimum region in η values around 100 K, suggesting a temperature regime in which rotator-lattice dynamic coupling becomes weakest. It should be mentioned, however, that a smaller damping coefficient does not necessarily imply superior performance of a molecular rotor. Excessively low damping may lead to underdamped responses, potentially causing oscillatory or unstable behaviors when the rotor operates under external fields in practical molecular machine applications. Nevertheless, taken together, these results indicate that BCP-5 and CUB-5 remain considerably closer to the dynamical limit of a free molecular rotor across the examined temperature range, whereas BCO-5, BAR-5, and DIA-5 experience more pronounced environmental coupling and dissipation.

2.6 Conclusion

In summary, through combined quantum mechanical (QM) calculations and molecular dynamic (MD) simulations, we have presented a systematic computational investigation of five structurally rigid, highly symmetric cage-like hydrocarbon rotors embedded in the MOF-5 framework that enables direct comparison of their intrinsic barriers and lattice-coupled rotational dynamics. Quantum mechanical calculations confirm that all five rotors possess ultralow intrinsic periodic rotational barriers arising from their rigid, nonaromatic architectures, and effective 3-fold symmetry. Molecular dynamic simulations further reveal that these rotors exhibit rich dynamic behavior within their crystalline environments, including stochastic barrier-crossing events and sustained unidirectional rotations.

Analyses of the temperature dependence of the 360° turnover frequencies reveal distinct dynamic regimes among the rotators. BCP-5 and CUB-5 maintain smooth and continuous dynamics dominated by continuous rotation across the entire examined temperature range from 300 to 30 K, while BCO-5, BAR-5, and DIA-5 show pronounced regime transitions driven by the interplay among the thermally activated barrier crossings, inertia, and thermal fluctuations.

Application of the Langevin theory to the mean squared net angular displacement of the rotors further quantifies the extent of environmental coupling. BCP-5 and CUB-5 possess substantially longer inertia-dominated time scales and remarkably smaller damping coefficients than the other three systems, indicating weaker lattice coupling and closer proximity to the free-rotor limit in the solid state. In contrast, BCO-5, BAR-5, and DIA-5 exhibit stronger dissipation and temperature-dependent damping responses.

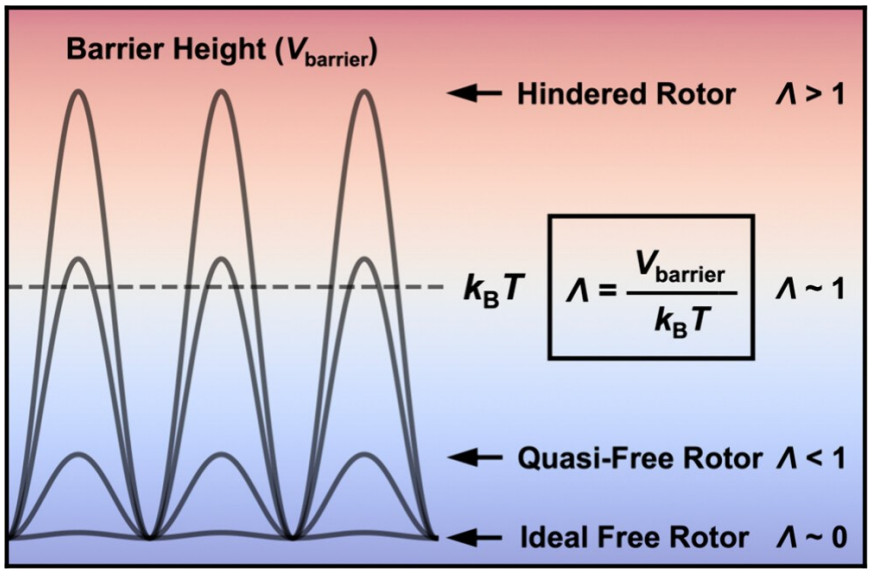

Figure 22. Schematic illustration of the rotational regimes of molecular rotors as a function of Λ. The blue-to-red gradient qualitatively represents the transition from free to hindered rotation.

A simple yet practical parameter Λ was also introduced to characterize the interplay between the rotational barrier (more precisely, the free energy barrier in the real environment) and thermal energy, as summarized in **Figure 22**. When $\Lambda < 1$, the rotor can be regarded as operating in a quasi-free regime, where barrier effects are negligible and the dynamics approach that of an ideal free rotor ($\Lambda \sim 0$). The rotor thus exhibits inertia-dominated motion at short times and diffusive Brownian behavior at longer times. In contrast, when $\Lambda > 1$, the rotor rapidly transitions into a hindered regime, where the intrinsic barrier can no longer be neglected and instead plays a dominant role in governing the rotational dynamics, leading to a thermally activated behavior and loss of sustained directional motion. It should be noted that, however, the term "hindered" in this work is defined relative to the free-rotor limit where $\Lambda \sim 0$. Compared to conventional molecular rotors, these systems still exhibit a significantly higher degree of freedom.

Together, this work establishes a quantitative physical framework for the fundamental understanding of molecular rotors operating in the ultralow barrier regime. Such understanding also offers guiding principles for the rational design of rotor-based molecular machines, including dipolar rotor arrays where dipole−dipole interactions and external fields become the dominant interaction and a promising handle for a wide range of materials applications.

2.7 References

(1) Garcia-Garibay, M. A. Crystalline molecular machines: Encoding supramolecular dynamics into molecular structure. *Proc. Natl. Acad. Sci. U.S.A.* **2005**, *102*, 10771.

(2) Kottas, G. S.; Clarke, L. I.; Horinek, D.; Michl, J. Artificial Molecular Rotors. *Chem. Rev.* **2005**, *105*, 1281.

(3) Garcia-Garibay, M. A.; Vogelsberg, C. S. Crystalline molecular machines: function, phase order, dimensionality, and composition. *Chem. Soc. Rev.* **2012**, *41*, 1892.

(4) Liepuoniute, I.; Jellen, M. J.; Garcia-Garibay, M. A. Correlated motion and mechanical gearing in amphidynamic crystalline molecular machines. *Chem. Sci.* **2020**, *11*, 12994.

(5) Jiang, P.; Jin, M. Design of Molecular Crystals toward Crystalline Molecular Machines: Rotors, Gears, and Motors. *ACS Nanosci. Au* **2025**, *5*, 428.

(6) (a) Catalano, L.; Perez-Estrada, S.; Wang, H.-H.; Ayitou, A. J.-L.; Khan, S. I.; Terraneo, G.; Metrangolo, P.; Brown, S.; Garcia-Garibay, M. A. Rotational Dynamics of Diazabicyclo[2.2.2]octane in Isomorphous Halogen-Bonded Co-crystals: Entropic and Enthalpic Effects. *J. Am. Chem. Soc.* **2017**, *139*, 843. (b) Jiang, X.; O'Brien, Z. J.; Yang, S.; Lai, L. H.; Buenaflor, J.; Tan, C.; Khan, S.; Houk, K. N.; Garcia-Garibay, M. A. Crystal Fluidity Reflected by Fast Rotational Motion at the Core, Branches, and Peripheral Aromatic Groups of a Dendrimeric Molecular Rotor. *J. Am. Chem. Soc.* **2016**, *138*, 4650. (c) Ando, R.; Sato-Tomita, A.; Ito, H.; Jin, M. Giant Crystalline Molecular Rotors that Operate in the Solid State. *Angew. Chem., Int. Ed.* **2023**, *62*, No. e202309694. (d) Ogawa, T.; Ishiwari, F.; Hajjaj, F.; Shoji, Y.; Kajitani, T.; Yazawa, K.; Ohkubo, T.; Fukushima, T. 2D hexagonal assembly of a dipolar rotor with a close interval of 0.8 nm using a triptycene-based supramolecular scaffold. *Chem. Sci.* **2024**, *15*, 11021. (e) Navarro-Huerta, A.; Jellen, M. J.; Arcudia, J.; Teat, S. J.; Toscano, R. A.; Merino, G.; Rodríguez-Molina, B. Tailoring the cavities of hydrogen-bonded amphidynamic crystals using weak contacts: towards faster molecular machines. *Chem. Sci.* **2021**, *12*, 2181.

(7) (a) Vogelsberg, C. S.; Uribe-Romo, F. J.; Lipton, A. S.; Yang, S.; Houk, K. N.; Brown, S.; Garcia-Garibay, M. A. Ultrafast Rotation in an Amphidynamic Crystalline Metal Organic Framework. *Proc. Natl. Acad. Sci. U.S.A.* **2017**, *114*, 13613. (b) Perego, J.; Bracco, S.; Negroni,

M.; Bezuidenhout, C. X.; Prando, G.; Carretta, P.; Comotti, A.; Sozzani, P. Fast Motion of Molecular Rotors in Metal−Organic Framework Struts at Very Low Temperatures. *Nat. Chem.* **2020**, *12*, 845. (c) Perego, J.; Bezuidenhout, C. X.; Bracco, S.; Prando, G.; Marchio, L.; Negroni, M.; Carretta, P.; Sozzani, P.; Comotti, A. Cascade Dynamics of Multiple Molecular Rotors in a MOF: Benchmark Mobility at a Few Kelvins and Dynamics Control by CO_2. *J. Am. Chem. Soc.* **2021**, *143*, 13082. (d) Shan, J.-R.; Zhou, Q.; Yamamoto, R.; Saib, S. M.; Chavez, R.; Brown, S. E.; Houk, K. N.; Garcia-Garibay, M. A. Gas-Phase-like Inertial Rotation of a Platonic Solid in Reticular Amphidynamic Crystals of CUB-5: Molecular Dynamics and Experiment. *J. Am. Chem. Soc.* **2025**, *147*, 41809.

(8) (a) Macreadie, L. K.; Mensforth, E. J.; Babarao, R.; Konstas, K.; Telfer, S. G.; Doherty, C. M.; Tsanaktsidis, J.; Batten, S. R.; Hill, M. R. CUB-5: A Contoured Aliphatic Pore Environment in a Cubic Framework with Potential for Benzene Separation Applications. *J. Am. Chem. Soc.* **2019**, *141*, 3828. (b) Macreadie, L. K.; Qazvini, O. T.; Babarao, R. Reversing Benzene/Cyclohexane Selectivity through Varying Supramolecular Interactions Using Aliphatic. Isoreticular MOFs. *ACS Appl. Mater. Interfaces* **2021**, *13*, 30885. (c) Chen, C.; Maynard-Casely, H. E.; Duyker, S. G.; Babarao, R.; Kepert, C. J.; Evans, J. D.; Macreadie, L. K. Lowering the Energetic Landscape for Negative Thermal Expansion in 3D-Linker Metal− Organic Frameworks. *Chem. Mater.* **2023**, *35*, 9945.

(9) (a) Li, H.; Eddaoudi, M.; O'Keeffe, M.; Yaghi, O. M. Design and synthesis of an exceptionally stable and highly porous metal-organic framework. *Nature* **1999**, *402*, 276. (b) Eddaoudi, M.; Kim, J.; Rosi, N.; Vodak, D.; Wachter, J.; O'Keeffe, M.; Yaghi, O. M. Systematic Design of Pore Size and Functionality in Isoreticular MOFs and Their Application in Methane Storage. *Science* **2002**, *295*, 469.

(10) Frisch, M. J.; Trucks, G. W.; Schlegel, H. B.; Scuseria, G. E.; Robb, M. A.; Cheeseman, J. R.; Scalmani, G.; Barone, V.; Petersson, G. A.; Nakatsuji, H.; Li, X.; Caricato, M.; Marenich, A. V.; Bloino, J.; Janesko, B. G.; Gomperts, R.; Mennucci, B.; Hratchian, H. P.; Ortiz, J. V.; Izmaylov, A. F.; Sonnenberg, J. L.; Williams-Young, D.; Ding, F.; Lipparini, F.; Egidi, F.; Goings, J.; Peng, B.; Petrone, A.; Henderson, T.; Ranasinghe, D.; Zakrzewski, V. G.; Gao, J.; Rega, N.; Zheng, G.; Liang, W.; Hada, M.; Ehara, M.; Toyota, K.; Fukuda, R.; Hasegawa, J.; Ishida, M.; Nakajima, T.; Honda, Y.; Kitao, O.; Nakai, H.; Vreven, T.; Throssell, K.; Montgomery, J. A., Jr.; Peralta, J. E.; Ogliaro, F.; Bearpark, M. J.; Heyd, J. J.; Brothers, E. N.; Kudin, K. N.; Staroverov, V. N.; Keith, T. A.; Kobayashi, R.; Normand, J.; Raghavachari, K.; Rendell, A. P.; Burant, J. C.; Iyengar, S. S.; Tomasi, J.; Cossi, M.; Millam, J. M.; Klene, M.; Adamo, C.; Cammi, R.; Ochterski, J. W.; Martin, R. L.; Morokuma, K.; Farkas, O.; Foresman, J. B.; Fox, D. J. Gaussian 16, Revision 02C; Gaussian, Inc.: Wallingford, CT, 2019.

(11) Zhao, Y.; Truhlar, D. G. The M06 Suite of Density Functionals for Main Group Thermochemistry, Thermochemical Kinetics, Noncovalent Interactions, Excited States, and Transition Elements: Two New Functionals and Systematic Testing of Four M06-Class Functionals and 12 Other Functionals. *Theor. Chem. Acc.* **2008**, *120*, 215.

(12) (a) Weigend, F.; Ahlrichs, R. Balanced basis sets of split valence, triple zeta valence and quadruple zeta valence quality for H to Rn: Design and assessment of accuracy. *Phys. Chem. Chem. Phys.* **2005**, *7*, 3297. (b) Weigend, F. Accurate Coulomb-fitting basis sets for H to Rn. *Phys. Chem. Chem. Phys.* **2006**, *8*, 1057.

(13) Kühne, T. D.; Iannuzzi, M.; Del Ben, M.; Rybkin, V. V.; Seewald, P.; Stein, F.; Laino, T.; Khaliullin, R. Z.; Schütt, O.; Schiffmann, F.; Golze, D.; Wilhelm, J.; Chulkov, S.; Bani-Hashemian, M. H.; Weber, V.; Borstnik, U.; Taillefumier, M.; Jakobovits, A. S.; Lazzaro, A.;

Pabst, H.; Müller, T.; Schade, R.; Guidon, M.; Andermatt, S.; Holmberg, N.; Schenter, G. K.; Hehn, A.; Bussy, A.; Belleflamme, F.; Tabacchi, G.; et al. CP2K: An Electronic Structure and Molecular Dynamics Software Package - Quickstep: Efficient and Accurate Electronic Structure Calculations. *J. Chem. Phys.* **2020**, *152*, 194103.

(14) Perdew, J. P.; Ruzsinszky, A.; Csonka, G. I.; Vydrov, O. A.; Scuseria, G. E.; Constantin, L. A.; Zhou, X.; Burke, K. Restoring the Density-Gradient Expansion for Exchange in Solids and Surfaces. *Phys. Rev. Lett.* **2008**, *100*, No. 136406.

(15) VandeVondele, J.; Hutter, J. Gaussian Basis Sets for Accurate Calculations on Molecular Systems in Gas and Condensed Phases. *J. Chem. Phys.* **2007**, *127*, 114105.

(16) (a) Lu, T.; Chen, F. Multiwfn: A Multifunctional Wavefunction Analyzer. *J. Comput. Chem.* **2012**, *33*, 580. (b) Lu, T. A comprehensive electron wavefunction analysis toolbox for chemists Multiwfn. *J. Chem. Phys.* **2024**, *161*, 082503.

(17) Marenich, A. V.; Jerome, S. V.; Cramer, C. J.; Truhlar, D. G. Charge Model 5: An Extension of Hirshfeld Population Analysis for the Accurate Description of Molecular Interactions in Condensed Phases. *J. Chem. Theory Comput.* **2012**, *8*, 527.

(18) Wang, J.; Wolf, R. M.; Caldwell, J. W.; Kollman, P. A.; Case, D. A. Development and Testing of a General Amber Force Field. *J. Comput. Chem.* **2004**, *25*, 1157.

(19) Lu, T. Sobtop, Version 1.0 (dev4), **http://sobereva.com/soft/Sobtop/**. (accessed on November 04, 2025).

(20) Abraham, M. J.; Murtola, T.; Schulz, R.; Páll, S.; Smith, J. C.; Hess, B.; Lindahl, E. GROMACS: High Performance Molecular Simulations through Multi-Level Parallelism from Laptops to Supercomputers. *SoftwareX* **2015**, *1−2*, 19.

(21) Bussi, G.; Donadio, D.; Parrinello, M. Canonical Sampling through Velocity Rescaling. *J. Chem. Phys.* **2007**, *126*, 014101.

(22) Berendsen, H. J. C.; Postma, J. P. M.; van Gunsteren, W. F.; DiNola, A.; Haak, J. R. Molecular Dynamics with Coupling to an External Bath. *J. Chem. Phys.* **1984**, *81*, 3684.

(23) Martyna, G. J.; Klein, M. L.; Tuckerman, M. Nosé-Hoover Chains: A New Approach to Constant Temperature Molecular Dynamics. *J. Chem. Phys.* **1992**, *97*, 2635.

(24) Darden, T.; York, D.; Pedersen, L. Particle Mesh Ewald: An Nlog(N) Method for Ewald Sums in Large Systems. *J. Chem. Phys.* **1993**, *98*, 10089.

(25) The in-house RadVCalc program can be downloaded from GitHub (**https://github.com/zhouoh/Radcalc**).

(26) Gould, S. L.; Tranchemontagne, D.; Yaghi, O. M.; GarciaGaribay, M. A. Amphidynamic Character of Crystalline MOF-5: Rotational Dynamics of Terephthalate Phenylenes in a Free-Volume, Sterically Unhindered Environment. *J. Am. Chem. Soc.* **2008**, *130*, 3246.

(27) Joachim, J.; Gimzewski, J. K. Single Molecular Rotor at the Nanoscale. *Struct. Bonding (Berlin)* **2001**, *99*, 1.

(28) Reif, F. *Fundamentals of Statistical and Thermal Physics*; Waveland Press, 2009; p 566.

(29) de la Torre, J. A.; Español, P. Internal dissipation in the Dzhanibekov effect. *Eur. J. Mechanics. A Solids* **2024**, *106*, No. 105298.

(30) Shan, J.-R.; Zhou, Q.; Houk, K. N.; Garcia-Garibay, M. A. Computational Insight into Free Molecular Rotors in Crystalline Solids: Inertial Rotation and Langevin Dynamics. *J. Am. Chem. Soc.* **2026**, *148*, 26373.

Chapter 3: Computational Study of Ground-State Destabilization Effects and Dipole−Dipole Interaction Energies in Amphidynamic Crystals

3.1 Contribution

This chapter is based on the following published article: Ieva Liepuoniute, Jing-Ran Shan, K. N. Houk, and Miguel A. Garcia-Garibay, "Computational Study of Ground-State Destabilization Effects and Dipole−Dipole Interaction Energies in Amphidynamic Crystals," *J. Org. Chem.* **2024**, *89*, 9−15. I am listed as the co-author of this article. I carried out the studies of the dual-rotor systems presented in this work. I also contributed to the writing of the manuscript.

3.2 Abstract

Ground-state destabilization is a promising strategy to modulate rotational barriers in amphidynamic crystals. Density functional theory studies of polar phenylenes installed as rotators in pillared paddle-wheel metal organic frameworks were performed to investigate the effects of ground-state destabilization on their rotational dynamics. We found that as the steric size of phenylene substituents increases, the ground-state destabilization effect is also increased. Specifically, a significant destabilization of the ground-state energy occurred as the size of the substituents increased, with values ranging from 2 to 11.7 kcal/mol. An evaluation of the effects of substituents on dipole−dipole interaction energies and rotational barriers suggests that it should be possible to engineer amphidynamic crystals where the dipole−dipole interaction energy becomes comparable to the rotational barriers. Notably, while pure dipole−dipole interaction energies reached values ranging from 0.6 to 2.4 kcal/mol, the inclusion of electronic and steric

effects can alter dipolar orientations to significantly greater values. We propose that careful selection of polar substituents with different sizes may help create temperature-responsive materials with switchable collective polarization.

3.3 Introduction

Amphidynamic crystals constitute a promising new class of functional materials characterized by structurally encoded order and motion in the same phase space.[1,2,3] With static, lattice-forming elements linked to mobile molecular components (**Figure 23a**), the amphidynamic crystal's dynamic behavior may be altered by a careful choice of structural elements. In the case of crystalline rotor arrays, rotational barriers are determined by their potential energy surfaces, which have contributions from their intrinsic (gas phase) torsional barriers and from intermolecular interactions with neighbors in the lattice. In particular, amphidynamic crystals derived from porous materials[4–7] with an empty volume that is greater than the volume of revolution of the rotator has barriers determined by the electronics of the bond serving as an axle and, as such, their rotational dynamics fall in the regime of activation control. By contrast, rotational barriers in densely packed molecular crystals have dynamics determined by their environment and fall in the regime of diffusion control as local displacements and librations, or "crystal fluidity", become rate-limiting.[8]

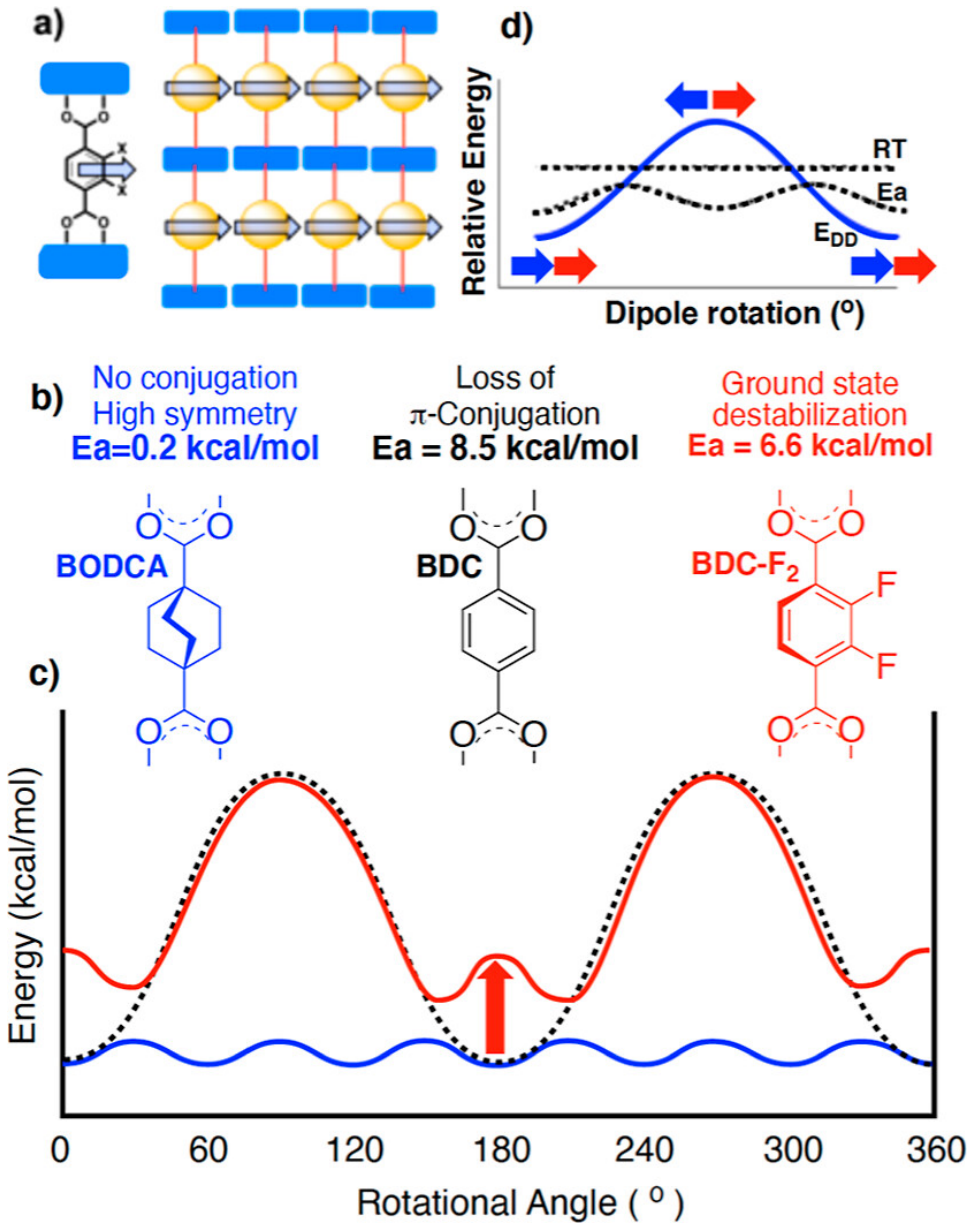

Figure 23. (a) Schematic representation of an amphidynamic crystal composed of a rotary dipole array. (b) Structures and rotational transition state energies for BDC, BODCA, and BDC-F_2. (c) Structural effects on the rotational potential of BDC, BODCA, and BDC-F_2 (please see text), and (d) ideal energetics required for spontaneous alignment and collective polarization include conditions where dipole−dipole interactions (E_{DD}) are greater than thermal agitation (RT), which should be greater than the rotational barrier (E_a).

In previous work on metal organic frameworks (MOFs) based on Zn paddlewheel complexes with 1,4-diazabicyclo[2.2.2]-octane (dabco) spacers and dicarboxylate rotators, we showed that changes in electronic conjugation and rotational symmetry lead to large variations in the potential energy surface (**Figure 23b** and **Figure 23c**). A high barrier of 8.5 kcal/mol reported in MOFs prepared with 1,4-benzenedicarboxylate[9,10] (BDC, **Figure 23b**) was reduced to 0.2 kcal/mol when an aliphatic 3-fold symmetric 1,4-bicyclo[2.2.2]octane-dicarboxylate (BODCA) was used.[11] We also showed an alternative with 2,3-difluoro-benzene-dicarboxylate (BDC-F_2), where lower barriers were observed as a result of the ground-state destabilization[12] that occurs from repulsive steric and/or electronic interactions between the rotator and the stator. These interactions prevent planarization and full electronic conjugation between the aromatic ring and the framework carboxylates (**Figure 23b** and **Figure 23c**).[13,14]

Results with BDC-F_2 suggest that substituents leading to greater dipole moments may have lower rotational barriers, making it possible to design tunable bulk polarization by collective dipole rotation.[15] In fact, we recently showed that amphidynamic crystals with rotary dipolar arrays can display emergent spontaneous alignment and respond collectively to strong electric fields, offering exciting possibilities in the field of stimuli-responsive materials.[16] Notably, ideal polarization by collective dipole reorientation would require rotational energy barriers (E_a, **Figure 23d**) to be smaller than orientation-dependent dipole−dipole interactions (E_{DD}), which should be greater than the energetics of thermal agitation (RT) in order to avoid random Brownian motion. Optimal E_{DD} values require short lattice dimensions and dipoles with strong electron-donating and/or electron-withdrawing substituents.[16]

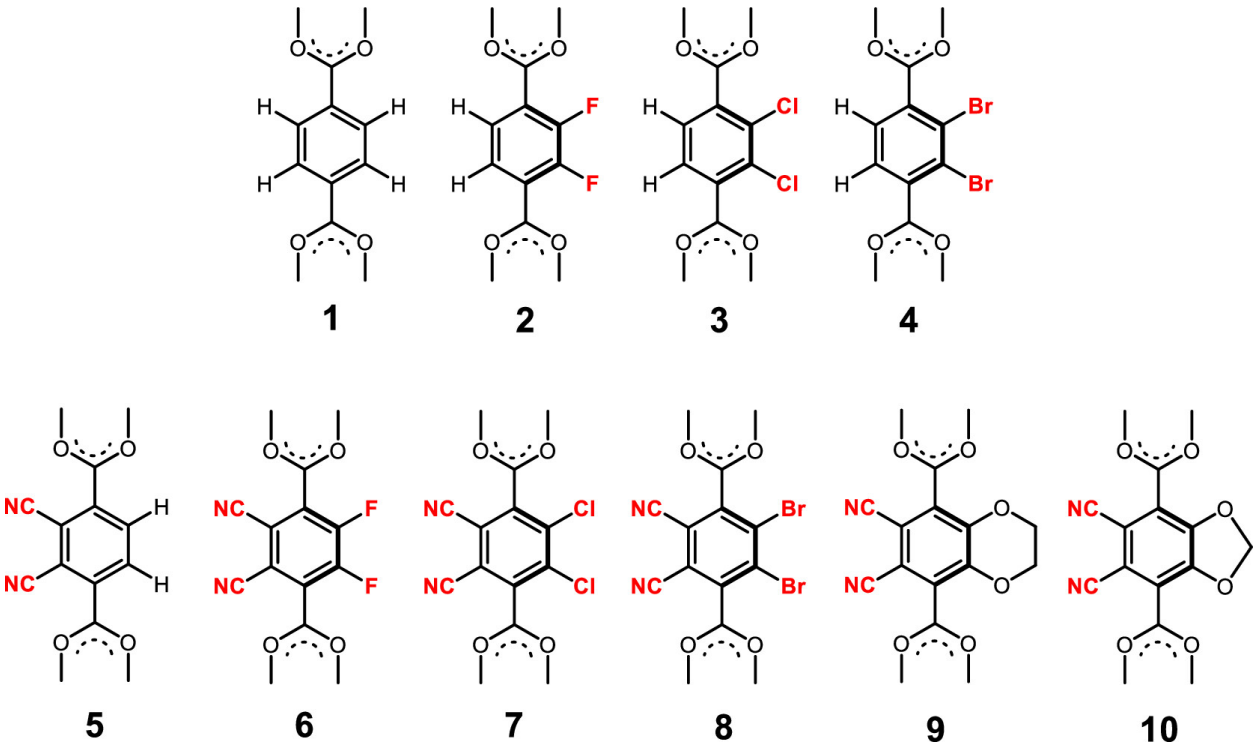

Scheme 1. Structures of polar benzene-1,4-dicarboxylate rotators.

In this paper, we describe the use of quantum mechanical calculations to explore the extent to which the destabilization of the global minimal structure, which we refer to as "ground-state destabilization", could be utilized as a rotational barrier-lowering strategy in paddle-wheel MOFs with polar phenylenes. Our computational studies comprise the aromatic groups in **Scheme 1**, including the previously analyzed unsubstituted benzene 1,4-dicarboxylate rotator **1** and 2,3-difluoro-benzene-1,4-dicarboxylate rotator **2**, as well as the higher halogenated homologues with 2,3-dichloro- and 2,3-dibromo-benzene-1,4-dicarboxylates **3** and **4**, respectively (**Scheme 1**).

By computing potential energy barriers for the rotation of phenylenes **1**−**4**, we sought to determine the effect of each halogen on the corresponding rotator coplanar ground-state destabilization. Additionally, with the goal of exploring the viability of amphidynamic crystals

where dipole−dipole interaction energies are comparable to the height of the structural barrier, we explore the "flattening potential" effect of F_2, Cl_2, and Br_2 on the barriers of the phenylenes containing polar 2,3-dicyano-benzenedicarboxylates. To that end, we calculated the potential energy barriers for the rotation of cyanophenylenes **5**−**8** with H, F, Cl, and Br substituents, respectively (**Scheme 1**). Recognizing that some of the largest dipole moments reported for substituted phenylene groups can be obtained by combining dicyano and dialkoxy substitutions, we explore molecular rotors **9** and **10** (**Scheme 1**). With this computational study, we aim at identifying suitable rotator candidates with low rotational barriers and the promise of spontaneous polarization.

3.4 Computational Methods

Our computational model was based on a rigid Zn paddle-wheel MOF analogue with $Zn_2(CO_2)_4$ metal clusters acting as stators, dacbo as spacers, and substituted BDC as rotators, making up a tetragonal structure (**Figure 24**). All computations were performed with Gaussian 16.[17] Molecular geometries were optimized using the B3LYP-D3[18] functional and the 6-311G(d,p) basis set for nonmetal atoms and the Lanl2DZ[19] basis set with effective core potential (ECP) for Zn. Stationary points such as energy minima (no imaginary frequencies) or saddle points (one imaginary frequency) on the potential energy surface were characterized by frequency calculations with the B3LYP-D3 functional and the 6-311++G(d,p)[20] basis set for nonmetal atoms and the Lanl2DZ basis set with ECP for Zn.

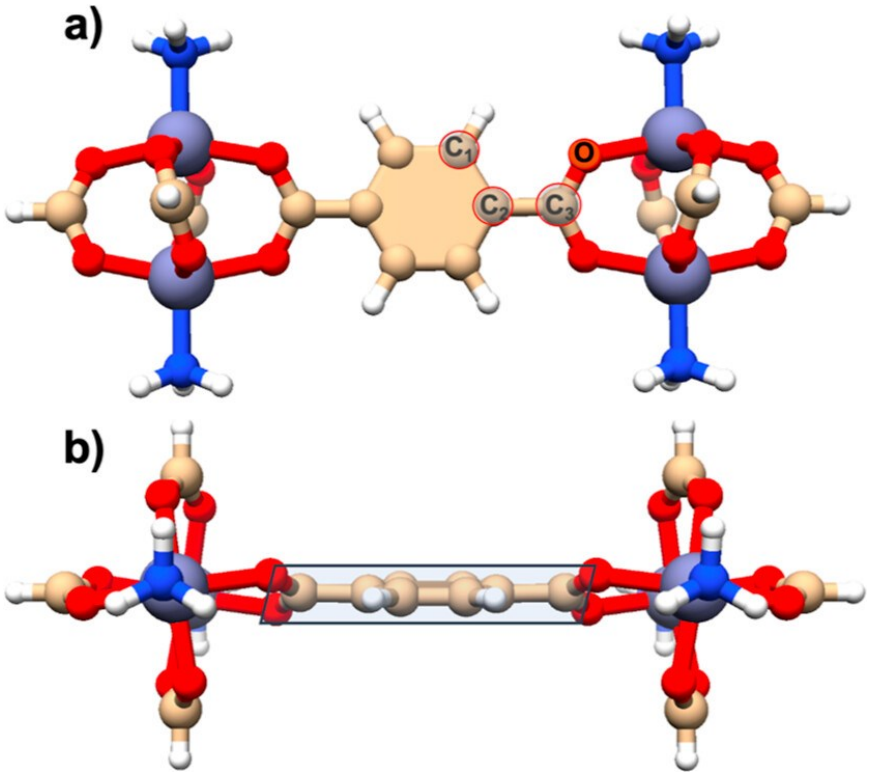

Figure 24. Computational model of the H_2BDC rotor: (a) dihedral angle $C_1{-}C_2{-}C_3{-}O$ (atoms circled in gray) was used to define phenylene rotation. (b) Crystal lattice environment was simulated by constraining the motion of zinc(II) oxide nodes and dabco spacers, represented as ammonia in the model. The plane of the phenylene dicarboxylate rotator (indicated with a box) was allowed to relax after each angular displacement step in performing potential energy calculations.

In the computational model, the motion of the zinc(II) metal center and dabco spacers is fixed to approximate the crystal lattice behavior. The dihedral angle for each rotator is defined as the angle between the plane of the carboxylates that coordinate to the zinc(II) oxide node and the plane of the phenylene rotator ($C_1{-}C_2{-}C_3{-}O$) (**Figure 24**). The dihedral angle was scanned in 5° increments, and electronic energy calculations were performed for each angular displacement step. The ground-state destabilization phenomenon was explored by a set of potential energy

calculations for symmetric dihalogenated phenylenes with fluorine, chlorine, and bromine substituents at the 2' and 3' positions, respectively.

3.5 Results and Discussion

Quantum mechanical calculations indicate that 1,4-benzenedicarboxylate **1** has a 2-fold degenerate ground state with a coplanar conformation and dihedral angles at 0° and 180° (**Figure 25**, gray squares). The two carboxylates and the aromatic ring experience full electronic conjugation. The rotational potential is characterized by transition states with dihedral angles of 90° and 270° that occur when all electronic conjugation is lost, leading to a high energy barrier. Calculations also revealed that rotational barriers caused by the *ortho* substituents in the halogen series **2**−**4** have a significant effect on the potential energy surface, with a degree of ground-state destabilization that depends on the substituent. While the presence of F atoms in **2** results in a local transition state at 180° that is flanked by two twisted minima (**Figure 25**, green circles), Cl (**3**) and Br (**4**) increase the energy of the coplanar conformation beyond that of the twisted transition state such that the 180° rotation becomes the highest maximum (red rhombs and blue triangles, respectively). As illustrated in **Figure 25**, with the 90° energies normalized, the effective barrier height of **1** can be lowered by up to ca. 50% as the 2-fold symmetric potential of the coplanar phenylene and carboxylate groups transforms into a 4-fold potential of the twisted conformations.

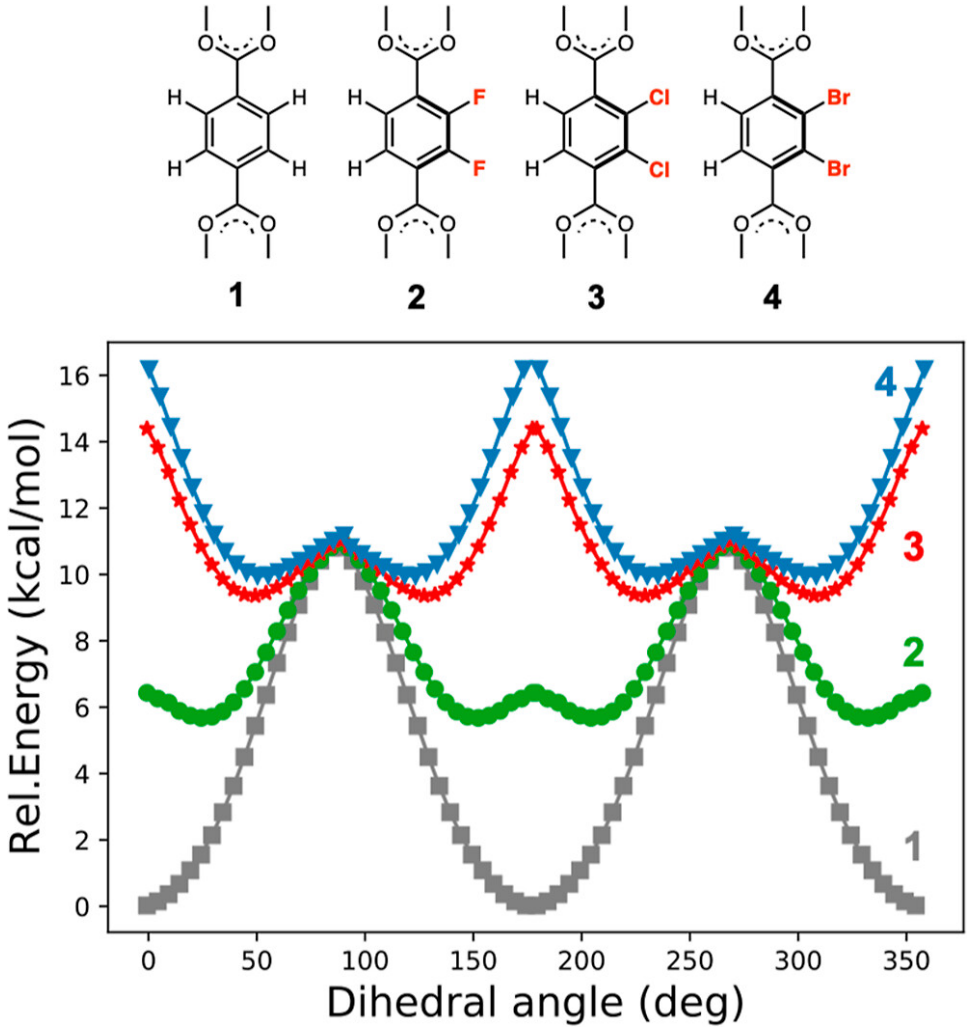

Figure 25. Potential energy scan for *ortho*-dihalogenated benzene dicarboxylate molecular rotators, **1**−**4**, with energies normalized at a dihedral angle of 90° between the planes of the two carboxylates and the corresponding aromatic ring.

While the rotational barrier calculated for the nonpolar BDC **1** was 11.0 kcal/mol, values obtained for the 2,3-disubstituted analogues were 5.6, 5.0, and 6.3 kcal/mol for fluorine **2**, chlorine **3**, and bromine **4** derivatives, respectively (**Figure 25**). The ground state for difluoro-phenylene **2** was twisted 25° from the plane with the two carboxylates, with a local maximum when the ring and the carboxylate become coplanar. Considering that the van der Waals volumes of Cl (13.51

cm^3/mol) and Br (15.96 cm^3/mol) are close, one may expect steric effects to be qualitatively similar, as was confirmed with the calculated rotational barriers. Sterically larger chlorine and bromine destabilized the ground state to a higher extent, making the rotator twist by 45° and 50° off the plane, respectively. The fact that the highest barriers occur when the rotators are coplanar with the stator suggests that conjugation effects are smaller than the encountered steric repulsion. A common transition state at 90° for all three polar phenylenes supports the notion that the lower barrier for rotation is due to destabilization of the original ground state instead of being the result of a lower transition state.

While F, Cl, and Br substituents on one side of the ring may assist in "flattening" the potential by increasing the number of energy minima and bringing the ground-state energy closer to that of their transition state, the magnitude of the dipole moment decreases in the halogen series. In fact, the dipole moments (μ) of **2**, **3**, and **4** decrease from μ = 3.0 to μ = 2.3 to μ = 2.1 Debye, respectively, which leads to a significant decrease in the interaction energy E_{DD} between pairs of point dipoles (**eq 7**):

$$E_{DD} = \frac{\mu_1 \mu_2}{4\pi\varepsilon_0 r_{12}^3}(\cos\theta_{12} - 3\cos\theta_1 \cos\theta_2) \quad \textbf{(eq 7)}$$

where μ_1 and μ_2 are the magnitude of the interacting dipoles ($\mu_1 = \mu_2$ in this case), ε_0 is the permeability of space, r is the center-to-center distance between dipole vectors, θ_{12} is an angle between the two dipole vectors, and θ_1 and θ_2 are angles formed between each dipole and the line that connects their centers. Assuming the tetragonal symmetry and rotor-to-rotor distance of ca. 1 nm previously encountered for difluoro (F_2BDC MOF)[9] and tetrafluoro rotators (F_4BDC MOF),[21]

point dipole−dipole interaction energies vary from 0.3 and 0.2 to 0.1 kcal/mol as the halogen changes from fluorine (**2**) to chlorine (**3**) to bromine (**4**). Naturally, these values are too small compared to the intrinsic rotational barriers of 6.6, 6.0, and 4.5 kcal/mol to result in the correlated motion of dipoles.

Based on the above results, we envisioned a strategy that may help increase the magnitude of the dipole moment while reducing the height of the rotational barrier. This concept relies on the installation of groups with a relatively small size and a large permanent dipole moment on one side of the aromatic rotator, such as two neighboring cyano groups (CN), while taking advantage of the barrier-lowering effect of the larger halogens on the other side. We calculated the dipole moments of 2,3-dicyano-benzenedicarboxylate **5** to be 6.6 D and those of dihalogenated 2,3-dicyano-benzenedicarboxylates **6**, **7**, and **8** to be 4.9, 4.7, and 4.9 D, respectively. These values result in dipole−dipole interaction energies on the order of 0.7 to 1.3 kcal/mol − significantly greater than those in the benzene dicarboxylates **2**−**4**.

Table 2. Dipole moments, dipole−dipole interaction energies, and rotational barriers when the rotors **5**−**10** are in plane (ground-state destabilization effects) and 90° off the plane with the two dicarboxylate linkers.

rotator	μ (Debye)	E_{DD} (kcal/mol)	E_a (0/90) (kcal/mol)
5	6.6	1.3	2.0/12.8
6	4.9	0.7	6.0/7.4
7	4.7	0.6	11.7/3.0
8	4.9	0.7	10.2/2.3
9	9.4	2.4	8.1/5.5
10	7.9	1.8	2.1/10.5

A further increase in the dipole moment of phenylene rotators can be achieved by installing electron-donating and electron-withdrawing substituents on the opposite sides of phenylene as recently shown by Müllen[22] and Herges.[18] The installation of electron-withdrawing cyano substituents opposite to electron-donating benzo-1,4-dioxane (**9**) and benzo-1,3-dioxole (**10**) substituents gives rise to dipole moments of 7.8 and 9.4 D, respectively (**Table 2**).[23] With that in mind, we decided to explore analogous molecular rotors with *para*-dicarboxylate groups **9** and **10** in **Scheme 1** in order to establish the relation between rotational barriers and their orientation-dependent dipole−dipole−dipole interactions.

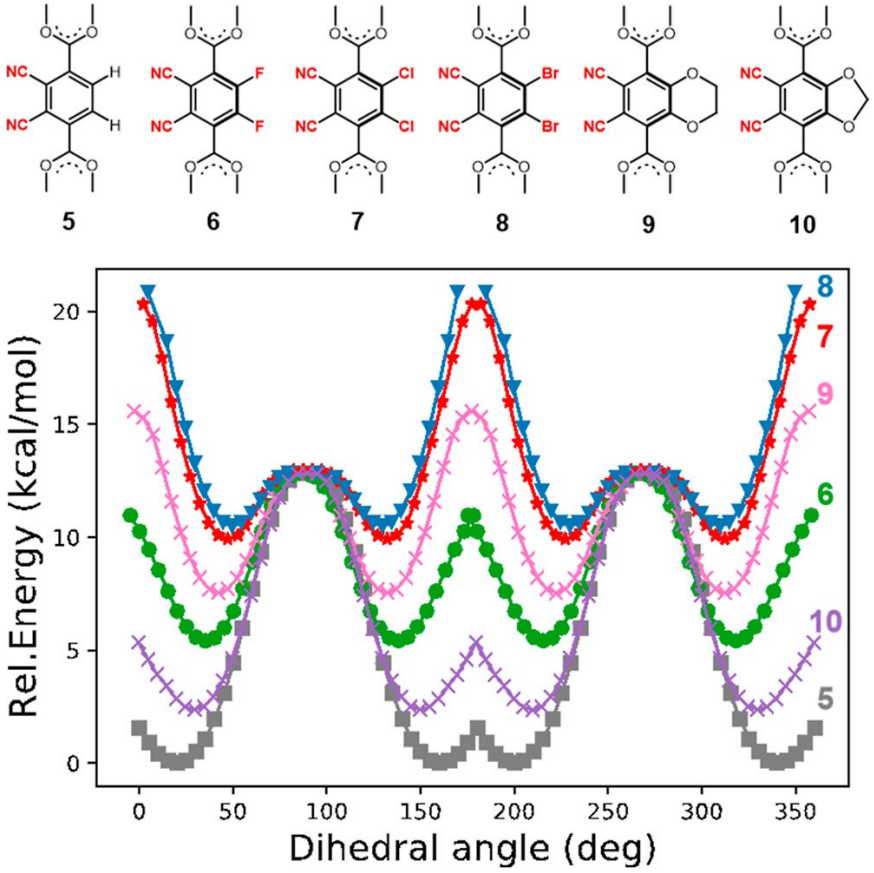

Figure 26. Potential energy scan for dihalogenated phenylene rotors **5**−**8** and benzo-1,4-dioxane phenylenes **9** and benzo-1,3-dioxole-dicyano **10**.

The potential energy surface of 2,3-dicyano-benzene-dicarboxylate **5** shown in **Figure 26** revealed that a local maximum of 2 kcal/mol appears when the rotator is in conjugation with the carboxylates due to the ground-state destabilization effect, which creates a ground state that is twisted by ± 20° from the plane of the carboxylates. Evaluation of the potential energy surfaces for 2,3-dihalogenated-5,6-dicyano phenylenes **6**, **7**, and **8** revealed an angular increase of the local minima from 35° for fluorinated analogues to 47° for both chlorinated and brominated dicyano analogues. Notably, for rotors **5**, **6**, and **10**, the ground-state configuration was connected to local coplanar maxima with the highest maxima being perpendicular to the plane (**Figure 26**). For rotors **7**, **8**, and **9**, the two maxima were swapped in magnitude, with the highest energy corresponding to the coplanar alignment. The smallest relative barrier was identified to be 6 kcal/mol for difluoro-dicyano rotator **6**. The rotational barriers for dicyano-benzo-1,3-dioxole (**10**) and dicyano-benzo-1,4-dioxane-phenylene (**9**) were 10.5 and 8.1 kcal/mol, respectively, which are 2.3 and 5.7 kcal/mol lower than those in unsubstituted dicyano-phenylene **5** (**Table 2**).

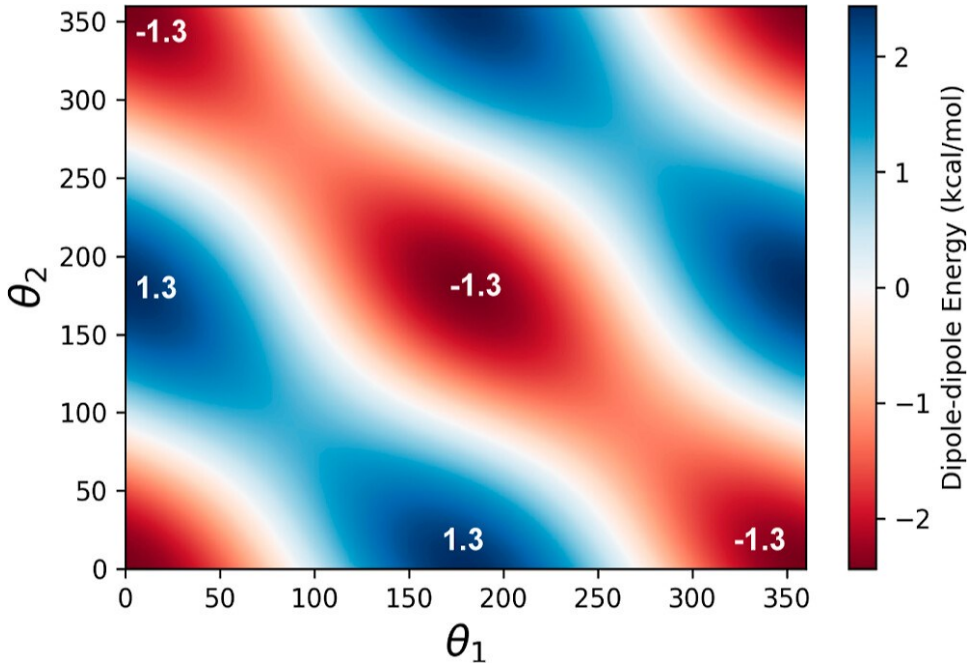

Figure 27. Dipole−dipole interaction energies calculated using a point dipole approximation for 2,3-dicyanophenylene **5** (μ = 6.6 D) with rotators positioned at a distance of 10 Å with θ_1 and θ_2 being the angles formed between each dipole vector and the line that connects their centers (**eq 7**).

Using the point-dipole approximation in **eq 7**, we calculated the pairwise dipole−dipole interaction energy for 2,3-dicyanophenylene **5** (μ = 6.6 D) as a function of the rotational angles formed between each of the two dipoles, θ_1 and θ_2, and the line that connects their centers at a distance of 10 Å. As shown in **Figure 27**, variations in energy of ± 1.3 kcal/mol occur as the rotational angle changes from a preferred, coaligned orientation to a disfavored one that is anti-aligned, with angles of $\theta_1 = \theta_2 = 0°$ or the symmetry equivalent in the first case, and $\theta_1 = 0°$, $\theta_2 = 180°$ in the second. The 2D contour plot shows how pairwise dynamic correlations resulting from rotational motion and dipole−dipole interactions result in preferred paths from top left to bottom right with angle θ_1 increasing and θ_2 decreasing in a conrotatory motion.

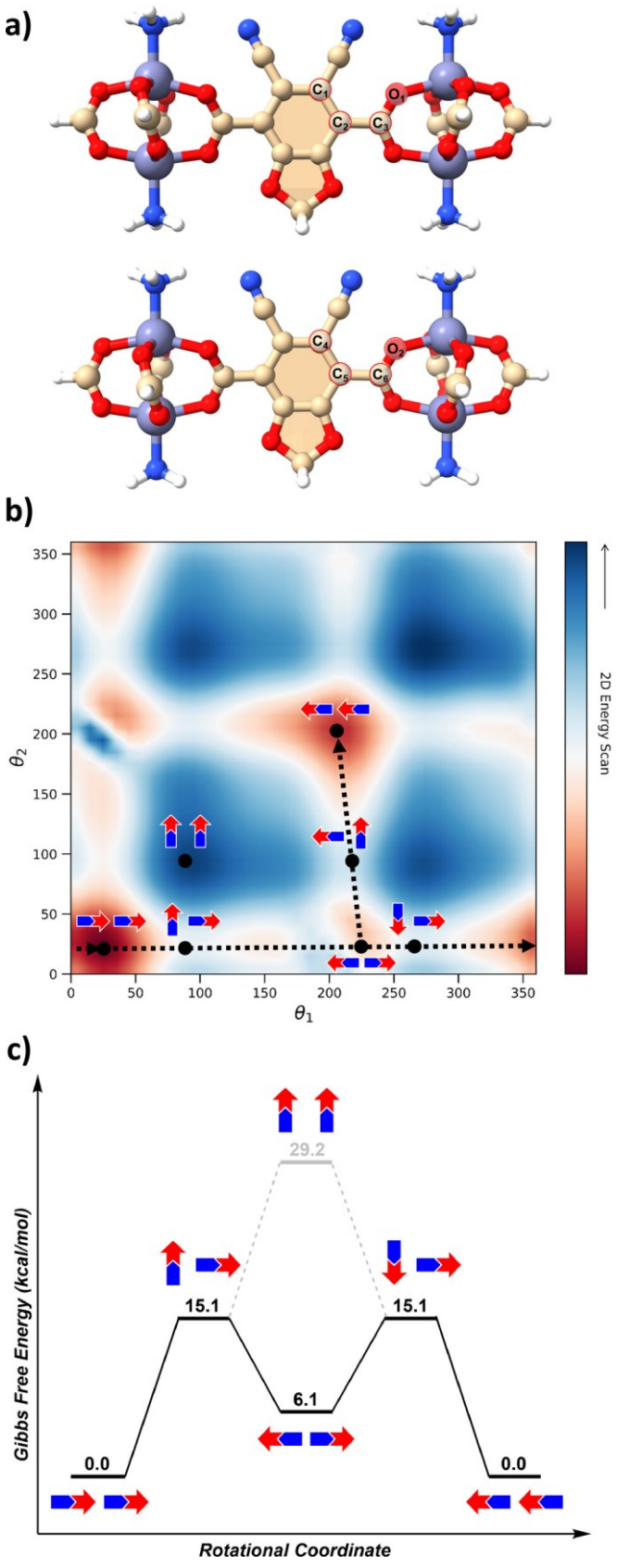
a)
C1
C2
C3
O1
C4
C5
C6
O2
b)
θ2
θ1
2D Energy Scan
c)
Gibbs Free Energy (kcal/mol)
Rotational Coordinate
29.2
15.1
15.1
6.1
0.0
0.0

Figure 28. Energy profile calculated using two neighboring rotors **10**. (a) Computation model of two interacting dicyano-benzo-1,3-dioxole dicarboxylates **10**. Dihedral angles $C_1{-}C_2{-}C_3{-}O_1$ and $C_4{-}C_5{-}C_6{-}O_2$ (atoms in gray) were used to define phenylene rotation. (b) Energy surface plotted by performing rigid scans on the dual rotor (**10**) model in the B3LYP-D3/6-311G(d,p) level of theory (Lanl2DZ for Zn atoms). Colors were used to reflect the relative electronic energies (red: low; blue: high). (c) Gibbs free energy of the most representative structures in the rotational pathway calculated at the B3LYP-D3/6-311++G(d,p)//B3LYP-D3/6-31G(d,p) level of theory (Lanl2DZ for Zn atoms).

The results in **Figure 27** represent a hypothetical structure with no steric or electronic contributions to the rotational potential. A more realistic insight can be obtained by building a similar potential energy surface where all contributions to the potential are included. We decided to explore that for two neighboring dicyano-benzo-1,3-dioxoles **10** by performing rigid scans on the dual system by only allowing the phenylene moiety to rotate, with the stator, spacer, and carboxylate frozen. The energy landscape was obtained with respect to rotational angles θ_1 and θ_2, as defined by $C_1{-}C_2{-}C_3{-}O_1$ and $C_4{-}C_5{-}C_6{-}O_2$ (**Figure 28a**), with the region of all stationary points analyzed in more detail and with higher levels of theory that confirmed their nature as energy minima, transition states, or second-order saddle points by the number of imaginary frequencies (**Figure 28c**). In analogy to the simple dipole−dipole interactions for dicyano rotor **5** in **Figure 27**, the global energy minimum consists of close to coaligned dipoles in a surface that is significantly asymmetric. A substantial barrier in the form of a second-order saddle point is encountered when two rotors simultaneously approach the transition state, where all electronic conjugation is lost ($\theta_1 \approx \theta_2 \approx 90°$). This configuration indicated with a deep blue color in **Figure 28** corresponds to a second-order saddle point with a Gibbs free energy of 29.2 kcal/mol, as illustrated in **Figure 28c**. These results suggest stepwise rotational trajectories as indicated by the dashed lines in **Figure 28b**, where the first rotator transitions to the anti-aligned position, while

the second one remains essentially stationary. From that point, continued rotation of the first rotator completes a full cycle back to the starting point, or alternatively, the second rotor initiates its half-turn by flipping the orientation in the same manner, leading to another degenerate global minimum. Consequently, a divergent rotational mechanism is suggested by the 2D contour plot derived from the rigid scans (see the Supporting Information of our published work for a more detailed discussion).[24]

3.6 Conclusions

In search of building blocks for the construction of rotary dipole arrays capable of displaying emergent dipolar order and macroscopic polarization in response to external fields, we explored the rotational potential of several 1,4-benzenedicarboxylates with polar substituents in the *ortho*-positions. Quantum mechanical calculations were carried out on conformations where the two carboxylates are kept coplanar, as expected for ligands engaged in dimetallic paddle wheel MOF structures. Calculations confirmed that unsubstituted 1,4-benzenedicarboxylates have equienergetic ground-state conformations at 0° and 180° where the aromatic ring is coplanar with the flanking carboxylates and orthogonal rotational transition states at 90° and 270° where there is no conjugation between the corresponding π-systems. We also confirmed that steric repulsions by the *ortho*-polar substituents raise the energy of the coplanar conformation, resulting in two barriers at 0° and 180°, each flanked by two shallow minima. Calculations suggest that *ortho*-fluoro and *ortho*-cyano groups create local barriers for the coplanar structures that are lower than those of the orthogonal conformation. By contrast, *ortho*-chloro and *ortho*-bromo substituents destabilize the coplanar conformations to the extent that they become the global maximum. Structures known to generate large dipole moments with electron-withdrawing cyano substituents opposite to electron-

donating benzo-1,3-dioxole and benzo-1,4-dioxane substituents were also studied. They were found to create similar rotational profiles with two sets of equivalent energy maxima at 0°/180° and 90°/270°, respectively. Our results support the original suggestion that *ortho*-substituted 1,4-benzenedicarboxylates can lead to global energy barriers smaller than those of the parent compound by destabilizing the coplanar ground state. From all of the structures investigated, the installation of cyano substituents opposite to electron-donating benzo-1,3-dioxole **9** results in the greatest dipole moment (μ = 9.2 D) and the second lowest global barrier (7.8 kcal/mol). While previous experimental work with MOFs containing 1,4-benzenedicarboxylate **1** and 2,3-difluoro-1,4-benzenedicarboxylate **2** supports this hypothesis, work is now in progress to test predictions on some of the other structures.

3.7 References

(1) Vogelsberg, C. S.; Garcia-Garibay, M. A. Crystalline molecular machines: function, phase order, dimensionality, and composition. *Chem. Soc. Rev.* **2012**, *41*, 1892−1910.

(2) Garcia-Garibay, M. A. Crystalline molecular machines: encoding supramolecular dynamics into molecular structure. *Proc. Natl. Acad. Sci. U.S.A.* **2005**, *102*, 10771−10776.

(3) Khuong, T.-A. V.; Nuñez, J. E.; Godinez, C. E.; Garcia-Garibay, M. A. Crystalline molecular machines: a quest toward solid-state dynamics and function. *Acc. Chem. Res.* **2006**, *39*, 413−422.

(4) Terzopoulou, A.; Nicholas, J. D.; Chen, X.-Z.; Nelson, B. J.; Pané, S.; Puigmartí-Luis, J. Metal-Organic Frameworks in Motion. *Chem. Rev.* **2020**, *120*, 11175−11193.

(5) Comotti, A.; Bracco, S.; Sozzani, P. Molecular Rotors Built in Porous Materials. *Acc. Chem. Res.* **2016**, *49*, 1701−1710.

(6) Lucier, B. E. G.; Chen, S.; Huang, Y. Characterization of Metal-Organic Frameworks: Unlocking the Potential of Solid-State NMR. *Acc. Chem. Res.* **2018**, *51*, 319−330.

(7) Inukai, M.; Fukushima, T.; Hijikata, Y.; Ogiwara, N.; Horike, S.; Kitagawa, S. Control of Molecular Rotor Rotational Frequencies in Porous Coordination Polymers Using a Solid-Solution Approach. *J. Am. Chem. Soc.* **2015**, *137*, 12183−12186.

(8) Howe, M. E.; Garcia-Garibay, M. A. The Roles of Intrinsic Barriers and Crystal Fluidity in Determining the Dynamics of Crystalline Molecular Rotors and Molecular Machines. *J. Org. Chem.* **2019**, *84*, 9835−9849.

(9) Khudozhitkov, A. E.; Kolokolov, D. I.; Stepanov, A. G.; Bolotov, V. A.; Dybtsev, D. N. Metal-Cation-Independent Dynamics of Phenylene Ring in Microporous MOFs: A ^{2}H Solid-State NMR Study. *J. Phys. Chem. C* **2015**, *119*, 28038−28045.

(10) Gould, S. L.; Tranchemontagne, D.; Yaghi, O. M.; Garcia-Garibay, M. A. Amphidynamic Character of Crystalline MOF-5: Rotational Dynamics of Terephthalate Phenylenes in a Free-Volume, Sterically Unhindered Environment. *J. Am. Chem. Soc.* **2008** , *130* , 3246−3247.

(11) Vogelsberg, C. S.; Uribe-Romo, F. J.; Lipton, A. S.; Yang, S.; Houk, K. N.; Brown, S.; Garcia-Garibay, M. A. Ultrafast rotation in an amphidynamic crystalline metal organic framework. *Proc. Natl. Acad. Sci. U.S.A.* **2017** , *114* , 13613−13618.

(12) Baudry, J. van der Waals Interactions and Decrease of the Rotational Barrier of Methyl-Sized Rotators: A Theoretical Study. *J. Am. Chem. Soc.* **2006** , *128* , 11088−11093.

(13) Liepuoniute, I.; Huynh, C. M.; Perez-Estrada, S.; Wang, Y.; Khan, S. I.; Houk, K. N.; Garcia-Garibay, M. A. Enhanced Rotation by Ground State Destabilization in Amphidynamic Crystals of

a Dipolar 2,3-Difluorophenylene Rotator as Established by Solid State 2 H NMR and Dielectric Spectroscopy. *J. Phys. Chem. C* **2020** , *124* (28), 15391−15398.

(14) Winston, E. B.; Lowell, P. J.; Vacek, J.; Chocholousová, J.; Michl, J.; Price, J. C. Dipolar molecular rotors in the metal-organic framework crystal IRMOF-2. *Phys. Chem. Chem. Phys.* **2008** , *10* , 5188−5191.

(15) Horansky, R. D.; Clarke, L. I.; Price, J. C.; Khuong, T.-A. V.; Jarowski, P. D.; Garcia-Garibay, M. A. Dielectric response of a dipolar molecular rotor crystal. *Phys. Rev. B* **2005** , *72* , 014302.

(16) Su, Y.-S.; Lamb, E. S.; Liepuoniute, I.; Chronister, A.; Stanton, A. L.; Guzman, P.; Pérez-Estrada, S.; Chang, T. Y.; Houk, K. N.; Garcia-Garibay, M. A.; Brown, S. E. Dipolar order in an amphidynamic crystalline metal-organic framework through reorienting linkers. *Nat. Chem.* **2021**, *13*, 278−283.

(17) Frisch, M. J.; Trucks, G. W.; Schlegel, H. B.; Scuseria, G. E.; Robb, M. A.; Cheeseman, J. R.; Scalmani, G.; Barone, V.; Petersson, G. A.; Nakatsuji, H.; Li, X.; Caricato, M.; Marenich, A. V.; Bloino, J.; Janesko, B. G.; Gomperts, R.; Mennucci, B.; Hratchian, H. P.; Ortiz, J. V.; Izmaylov, A. F.; Sonnenberg, J. L.; Williams-Young, D.; Ding, F.; Lipparini, F.; Egidi, F.; Goings, J.; Peng, B.; Petrone, A.; Henderson, T.; Ranasinghe, D.; Zakrzewski, V. G.; Gao, J.; Rega, N.; Zheng, G.; Liang, W.; Hada, M.; Ehara, M.; Toyota, K.; Fukuda, R.; Hasegawa, J.; Ishida, M.; Nakajima, T.; Honda, Y.; Kitao, O.; Nakai, H.; Vreven, T.; Throssell, K.; Montgomery, Jr., J. A.; Peralta, J. E.; Ogliaro, F.; Bearpark, M. J.; Heyd, J. J.; Brothers, E. N.; Kudin, K. N.; Staroverov, V. N.; Keith, T. A.; Kobayashi, R.; Normand, J.; Raghavachari, K.; Rendell, A. P.; Burant, J. C.; Iyengar, S. S.; Tomasi, J.; Cossi, M.; Millam, J. M.; Klene, M.; Adamo, C.; Cammi, R.; Ochterski, J. W.; Martin, R. L.; Morokuma, K.; Farkas, O.; Foresman, J. B.; Fox, D. J. Gaussian 16, Revision C.01; Gaussian, Inc.: Wallingford, CT, 2016.

(18) Grimme, S.; Antony, J.; Ehrlich, S.; Krieg, H. A consistent and accurate ab initio parametrization of density functional dispersion correction (DFT-D) for the 94 elements H-Pu. *J. Chem. Phys.* **2010** , *132* , 154104.

(19) Andrae, D.; Häußermann, U.; Dolg, M.; Stoll, H.; Preuß, H. Energy-adjusted ab initio pseudopotentials for the second and third row transition elements. *Theor. Chem. Acc.* **1990** , *77*, 123 −141.

(20) Frisch, M. J.; Pople, J. A.; Binkley, J. S. Self-Consistent Molecular Orbital Methods. 25. Supplementary Functions for Gaussian Basis Sets. *J. Chem. Phys.* **1984** , *80* , 3265−3269.

(21) Chun, H.; Dybtsev, D. N.; Kim, H.; Kim, K. Synthesis, X-ray Crystal Structures, and Gas Sorption Properties of Pillared Square Grid Nets Based on Paddle-Wheel Motifs: Implications for Hydrogen Storage in Porous Materials. *Chem. Eur. J.* **2005** , *11* , 3521−3529.

(22) Wudarczyk, J.; Papamokos, G.; Margaritis, V.; Schollmeyer, D.; Hinkel, F.; Baumgarten, M.; Floudas, G.; Müllen, K. Hexasubstituted Benzeneswith Ultrastrong Dipole Moments. *Angew. Chem., Int. Ed.* **2016** , *55* , 3220−3223.

(23) Hamer, S.; Röhricht, F.; Jakoby, M.; Howard, I. A.; Zhang, X.; Näther, C.; Herges, R. Synthesis of dipolar molecular rotors as linkers for metal-organic frameworks. Beilstein *J. Org. Chem.* **2019** , *15* , 1331−1338.

(24) Liepuoniute, I.; Shan, J.-R.; Houk, K. N.; Garcia-Garibay, M. A. Computational Study of Ground-State Destabilization Effects and Dipole−Dipole Interaction Energies in Amphidynamic Crystals. *J. Org. Chem.* **2024**, *89*, 9−15.

Chapter 4: Evidence for a Photochemically Triggered Thermal Chain Reaction of Nanocrystalline 2-Azidobiphenyl to Carbazole Enabled by Energy Release in the Time Scales of Intramolecular Vibrational Redistribution and Vibrational Energy Transfer

4.1 Contributions

This chapter is based on the following unpublished manuscript: Indrajit Paul, Sahil Kapila, Rishika Rai, Jing-Ran Shan, Krzysztof A. Konieczny, K. N. Houk, and Miguel A. Garcia-Garibay, "Evidence for a Photochemically Triggered Thermal Chain Reaction of Nanocrystalline 2-Azidobiphenyl to Carbazole Enabled by Energy Release in the Time Scales of Intramolecular Vibrational Redistribution and Vibrational Energy Transfer," **2026**, *submitted*. I am listed as the co-author of this manuscript. I designed and carried out all computational studies presented in this work. I also contributed to the writing of the manuscript.

4.2 Abstract

Chemical amplification in crystals occurs by mechanisms where a single activation event leads to products while releasing or transferring sufficient energy to activate other close neighboring reactants in the lattice to start a chain reaction. Recent examples include exciton-enabled quantum chains and polaron-enabled single-electron-transfer (SET) chain reactions. In this paper we report quantum mechanical calculations and experimental results from four crystalline 2-azidobiphenyl derivatives shown to undergo a solid-state reaction with a ca. 5-fold amplification as compared to reactions in solution. These observations, combined with results from H/D isotopic substitution, are consistent with a mechanism that involves an ultrafast

photochemical reaction within the time scale of intramolecular vibrational redistribution (IVR) and vibrational energy transfer (VET), that generates a hot spot able to sustain a short thermal chain in competition with thermal dissipation through the lattice.

4.3 Introduction

The realm of chemical reactivity in crystalline solids has expanded from structural analyses that confirm the topochemical postulate, to mechanistic studies,[1,2] green chemistry, complex chemical syntheses,[3–5] and the transduction of molecular to macroscopic mechanical forces.[6] New frontiers include the design of crystals with engineered internal dynamics,[7] and a deeper understanding of material properties for applications in materials science. Over the last few years our group has also explored chemical amplification processes that take advantage of energetic, electronic, and mechanical intermolecular coupling in the crystal lattice. Controlled chemical amplification in crystalline solids involves the activation of a reactant (**R**) that undergoes a solid-to-solid reaction to give a product (**P**), where sufficient energy remains available to activate subsequent reactions (**Figure 29a**). Recently, we have shown examples of chemical amplification that occurs via singlet[8,9] and triplet[10,11] exciton-enabled quantum chains, and via oxidative and reductive single electron transfer (SET) chain reactions[12–14] (**Figure 29b**). Quantum chains rely on excited state adiabatic reactions where an excited reactant transforms into an excited photoproduct ($R_1^* \rightarrow P_1^*$) that can transfer energy to a neighboring ground state reactant ($P_1^* + R_2 \rightarrow P_1 + R_2^*$)[9,15] to enter a repeating cycle. Similarly, SET chain reactions, also known as SET catalysis,[16] start by the generation of a radical ion (**R*** = $R^{\bullet+}$ or $R^{\bullet-}$, **Figure 29b**), which undergoes an adiabatic reaction to give the corresponding radical-ion product (**P*** = $P^{\bullet+}$ or $P^{\bullet-}$). The latter

propagates the chain by transferring an electron to or from a neighboring reactant molecule in the crystal.

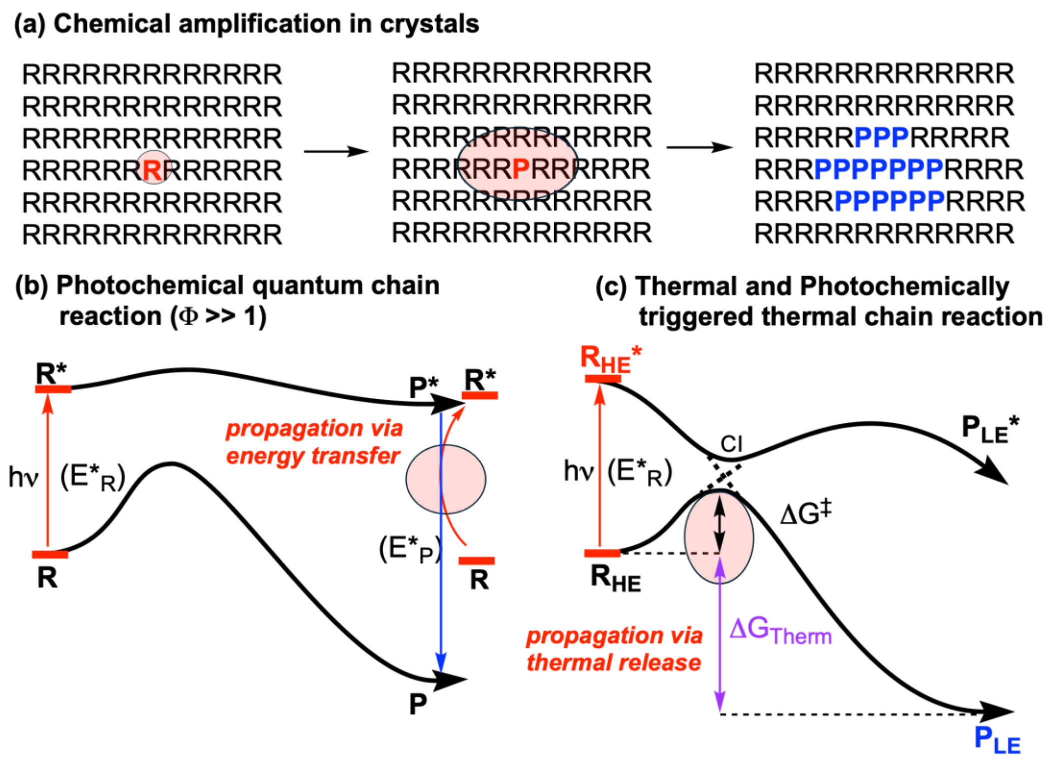

Figure 29. (a) Chemical amplification by a chemical process that releases enough energy to start a chain reaction. (b) Chemical amplification based on a photochemical quantum chain, or single electron transfer (SET) catalysis. (c) Chemical amplification based on photochemically triggered thermal chain reaction.

These amplification mechanisms give rise to multiple products per photon absorbed or per ionization event.[17] In the case of crystalline Dewar benzene (**Figure 30a**), chemical amplification via a triplet state quantum chain results in ca. 520 reactions per photon absorbed,[11] and up to 90,000 reactions per incident electron when a radical cation chain reaction is initiated with an electron microscope.[12] In this paper, using four crystalline 2-azido-biphenyl derivatives, we report strong

evidence for a chemical amplification scheme based on a photochemical triggering event where a single photon gives rise to multiple product molecules by taking advantage of the energy released during an ultrafast photochemical reaction that generates a hot spot that is transiently sustained by several highly exothermic thermal steps.

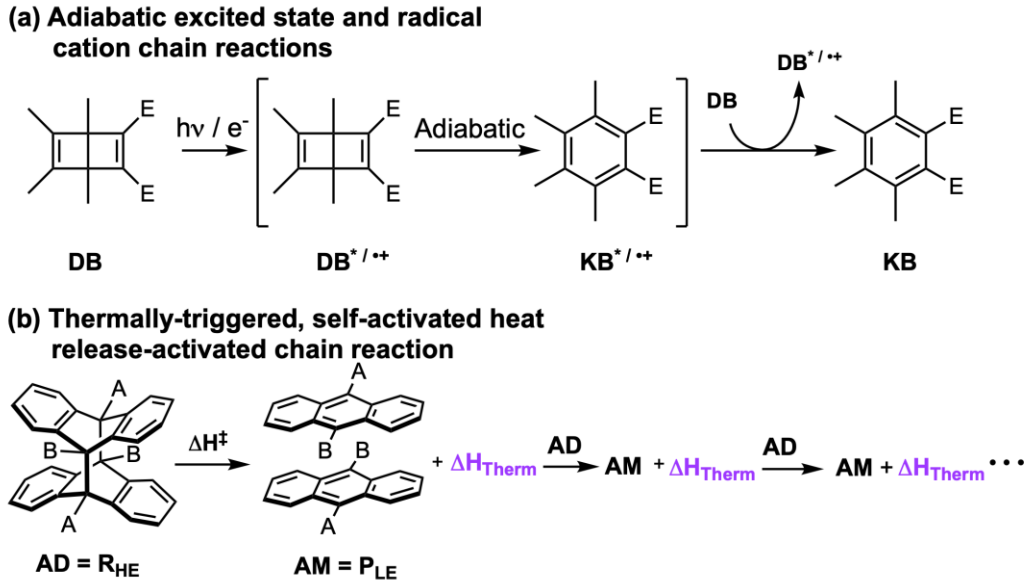

Figure 30. (a) Adiabatic Dewar benzene (DB) to Kekule benzene (KB) reactions occur both in the excited state and in the radical cation manifold. (b) Thermal self-activated anthracene dimer splitting chain reaction.

4.4 Results and Discussion

4.4.1 Photochemically Triggered Thermal Chain Reactions

The suggested scenario includes: (1) a photo-triggering event in the form of a highly exothermic non-adiabatic solid-state photo-chemical reaction that occurs in the femtosecond time scale, potentially by activation of specific reaction modes, through intra-molecular vibrational redistribution (IVR).[18,19] Photo-triggering should generate a hot spot that activates subsequent (2)

highly exothermic ground state reactions that self-propagate by a thermal chain regime,[20] until (3) heat is dissipated and the hot spot local temperature (T_{loc}) is no longer high enough for the reactant to reach its transition state.

In analogy to well-known photothermal systems, the proposed amplification strategy requires molecules that transduce light into heat, but instead of going back to the ground state reactant via internal conversion (**Figure 29c**, $\mathbf{R_{HE}^*} \rightarrow \mathbf{R_{HE}}$ + heat), heat should be released with formation of a photoproduct ($\mathbf{R_{HE}^*} \rightarrow \mathbf{P_{LE}}$ + heat). A promising energy profile (**Figure 29c**) consists of high-energy reactants ($\mathbf{R_{HE}}$) with high excitation energies (**E***) that release most of this energy (**E*** + ΔG_{Therm}) by an ultra-fast, non-adiabatic photochemical reaction to a low energy product ($\mathbf{P_{LE}}$). In contrast to photothermal systems, which are designed to increase the equilibrium temperature of the bulk, the proposed photo-triggering event would have to occur under non-equilibrium dynamics, as the excited state transduces electronic to vibrational energy through internal conversion (IC), motion towards a conical intersection (CI), and vibrational cooling (IVR) to form the product. The energy released should generate a hot spot to facilitate the reaction of close neighbors before heat is dissipated through the lattice (**Figure 31**). Subsequent reactions would rely on a self-propagated thermal chain that takes advantage of the energy released during subsequent ground state reactions ($\mathbf{R_{HE}} \rightarrow \mathbf{P_{LE}}$ + ΔG_{Therm}). An elegant demonstration of the latter was recently shown by Han and coworkers[20] with crystalline anthracene dimers **AD** undergoing a self-activated thermal reaction to anthracene monomers **AM** (**Figure 30b**). Their experimental results showed how reactions depend both on the heat released by the chemical reaction being greater than its activation energy ($\Delta G_{Therm} >> \Delta G^{\ddagger}$), and on the relative rates of heat input and heat dissipation.[21] Notably, while the description of photochemical energy input, thermal energy accumulation (heating), and thermal energy dissipation (cooling) in macroscopic photothermal

systems can be accounted for with thermodynamic equilibrium properties, ultra-fast energy dissipation at the molecular level requires consideration of femtosecond IVR, picosecond vibrational energy transfer (VET) to close neighbors, and dissipation through lattice phonons.[22,23]

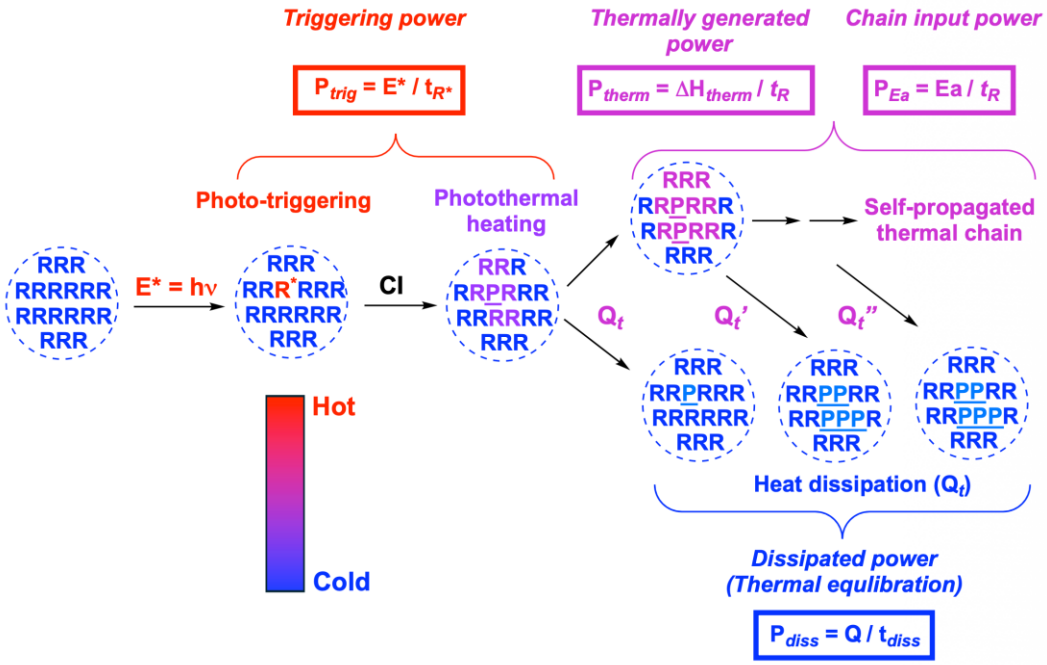

Figure 31. Chemical amplification by photo-triggering and thermal self-propagation in terms of the power (energy/time) available for photochemical triggering for thermal power generation used to sustain a thermal chain reaction, and thermal dissipation through the crystal lattice.

4.4.2 Power Balance

The critical relation between the time that it takes for the excited state to dissipate its excess energy, and for each thermal reaction step to be able to use it before it thermally dissipates, makes it conceptually useful to consider the proposed mechanism in terms of the power (P = Energy/time) input and output involved in each step of the reaction (**Figure 31**).[24] Ideally, the triggering power

is given by the combined excitation energy and the energy released by the reaction within the lifetime of the excited state [$P_{trig} = (E^* + \Delta G_{therm})/\tau^*$]. Triggering results in the formation of the first product molecule (or molecules) and the generation of a local hot spot. The thermal power generated by a subsequent exothermic reaction ($P_{therm} = \Delta G_{therm}/\tau_R$) is determined by the energy released within the time constant τ_R, determined by the local temperature of the hot spot, i.e., $k_R = 1/\tau_R = f(T_{loc})$. The power input needed to sustain additional steps in a thermal chain is given by the activation energy (E_a) for the reaction and its time constant τ_R', which also depends on the decreasing local temperature T_{loc} of the hot spot ($P_{Ea} = E_a/\tau_R'_{(T loc)}$). In order to satisfy energy requirements, the power input for each reaction step must be greater than the power dissipated ($P_{diss} = Q/\tau_{diss}$]. Thus, a photochemically triggered chain reaction can be expected only when energies and time constants are ranked in the order $(E^* + \Delta H_{therm}) > \Delta H_{therm} > E_a$, and $\tau^* < \tau_R << \tau_{diss}$.

4.4.3 2-Azidobiphenyl

To explore the suggested photochemically triggered thermal chain reaction (**Figure 31**) we identified crystals of 2-azido-biphenyl (**Az-1**, **Scheme 2**) as a promising target. We had recently shown **Az-1** to undergo a very clean and efficient solid-to-solid reaction to form crystalline carbazole as the only product (**Cbz-1**, **Scheme 2**).[25] Previous studies with crystals of **Az-1** at 80 K led to the detection of the nitrene intermediate,[26] and flash photolysis measurements in 3-methylpentane glasses at 77 K revealed that singlet 2-biphenyl-nitrene gradually evolved into the triplet state, which is established as the ground state.[27,28] Subsequent femtosecond studies of **Az-1** in solution at ambient temperatures by Platz and coworkers revealed that loss of N_2 gives the singlet nitrene within 450 fs followed by formation of *iso*-carbazole (***iso*-Cbz-1**) and small

amounts of cyclohepta-1,2,4,6-tetraene (CHT) within the next ca. 16 ps.[29] The reaction in solution ends when ***iso*-Cbz-1** undergoes a 1,5-H shift to form carbazole (**Cbz-1**) while CHT goes through multiple decomposition pathways. Consistent with ultrafast nitrene formation and cyclization reaction, transient absorption measurements with nanocrystalline suspensions of **Az-1** at 300 K[30] revealed the loss of nitrogen and the exclusive formation of ***iso*-Cbz-1** to be complete within a 10 ns laser pulse, followed by a 1,5-H shift that occurs within ca. 500 ns (**Scheme 2**).

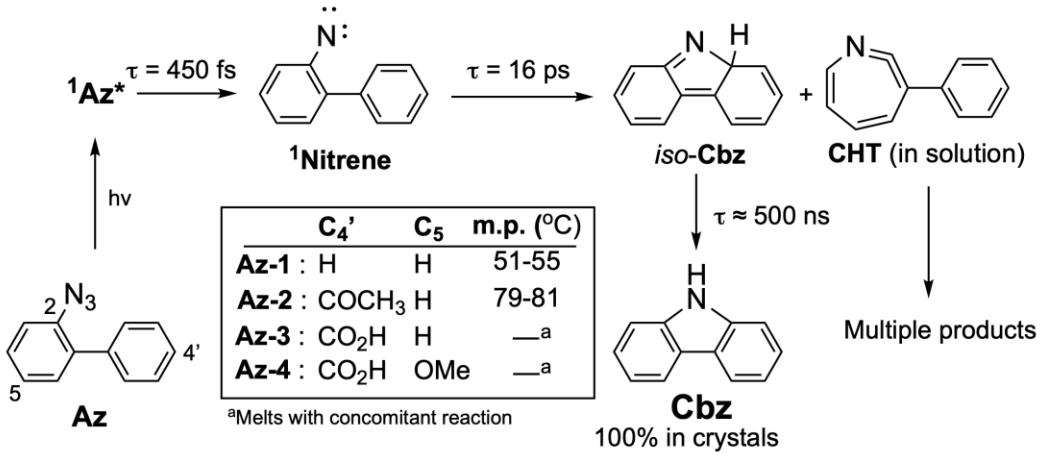

	C_4'	C_5	m.p. (°C)
Az-1 :	H	H	51-55
Az-2 :	$COCH_3$	H	79-81
Az-3 :	CO_2H	H	—[a]
Az-4 :	CO_2H	OMe	—[a]

Scheme 2. Photoinduced reaction of 2-azidobiphenyl.

Quantum mechanical calculation of the **Az-1** to **Cbz-1** reaction coordinate summarized in **Figure 32** support the energetic expectations shown in **Figure 29c**. Geometry optimizations and vibrational frequency analyses of all intermediates and transition states were carried out using the functional M06-2X, at the (u)M06-2X-D3/def2-SVP level (u denotes the unrestricted DFT calculations).[31–33] Single-point energies were then calculated at the (u)M06-2X-D3/def2-TZVPP level to construct the reaction profiles along singlet and triplet energy surfaces, as indicated in **Figure 32** with black and blue lines, respectively.

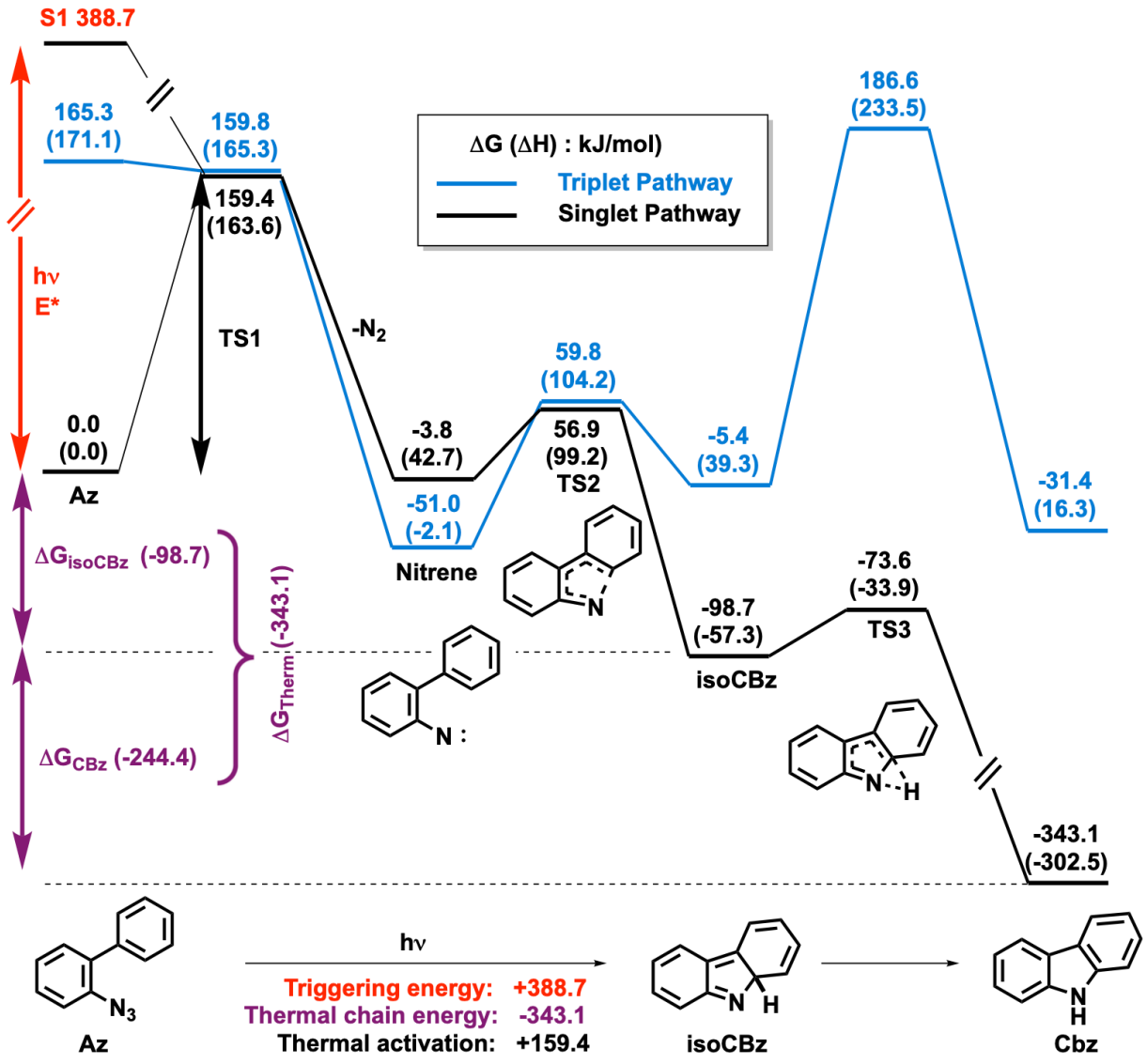

Figure 32. Calculated reaction coordinate for the transformation of 2-azido-biphenyl into carbazole. Gibbs free energy calculations were performed at the (u)M06-2X(D3)/def2-TZVPP//(u)M06-2X(D3)/def2-SVP level of theory at 298.15 K with Grimme's entropy correction applied.

We recognize that calculated gas phase energetics must be considered qualitative when exploring a solid-state reaction that involves the transduction of electronic excitation into non-equilibrium chemical changes and heat release. With that in mind, the reaction coordinate in **Figure 32** starts with vertical excitation to the singlet excited state of 2-azido-biphenyl ^{1}**Az-1***,

which results in a large energy input (E* = 388.7 kJ/mol) by the absorption of 308 nm photons. Based on the greater experimental rates for the loss of nitrogen (~10^{14} s^{-1}) compared with those of intersystem crossing (~10^{11} s^{-1}) we consider only the energetics of the singlet state reaction, and we assume calculated free energies at 298 K to be a reasonable choice (values shown in black ink). The excited state reaction proceeds on the S_1 surface by formation of a singlet nitrene via a conical intersection (CI) with a geometry that is very similar to the transition state **TS1** predicted for the thermal pathway, with an energy release of ca. 392.5 kJ mol^{-1}. The singlet nitrene thus formed undergoes a cyclization reaction through **TS2** (+60.7 kJ mol^{-1}) to the unstable ***iso*-Cbz-1** with an energy release of −94.9 kJ mol^{-1}. In the final step, a 1,5-sigmatropic hydrogen shift via **TS3** occurs over a height of only 25.1 kJ mol^{-1} to release an additional 244.4 kJ mol^{-1}. One can see from the diagram that the energy needed to activate a thermal reaction is E(**TS1**) = 159.4 kJ mol^{-1}, and that the energy released is more than twice as large, ΔG_{Therm} = −343.1 kJ mol^{-1}. Based on the calculated energies and known reaction time constants, photochemical triggering would generate a significant amount of power in three steps: (1) the photo-triggering power (per mol) produced by the primary photochemical reaction (loss of N_2) is a remarkable, P_{trig} = −392.5 kJ mol^{-1}/450 × 10^{-15} s = 0.872 EW/mol (Exa = 10^{18}); (2) the thermal formation of *iso*-carbazole generates P_{therm} = −94.9 kJ mol^{-1}/16 × 10^{-12} s = 593 GW/mol, and (3) the formation of carbazole from *iso*-carbazole, $P_{iso\text{-}Cbz}$ = 244.4 kJ mol^{-1}/500 × 10^{-9} s = 48 MW/mol.

According to Fermi's golden rule, ultrafast energy dissipation at the molecular scale by IC and IVR occurs through high vibrational modes and, in solids, it is followed by intermolecular VET and optical phonons.[22,23,34,35] Notably, beyond C−H stretching modes (ca. 3,000 cm^{-1}), the next high frequency mode in **Az-1** is the asymmetric $^{-}N{=}N^{+}{=}N^{-}$ stretching at ca. 2200 cm^{-1}, which is also the denitrogenation reaction coordinate! Thus suggests a path for mode-selective intra- and

inter-molecular vibrational energy dissipation to accelerate the denitrogenation of close neighbors via intermolecular VET.[22,23] As the loss of N_2 occurs, a transient hot spot with a local temperature T_{loc} will be generated where further reactions could follow an Arrhenius type behavior [$1/\tau_R = A \exp(-E_a/RT_{loc})$]. To estimate the T_{loc} needed for a thermal chain to occur under those conditions we can take the calculated E_a =163.6 kJ mol^{-1} (**Figure 32**) and assume a reported pre-exponential factor for the N_2 dissociation reaction[36] of $A \approx 10^{14}$ s^{-1}. Knowing that the thermal reaction must occur in the time scale of thermal energy release, we can estimate that a chain reaction occurring within $\tau_R \approx 100$ ps would require a hot spot with a local temperature of ca. $T_{loc} \approx 870$ K, which is within the temperature range estimated for hot spots in energetic materials.[37,38] Notably, there are interesting examples in the literature reporting measurable photothermal effects lasting a few nanoseconds in nanocrystalline suspensions of photochromic crystals,[39–41] and mode-selective reaction acceleration under high power millisecond pulsed IR excitation.[42–44]

4.4.4 Crystalline 2-Azidobiphenyls

To test our hypothesis, we targeted four samples with different molecular and crystal structures. In addition to 2-azidobiphenyl **Az-1**, we decided to explore 4'-acetyl-2-azidobiphenyl **Az-2** with a carbonyl triplet sensitizer to exclude with confidence the potential involvement of a triplet state reaction. We also included samples of 4'-carboxy-2-azidobiphenyl **Az-3**, and 4'-carboxy-5-methoxy-2-azidobiphenyl **Az-4** with the expectation that they would have very high melting points and would undergo the purely thermal reaction in the solid state (**Scheme 2**). All four compounds were prepared by diazotization of the corresponding 2-amino-biphenyls followed by reaction with sodium azide. Crystals of all four compounds were obtained by slow evaporation from MeOH, and in the case **Az-4** with one third EtOAc. Melting points changed from 51−55°C

for **Az-1** and 79−81°C for **Az-2**. Reaction without melting was observed at ca. 180°C and ca. 170°C, respectively, for carboxylic acids **Az-3** and **Az-4**.

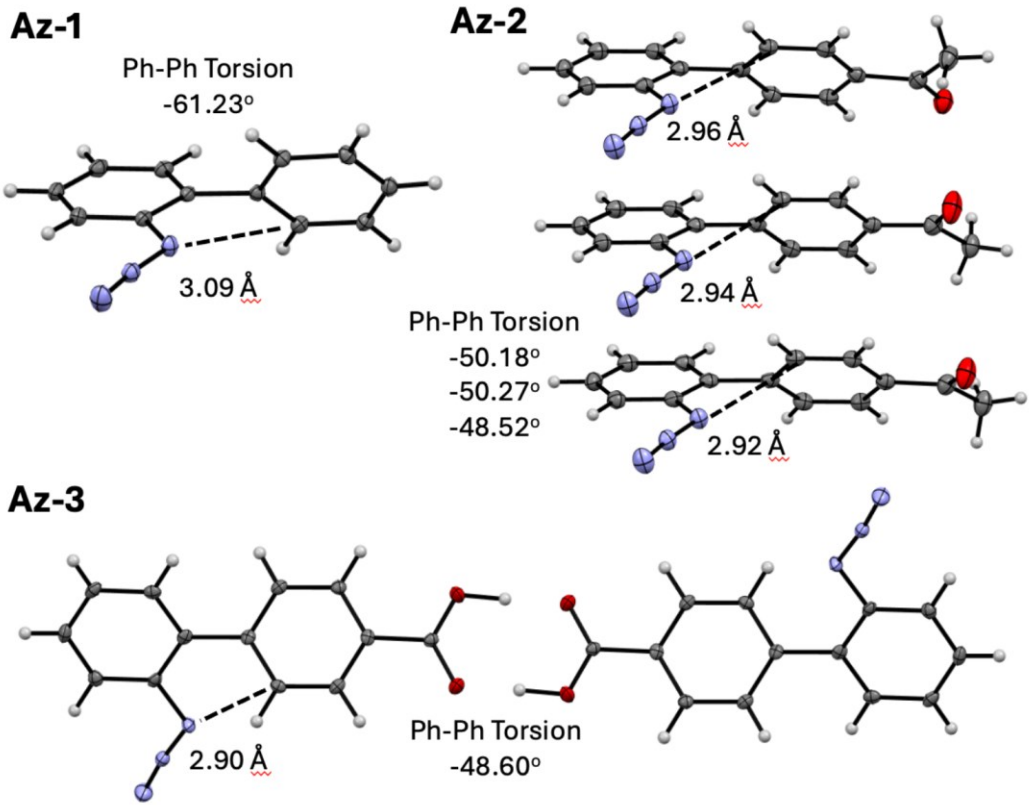

Figure 33. Crystals structure parameters that may influence the reaction of **Az-1**, **Az-2**, and **Az-3**.

While the crystal structure **Az-1** has been reported in the literature,[30] we determined the structures of **Az-2** and **Az-3** for the first time by single crystal X-ray diffraction (**Figure 33**). We have not been able to obtain crystals of **Az-4** that are suitable for diffraction analysis. Acetyl-azidobiphenyl **Az-2** crystallized in the space group P1-bar with three different molecules per asymmetric unit and carboxylic acid **Az-3** formed self-complementary hydrogen bonding dimers, also in the space group P1-bar (**Figure 33**). The possibility of topochemically allowed nitrene-

nitrene reactions to give diaryl-azo compounds seems unlikely, considering intermolecular N···N distances in the range of 6.95 Å to 7.39 Å, which are very far apart from the ca. 1.19 Å Ar-N=N-Ar distance in *trans*-azo-arenes.[45] By contrast, the structures of **Az-1** to **Az-3** are well positioned to undergo topochemically allowed intramolecular nitrene cyclization reactions, and based on results described below we infer the same to be true for **Az-4**. The distance between the prospective nitrene nitrogen and the aromatic C-atom ranges from 2.90 Å to 3.09 Å (**Figure 33**), which is less than the sum of the van der Waals radii for nitrogen and carbon, and relatively close to the C−N distance in the final product (d_{N-C} = 1.42 Å). Another structural change to occur along the reaction coordinate is given by torsion angles between the two aryl groups, which are twisted in the reactant and must be co-planar in the final product. In the case of the azide reactants, the inter-phenyl dihedral angle varies from −48.69° in **Az-3** and −50.27° in one of the three non-equivalent molecules **Az-2**, to as much as −61.23° in **Az-1**. While the torsional displacement is relatively large, planarization does not require a large change in volume and is not expected to be difficult at ambient temperatures.

4.4.5 Solid State Photochemical and Thermal Reactions

As expected for a highly reactive intermediate, photochemical experiments carried out in solution with **Az-1** to **Az-4** yielded the corresponding carbazole along with minor amounts of unidentified photoproducts. By contrast, photochemical experiments carried out in the solid state with single crystals or dry powders proceeded remarkably fast and with the exclusive formation of the carbazole derivatives. PXRD analysis of azide samples before and after photochemical exposure indicated that the as formed solid carbazole (**Cbz**) is also crystalline, sometimes in the same phase as the recrystallized sample (**Cbz-1**, **Cbz-3**), and sometimes in what appears to be a

different polymorph (**Cbz-2** and **Cbz-4**). PXRD analysis also suggested that solids obtained in situ from thermal reactions in the melt (**Cbz-1** and **Cbz-2**), or via solid-to-solid reactions (**Cbz-4**) are different from those obtained photochemically. The only exception was **Cbz-3**, which displays the same PXRD pattern upon solid-to-solid thermal or photochemical synthesis, and after recrystallization. Visual inspection with an optical microscope revealed destruction of the original crystals by photochemically induced micro-explosions, as illustrated with **Az-1** in **Figure 34** (top frames). Crystals of **Az-1** exposed to light while immersed in mineral oil displayed multiple fractures accompanied by vigorous release of N_2 bubbles (**Figure 34**, bottom frames) while the carbazole products crystallized, all within less than 30 s (**Figure 34**).

4.4.6 Nanocrystalline Suspensions

Crystals of **Az-1** to **Az-4** were amenable to the preparation of aqueous nanocrystalline suspensions by precipitation from saturated methanol solutions into a vortexing solvent. While nanocrystalline suspensions of hydrophobic **Az-1** and **Az-2** were prepared in water, nanocrystalline suspensions of **Az-3** and **Az-4** were prepared in hexanes. It should be noted that crystals with sizes on the order of the wavelength of light used in a given experiment (ca. 300−400 nm) mitigate many of the optical challenges arising from the high absorbance, birefringence, dichroism, specular reflection, and scattering, that complicate the reactions of large crystals and dry powders. In fact, nanocrystalline suspension may be viewed as a state in transition between supramolecular complexes and bulk matter. The identify of the suspended solids and the previously characterized crystals was confirmed by PXRD analysis of the corresponding filtrates and simulated patterns.

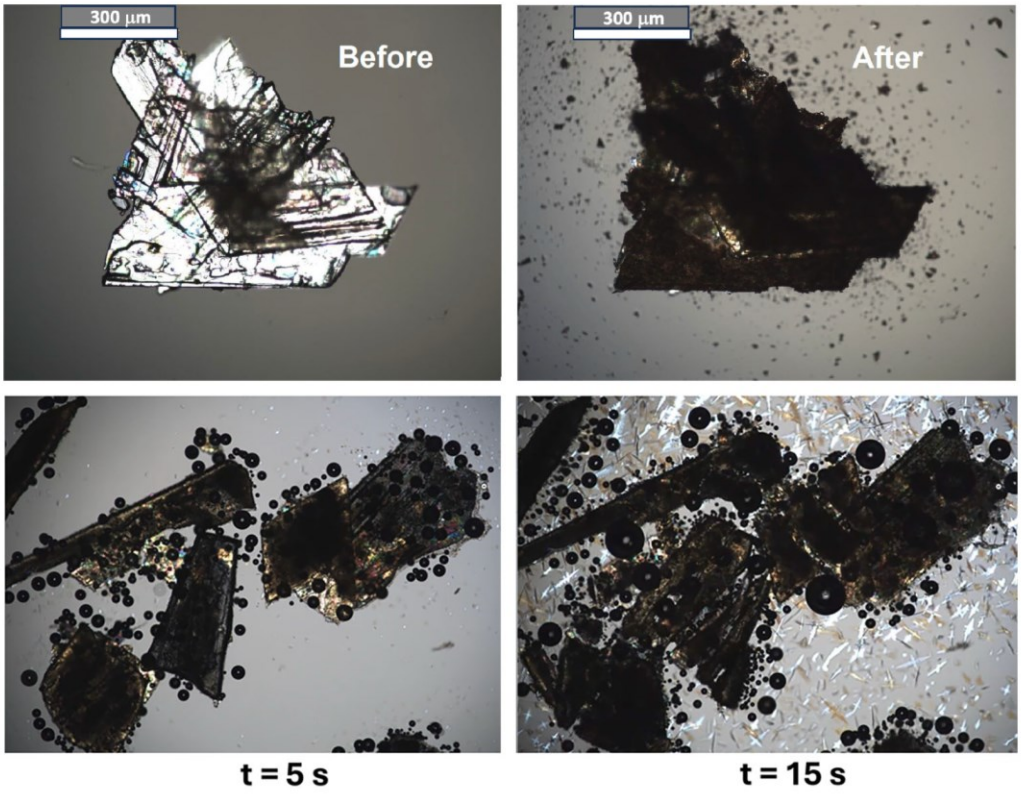

Figure 34. Top: Conglomerate of dry crystals of **Az-1** before (left) and after (right) photochemical reaction showing the destruction of the crystal lattice. Bottom: Crystals exposed to UV-light while immersed in mineral oil showing the vigorous release of N_2 bubbles within 5 s of irradiation and the fragmentation of the original specimens and crystallization of the product within 15 s of exposure.

4.4.7 Solid State Reaction Amplification and Solution Quantum Yields

In order to determine the potential photochemically triggered thermal chain, we devised a simple experimental protocol based on side-by-side irradiation of samples prepared with the same azide loading, both as aqueous nanocrystalline suspensions (Az_{susp}) and as a homogeneous solution (Az_{soln}). If there are no major absorption differences in the solution and light scattering is mitigated in suspension, the two samples would absorb a similar number of photons. Under these conditions, the percent reaction from Az_{susp} and Az_{soln} should be proportional to the corresponding quantum

yields, Φ_{susp} and Φ_{soln}. A photochemically triggered thermal chain can be determined with a high level of confidence when the percent product yield (%Az) in the suspended azide nanocrystals is greater than the one formed in homogeneous azide solution, such that there is an observable solid-state amplification (SSA = $\%Az_{susp}/\%Az_{soln} > 1.0$). Knowing that suspended nanocrystals are likely to have lower absorption due to light losses in the form of Tyndall scattering, SSA values are likely to represent a lower limit, SSA = $(\%Az_{susp}/\%Az_{soln}) \leq (\Phi_{susp}/\Phi_{soln})$. To validate the method, we analyzed the reaction of dicumyl ketone to dicumene, which previously shown to have quantum yields of $\Phi_{susp} = 0.20$ in suspended nanocrystals and $\Phi_{soln} = 0.41$ in solution.[46] As expected, side by side experiments carried out with loadings in the range of 1.4 mg/ml to 0.37 mg/ml) resulted reaction yields that mirror the solution and suspensions quantum yields, $\Phi_{susp}/\Phi_{soln} \approx 0.50 \pm 0.05$.

Table 3. Solid-state amplification (SSA) by parallel experiments with solution[a] and crystalline suspensions of **Az-1**. [a] Solution experiments were carried out in DMSO for all azides to be studied in the same solvent.

En-try	Sample	Loading (mg/ml)	Time (min)	% Yield Susp/Soln	SSA
1	**Az-1**	2.3	30	45 / 11	5.1
2	**Az-1**	1.4	20	54 / 12	4.5
3	**Az-1**	0.73	10	74 / 13	5.7
4	**Az-1**	0.37	7	83 / 15	5.5
5	**Az-1**	1.04	15	65 / 12	5.4
6	**Az-1-d_5**	1.05	15	56 / 9	6.2

The results from analogous experiments carried out with **Az-1** are summarized in **Table 3**. Sample loadings were varied from 0.37 mg/ml (0.19 mM) to 2.3 mg/ml (11.8 mM). Irradiations times ranged from 7 min for the lowest loading samples up to 30 min for the highest loading ones. Reaction yields consistently showed SSA values with product formation in the solid state being about 5 times more efficient than in solution, as indicated in the SSA column. No systematic changes in SSA values occurred as a function of loading within the range explored. Based on these results, we carried out analogous measurements with loading values of 0.37 and 0.73 mg/ml for azides **Az-2**, **Az-3** and **Az-4**. The SSA results in **Table 4** and **Figure 35** reveal remarkable consistency with SSA values that vary between 4.1 and 6.0 despite different molecular and crystal structures. It should be noted that results with **Az-2** are consistent with a singlet state reaction despite having an aromatic ketone that could have acted as a triplet sensitizer. Nanosecond laser pump-probe experiments were consistent with previous reports[25] where the *iso*-carbazole product is already formed within a ca. 10 ns laser pulse. These results are consistent with a fast (ca. ~500 fs) singlet state N_2 dissociation reaction that is about an order of magnitude faster than the time constant for intersystem crossing in substituted acetophenones (5−10 ps).[47]

Table 4. Solution quantum yields[a] and solid-state amplification (SSA) in crystalline suspensions of **Az-1** to **Az-4**. [a] Solution quantum yields measured in DMSO compared to relative to the loss of CO from dicumyl ketone in C_6H_6. [b] Quantum yields in suspension are defined as $\Phi_{susp} = \Phi_{soln} \times$ SSA.

Sample	Φ_{Soln}[a]	Loading (mg/ml)	SSA (Φ_{Susp})[b]
Az-1	0.45	0.37	5.2 (2.37)
		0.73	4.1 (1.86)
Az-2	0.49	0.37	6.0 (2.94)
		0.73	5.8 (2.84)
Az-3	0.49	0.37	5.9 (2.90)
		0.73	5.8 (2.82)
Az-4	0.43	0.37	6.0 (2.58)
		0.73	5.7 (2.47)

Experimental determination of the quantum yields of reaction of all four azides in solution (**Table 4**) led us to confirm the previously reported quantum yields of **Az-1** at $\Phi = 0.45$,[48] and unveil similar values for **Az-2** ($\Phi = 0.49$), **Az-3** ($\Phi = 0.49$), and **Az-4** ($\Phi = 0.43$). Based on these, we can estimate the quantum yield in the solid state to have values in the range of $\Phi_{susp} = 2.4$ to 2.9 per triggering photon, which is consistent with a short thermal chain reaction that completes with fast thermal dissipation.

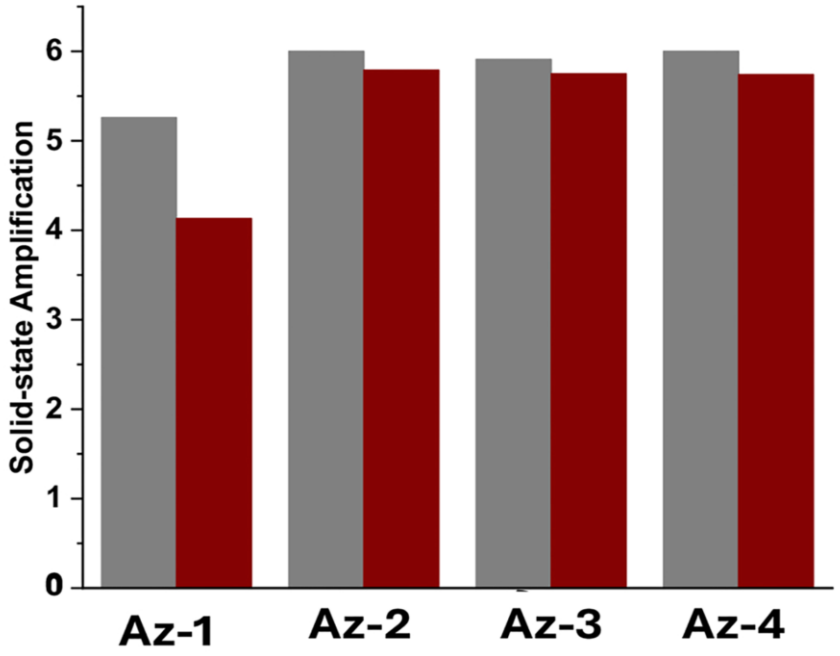

Figure 35. Solid-state amplification (SSA) values for **Az-1** to **Az-4** at loadings values of 0.37 mg/ml (grey) and 0.73 mg/ml (red).

4.4.8 Isotope Effects

To explore the suggested role of mode-selective nuclear dynamics and phonon-mediated heat transport, we decided to test the effects of deuterium substitution using 2-(phenyl-d_5)-phenyl azide isotopologue **Az-1-*d*$_5$**, prepared by Suzuki coupling of perdeuterated bis(pinacolato)diboron and 2-bromoaniline, followed by conversion into the desired azide by a diazotization reaction.

Isotope effects on product yields are determined by the product-determining step, which in solution corresponds to the photoinduced loss of N_2. By contrast, isotope effects on product yield amplification in the solid state depend on a combination of isotope effects on the photoinduced dissociation of N_2, and the proposed thermal denitrogenation that competes with phonon-mediated thermal dissipation.

Side by side reactions with samples of **Az-1** and **Az-1-*d*$_5$** in solution resulted in a positive isotope effect on the percent of reacted azide (%**Az-1**/%**Az-1-*d*$_5$**)$_{soln}$ = ***kie***$_{soln}$ = 1.33 ± 0.015. A positive isotope effect in solution suggest that the rate of N_2 loss from the excited state of the natural abundance azide is greater than the one in the deuterated isotopologue ($k_{\text{-N2(H)}} > k_{\text{-N2(D)}}$), or that the rate in internal conversion back to starting material is greater for the deuterated sample ($k_{\text{-IC(D)}} > k_{\text{-IC(H)}}$), as expected for an ultrafast mode-selective process. Analogous experiments with suspended crystals resulted in a smaller positive value (%**Az-1**/%**Az-1-*d*$_5$**)$_{susp}$ = ***kie***$_{susp}$ = 1.14 ± 0.09, with expected contributions from both excited state and thermal reactions. By contrast, isotope effects on the extent of solid-state amplification (SSA-***ie***) determined by comparing values from nanocrystals and solutions of **Az-1** [SSA(**Az-1**) = 5.4 ± 0.12] with those obtained from **Az-1-*d*$_5$** [SSA(**Az-1-*d*$_5$**) = 6.2 ± 0.10] led to inverse SSA-***ie*** (**Az-1**/**Az-1-*d*$_5$**) = 0.84. These results are combined in **Figure 36** as a plot of quantum yields vs SSA for the two **Az-1** isotopologues. While variations in the average quantum yields in **Figure 36** show that the number of reactions per photon in solution and in the solid state are greater for the natural abundance sample (dotted blue line), reaction amplification by the solid state (solid orange line) is improved to a greater extent in the deuterated sample. We propose that this effect is likely the result of a decrease in the rate of thermal dissipation[49] of the latter, which extends the lifetime of the photochemically-triggered hot spot. This interpretation is consistent with solid state quantum yields given by a convergent series of product formation probabilities at each step of the chain: $\Phi_{susp} = \Phi_{soln} + (\Phi_{soln})^{P1} + (\Phi_{soln})^{P2} +, \ldots (\Phi_{soln})^{Pn}$, with $P_n \rightarrow 0$, as determined by the ratio of the power available and power dissipated at each step. In the latter series, we assume that the quantum yield of the triggering reaction (Φ_{soln}) in solution is the same in solution and in the solid state, and that thermal dissipation and P_n decreases more slowly for the ^{2}H labelled sample.

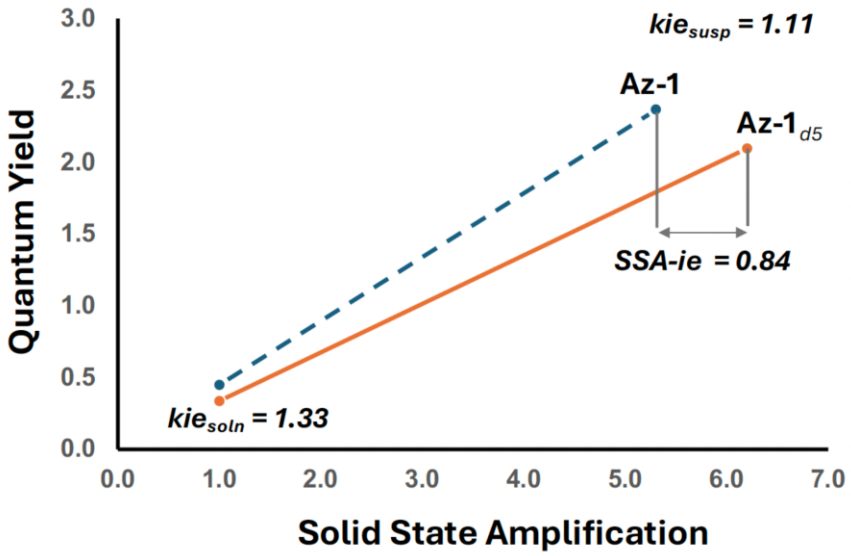

Figure 36. Quantum yields vs solid-state amplification (SSA) for **Az-1** and **Az-1-d_5**. All quantum yield values are relative to the quantum yield of **Az-1** determined in solution ($\Phi = 0.45$). SSA values are obtained by comparing solution and suspension yields.

4.4.9 Thermal Analysis

We analyzed computational and experimental enthalpies for the thermal reaction of compounds **Az-1** to **Az-4** (**Table 5**). Calculations indicate reaction enthalpies for the thermal denitrogenation (ΔH_{React}) to be similar for all four azides, with values ranging from −302.4 to −305.9 kJ/mol. Calculations also predict that activation enthalpies for the cyclization of nitrenes from **Az-1** to **Az-3** are identical ($\Delta H^{\ddagger}$ = 163.6 kJ/mol), while the barrier for **Az-4** is predicted to ca. 10 kJ/mol lower. DSC measurements revealed crystals of compounds **Az-1** and **Az-2** to melt before thermal denitrogenation. Crystals of **Az-1** displayed a melting endotherm at 54°C and a reaction exotherm in the range of 160−220°C with a reaction enthalpy of ΔH_{React} = −262.7 kJ/mol. Similarly, **Az-2** melts at 82°C and reacts within the same temperature range giving a value ΔH_{React} = −231.5 kJ/mol. Unfortunately, measurements with both **Az-1** and **Az-2** were complicated by the

fact that the carbazole product undergoes an exothermic crystallization from the melt before the reaction is completed. Results with crystals of **Az-3** and **Az-4** displayed exothermic transitions over a similar temperature range (ca. 170−230°C) with values of ca. −245.0 kJ/mol and −256.8 kJ/mol, respectively. However, the thermograms of these samples displayed reproducible features superimposed with the exothermic peaks, suggesting that the thermal reaction is accompanied by a solid-to-solid phase transition. This was confirmed by powder X-ray diffraction analysis of the as-formed solid-to-solid carbazoles, which patterns that were different from than the ones obtained after recrystallization. While variations between experimental and calculated values on the order of 15−25% include differences corresponding to gas phase models vs real crystalline phases, variations within the experimental values on the order of 5−13% reveal differences between reactions in the melt and solid-to-solid reactions via a reconstructive phase transition.

Table 5. Enthalpies of activation, reaction, and melting for the 2-azidobiphenyl crystals studied in this work. Enthalpy values are reported in kJ/mol. [a] Samples melt before undergoing thermal denitrogenation, which overlaps with crystallization of carbazole from the melt. [b] Samples undergo a reconstructive solid-to-solid phase transition early in the denitrogenation reaction. [c] DSC onset (T_{onset}) and peak (T_{peak}) temperatures in °C with heating rates of 5°C/min.

Azide	ΔH_{React} calc.	ΔH_{React} exp.	$\Delta H^{\ddagger}$ calc.	T_{onset} - T_{peak}[c]
Az-1	-302.5	-262.7[a]	163.6	170 - 211
Az-2	-305.9	-231.5[a]	163.6	160 - 190
Az-3	-305.4	-245.0[b]	163.6	180 - 224
Az-4	-302.5	-256.8[b]	152.3	170 - 211

The onset reaction temperature (T_{onset}) and the peak temperature (T_{peak}) fall in the range of 160−180°C and 190−224°C, respectively, and are significantly higher than those shown to support self-sustaining thermal chain reaction in anthracene dimers (59−75°C). Those reactions are sustained by equilibrium photothermal effects, rely on conductive heat transfer, and are primarily terminated by radiative heat losses at the macroscopic scale. We propose that these large differences explain the small chain lengths observed in this study, where the lifetime of a hot spot is not long enough to support more than ca. 5 reactions per triggering event.

4.5 Conclusion

In conclusion, photochemically triggered thermal chain reactions rely on the critical interplay between the time scales heat generation, heat utilization, and heat dissipation, such that the parameters to control have units of power. Using four crystalline 2-azido-biphenyl derivatives we obtained strong evidence that the power available from an ultrafast photochemical reaction can trigger a process that results in as many as 5 reactions per photon absorbed. The proposed mechanism involves a photochemical denitrogenation known to occur within 450 fs, which based on calculated reaction energies should generate ca. 860 GW/mol of power as the first product molecule is formed. The resulting singlet nitrene goes on to form a transient *iso*-carbazole molecule within 16 ps, which generates 6.41 GW/mol of power. Based on a calculated thermal denitrogenation barrier of 163.6 kJ/mol, and assuming that the energy used for the thermal reaction should occur with a time scale that is within the same order of magnitudes as the rate for energy generation (ca. 100 ps), we can estimate an upper limit for a hot spot temperature of ca. 875 K, which is within the range estimated for energetic materials. While power dissipation within the dimensions and time scales involved in this study cannot be obtained with macroscopic

thermodynamic parameters, it is well known that molecular crystals are not good heat conductors. We propose that photo-triggering takes advantage of intramolecular vibrational relaxation (IVR) and vibrational energy transfer (VET), potentially in a mode selective manner. Photochemical experiments carried out with nanocrystalline suspensions and solutions resulted in a 5-fold solid state amplification from a quantum yield $\Phi = 0.49$ in solution to $\Phi \approx 2.5$ in the solid state. The relatively small reaction enhancement is determined by the relatively high barrier for the thermal reaction, which would require a longer-lived high temperature hot spot. However, one may expect crystalline photo-triggered azides with increasingly lower activation energies for the loss of N_2 to transition from modest self-activated thermal chain reactions to efficient systems that can safely go to full conversion, to thermal runaway reactions that could result in crystal melting, all the way to ignition and explosion.

4.6 References

(1) Scheffer, J. R. Crystal lattice control of unimolecular photorearrangements. *Acc. Chem. Res.* **1980**, *13*, 283−290.

(2) Hipwell, V. M.; Garcia-Garibay, M. A. Mechanistic Studies of Adamantylacetophenones with Competing Reaction Pathways in Solution and in the Crystalline Solid State, *J. Org. Chem.* **2019**, *84*, 11103−11113.

(3) Dotson, J. J.; Liepuoniute, L.; Bachman, J. L.; Hipwell, V. M.; Saeed I. Khan, S. I.; Houk, K. N.; Garg, N. K.; Garcia-Garibay, M. A. Taming Radical Pairs in the Crystalline Solid State: Discovery and Total Synthesis of Psychotriadine. *J. Am. Chem. Soc.* **2021**, *143*, 4043−4054.

(4) MacGillivray, L. T.; Papaefstathiou, G. S.; Friščić, T.; Hamilton, T. D.; Bučar, D.-K.; Chu, Q.; Varshney, D. V.; Georgiev, I. G. Supramolecular control of reactivity in the solid state: from templates to ladderanes to metal−organic frameworks. *Acc. Chem. Res.* **2008**, *41*, 280−291.

(5) Yamagishi, H.; Small, D. W.; Sarpong, R. Unified Total Synthesis of C_2-Symmetric Bis(cyclotryptamine) Alkaloids Utilizing a Single-Atom Insertion/Deletion Strategy. *J. Am. Chem. Soc.* **2025**, *147*, 47322−47329.

(6) Naumov, P.; Chizhik, S.; Panda, M. K.; Nath, N. K.; Boldyreva, E. Mechanically Responsive Molecular Crystals. *Chem. Rev.* **2015**, *115*, 12440−12490.

(7) Karlen, S.D.: Reyes, H.; Taylor, R. E.; Khan, S.I.; Hawthorne, M.F.; Garcia-Garibay, M.A. Symmetry and Dynamics of Molecular Rotors in Amphidynamic Molecular Crystals. *Proc. Nat. Acad. Sci. USA* **2010**, *107*, 14973−14978.

(8) Kuzmanich, G.; Natarajan, A,; Chin, K. K.; Veerman, M.; Mortko, C. J.; Garcia-Garibay, M. A. Solid State Photodecarbonylation of Diphenylcyclopropenone: A Singlet State Quantum Chain Reaction Made Possible by Ultrafast Energy Transfer. *J. Am. Chem. Soc.* **2008**, *130*, 1140−1141.

(9) Kuzmanich, G.; Gard, M. N. and Garcia-Garibay, M. A. Photonic Amplification by a Singlet State Quantum Chain Photodecarbonylation Reaction in Crystalline Diarylcyclopropenones. *J. Am. Chem. Soc.* **2009**, *131*, 11606−11614.

(10) Rivera, E.; Paul, I.; Fajardo Jr, J.; Garcia-Garibay. M. A. Quantum Chain Amplification in Nanocrystalline Dewar Benzenes by Intramolecular Sensitization. *Chem. Sci.* **2023**, *14*, 5802−5810.

(11) Paul, I.; Konieczny, K. A.; Chavez, R.: Garcia-Garibay, M. A. Reaction amplification with a gain: Triplet exciton-mediated quantum chain using mixed crystals with a tailor-made triplet sensitizer. *Proc. Natl. Acad. Sci. USA* **2024**, *121*, e2401982121.

(12) Konieczny, K. A.; Paul, I.; Rodriguez, J. A. Garcia-Garibay, M. A. From Beam Damage to Massive Reaction Amplification Under the Electron Microscope: An Ionization-Induced Chain Reaction in Crystals of a Dewar Benzene. *ACS Cent. Sci*. **2024**, *10*, 2346−2352.

(13) Konieczny, K. A.; Rai, R.; Garcia-Garibay, M. A. Topochemical Synthesis, micro-Electron Diffraction (3D ED), and Electron Beam-Initiated Topotactic Dimer Splitting of cis,syn-Thymine Dimer Crystals. *J. Am. Chem. Soc.* **2025**, *147*, 20426−20430.

(14) Konieczny, K. A.; Rai, R.; Rodriguez, J.; Garcia-Garibay, M. A. Mitigation of Electron Beam Damage in Crystals Undergoing a Topotactic Radical Ion Chain Reaction. Single-Crystal-to-Single-Crystal Radical Ion Chain Reactions under the Electron Microscope: A Chemical Design to Repurpose Electron Beam Damage. *J. Am. Chem. Soc.* **2025**, *147*, 44285−44292.

(15) The first documented quantum chain reaction involves the triplet sensitized photoisomerization of 2,4-hexadiene: Hyndman, H. L.; Monroe, B. M.; Hammond, G. S. *J. Am. Chem. Soc.* **1969**, *91*, 2852.

(16) Romero, N. A.; Nicewicz, D. A. Organic Photoredox Catalysis. *Chem. Rev.* **2016**, *116*, 10075−10166.

(17) Rai, R.; Konieczny, K. A.; Chavez, R. Garcia-Garibay, M. A. Crystalline Thymine Dimers Splitting by Photomechanochemical Interfacial Single Electron Transfer-Initiated Chain Reaction. *J. Am. Chem. Soc.* **2025**, *148*, 2103−2107.

(18) Xu, H.; Han P.; Wang, W.; Qin, A,; Tang, B. Z. Recent Progress in Organic High-Temperature Photothermal Materials *Chem Asian J.* **2025**, *20*, e202500034.

(19) Zhao, L.; Liu, Y.; Xing, R.; Yan, X. Supramolecular Photothermal Effects: A Promising Mechanism for Efficient Thermal Conversion *Angew. Chem. Int. Ed.* **2020**, *59*, 3793−3801.

(20) Chakraborty, S.; Nguyen, H. P. Q.; Usuba, J.; Choi, J. Y.; Sun, Z.; Raju, C.; Sigelmann, G.; Qiu Q.; Cho, S.; Tenney, S. M.; Shulenberger, K. E.; Schmidt-Rohr, K.; Park, J.; Han, G. G. D. Self-activated energy release cascade from anthracenebased solid-state molecular solar thermal energy storage systems. *Chem* **2024**, *10*, 3309−3322.

(21) It is worth noting, that the limit of high exothermicity with low reaction barriers ($\Delta G_{React} >> \Delta G^{‡}$) and slow heat dissipation rates includes ignition and explosions.

(22) Ostrander, J. S.; Knepper, R.: Tappan, A. S.; Kay, J.J.; Zanni, M. T.; Farrow, D. A. Energy Transfer Between Coherently Delocalized States in Thin Films of the Explosive Pentaerythritol Tetranitrate (PETN) Revealed by Two-Dimensional Infrared Spectroscopy. *J Phys Chem B* **2017**, *121*, 1352−1361.

(23) Cole-Filipiak, N. C.; Knepper, R.; Wood, M.; Ramasesha, K. Sub-picosecond to sub-nanosecond vibrational energy transfer dynamics in pentaerythritol tetranitrate. *J. Phys. Chem. Lett.* **2020**, *11*, 16, 6664−6669.

(24) Azatyan, V. V. Role of Semenov's Theory of Chain Reactions in the Formation of Modern Concepts on the Processes of Combustion, Explosion, and Detonation of Gases. *Russ. J. Phys. Chem. B* **2021**, *15*, 278−284.

(25) Chung, T. S.; Ayitou, A. J.-L.; Park, J.; Breslin, V. M.; Garcia-Garibay, M. A. Photochemistry and Transmission Pump-Probe Spectroscopy of 2-Azidobiphenyls in Aqueous Nanocrystalline Suspensions: Simplified Kinetics in Crystalline Solids *J. Phys. Chem. Lett.* **2017**, *8*, 1845−1850.

(26) Takayama, T.; Mitsumori, T,; Kawano, M.; Sekine, A.; Uekusa, H.; Ohashi, Y.; Sugawara, T. Direct observation of aryl nitrene formation in the photoreaction of arylazide crystals. *Acta Cryst.* **2010**, *66*, 639−646.

(27) Sasaki, A., Mahé, L., Izuoka, A. & Sugawara, T. Chemical consequences of arylnitrenes in the crystalline environment. *Bull. Chem. Soc. Jpn*. **1998**, *71*, 1259−1275.

(28) Tsao, M.-L.; Gritsan, N.; James, T. R.; Platz, M. S.; Hrovat, D. A.; Borden, W. T. Study of the chemistry of *ortho*- and *para*-biphenylnitrenes by laser flash photolysis and time-resolved IR experiments and by B3LYP and CASPT2 Calculations *J. Am. Chem. Soc.* **2003**, *125*, 9343−9358.

(29) Burdzinski, G. T.; Gustafson, T. L. Hackett, J. C.; Hadad, C. M.; Platz, M. S. The Direct Detection of an Aryl Azide Excited State: An Ultrafast Study of the Photochemistry of para- and *ortho*-Biphenyl Azide. *J. Am. Chem. Soc.* **2005**, *127*, 13764−13765.

(30) Chung, T.S.; Ayitou, A. J.-L.; Park, J.; Breslin, V. M.; Garcia-Garibay, M. A. Photochemistry and Transmission Pump-Probe Spectroscopy of 2-Azidobiphenyls in Aqueous Nanocrystalline Suspensions: Simplified Kinetics in Crystalline Solids. *J. Phys. Chem. Lett.* **2017**, *8*, 1845−1850.

(31) Zhao, Y.; Truhlar, D. G. The M06 Suite of Density Functionals for Main Group Thermochemistry, Thermochemical Kinetics, Noncovalent Interactions, Excited States, and Transition Elements: Two New Functionals and Systematic Testing of Four M06-Class Functionals and 12 Other Functionals. *Theor. Chem. Acc.* **2008**, *120*, 215−241.

(32) Grimme, S.; Antony, J.; Ehrlich, S.; Krieg, H. A Consistent and Accurate Ab Initio Parametrization of Density Functional Dispersion Correction (DFT-D) for the 94 Elements H-Pu. *J. Chem. Phys.* **2010**, *132*, No. 154104.

(33) Weigend, F.; Ahlrichs, R. Balanced basis sets of split valence, triple zeta valence and quadruple zeta valence quality for H to Rn: Design and assessment of accuracy. *Phys. Chem. Chem. Phys.* **2005**, *7*, 3297−305.

(34) Ventura, E.; Andrade do Monte, S. do Casal, M. T.; Pinheiro Jr, M.; Toldo, J. M.; Barbatti. M. Modeling the heating and cooling of a chromophore after photoexcitation. *Phys. Chem. Chem. Phys.* **2022**, *24*, 9403.

(35) Y. Zhang, J. Chen and B. Kohler, Hydrogen Bond Donors Accelerate Vibrational Cooling of Hot Purine Derivatives in Heavy Water. *J. Phys. Chem. A* **2013**, *117*, 6771−6780.

(36) Azide pre-exponential 10^{14}.

(37) Zhang, Y.; Wang, T.; He, Y. Hot spot formation and initial chemical reaction of PETN containing nanoscale spherical voids under high shock loading. *RSC Adv.* **2022**, *12*, 11060−11074.

(38) Shan, T-R; Wixom, R. R.; Thompson, A. P. Extended asymmetric hot region formation due to shockwave interactions following void collapse in shocked high explosive. *Phys. Rev. B* **2016**, *94*, 054308.

(39) Ishibashi, Y.; Nakai, S.; Masuda, K.; Kitagawa, D.; Kobatake, S.; Asahi, T. Nanosecond laser photothermal effect-triggered amplification of photochromic reactions in diarylethene nanoparticle. *Chem. Commun.* **2020**, *56*, 7088−7091.

(40) Ishibashi, Y.; Nishimoto, A.; Ogura, Y.; Asahi, T. Photocoloring Reaction Behavior in Spironaphthooxazine Nanoparticles under Nanosecond Pulse Laser Irradiation. *J. Phys. Chem. C* **2024**, *128*, 21462−21471.

(41) Ishibashi, Y.; Omoda, H.; Asah, T. Photothermal Conversion Dynamics of Aqueous Quinacridone Nanocrystal Colloid by Femtosecond Transient Absorption Spectroscopy. *J. Phys. Chem. C* **2024**, *128*, 226−233.

(42) Pannir-Sivajothi, S.; Poh, Y. R.; Liu, Z.-J.; Imperatore, M.; Naeini, A. A.; Myeong, I.-S. Movassaghi, M.; Giebink, N. C.; Nel- son, K. A. Yuen-Zhou, J. Mode-Specific versus Local Heating Effects in Infrared-Laser-Driven Reactions. *J. Phys. Chem. A* **2026**, *130*, 1153−1161.

(43) Windhorn, L.; Yeston, J. S.; Witte, T.; Fu., W.; Motzkus, M.; Proch, D.; Kompa, K.-L.; Moore, C. B. Getting ahead of IVR: A demonstration of mid-infrared induced molecular dissociation on a sub-statistical time scale. *J. Chem. Phys.* **2003**, *119*, 641−645.

(44) Stensitzki, T.; Yang, Y.; Kozich, V.; Ahmed, A. A.; Kössl, F.; Kühn, O.; Heyne, K. Acceleration of a ground-state reaction by selective femtosecond-infrared-laser-pulse excitation. *Nat. Chem.* **2018**, *10*, 126−131.

(45) Harada, J.; Ogawa, K.; Tomoda, S. Molecular Motion and Conformational Interconversion of Azobenzenes in Crystals as Studied by X-ray Diffraction. *Acta Crystallogr. B* **1997**, *53*, 662−672.

(46) Veerman, M.; Resendiz, M. J. E.; Garcia-Garibay, M. A., Large-Scale Photochemical Reactions of Nanocrystalline Suspensions: A Promising Green Chemistry Method. *Org. Lett.* **2006**, *8*, 2615−2617.

(47) Murov, S. L.; Carmichael, I.; Hug, G. L. Handbook of Photo-chemistry; Marcel Dekker, Inc.: New York, 1993.

(48) Reiser A.; Marley, R. Photolysis of aromatic azides. Part 3. − Quantum yield and mechanism. *Trans. Faraday Soc.* **1968**, *64*, 1806−1815.

(49) Manley, M. E.; Hong, K.; Yin, P.; Chi, S.; Cai, Y.; Hua, C.; Daemen, L. L.; Hermann, R. P.; Wang, H.; May, A. F.; Asta, M.; Ahmadi, M. Giant isotope effect on phonon dispersion and thermal conductivity in methylammonium lead iodide. *Sci. Adv.* **2020**, *6*: eaaz1842.

Chapter 5: Stereoselective Radical Acylfluoroalkylation of Bicyclobutanes via N-Heterocyclic Carbene Catalysis

5.1 Contributions

This chapter is based on the following published article: Chuyu Xiao, Jing-Ran Shan, Wen-Deng Liu, Xingyuan Gao, Jingwei Dai, Zuwei Wang, Wentao Wang, K. N. Houk, and Jiannan Zhao, "Stereoselective Radical Acylfluoroalkylation of Bicyclobutanes via N-Heterocyclic Carbene Catalysis," *Angew. Chem. Int. Ed.* **2025**, *64*, e202416781. This work was carried out in collaboration with Prof. Jiannan Zhao and his group at Dalian University of Technology, as well as Prof. Wentao Wang at the Dalian Institute of Chemical Physics, Chinese Academy of Sciences. Chuyu Xiao and I contributed equally to this work and are listed as co-first authors. I designed and carried out all computational studies presented in this work, except for the simulations of the X-band EPR spectra, which were performed by Zuwei Wang. I also contributed to the writing of the manuscript.

5.2 Abstract

Cyclobutanes are prominent structural components in natural products and drug molecules. With the advent of strain-release-driven synthesis, ring-opening reactions of bicyclo[1.1.0]butanes (BCBs) provide an attractive pathway to construct these three-dimensional structures. However, the stereoselective difunctionalization of the central C−C σ-bonds remains challenging. Reported herein is a covalent-based organocatalytic strategy that exploits radical NHC catalysis to achieve diastereoselective acylfluoroalkylation of BCBs under mild conditions. The Breslow enolate acts

as a single electron donor and provides an NHC-bound ketyl radical with appropriate steric hindrance, which effectively distinguishes between the two faces of transient cyclobutyl radicals. This operationally simple method tolerates various fluoroalkyl reagents and common functional groups, providing a straightforward access to polysubstituted cyclobutanes (75 examples, up to > 19:1 d.r.). The combined experimental and theoretical investigations of this organocatalytic system confirm the formation of the NHC-derived radical and provide an understanding of how stereoselective radical-radical coupling occurs.

5.3 Introduction

Cyclobutanes constitute an important structural motif found in numerous biologically active natural products.[1] Their favorable physicochemical properties, along with their utility as functional group bioisosteres, render them particularly attractive in the context of drug discovery.[2] Consequently, the development of new strategies for the efficient and rapid synthesis of these three-dimensional structures has garnered considerable attention from the synthetic chemistry community.[3,4] The most straightforward strategies for synthesizing cyclobutanes involve [2+2] cycloadditions of alkenes, facilitated by Lewis acid catalysis or photocatalysis.[4] Furthermore, with the emergence of strain-release-driven synthesis,[5] bicyclo[1.1.0]butanes (BCBs) have gained prominence as versatile precursors, offering a divergent pathway for the construction of these carbocycles.[6–8]

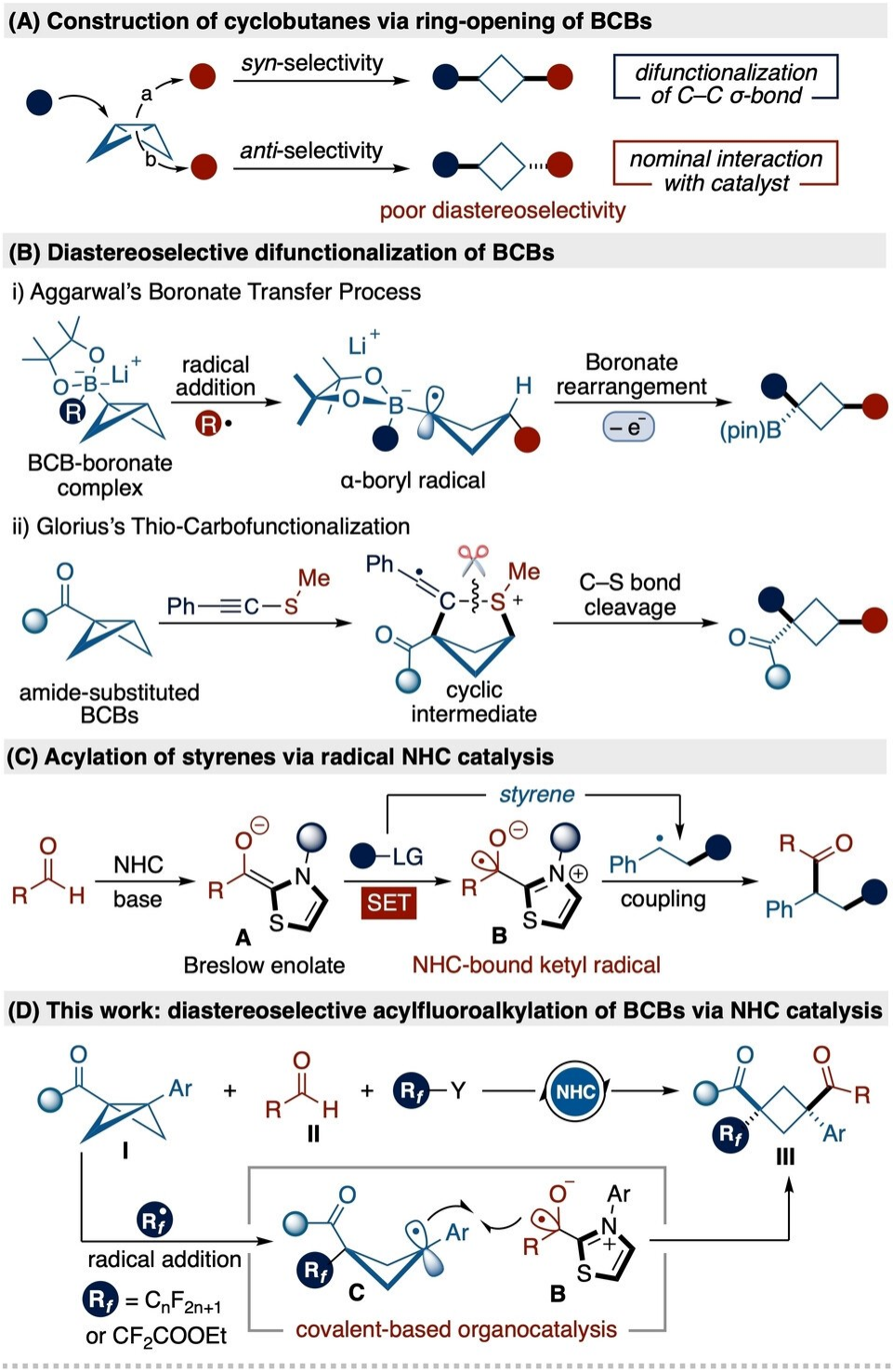

Figure 37. Stereoselective construction of cyclobutanes via acylfluoroalkylation of BCBs.

The reactivity of the BCB scaffold involves mainly its central C−C bond (**Figure 37a**). Regioselective ring-opening of this bond has been achieved by both nucleophiles[6a–f] and electrophiles.[6h] Moreover, recent advancements in photocatalysis have enabled radical-involved difunctionalization of these strained σ-bonds, presenting an attractive approach to access polysubstituted cyclobutanes.[7] However, controlling diastereoselectivity (*syn* vs *anti*) in this process remains a considerable challenge.[7a,b] This is largely due to the limited interaction between the photocatalyst and the radical-based intermediates, which undergo the reaction with minimal activation barriers. In a notable report, Aggarwal demonstrated that the central C−C bond in boronate-substituted BCBs was readily cleaved by electrophilic radicals (**Figure 37b**, path i).[7c,d] The radical addition led to the formation of an α-boryl radical intermediate, inducing a stereospecific 1,2-migration of the boron substituent to the α-carbon. More recently, Glorius and co-workers have explored the reaction of BCBs with sulfur-containing bifunctional reagents under photoredox conditions (Figure 1B, path ii).[7e] The cleavage of C−S σ-bonds in the cyclic radical cationic intermediates resulted in *syn*-selective thio-carbofunctionalization of the strained C−C bond. While these approaches have achieved impressive diastereoselectivities with carefully designed substrates, the development of methods that utilize stereodifferentiating catalysts is less developed.

N-Heterocyclic carbene (NHC) radical organocatalysis has recently emerged as a powerful platform for the invention of versatile transformations.[9–13] The Breslow enolate **A**, generated upon nucleophilic addition of an NHC to an aldehyde, is recognized as a potent reductant ($E_{1/2}$[**B**/**A**] = −1.2 ~ −1.7 V vs SCE),[10] capable of initiating single-electron transfer (SET) with appropriate redox partners (**Figure 37c**).[11] A primary reaction pathway involves the addition of the generated radicals to styrene, leading to the formation of a more stable benzyl radical. This radical

subsequently undergoes cross-coupling with the NHC-derived ketyl radical **B**, achieving the difunctionalization of the C=C bond. Furthermore, since the ketyl radical was covalently bound to the organocatalyst, this strategy allowed us to develop stereoselective radical-radical coupling reactions.[11g,12i,12j] In contrast to the extensively studied NHC-catalyzed radical acylation reactions of π-systems (e.g. alkenes, alkynes, allenes), we explored the covalent-based organocatalytic strategy for the stereoselective acylation of the BCB group (**Figure 37d**).

Based on the above hypothesis, we speculated that electrophilic fluoroalkyl radicals ($R_f^{\bullet}$), generated via NHC-catalyzed SET reduction,[13] could trigger radical ring-opening reactions of BCBs, leading to the formation of benzyl radicals **C**. We envisioned that the ensuing NHC-bound ketyl radical **B** could differentiate between competing stereomeric transition states of the transient cyclobutyl radical **C**, thereby enabling diastereoselective acylfluoroalkylation of BCBs. This organocatalytic protocol provides access to polysubstituted cyclobutanes, which can be further transformed into oxa-bridged bicyclic structures. Integrated experimental, computational, and spectroscopic studies substantiated the formation of the NHC-derived radical and elucidated the origin of stereocontrol.

5.4 Results and Discussion

5.4.1 Reaction Development

Figure 38 depicts our proposed catalytic cycle, which is initiated by the formation of Breslow enolate A through the nucleophilic addition of a thiazolium-derived NHC to aldehyde **1** in the presence of a base. This step is followed by the SET reduction of the fluoroalkyl source **3** (R_f−Y), converting enolate **A** into a ketyl radical **B**. The subsequent addition of the fluoroalkyl

radical to the central C−C bond of BCB **2** delivers the benzyl radical **C**, which would undergo diastereoselective radical cross-coupling with the NHC-bound radical **B**. Finally, the elimination of NHC from intermediate **D** affords the fluorine-containing cyclobutane **4** and completes the catalytic cycle.

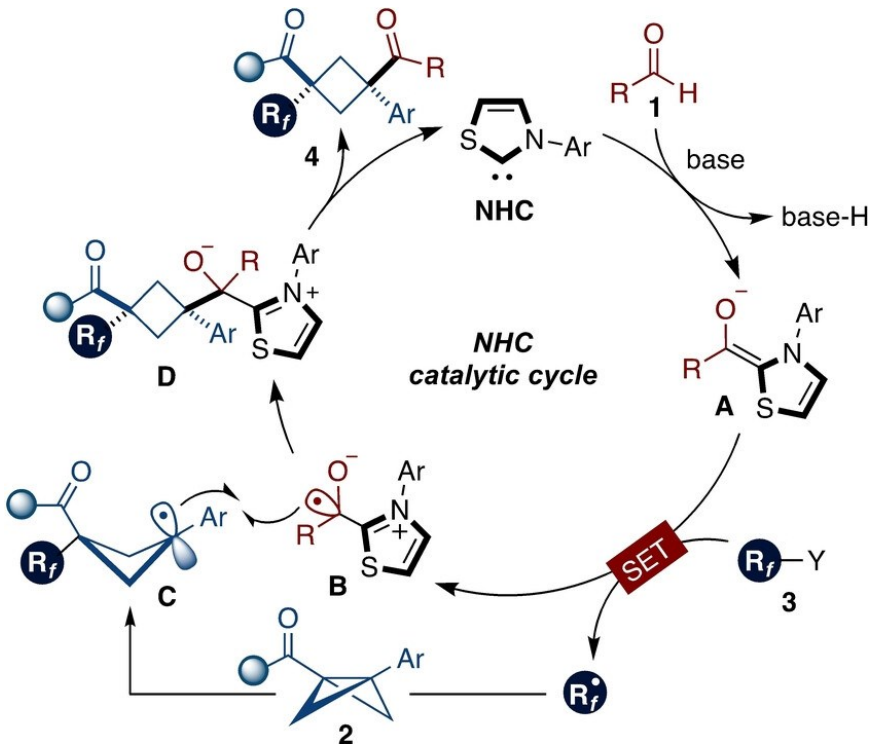

Figure 38. Prospective catalytic cycle.

The feasibility of the organocatalytic plan was evaluated by exploring the reaction of 1,3-disubstituted BCB **2a** with benzaldehyde **1a** (**Table 6**). The Togni **I** reagent **3a** was initially selected as the fluoroalkyl source due to its ability to participate in SET with Breslow enolates. Upon optimizing various reaction parameters, the desired carbocycle **4** was obtained in 81% isolated yield after reaction under a nitrogen atmosphere for 18 hours (entry 1). Remarkably, in

alignment with our expectations, the tetrasubstituted cyclobutane **4** was isolated as a single diastereomer with > 19:1 d.r., when employing *N*-2,4,6-trimethylphenyl-substituted thiazolium salt **N1** as the catalyst. Further investigation of the catalyst revealed that the use of either *N*-neopentyl-substituted **N3** or *N*-benzyl-substituted **N4** resulted in diminished diastereoselectivies (entries 3 and 4). These outcomes suggested that steric hindrance adjacent to the NHC moiety plays a critical role in dictating stereocontrol. Additionally, alternative trifluoromethyl sources, such as the Togni **II** reagent and Umemoto's reagent, were found to significantly compromise the reaction yield (entries 5 and 6). Switching the base to either Cs_2CO_3 or $NaHCO_3$ yielded inferior results compared to the optimized result (entries 7 and 8). Further examination of different solvents highlighted DMSO as the superior solvent for this transformation (entries 9 and 10).

Table 6. Investigation of the reaction parameters.[a]

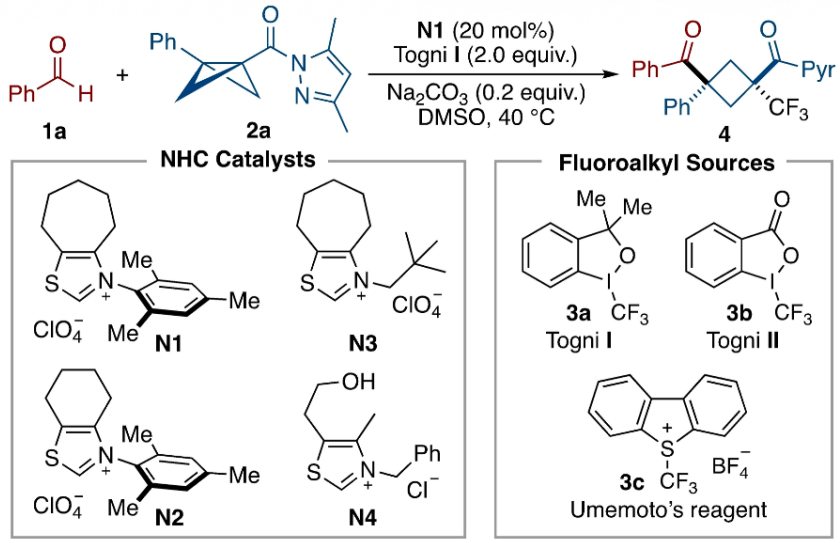

entry	variation from above conditions	yield [%][b]	d.r.[c]
1	none	81	>19:1
2	**N2** instead of **N1**	50	>19:1
3	**N3** instead of **N1**	29	6:1
4	**N4** instead of **N1**	37	4:1
5	**3b** instead of **3a**	N.R.	–
6	**3c** instead of **3a**	N.R.	–
7	Cs_2CO_3 instead of Na_2CO_3	56	>19:1
8	$NaHCO_3$ instead of Na_2CO_3	38	>19:1
9	CH_3CN instead of DMSO	Trace	–
10	DMF instead of DMSO	30	>19:1

[a] The reactions were carried out with **1a** (0.1 mmol), **2a** (0.2 mmol), **3a** (0.2 mmol), NHC catalyst (20 mol%) and Na_2CO_3 (20 mol%) in 1.0 mL of DMSO at 40 °C for 18 h. [b] Yields of isolated products. [c] Diastereomeric ratio (d.r.) values were determined by ^1H NMR.

5.4.2 Substrate Scope

Upon establishing the optimized conditions, we proceeded to investigate the scope and limitations of the organocatalytic acylfluoroalkylation reaction. The observed excellent stereoselectivity prompted us to initially examine the reaction of bicyclobutane **2a** with a diverse

array of aldehydes (**Scheme 3**). The NHC catalyzed radical reaction proved effective with a broad spectrum of aryl aldehydes, yielding the corresponding cyclobutane derivatives with satisfying yields and consistently high diastereoselectivities (**5–35**). The reaction outcomes were influenced by the positions of the substituents on the aromatic ring. Generally, benzaldehydes bearing *para*-substitutions afforded the desired products (**10–14**) in better yields compared to their *meta*-substituted analogues (**5–9**). In line with previous studies,[11] aldehydes featuring *ortho*-substituted aromatic rings were sterically challenging under current reaction conditions.[14] X-ray crystallographic analysis of compound **4** unequivocally demonstrated that the *N*-acylpyrazole and carbonyl groups are positioned cis to each other on the cyclobutane scaffold. Notably, our research has effectively incorporated a spectrum of functionalities, such as nitrile, ester, thioether, sulfonyl, and trifluoromethyl groups (**17–23**), which are frequently employed in medicinal chemistry. The reaction with *para*-B(pin)-benzaldehyde yielded product **24**, which is amenable to conventional cross-coupling chemistry. Furthermore, the stereoselective transformation proceeded smoothly with 2-naphthaldehyde (**25**) and various heteroaryl aldehydes, encompassing derivatives of pyridine (**26–28**), furan (**29**) and thiophene (**30**). In addition to aromatic aldehydes, the organocatalytic system also allowed the use of aliphatic aldehydes as the acyl source (**31–32**), albeit with lower yields. The broad functional group compatibility of the reaction prompted us to explore its practicality for late-stage functionalization of biorelevant compounds. Aldehydes derived from dicamba, gemfibrozil, and estrone also underwent the acylfluoroalkylation reaction efficiently, affording the corresponding products (**33–35**) with complete diastereoselectivity and yields ranging from 54% to 81%.

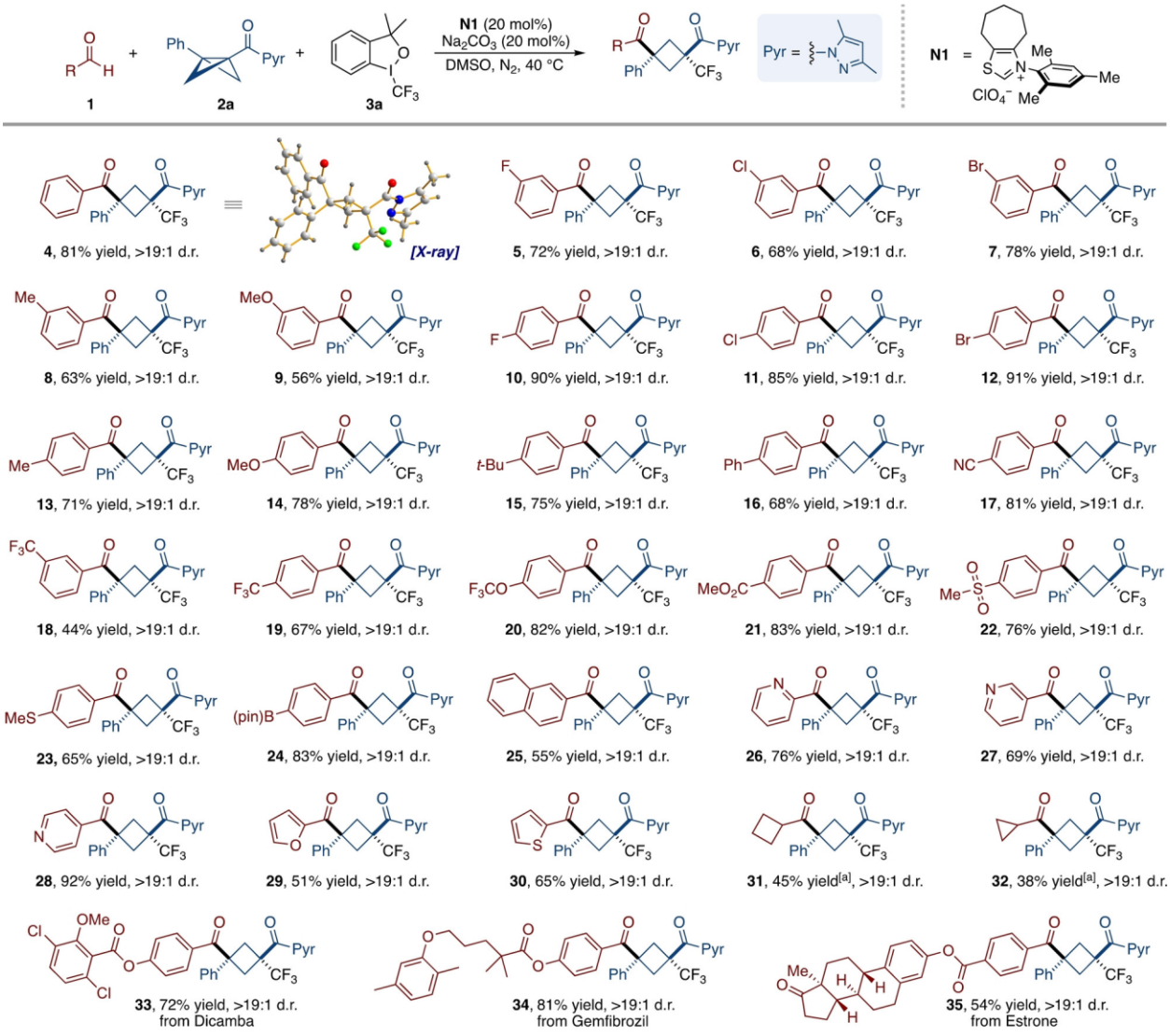

Scheme 3. Scope of aldehydes. Reactions generally performed with aldehyde **1** (0.1 mmol), bicyclobutane **2a** (0.2 mmol), Togni **I** reagent **3a** (0.2 mmol), NHC precatalyst **N1** (20 mol %) and Na_2CO_3 (20 mol %) in DMSO (1.0 mL) at 40°C for 18 h. Isolated product yields. Diastereomeric ratio (d.r.) values were determined by ^1H NMR. [a]Reactions were carried out with aliphatic aldehyde **1** (0.15 mmol), bicyclobutane **2a** (0.1 mmol) and Na_2CO_3 (50 mol %).

Upon investigating the scope of aldehydes, we turned our attention to the compatibility of this diastereoselective acylfluoroalkylation reaction with other bicyclobutanes (**Scheme 4**). To this end, modifications on both the aromatic ring (R^1) and the carbonyl moiety (R^2) were investigated.

As summarized in **Scheme 4**, variations in the electronic characteristics of substituents on the aryl moiety exerted a minimal impact on the reaction efficiency (**36–44**). Ester-substituted bicyclobutanes readily participated in the reaction, furnishing the desired product (**45**) in good yields. Unfortunately, BCB with an alkyl substituent (R^1 = Me) was not successful, presumably due to the instability of the cyclobutyl radical generated by ring-opening.[15] Next, we evaluated the influence of electron-withdrawing substituents at the bridgehead of BCB. All explored cyclic amides were found to be compatible with this organocatalytic system (**46–48**), affording the corresponding products in good yields. Furthermore, the successful incorporation of Weinreb amide (**49**) underscores the functional group tolerance of our method, offering a versatile platform for subsequent chemical modifications. Apart from the amide, ester functionalized BCBs were also successfully employed (**50–52**), although only moderate levels of diastereoselectivity were achieved. Furthermore, BCBs featuring aromatic ketones underwent the reaction smoothly, delivering the products (**53–55**) in good yields and diastereocontrol.

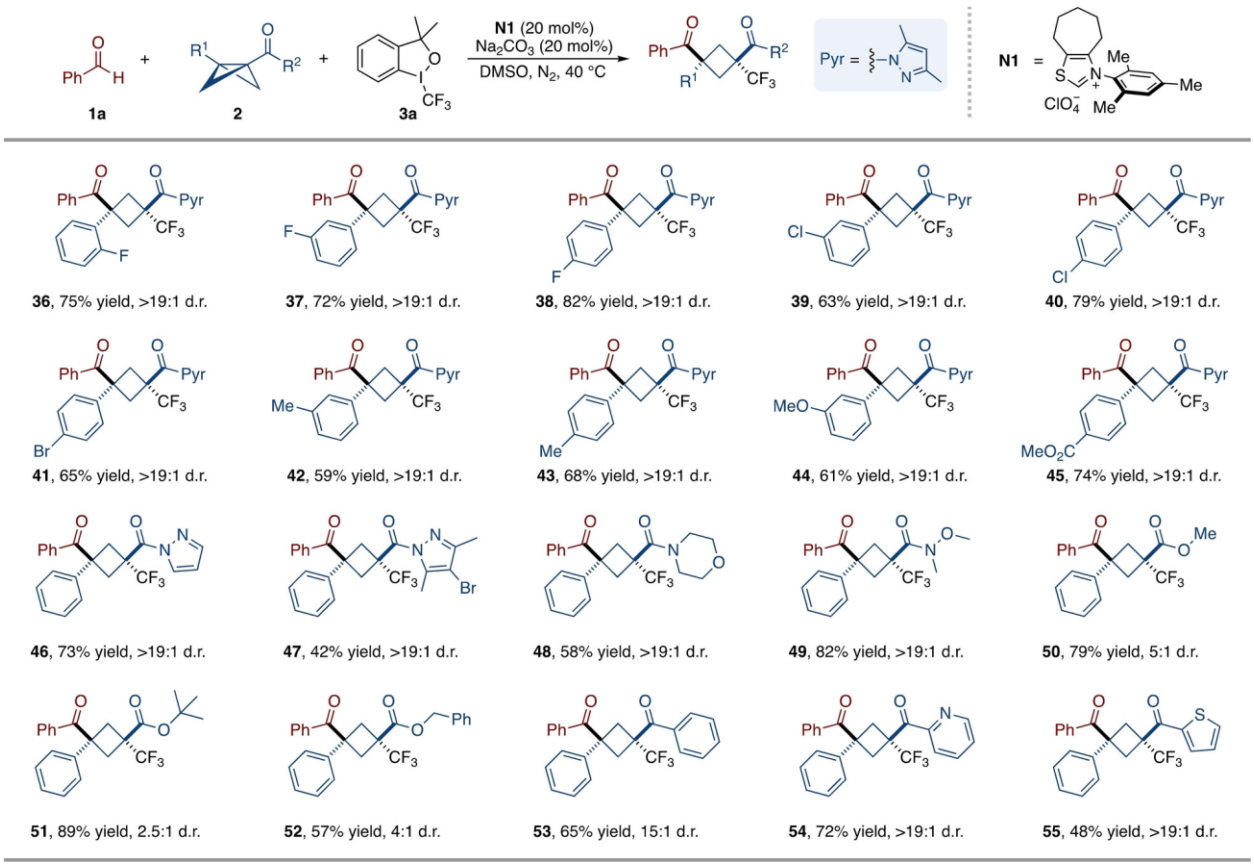

Scheme 4. Scope of bicyclobutanes. Reactions generally performed with benzaldehyde **1a** (0.1 mmol), bicyclobutane **2** (0.2 mmol), Togni **I** reagent **3a** (0.2 mmol), NHC precatalyst **N1** (20 mol %) and Na_2CO_3 (20 mol %) in DMSO (1.0 mL) at 40°C for 18 h. Isolated product yields. Diastereomeric ratio (d.r.) values were determined by ^{1}H NMR.

Considering the significance of fluoroalkyl-substituted organic compounds in the pharmaceutical and agrochemical industries,[16] we endeavored to expand the applicability of this organocatalytic strategy to incorporate other fluoroalkyl groups onto cyclobutanes (**Scheme 5**). It was gratifying to find that this method was applicable to the construction of the difluoromethyl-substituted cyclobutanes **56** using $BrCF_2COOEt$, albeit with an initially low yield. Further optimization of the reaction conditions, particularly the addition of Li_2CO_3, significantly improve the yield to 72%. When these modified conditions were extended to aldehydes with either electron-

rich or electron-deficient groups at the para-position, the cyclic products **57**–**60** were obtained in good yields with > 19:1 d.r. Notably, this strategy also proved compatible with both acyclic and cyclic aliphatic aldehydes, which efficiently coupled with BCB to produce difluoroalkyl-substituted carbocycles (**61**–**65**) with excellent diastereoselectivities. Encouraged by these promising results, we proceeded to explore the perfluoroalkylation of BCBs. As further illustrated in **Scheme 5**, a variety of accessible perfluoroalkyl iodides, with varying fluoroalkyl chain lengths, proved to be suitable substrates in this NHC organocatalytic system, providing the perfluorinated cyclobutanes in 33–74% yields (**75**–**78**).

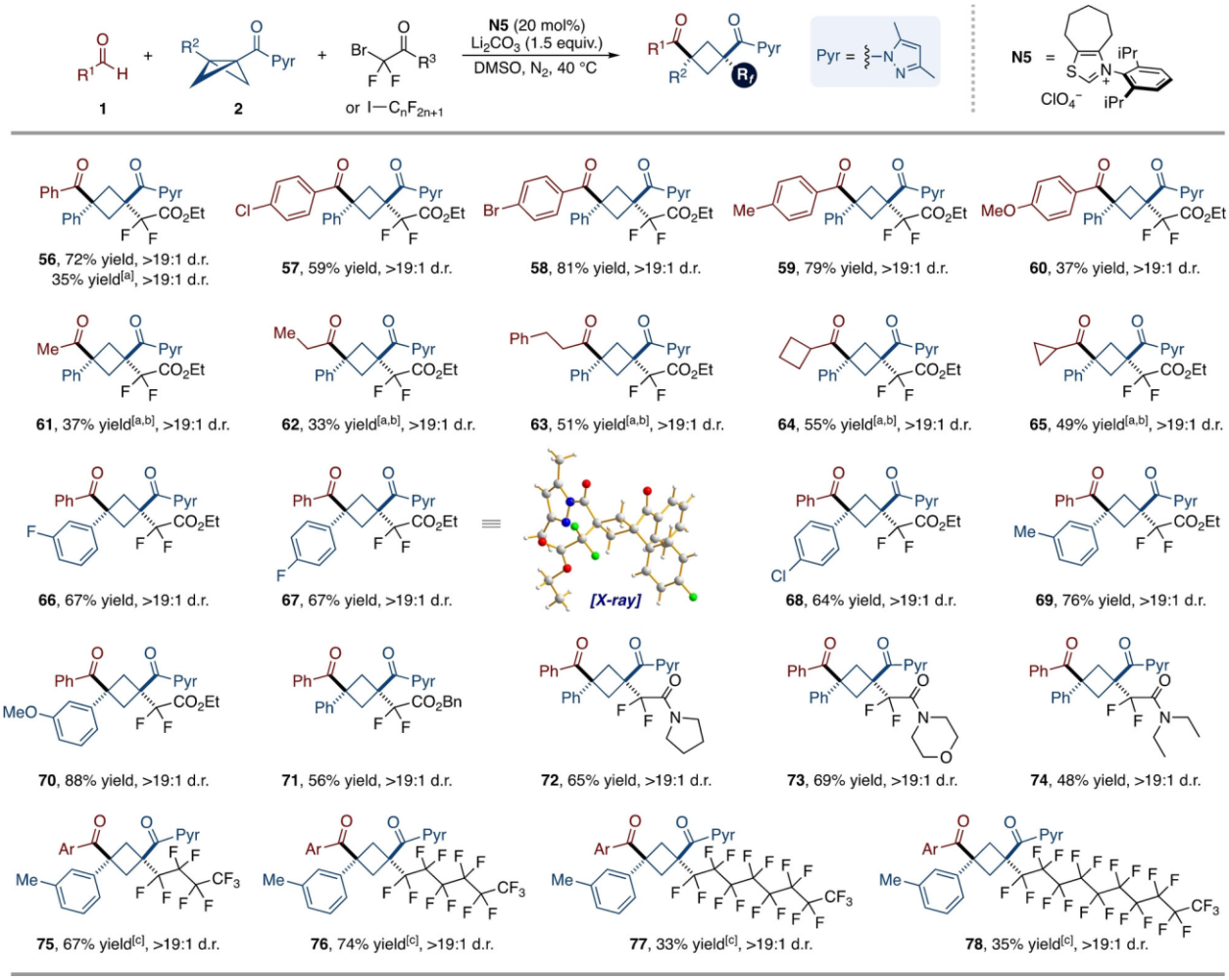

Scheme 5. Scope of fluoroalkylating Reagents. Reactions generally performed with aldehyde **1** (0.15 mmol), bicyclobutane **2** (0.1 mmol), fluoroalkylating reagent **3** (0.2 mmol), NHC precatalyst **N5** (20 mol %) and Li_2CO_3 (1.5 equiv.) in DMSO (1.0 mL) at 40°C for 18 h. Isolated product yields. Diastereomeric ratio (d.r.) values were determined by ^1H NMR. [a] Na_2CO_3 was used instead of Li_2CO_3. [b] NHC precatalyst **N1** was used instead of **N5**. [c] Cs_2CO_3 was used instead of Li_2CO_3, Ar = 4-Cl-C_6H_4.

5.4.3 Synthetic Applications

To demonstrate the practicality of this organocatalytic reaction, we conducted a gram-scale synthesis (**Scheme 6a**). Bicyclobutane **2a** (5.0 mmol) reacted smoothly with benzaldehyde **1a** and Togni **I** reagent under standard conditions, affording the carbocycle **4** in 66% yield (1.41 g). Taking

advantage of the cis configuration of the carbonyl moieties, manipulation of the cyclic products facilitated the synthesis of bicyclic scaffolds (**Scheme 6b**). Treatment of **4** with $NaBH_4$ afforded diol **79**, which subsequently underwent dehydration with triflic acid (TfOH) to afford 3-oxabicyclo[3.1.1]heptane derivative **80**. Additionally, selective reduction of **50**, followed by transesterification, yielded the bridged [3.1.1] bicyclic lactone **81**, whose structure was confirmed by X-ray crystallographic analysis. Since the cyclobutyl moiety frequently acts as an aryl ring isostere,[2] the ester-containing product **45** was converted to the amide **82**, which may exhibit potential affinity for the histamine H_3 receptor.[17]

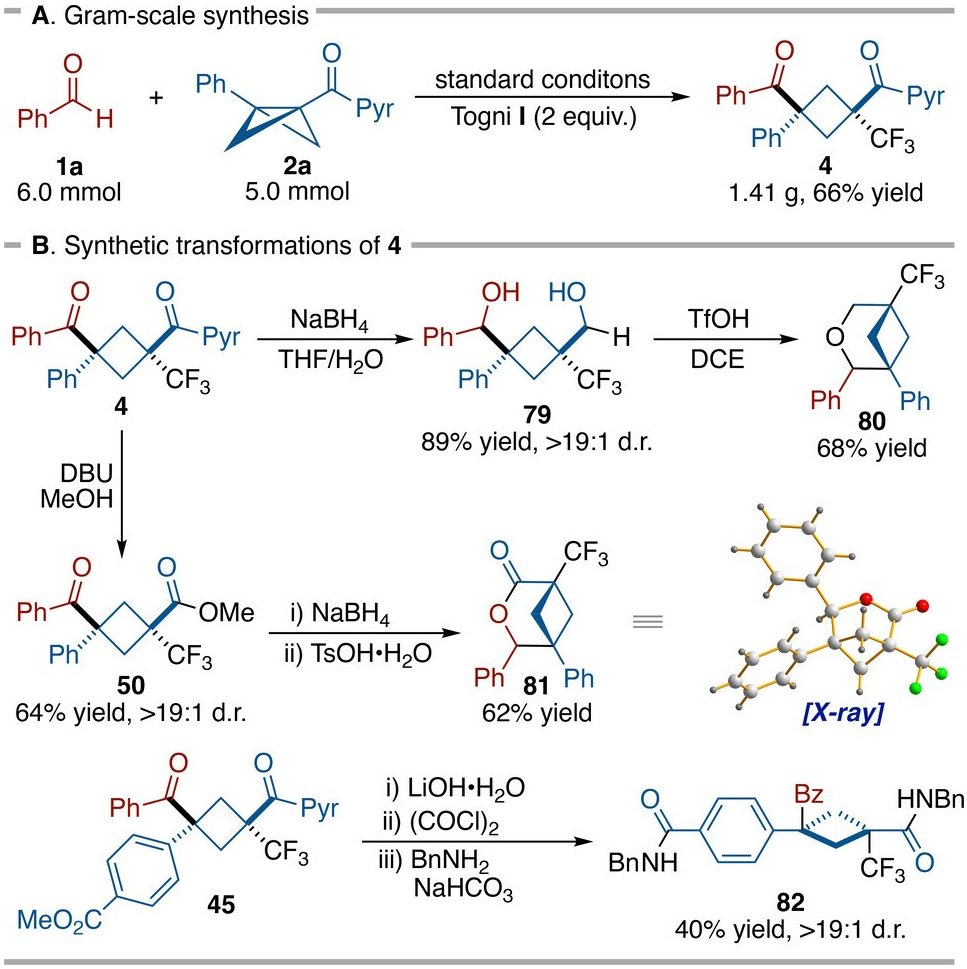

Scheme 6. Gram-scale synthesis and transformation of the product.

5.4.4 Experimental Investigation on the Reaction Pathways

To support the mechanism suggested in **Figure 38**, a radical-trapping experiment was performed. As illustrated in **Scheme 7**, the transformation was completely inhibited by the addition of a stoichiometric amount of 2,2,6,6-tetramethyl-1-piperidinyloxy (TEMPO). The alkyl radical-TEMPO trapping adduct **84** was observed by HRMS analysis, suggesting a radical nature of the reaction pathway. To further investigate the involvement of the NHC-bound ketyl radical **B**, a mixture of the NHC precatalyst **N1** in DMSO with equimolar amounts of PhCHO, Togni **I** reagent,

and Na_2CO_3 was analyzed by electron paramagnetic resonance (EPR) spectroscopy (**Scheme 7b**, path a).[10,18] The observation of a strong EPR signal clearly indicated the generation of a radical species. Additionally, we attempted to prepare the acyl thiazolium **E** in situ from **N1** and benzoyl chloride (**Scheme 7b**, path b). We proposed that the SET reduction of intermediate **E** would also produce the ketyl radical **B**. As expected, the EPR spectrum of the solution was identical to previous observations. All these results are in line with our suggested mechanism and strongly support the formation of the ketyl radical **B**.

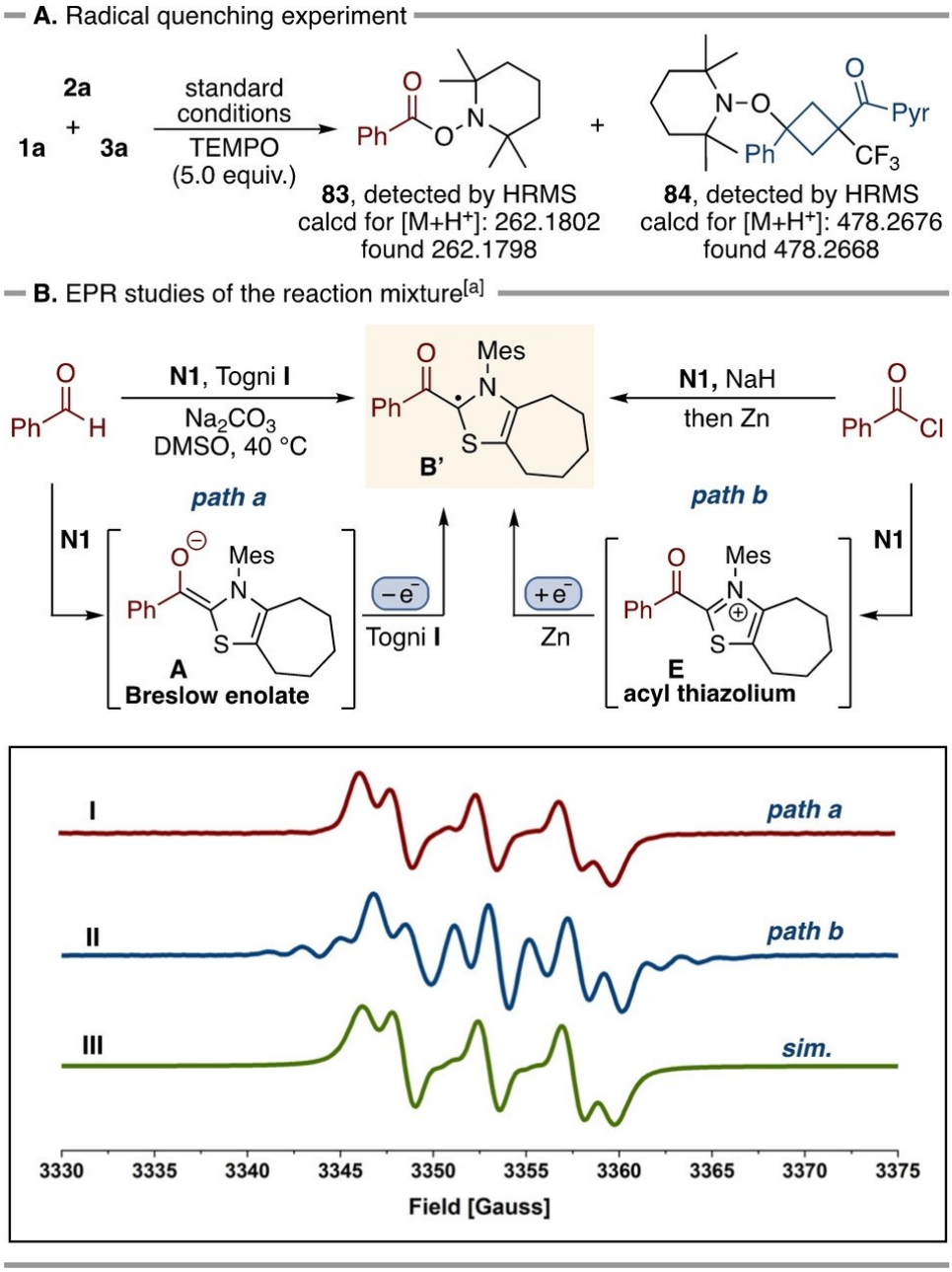

Scheme 7. Experimental mechanistic studies. [a] Experimental and simulated X-band EPR spectra of radical **B'** in the acylfluoroalkylation reaction. **I.** Reaction mixture of benzaldehyde **1a**, Togni **I** reagent, and **N1** (path a). **II.** Generation of radical **B'** via SET reduction of acylthiazolium intermediate (path b). **III.** Simulated EPR spectrum. g = 2.0051.

5.4.5 Computational Studies

Density functional theory (DFT) calculations were performed to investigate the proposed mechanism using **1a** and **2a** as model substrates (**Scheme 8**). Nucleophilic addition of NHC catalyst **N1'** to **1a** readily proceeds via **TS1** with an energy barrier of 18.5 kcal/mol, forming the zwitterionic intermediate **IN1**, which is subsequently deprotonated by Na_2CO_3. The Breslow enolate **IN2** undergoes SET with Togni **I** reagent **3a** to form ketyl radical **IN3**, while Togni **I** reagent undergoes fragmentation to **IN4** and the trifluoromethyl radical **IN5**. The SET process is exergonic by 13.2 kcal/mol. Attack of trifluoromethyl radical **IN5** on BCB **2a** via **TS2** has an energy barrier of 10.9 kcal/mol, elongating the BCB C−C bond from 1.53 Å to 1.63 Å. This strain-release step is exergonic by 55.0 kcal/mol, irreversibly resulting in the formation of stable benzyl radical **IN6** as the other coupling species. The radical-radical cross-coupling between **IN3** and **IN6** proceeds via the open-shell singlet diradical **TS3** to form **IN7**, which undergoes facile NHC elimination to afford the major product **IN8** and regenerate NHC catalyst **N1'**. The NHC-bound ketyl radical **IN3** can potentially approach the benzyl radical **IN6** from two directions, namely, from the front of the cyclobutane (facing the *N*-acylpyrazole, **TS3**) or from the back (facing the trifluoromethyl group, **TS3'**). DFT calculations show that **TS3** has an energy barrier of 17.4 kcal/mol, while **TS3'** has a barrier of 20.9 kcal/mol, leading to the formation of the minor product **IN8'**. This difference in transition state energies ($\Delta\Delta G^{\ddagger}$ = 3.5 kcal/mol) is in accord with the experimental result that **4** (**IN8**) was isolated as major product.

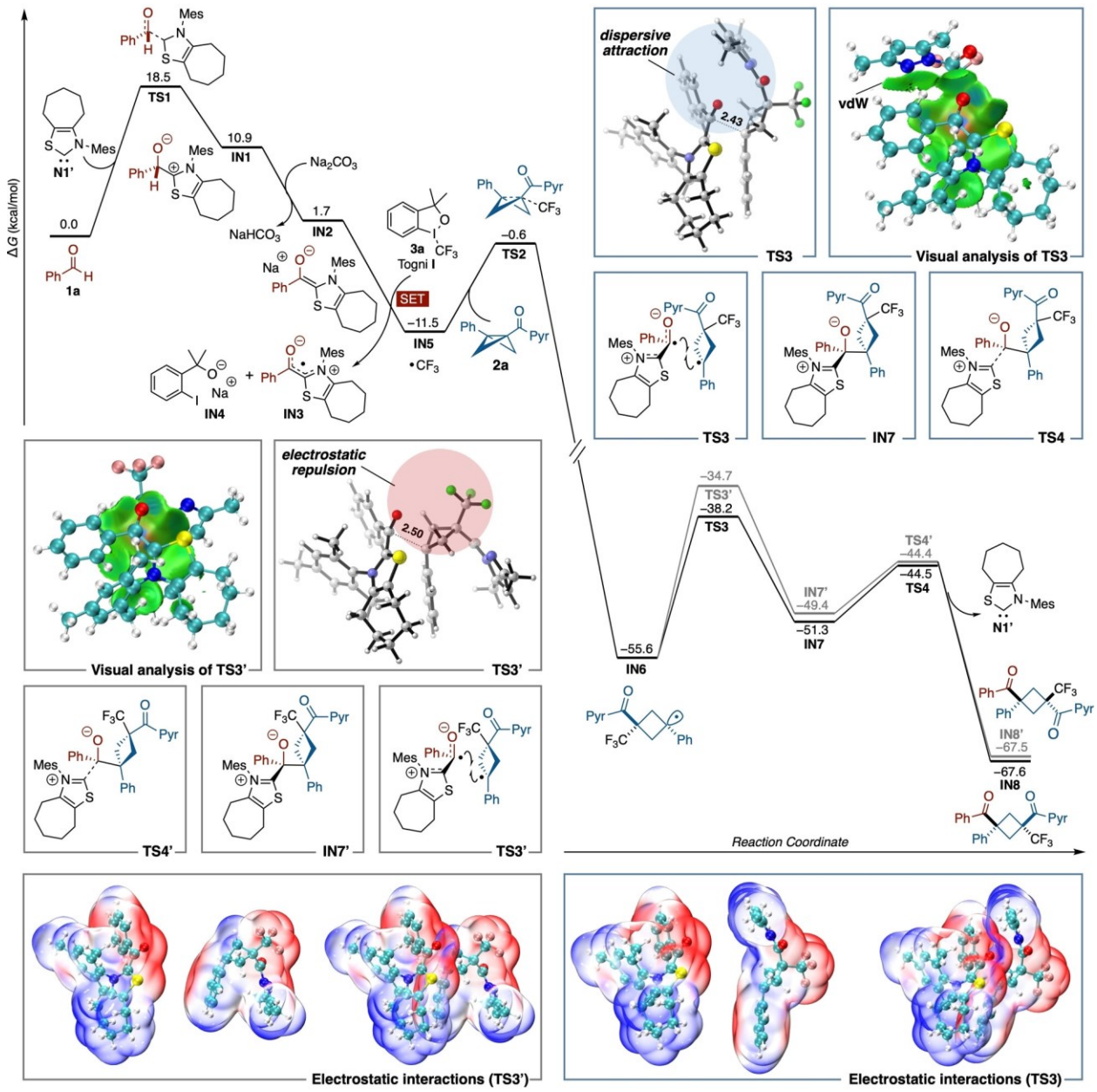

Scheme 8. Computational mechanistic studies. Computational studies were performed at the (u)ωB97X−D/def2-TZVPP/SMD(DMSO)//(u)ωB97X−D/def2-SVP/IEFPCM(DMSO) level of theory at 313.15 K with Grimme's entropic correction applied.[22] Structures of the transition states were illustrated by CYLview.[23] Dispersive and electrostatic interactions were analyzed in Multiwfn[24] and visualized in VMD.[25]

Since the *front* approach in the radical-radical cross-coupling step is favored regardless of the substituents on the ketyl radical – despite the varying diastereomeric ratios (d.r.) for some substrates – we wished to understand the origin of this strong preference. **Scheme 8** shows the favored transition state (**TS3**) in a blue frame. The preferred direction of approach by **IN3** in **TS3** is on the side of the dimethylpyrazolyl group and anti to the trifluoromethyl group. The analysis performed below suggests that this originates from 1) attractive dispersion and 2) repulsive electrostatic interactions between the two coupling species. The dimethylpyrazolyl group in **TS3** provides van der Waals or π–π interactions with the phenyl group on the ketyl radical, which likely enhances dispersive attraction and favors this transition state. In contrast, **TS3'** lacks this dispersion interaction.

We first explored the dispersion interactions by visual analysis of noncovalent interactions (NCIs)[19] using the independent gradient model based on Hirshfeld partition (IGMH).[20] As shown in **Scheme 8**, multiple C−H···π/van der Waals interactions are present between the two fragments (green blobs). The main regions of weak interactions within the two fragments are quite similar in both **TS3** and **TS3'**. However, a notable distinction is that in **TS3**, van der Waals interactions occur between the dimethylpyrazolyl and phenyl groups.

Electrostatic interactions were also investigated. The two electronegative groups – specifically the trifluoromethyl group and the oxygen atom in the ketyl radical – are positioned in close proximity in the *back* approach (**TS3'**), and the electrostatic repulsion might hinder their approach towards each other. Electrostatic potential profiles were calculated and plotted on the van der Waals surface of the two fragments in both transition states.[21] As depicted in **Scheme 8**, for two separated fragments, the electronegative regions are clearly localized on the oxygen atom of the ketyl radical and the trifluoromethyl group (in red) while the electropositive regions are

shown in blue. As the two fragments approach each other to form the transition state (right subfigures), the Coulombic interactions become evident. In particular, this is energetically favorable when the interacting colors are opposite, as observed in **TS3**. In contrast, the red electronegative regions are positioned "face-to-face" in **TS3'**, resulting in stronger electrostatic repulsion. Therefore, we believe that the preferred formation of **TS3** over **TS3'** is jointly determined by dispersion and electrostatic interactions.

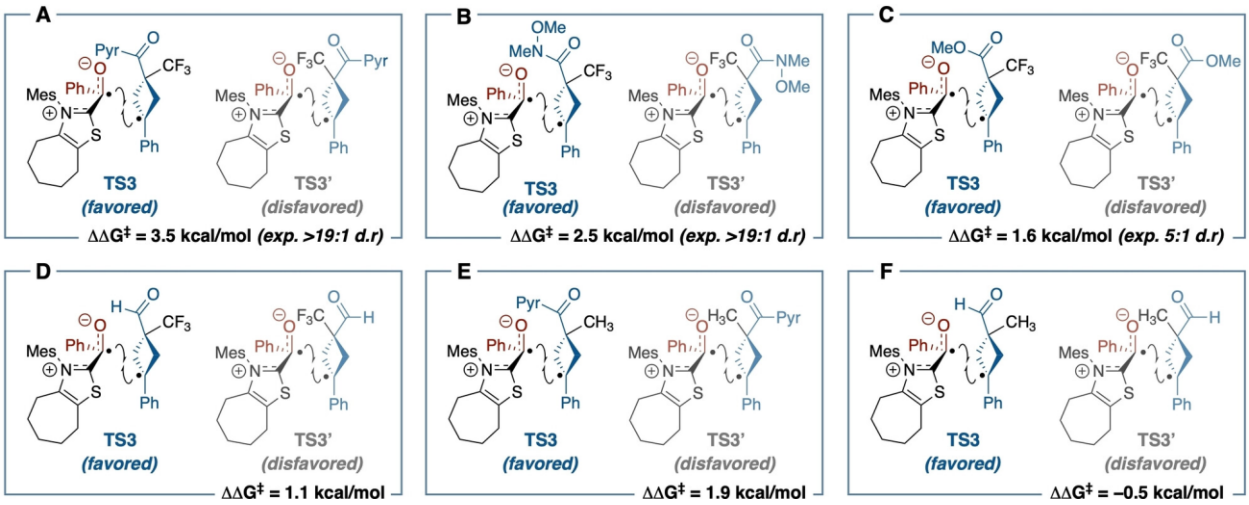

Scheme 9. Energy difference between **TS3** and **TS3'**. Computational studies are performed at the (u)ωB97X−D/def2-TZVPP/SMD(DMSO)//(u)ωB97X−D/def2-SVP/IEFPCM(DMSO) level of theory at 313.15 K with Grimme's entropic correction applied.[22]

To further investigate the dispersion and electrostatic effects induced by the substituents, we carried out calculations on three examples studied experimentally and three additional modified structures. **Scheme 9** shows the two competing transition states for the formation of two stereoisomers in each case. Structures in **Scheme 9a** have been described in **Scheme 8**, where the strongest dispersion and electrostatic interactions exist. Replacing the dimethylpyrazolyl in **TS3**

and **TS3'** with *N,O*-dimethylhydroxylamine decreases the energy difference from 3.5 kcal/mol to 2.5 kcal/mol (**Scheme 9b**). Replacing dimethylpyrazolyl with methyl ester leads to a further decrease in $\Delta\Delta G^{\ddagger}$, while still maintaining its diastereoselectivity (**Scheme 9c**). This is consistent with experiments for all three of the products (**4**, **49**, **50**). In order to minimize dispersion interactions, we replaced dimethylpyrazolyl with a hydrogen. As expected, the energy difference significantly decreases to 1.1 kcal/mol (**Scheme 9d**). Similarly, for electrostatic effects, we started by replacing the trifluoromethyl group with a methyl group, where the electrostatic repulsion with ketyl radical was notably weakened, reducing $\Delta\Delta G^{\ddagger}$ from 3.5 kcal/ mol to 1.9 kcal/mol (**Scheme 9e**). Ultimately, to eliminate both dispersion and electrostatic interactions, we substituted dimethylpyrazolyl and trifluoromethyl groups with hydrogen and methyl, respectively; a complete loss of diastereoselectivity was observed (**Scheme 9f**). These results further demonstrate the critical roles of dispersion and electrostatic effects in determining diastereoselectivity.

5.5 Conclusion

We have developed a diastereoselective method for the acylfluoroalkylation of bicyclobutanes under NHC catalysis. The key to the success of this strategy is the formation of an NHC-bound ketyl radical with appropriate steric properties, which has been confirmed by EPR spectroscopic studies. This method provides access to a series of 1,1,3,3-tetrasubstituted cyclobutanes that can be readily elaborated into bridged heterocycles. A detailed computational analysis of the catalytic system suggests that the exceptional stereoselectivity arises from dispersion and electrostatic interactions between the radical intermediates. Further application of this organocatalytic strategy to enantioselective radical-involved transformations are currently under investigation.

5.6 References

(1) For selected reviews, see: a) V. M. Dembitsky, *Phytomedicine* **2014**, *21*, 1559–1581; b) Y.-Y. Fan, X.-H. Gao, J.-M. Yue, *Sci. China Chem.* **2016**, *59*, 1126–1141; c) M. A. Beniddir, L. Evanno, D. Joseph, A. Skiredj, E. Poupon, *Nat. Prod. Rep.* **2016**, *33*, 820–842.

(2) For selected reviews, see: a) M. R. Bauer, P. D. Fruscia, S. C. C. Lucas, I. N. Michaelides, J. E. Nelson, R. I. Storer, B. C. Whitehurst, *RSC Med. Chem.* **2021**, *12*, 448–471; b) M. R. van der Kolk, M. A. C. H. Janssen, F. P. J. T. Rutjes, D. Blan-co-Ania, *ChemMedChem* **2022**, *17*, e202200020.

(3) For selected reviews regarding the synthesis of cyclobutanes, see: a) E. Lee-Ruff, G. Mladenova, *Chem. Rev.* **2003**, *103*, 1449–1483; b) J. Li, K. Gao, M. Bian, H. Ding, *Org. Chem. Front.* **2020**, *7*, 136–154; c) M. Mato, A. Franchino, C. García-Morales, A. M. Echavarren, *Chem. Rev.* **2021**, *121*, 8613–8684.

(4) For selected reviews on [2 + 2] cycloaddition reactions, see: a) T. Bach, *Synthesis* **1998**, 683–703; b) T. P. Yoon, *ACS Catal.* **2013**, *3*, 895–902; c) Y. Xu, M. L. Conner, M. K. Brown, *Angew. Chem. Int. Ed.* **2015**, *54*, 11918–11928; d) T. P. Yoon, *Acc. Chem. Res.* **2016**, *49*, 2307–2315; e) S. Poplata, A. Tröster, Y.-Q. Zou, T. Bach, *Chem. Rev.* **2016**, *116*, 9748–9815; f) R. Guo, M. K. Brown, *Acc. Chem. Res.* **2023**, *56*, 2253–2264.

(5) For selected reviews, see: a) M. A. A. Walczak, T. Krainz, P. Wipf, *Acc. Chem. Res.* **2015**, *48*, 1149–1158; b) A. Fawcett, *Pure Appl. Chem.* **2020**, *92*, 751–765; c) J. Turkowska, J. Durka, D. Gryko, *Chem. Commun.* **2020**, *56*, 5718–5734; d) C. B. Kelly, J. A. Milligan, L. J. Tilley, T. M. Sodano, *Chem. Sci.* **2022**, *13*, 11721–11737; e) M. Golfmann, J. C. L. Walker, *Commun. Chem.*

2023, *6*, 9; f) J. L. Tyler, V. K. Aggarwal, *Chem. Eur. J.* **2023**, *29*, e202300008; g) P. Bellotti, F. Glorius, *J. Am. Chem. Soc.* **2023**, *145*, 20716–20732.

(6) For selected examples on the ring-opening of BCBs to form cyclobutanes, see: a) R. Panish, S. R. Chintala, D. T. Boruta, Y. Fang, M. T. Taylor, J. M. Fox, *J. Am. Chem. Soc.* **2013**, *135*, 9283–9286; b) R. Gianatassio, J. M. Lopchuk, J. Wang, C.-M. Pan, L. R. Malins, L. Prieto, T. A. Brandt, M. R. Collins, G. M. Gallego, N. W. Sach, J. E. Spangler, H. Zhu, J. Zhu, P. S. Baran, *Science* **2016**, *351*, 241–246; c) L. Guo, A. Noble, V. K. Aggarwal, *Angew. Chem. Int. Ed.* **2021**, *60*, 212–216; d) A. Guin, S. Bhattacharjee, M. S. Hararіya, A. T. Biju, *Chem. Sci.* **2023**, *14*, 6585–6591; e) L. Tang, Q.-N. Huang, F. Wu, Y. Xiao, J.-L. Zhou, T.-T. Xu, W.-B. Wu, S. Qu, J.-J. Feng, *Chem. Sci.* **2023**, *14*, 9696–9703; f) A. Dasgupta, S. Bhattacharjee, Z. Tong, A. Guin, R. E. McNamee, K. E. Christensen, A. T. Biju, E. A. Anderson, *J. Am. Chem. Soc.* **2024**, *146*, 1196–1203; g) A. Fawcett, T. Biberger, V. K. Aggarwal, *Nat. Chem.* **2019**, *11*, 117–122; h) S. H. Bennett, A. Fawcett, E. H. Denton, T. Biberger, V. Fasano, N. Winter, V. K. Aggarwal, *J. Am. Chem. Soc.* **2020**, *142*, 16766–16775; i) H.-C. Shen, M. V. Popescu, Z.-S. Wang, L. de Lescure, A. Noble, R. S. Paton, V. K. Aggarwal, *J. Am. Chem. Soc.* **2023**, *145*, 16508–16516; j) B. Wölfl, N. Winter, J. Li, A. Noble, V. K. Aggarwal, *Angew. Chem. Int. Ed.* **2023**, *62*, e202217064; k) S.-L. Lin, Y.-H. Chen, H.-H. Liu, S.-H. Xiang, B. Tan, *J. Am. Chem. Soc.* **2023**, *145*, 21152–21158.

(7) a) G. Ernouf, E. Chirkin, L. Rhyman, P. Ramasami, J.-C. Cintrat, *Angew. Chem. Int. Ed.* **2020**, *59*, 2618–2622; b) M. Ociepa, A. J. Wierzba, J. Turkowska, D. Gryko, *J. Am. Chem. Soc.* **2020**, *142*, 5355–5361; c) M. Silvi, V. K. Aggarwal, *J. Am. Chem. Soc.* **2019**, *141*, 9511–9515; d) L. Lewis-Borrell, M. Sneha, I. P. Clark, V. Fasano, A. Noble, V. K. Aggarwal, A. J. Orr-Ewing, *J. Am. Chem. Soc.* **2021**, *143*, 17191–17199; e) H. Wang, J. E. Erchinger, M. Lenz, S. Dutta, C. G.

Daniliuc, F. Glorius, *J. Am. Chem. Soc.* **2023**, *145*, 23771–23780; f) Y. Xiao, T.-T. Xu, J.-L. Zhou, F. Wu, L. Tang, R.-Y. Liu, W.-B. Wu, J.-J. Feng, *Chem. Sci.* **2023**, *14*, 13060–13066.

(8) For selected recent examples on cyclization and insertion-type reactions of BCBs to form bridged bicyclic compounds, see: a) R. Kleinmans, T. Pinkert, S. Dutta, T. O. Paulisch, H. Keum, C. G. Daniliuc, F. Glorius, *Nature* **2022**, *605*, 477–482; b) H. Wang, H. Shao, A. Das, S. Dutta, H. T. Chan, C. Daniliuc, K. N. Houk, F. Glorius, *Science* **2023**, *381*, 75–81; c) S. Agasti, F. Beltran, E. Pye, N. Kaltsoyannis, G. E. M. Crisenza, D. J. Procter, *Nat. Chem.* **2023**, *15*, 535–541; d) R. Guo, Y.-C. Chang, L. Herter, C. Salome, S. E. Braley, T. C. Fessard, M. K. Brown, *J. Am. Chem. Soc.* **2022**, *144*, 7988–7994; e) Y. Zheng, W. Huang, R. K. Dhungana, A. Granados, S. Keess, M. Makvandi, G. A. Molander, *J. Am. Chem. Soc.* **2022**, *144*, 23685–23690; f) K. Dhake, K. J. Woelk, J. Becica, A. Un, S. E. Jenny, D. C. Leitch, *Angew. Chem. Int. Ed.* **2022**, *61*, e202204719; g) M. de Robichon, T. Kratz, F. Beyer, J. Zuber, C. Merten, T. Bach, *J. Am. Chem. Soc.* **2023**, *145*, 24466–24470; h) N. Radhoff, C. G. Daniliuc, A. Studer, *Angew. Chem. Int. Ed.* **2023**, *62*, e202304771; i) Y. Liang, F. Paulus, C. G. Daniliuc, F. Glorius, *Angew. Chem. Int. Ed.* **2023**, *62*, e202305043; j) D. Ni, S. Hu, X. Tan, Y. Yu, Z. Li, L. Deng, *Angew. Chem. Int. Ed.* **2023**, *62*, e202308606; k) S. Hu, Y. Pan, D. Ni, L. Deng, *Nat. Commun.* **2024**, *15*, 6128; l) Q. Fu, S. Cao, J. Wang, X. Lv, H. Wang, X. Zhao, Z. Jiang, *J. Am. Chem. Soc.* **2024**, *146*, 8372–8380.

(9) For selected reviews, see: a) T. Ishii, K. Nagao, H. Ohmiya, *Chem. Sci.* **2020**, *11*, 5630–5636; b) H. Ohmiya, *ACS Catal.* **2020**, *10*, 6862–6869; c) Q. Liu, X.-Y. Chen, *Org. Chem. Front.* **2020**, *7*, 2082–2087; d) J. Liu, X.-N. Xing, J.-H. Huang, L.-Q. Lu, W.-J. Xiao, *Chem. Sci.* **2020**, *11*, 10605–10613; e) L. Dai, S. Ye, *Chin. Chem. Lett.* **2021**, *32*, 660–667; f) Q.-Z. Li, R. Zeng, B. Han, J.-L. Li, *Chem. Eur. J.* **2021**, *27*, 3238–3250; g) A. V. Bay, K. A. Scheidt, *Trends Chem.* **2022**, *4*, 277–290; h) K. Liu, M. Schwenzer, A. Studer, *ACS Catal.* **2022**, *12*, 11984–11999; i) Q. Tang, D.

Du, J. Gao, *Eur. J. Org. Chem.* **2023**, *26*, e202300832; j) X. Wang, S. Wu, R. Yang, H. Song, Y. Liu, Q. Wang, *Chem. Sci.* **2023**, *14*, 13367–13383; k) F. Lu, F. Su, S. Pan, X. Wu, X. Wu, Y. R. *Chi, Chem. Eur. J.* **2024**, *30*, e202401811.

(10) a) I. Nakanishi, S. Itoh, T. Suenobu, S. Fukuzumi, *Angew. Chem. Int. Ed.* **1998**, *37*, 992–994; b) L. Delfau, S. Nichilo, F. Molton, J. Broggi, E. Tomás-Mendivil, D. Martin, *Angew. Chem. Int. Ed.* **2021**, *60*, 26783–26789.

(11) For selected examples on radical NHC catalysis via oxidative process, see: a) T. Ishii, Y. Kakeno, K. Nagao, H. Ohmiya, *J. Am. Chem. Soc.* **2019**, *141*, 3854–3858; b) T. Ishii, K. Ota, K. Nagao, H. Ohmiya, *J. Am. Chem. Soc.* **2019**, *141*, 14073–14077; c) I. Kim, H. Im, H. Lee, S. Hong, *Chem. Sci.* **2020**, *11*, 3192–3197; d) J.-L. Li, Y.-Q. Liu, W.-L. Zou, R. Zeng, X. Zhang, Y. Liu, B. Han, Y. He, H.-J. Leng, Q.-Z. Li, *Angew. Chem. Int. Ed.* **2020**, *59*, 1863–1870; e) Q.-Z. Li, R. Zeng, Y. Fan, Y.-Q. Liu, T. Qi, X. Zhang, J.-L. Li, *Angew. Chem. Int. Ed.* **2022**, *61*, e202116629; f) Q.-Z. Li, Y.-Q. Liu, X.-X. Kou, W.-L. Zou, T. Qi, P. Xiang, J.-D. Xing, X. Zhang, J.-L. Li, *Angew. Chem. Int. Ed.* **2022**, *61*, e202207824; g) W.-D. Liu, W. Lee, H. Shu, C. Xiao, H. Xu, X. Chen, K. N. Houk, J. Zhao, *J. Am. Chem. Soc.* **2022**, *144*, 22767–22777; h) Q.-Z. Li, W.-L. Zou, Z.-Y. Yu, X.-X. Kou, Y.-Q. Liu, X. Zhang, Y. He, J.-L. Li, *Nat. Catal.* **2024**, *7*, 900–911.

(12) For selected examples on dual NHC/photocatalysis, see: a) A. Mavroskoufis, K. Rajes, P. Golz, A. Agrawal, V. Ruß, J. P. Götze, M. N. Hopkinson, *Angew. Chem. Int. Ed.* **2020**, *59*, 3190–3194; b) M.-S. Liu, W. Shu, *ACS Catal.* **2020**, *10*, 12960–12966; c) A. V. Bay, K. P. Fitzpatrick, G. A. González-Montiel, A. O. Farah, P. H.-Y. Cheong, K. A. Scheidt, *Angew. Chem. Int. Ed.* **2021**, *60*, 17925–17931; d) X. Yu, Q.-Y. Meng, C. G. Daniliuc, A. Studer, *J. Am. Chem. Soc.* **2022**, *144*, 7072–7079; e) S. Jin, X. Sui, G. C. Haug, V. D. Nguyen, H. T. Dang, H. D. Arman, O. V. Larionov, *ACS Catal.* **2022**, *12*, 285–294; f) C.-Y. Tan, M. Kim, S. Hong, *Angew. Chem. Int. Ed.*

2023, *62*, e202306191; g) Y. Sato, Y. Miyamoto, T. Matsui, Y. Sumida, H. Ohmiya, *Chem Catal.* **2023**, *3*, 100736; h) Y. Goto, M. Sano, Y. Sumida, H. Ohmiya, *Nat. Synth.* **2023**, *2*, 1037–1045; i) S. Byun, M. U. Hwang, H. R. Wise, A. V. Bay, P. H.-Y. Cheong, K. A. Scheidt, *Angew. Chem. Int. Ed.* **2023**, *62*, e202312829; j) Y. Xu, H. Chen, L. Yu, X. Peng, J. Zhang, Z. Xing, Y. Bao, A. Liu, Y. Zhao, C. Tian, Y. Liang, X. Huang, *Nature* **2024**, *625*, 74–79.

(13) For NHC catalyzed fluoroalkylation reaction, see the following review and references therein: Z. Jin, F. Zhang, X. Xiao, N. Wang, X. Lv, L. Zhou, *Org. Chem. Front.* **2024**, *11*, 2112–2133.

(14) The NHC-bound ketyl radicals from ortho-substituted aromatic aldehyde are more congested and usually lead to unsuccessful radical – radical coupling.

(15) For a list of unsuccessful substrates, see the Supporting Information of our published work: C. Xiao, J.-R. Shan, W.-D. Liu, X. Gao, J. Dai, Z. Wang, W. Wang, K. N. Houk, J. Zhao, *Angew. Chem. Int. Ed.* **2025**, *64*, e202416781.

(16) For selected reviews, see: a) K. Müller, C. Faeh, F. Diederich, *Science* **2007**, *317*, 1881–1886; b) S. Purser, P. R. Moore, S. Swallow, V. Gouverneur, *Chem. Soc. Rev.* **2008**, *37*, 320–330; c) J. Wang, M. Sánchez-Roselló, J. L. Aceña, C. del Pozo, A. E. Sorochinsky, S. Fustero, V. A. Soloshonok, H. Liu, *Chem. Rev.* **2014**, *114*, 2432–2506.

(17) a) G. Morini, M. Comini, M. Rivara, S. Rivara, S. Lorenzi, F. Bordi, M. Mor, L. Flammini, S. Bertoni, V. Ballabeni, E. Barocelli, P. V. Plazzi, Bioorg. *Med. Chem. Lett.* **2006**, *16*, 4063–4067; b) T. T. Wager, B. A. Pettersen, A. W. Schmidt, D. K. Spracklin, S. Mente, T. W. Butler, H. Howard, D. J. Lettiere, D. M. Rubitski, D. F. Wong, F. M. Nedza, F. R. Nelson, H. Rollema, J. W. Raggon, J. Aubrecht, J. K. Freeman, J. M. Marcek, J. Cianfrogna, K. W. Cook, L. C. James, L. A.

Chatman, P. A. Iredale, M. J. Banker, M. L. Homiski, J. B. Munzner, R. Y. Chandrasekaran, *J. Med. Chem.* **2011**, *54*, 7602–7620.

(18) a) J. Rehbein, S.-M. Ruser, J. Phan, *Chem. Sci.* **2015**, *6*, 6013–6018; b) V. Regnier, E. A. Romero, F. Molton, R. Jazzar, G. Bertrand, D. Martin, *J. Am. Chem. Soc.* **2019**, *141*, 1109–1117.

(19) a) S. Grimme, *Angew. Chem. Int. Ed.* **2008**, *47*, 3430–3434; b) A. J. Neel, M. J. Hilton, M. S. Sigman, F. D. Toste, *Nature* **2017**, *543*, 637–646.

(20) T. Lu, Q. Chen, *J. Comput. Chem.* **2022**, *43*, 539–555.

(21) T. Lu, F. Chen, *J. Mol. Graph. Model.* **2012**, *38*, 314–323.

(22) S. Grimme, *Chem. Eur. J.* **2012**, *18*, 9955–9964.

(23) CYLview20; C. Y. Legault, Université de Sherbrooke, 2020 (**http://www.cylview.org**).

(24) T. Lu, F. Chen, *J. Comput. Chem.* **2012**, *33*, 580–592.

(25) W. Humphrey, A. Dalke, K. Schulten, *J. Mol. Graphics* **1996**, *14*, 33–38.

(26) Deposition numbers 2301935 (for **4**), 2344505 (for **67**), and 2393704 (for **81**) contain the supplementary crystallographic data for this work. These data are provided free of charge by the joint Cambridge Crystallographic Data Centre and Fachinformationszentrum Karlsruhe (CCDC).

Chapter 6: General Base-Free Suzuki-Miyaura Cross-Coupling Reaction via Electrophilic Substitution Transmetalation

6.1 Contributions

This chapter is based on the following published article: Meng Zhang, Jing-Ran Shan, Yuke Xie, Lannen Wei, Haigen Xiong, Ge-Ning Xie, Ting Qi, Qinqin Shi, K. N. Houk, and Hui Huang, "General Base-Free Suzuki-Miyaura Cross-Coupling Reaction via Electrophilic Substitution Transmetalation," *Angew. Chem. Int. Ed.* **2025**, *64*, e202512496. This work was carried out in collaboration with Prof. Hui Huang and his group at the University of Chinese Academy of Sciences and Tianjin University. Meng Zhang and I contributed equally to this work and are listed as co-first authors. I designed and carried out all computational studies presented in this work. I also contributed to the writing of the manuscript.

6.2 Abstract

The transition-metal-catalyzed Suzuki-Miyaura cross-coupling (SMC) reaction of organoboron nucleophiles with aryl (pseudo)halide electrophiles is a reliable method for carbon−carbon bond formation. This reaction generally requires the use of an exogenous base to promote transmetalation process, which limits the substrate scope of the reaction due to undesired protodeboronation and functional group incompatibilities. Here, we established a base-free SMC reaction via a conceptually different electrophilic substitution transmetalation (EST). This transformation is applicable to a wide range of base-sensitive and sterically hindered organoborons. Key to this advance is the formation of a stable cationic palladium(II) or nickel(II) intermediate

via experimental and theoretical investigations. In a broader context, this research further expands the synthetic boundary of cross-coupling chemistry.

6.3 Introduction

The transition-metal-catalyzed Suzuki-Miyaura cross-coupling (SMC) is one of the most widely used carbon-carbon bond construction reactions in materials and medicinal chemistry due to its high efficiency and the usage of air-stable, non-toxic organoboron reagents.[1–3] The traditional SMC reaction usually requires the addition of an exogenous base,[4–7] sometimes resulting in undesired hydrodehalogenation,[8,9] protodeboronation[10–12] or functional group incompatibilities.[13] The necessity for base limits the suitability for the diversification of high-complexity substrates and biomolecules. Previous efforts have primarily focused on strategies for mitigating base-mediated side reactions, such as masked organoboron reagents[14–16] or highly active palladium precatalysts.[17–19] An alternative approach that eludes the need for an exogenous base may simultaneously address all these challenges.

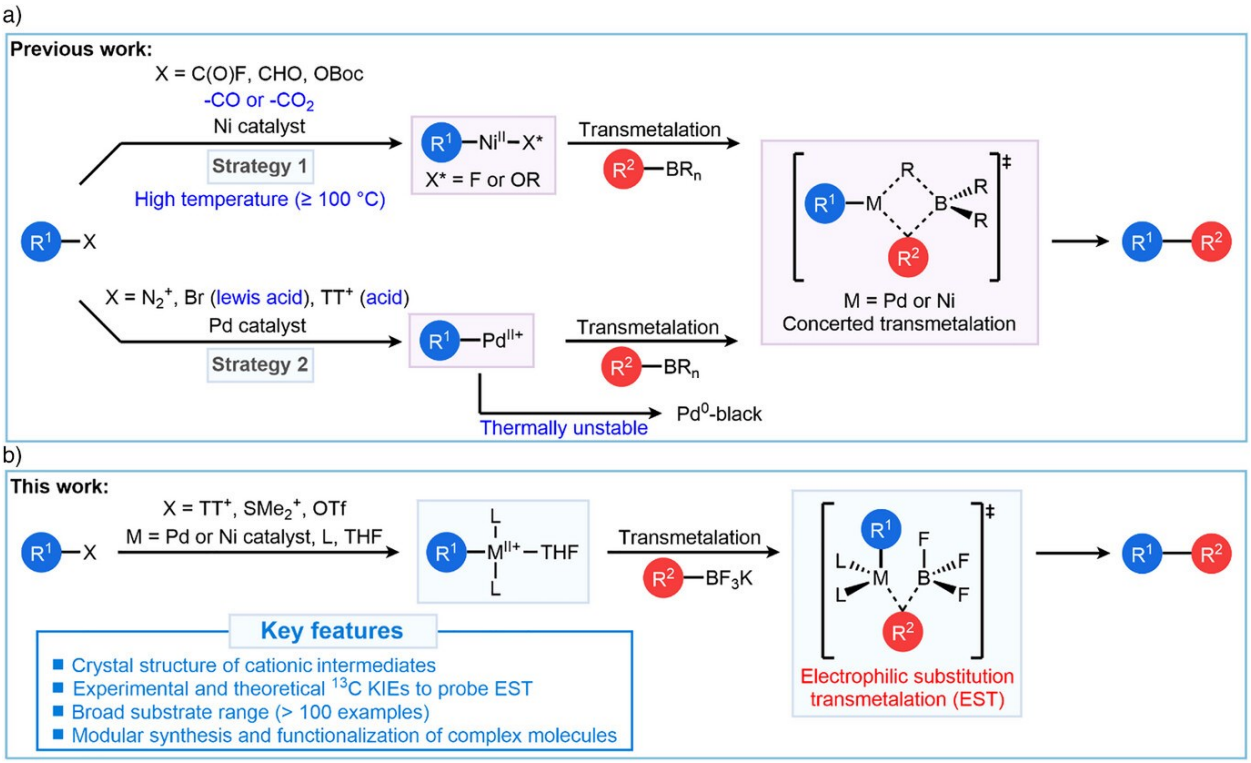

Figure 39. Suzuki-Miyaura cross-coupling reaction development. a) Summary of prior base-free Suzuki-Miyaura cross-coupling reaction via concerted transmetalation. b) Base-free Suzuki-Miyaura cross-coupling reaction via electrophilic substitution transmetalation (this work). R^1 or R^2, substituent; X or X*, leaving group; L, Ligand; BR_n, boryl group; TT, thianthrene; THF, tetrahydrofuran.

To date, two major strategies have been employed to achieve base-free SMC reactions via a concerted transmetalation mechanism (**Figure 39a**).[20] First, previous efforts have primarily focused on the use of designed electrophile reagents, including acyl fluorides,[21] aryl carbonates[22] and aldehydes.[23] These reagents are prone to undergo oxidative addition and subsequent decarbonylation or decarboxylation with nickel catalysts, resulting in the formation of neutral 'transmetalation-active' [R_1-Ni^{II}-X*] (X* = alkoxy or fluoride) intermediates. However, harsh reaction conditions (e.g. high temperature) limit the scope of the reactions (**Figure 39a**, strategy 1).[24] Second, palladium-based catalysts were developed to directly transmetalate with organoboron

reagents via coordinatively unsaturated cationic palladium(II) intermediate (R^1-Pd^{II+}) under mild conditions.[19,25–29] Note that the cationic palladium(II) species are unstable, since they are prone to generate off-cycle Pd^0-black even at room temperature (**Figure 39a**, strategy 2).[27,30–32] Particularly, it is well acknowledged that the concerted transmetalation mechanism typically disfavors the sterically hindered substrates owing to the steric encumbrance in the metallacyclobutane transition state, which limited the substrate scope of the reaction.[33]

We now report a base-free SMC reaction under mild conditions enabled by the generation of cationic palladium(II) or nickel(II) intermediates, which were isolated and unambiguously confirmed through X-ray crystal structures. Density functional theory (DFT) calculation and ^{13}C kinetic isotope effects (KIEs) study suggest that an electrophilic substitution transmetalation (EST) mechanism could serve as a viable complementary to conventional concerted transmetalation (**Figure 39b**). The generality and efficacy of this method were exemplified by broad substrate scope and functionalization of drugs.

6.4 Results and Discussion

6.4.1 Reaction Development

Our investigation commenced with exploration of a SMC model reaction between (pseudo)halide *p*-tolyl thianthrenium (TT) salt[34–36] **E1** and two equivalents of potassium benzo[*b*]thiophene-2-yltrifluoroborate **N1** in absence of an external base in THF solution (**Figure 40** and Supporting Information of our published work).[54] The initial trial of using $Pd_2(dba)_3$ as the catalyst at room temperature yielded no product (entry 1). Pleasantly, the addition of electron rich PPh_3 or $AsPh_3$ ligand afforded the target 2-(*p*-tolyl)benzo[*b*]thiophene **1** in over 74% yields

(entries 2,3). Given the ligand inhibition effect of dibenzylideneacetone (dba),[37] a highly reactive Pd(II) pre-catalyst (COD)Pd($CH_2TMS)_2$ was adopted to produce **1** in a 98% yield (entry 4) and a 94% isolated yield. In addition, the catalyst Pd($P^tBu_3)_2$ produced **1** in excellent yields (98%) regardless of the presence of $AsPh_3$ (entries 5,6). In comparison with aryl TT salts, aryl dimethylsulfonium salts are more easily accessed from widely-existed aryl sulfides.[38–42] A phenyl sulfonium salt[43,44] **E2** was tested with Pd($P^tBu_3)_2$ as the catalyst, which produced the 2-phenylbenzo[*b*]thiophene **2** in a low yield (24%) (entry 7). Considering the low cost and high reactivity of Ni catalyst, Ni($PPh_3)_4$ was selected to replace palladium catalyst. Impressively, this catalytic system can convert **E2** and **N1** to produce **2** in a 98% yield (entry 8). It is noteworthy that this is an unprecedented Ni cation catalyzed base-free SMC reaction. Since the low coordination strength of trifluoromethanesulfonate facilitates the formation of Ni cation, the phenyl trifluoromethanesulfonate **E3** was screened with Ni($PPh_3)_4$ as the catalyst, producing **2** in a high yield of 85% (entry 9) and 80% yield from a gram-scale reaction, underscoring the versatility of this base-free SMC reaction.

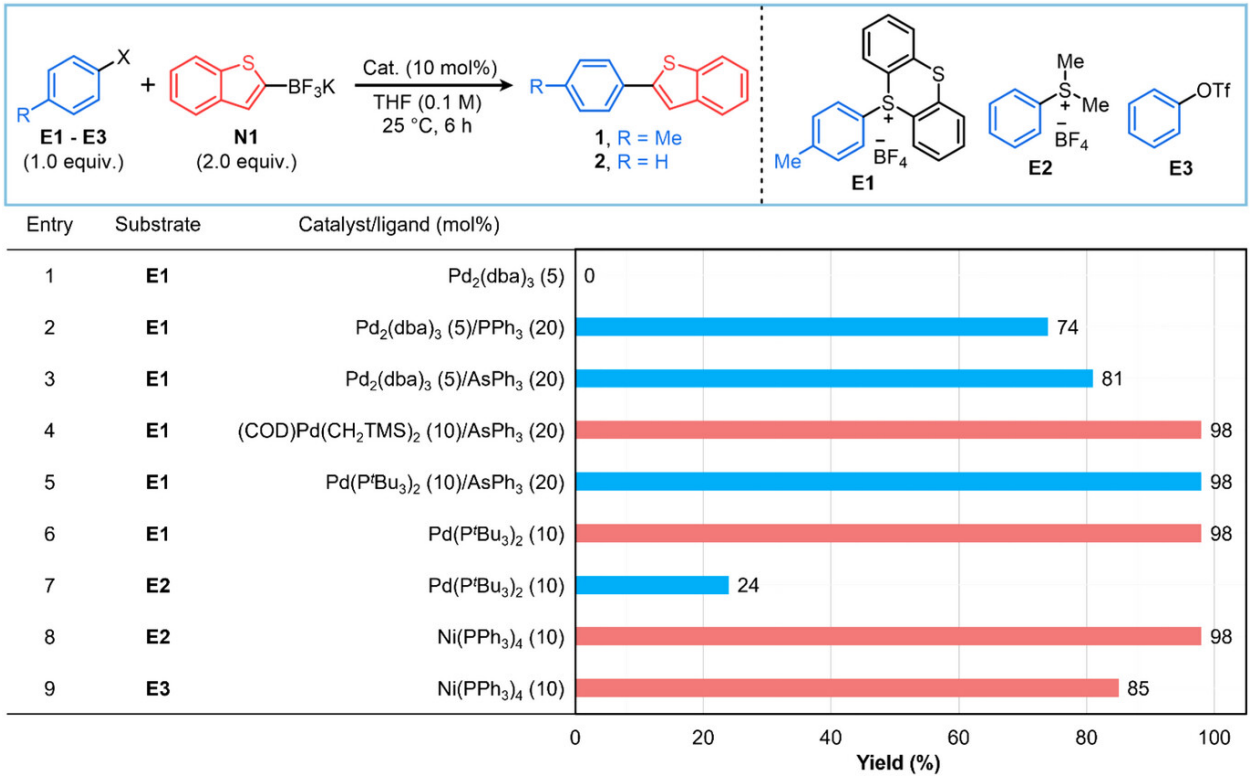

Figure 40. Optimization of Suzuki-Miyaura cross-coupling reaction conditions. Reaction conditions: (pseudo)halides **E1–E3** (0.10 mmol, 1.0 equiv.), **N1** (0.20 mmol, 2.0 equiv.), Pd or Ni catalyst (10 mol%), P or As ligand (if need), THF (1.0 mL), under nitrogen at 25°C for 6 h. Yields shown as determined by gas chromatography analysis with anthracene as an internal standard. Cat., catalyst; equiv., equivalent(s); THF, tetrahydrofuran; COD, 1,5-cyclooctadiene; TMS, trimethylsilyl; ^{t}Bu, *tert*-butyl. For detailed procedures, see the Supporting Information of our published work.[54]

6.4.2 Mechanistic Investigations

To probe the mechanism of the base-free SMC reaction, **E1** was treated with 1.1 equivalents of (COD)Pd(CH_2TMS)$_2$ in presence of $AsPh_3$ in THF solution for 24 h to afford a white powder **A** in a 52% isolated yield (**Figure 41a).** Interestingly, we initially used PPh_3 ligand to prepare cationic aryl-palladium(II) species, which is unstable and turned into black. We speculate that PPh_3 has a stronger electron donating ability than $AsPh_3$, but the arsenic atom is

much larger, which may result in slightly higher spatial tension and better stabilities of the metal complex after coordination. Meanwhile, the oxidative addition intermediate Ni cation complex **B** was isolated in a 95% yield (**Figure 41b**). The crystals of **A** and **B** suitable for single crystal X-ray diffraction were cultivated from THF and MeCN/THF mixture solution, respectively. The crystal analysis exhibited that the cation core of **A** and **B** presented a square-planar geometry, with two ligands and solvent molecules (THF for **A**; MeCN for **B-MeCN**) coordinated to the metal atom in a *trans*-arrangement (**Figure 41e** and **Figure 41f**). Interestingly, the cationic palladium(II) and nickel(II) complexes exhibited excellent stability for over 100 days at room temperature (**Figure 41c**). As expected, the stochiometric amount of both **A** and **B** can react with **N1** to generate **1** and **2**, respectively, indicating that **A** and **B** is an 'on-cycle' intermediate (**Figure 41a** and **Figure 41b**).[19,27] Pleasantly, the oxidative addition intermediate **B** showed notable reactivities when coupling with other series of phenylboron derivatives, including potassium phenyl(trifluoro)borate (**N2**), cesium phenyl(trifluoro)borate (**N3**), potassium tetraphenylborate (**N4**), phenylboronic acid (**N5**) and triphenylboroxin (**N6**), while the use of phenylboronic acid neopentyl glycol (**N7**), phenylboronic acid pinacol ester (**N8**) and phenyl-*N*-methyliminodiacetic acid ester (MIDA) (**N9**) produced the desired product in much low yields, demonstrating the broad reactivity and selectivity of organoboron reagents for SMC reaction (**Figure 41d**). In addition, the reaction of **B** and **N2** afforded the biaryl **2** in an excellent yield (90%) in the presence of 18-crown-6, indicating the potassium ion of boryl group does not interrupt the transmetalation process.[45,46] Based on above observations, a mechanism was proposed (**Figure 42**). The reaction commences with the oxidative addition of an electrophile **C** to generate the cationic aryl-palladium(II) or nickel(II) intermediates **A** or **B**. After the transmetalation between the cationic intermediate **A** or **B** with organic

trifluoroborate **D**, the resulting diaryl palladium(II) or nickel(II) **E** undergoes a reductive elimination to afford a biaryl **4** and regenerate metal catalyst to complete the catalytic cycle.

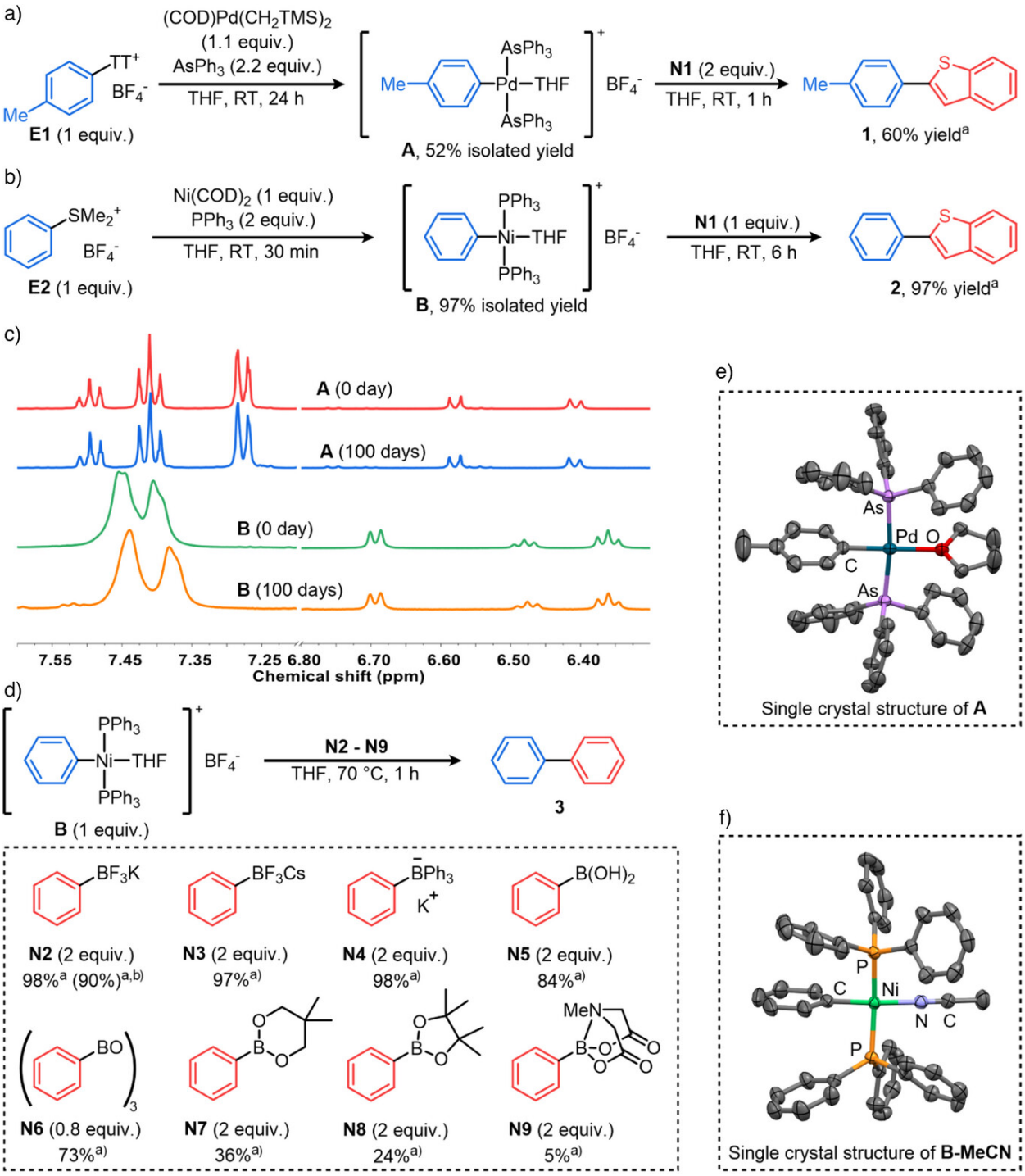

Figure 41. Stoichiometric reactions. a) Generation of intermediate **A** and its reaction with **N1**. b) Generation of intermediate **B** and its reaction with **N1**. c) Time course of ^{1}H NMR spectra in the aromatic region (chemical shift 7.60–6.30 ppm) of **A** (25°C, 0 day and 100 days) and **B** (25°C, 0 day and 100 days). The chemical shift was corrected by setting the residual CH_3CN signal to 1.94 ppm. d) Stoichiometric

reaction of intermediate **B** with phenylboronic acid derivatives (**N2–N9**). e) Single crystal structure of **A**. f) Single crystal structure of **B-MeCN**. [a] Yields shown as determined by gas chromatography analysis with anthracene as an internal standard. [b] Adding 2 equivalents of 18-crown-6. Single crystal structure of **A** and **B-MeCN**, hydrogen atoms and the BF_4 counteranion are omitted for clarity.

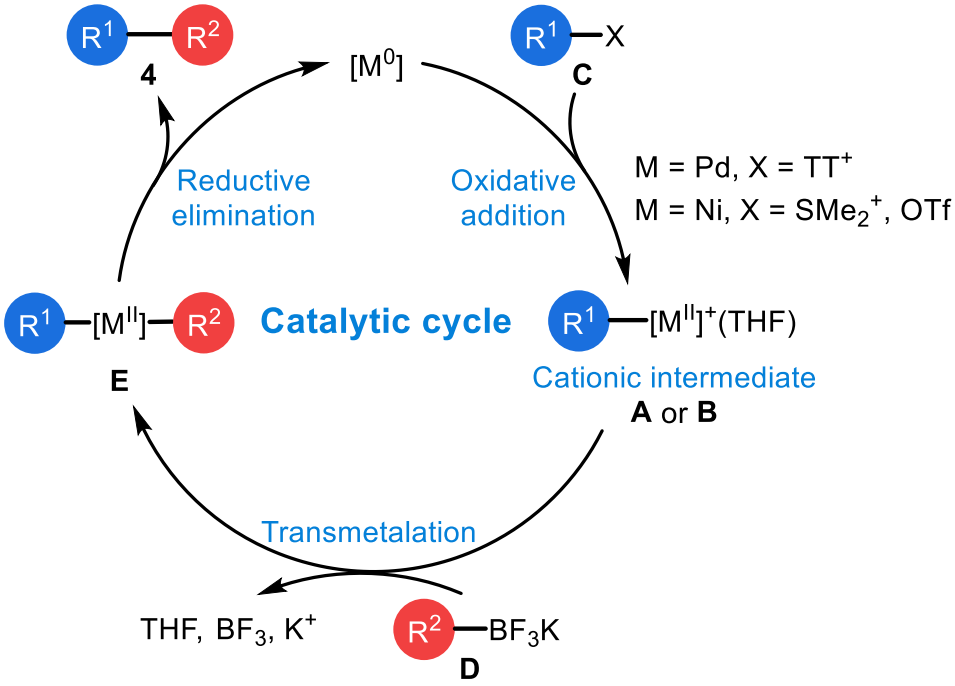

Figure 42. A plausible mechanism for the reaction studied in this work.

Given that the model reaction proceeds rapidly at room temperature, we performed DFT calculations to further investigate the origin of its remarkable reactivity. The calculations used phenyl sulfonium salt **E2** and potassium heteroaryl trifluoroborate **N1** as model substrates (**Figure 43a**). Starting with the substrate coordinated complex **I**, the insertion into the C−S bond readily occurs via a three-centered oxidative addition (**TS-1**) with an energy barrier of 10.0 kcal mol^{-1}. Intermediate **II** readily loses dimethylsulfide to form the THF complex **B**. The intermediate **B**, in accord with the single crystal structure of acetonitrile complex **B-MeCN** described above, adopts

a square planar geometry with a stable *trans* configuration. When treated with the benzothiophene trifluoroborate, this cationic Ni(II) species undergoes rapid ion exchange with **N1** to form the resting state **III**, which can be involved in two distinct transmetalation processes. The first pathway, as shown in **Figure 43a** (grey), starts by dissociation of one PPh_3 ligand to form the mono-phosphine-ligated intermediate **V**, which then undergoes transmetalation via **TS-3**. DFT calculations reveal that a four-centered concerted transition state via **TS-3** with migration of aryl group from boron to the metal center has a high energy barrier of 32.5 kcal mol^{-1}, and will not occur at room temperature. An alternative pathway (**Figure 43a**, blue) involves the transmetalation via bis-phosphine-ligated **TS-2**. In **TS-2**, both Ni−C bond and C−B bond are elongated to 2.08 Å and 2.51 Å, respectively, as compared to those in **TS-3** which has a sterically less crowded metal center (Ni−C bond: 1.91 Å, C−B bond: 2.44 Å). The distance between Ni and F in **TS-2** is also notably greater at 2.97 Å as compared to 2.16 Å in **TS-3**. **TS-2** does not proceed through a cyclic transition state as in **TS-3**. The intrinsic reaction coordinate (IRC) reveals that **TS-2** proceeds via an electrophilic aromatic substitution (EAS). This process is found to be concerted, lacking the formation of metastable Wheland intermediates that typically observed in classical EAS mechanisms. As the rate-determining step of this cross-coupling reaction, the energy barrier required for **TS-2** is 24.4 kcal mol^{-1}, thus making this pathway facile at room temperature. The subsequent reductive elimination of the cis- intermediate **VI** is facile via **TS-4**, with an energy barrier of only 8.4 kcal mol^{-1}. The irreversible generation of **VII** is exergonic by 25.3 kcal mol^{-1}, recovering Ni(0) and completing the catalytic cycle. To gain more insight into the mechanism of this reaction, we further explored the palladium catalytic cycle with the same substrates. Likewise, the transmetalation step can proceed through two transition states. The four-centered concerted **TS-7** is also more energetically demanding, with an energy barrier of 34.5 kcal mol^{-1}, whereas the

TS-6 via EST occurs with an energy barrier of 24.1 kcal mol^{-1} (**Figure 44**). Nevertheless, when the catalyst with bulky ligand $Pd(P^tBu_3)_2$ is used, no reaction pathway via the EST mechanism was identified computationally. Instead, the reaction still proceeds through the four-centered transition state **TS-10**, with an energy barrier of only 20.2 kcal mol^{-1} (**Figure 45**).

Determination of KIEs is a powerful tool that provides intimate details about the nature of bonding changes that occur at a carbon atom during the transition state (TS) of the rate-determining step (RDS) of a reaction. Experimental ^{13}C KIEs for **N1** were determined from analysis of the starting material using NMR methodology at natural abundance. Two separate reactions of **E2** and **N1** were taken to 83% and 75% conversion of **N1**. Unreacted **N1** was reisolated from the reaction mixture, and the ^{13}C isotopic composition was compared to that of samples of **N1** not subjected to the reaction conditions. From the changes in relative isotopic composition and the fractional conversion, the ^{13}C $KIE_{C-Boron}$ was determined to be 1.029(1).[54] Meanwhile, we calculated the theoretical $KIE_{C-Boron}$ based on electrophilic substituted transmetalation transition state **TS-2** and concerted transmetalation transition state **TS-3** to be 1.031 and 1.019 (**Figure 43b**). The consistency of experimental and theoretical $KIE_{C-Boron}$ further supported the EST pathway.

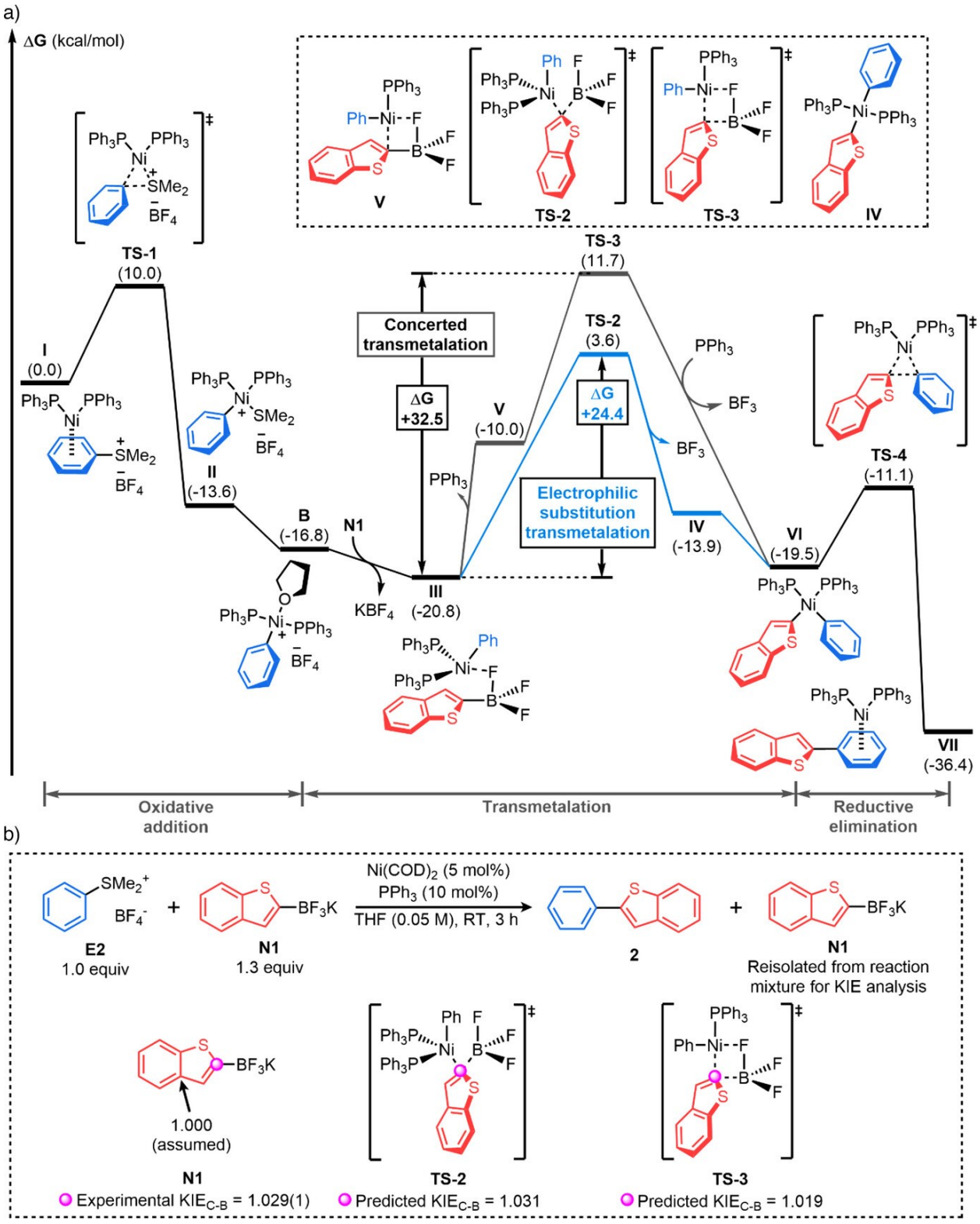

Figure 43. DFT calculation and ^{13}C KIEs studies. a) DFT calculation study. Gibbs free energies (ΔG, in kcal mol^{-1}) profile of the Ni-catalyzed Suzuki-Miyaura cross-coupling reaction calculated at the M06-

D3/def2-TZVPP/SMD(THF)//B3LYP-D3(BJ)/def2-SVP/IEFPCM(THF) level at 298.15 K. b) ^{13}C KIEs experiments to probe the electrophilic substitution transmetalation. Theoretical ^{13}C KIE values are calculated at the same level of theory as geometry optimization at 298.15 K.

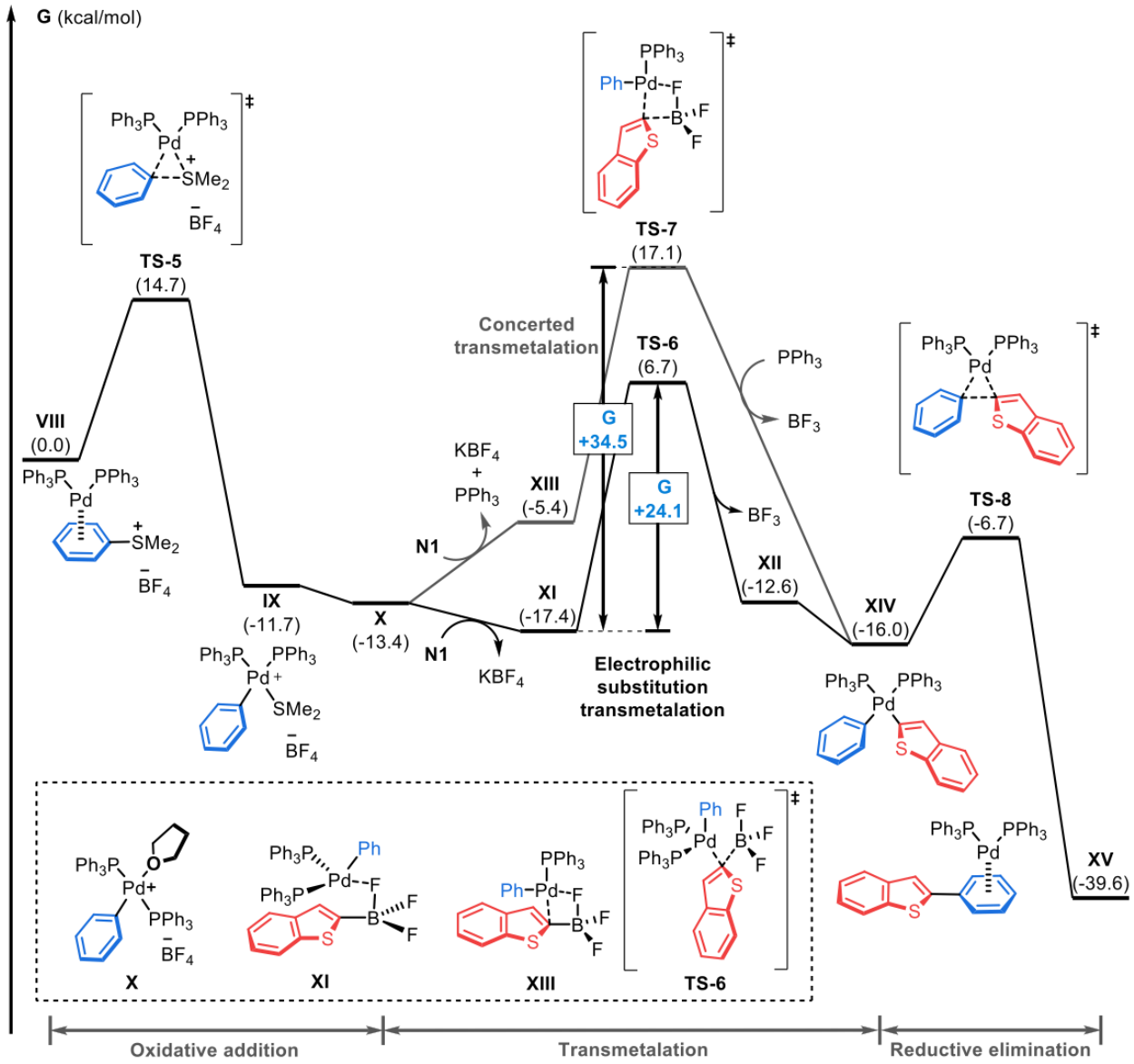

Figure 44. DFT calculation on the base-free Pd/PPh_3-catalyzed SMC reaction between **E2** and **N1**. Gibbs free energies (ΔG, in kcal mol^{-1}) are calculated at the M06-D3/def2-TZVPP/SMD(THF)//B3LYP-D3(BJ)/def2-SVP/IEFPCM(THF) level at 298.15 K.

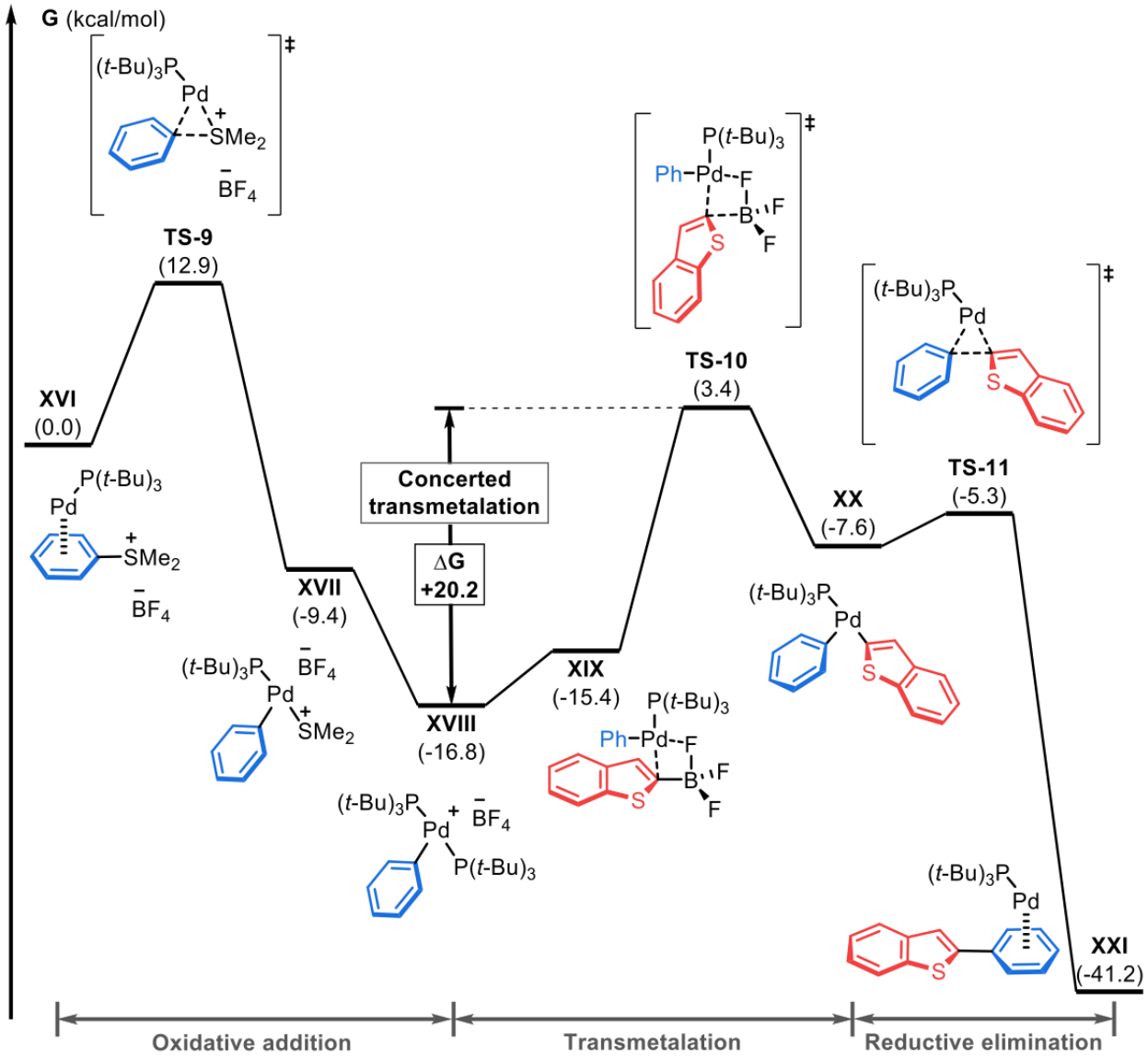

Figure 45. DFT calculation on the base-free Pd/P^{t}Bu$_3$-catalyzed SMC reaction between **E2** and **N1**. Gibbs free energies (ΔG, in kcal mol^{-1}) are calculated at the M06-D3/def2-TZVPP/SMD(THF)//B3LYP-D3(BJ)/def2-SVP/IEFPCM(THF) level at 298.15 K.

6.4.3 Substrate Scope

To explore the scope of this base-free SMC reaction, a broad range of arylsulfonium salts and potassium aryl(trifluoro)borates were investigated under the above optimal conditions (**Figure**

46). First, the scope with respect to the electrophilic coupling partners was examined. A series of substituted phenyl TT salts including *para*-carbamates, chloride, trifluoromethoxy, aryl halides and calone, were screened to produce target biaryls **5–9** in yields between 40% and 65%. Meanwhile, the reaction tolerates electron rich fluorene and nitrogen atom-containing five- and six-membered aromatic rings (**10–12**). Additionally, the alkene and alkyne formation can be successfully achieved by reacting alkene TT salts with various aryl, alkene and alkyne potassium trifluoroborates in good to excellent yields (**13–16**). Next, we sought to examine the scope of aryl sulfonium salts and triflates under Ni catalyzed condition. A broad array of *para*-methyl, methoxy, phenyl, phenyl oxide, cyano, fluoride and carboxylic ester substituted phenyl sulfonium salts and triflates can be tolerated in the reaction and produced arylated benzothiophenes (**17–24**) in over 60% yields. Other types of π-extended aryl sulfonium salts and triflate, including naphthalene, benzothiophene, etc., reacted under the Ni catalysis producing biaryls **25–28** in excellent yields.

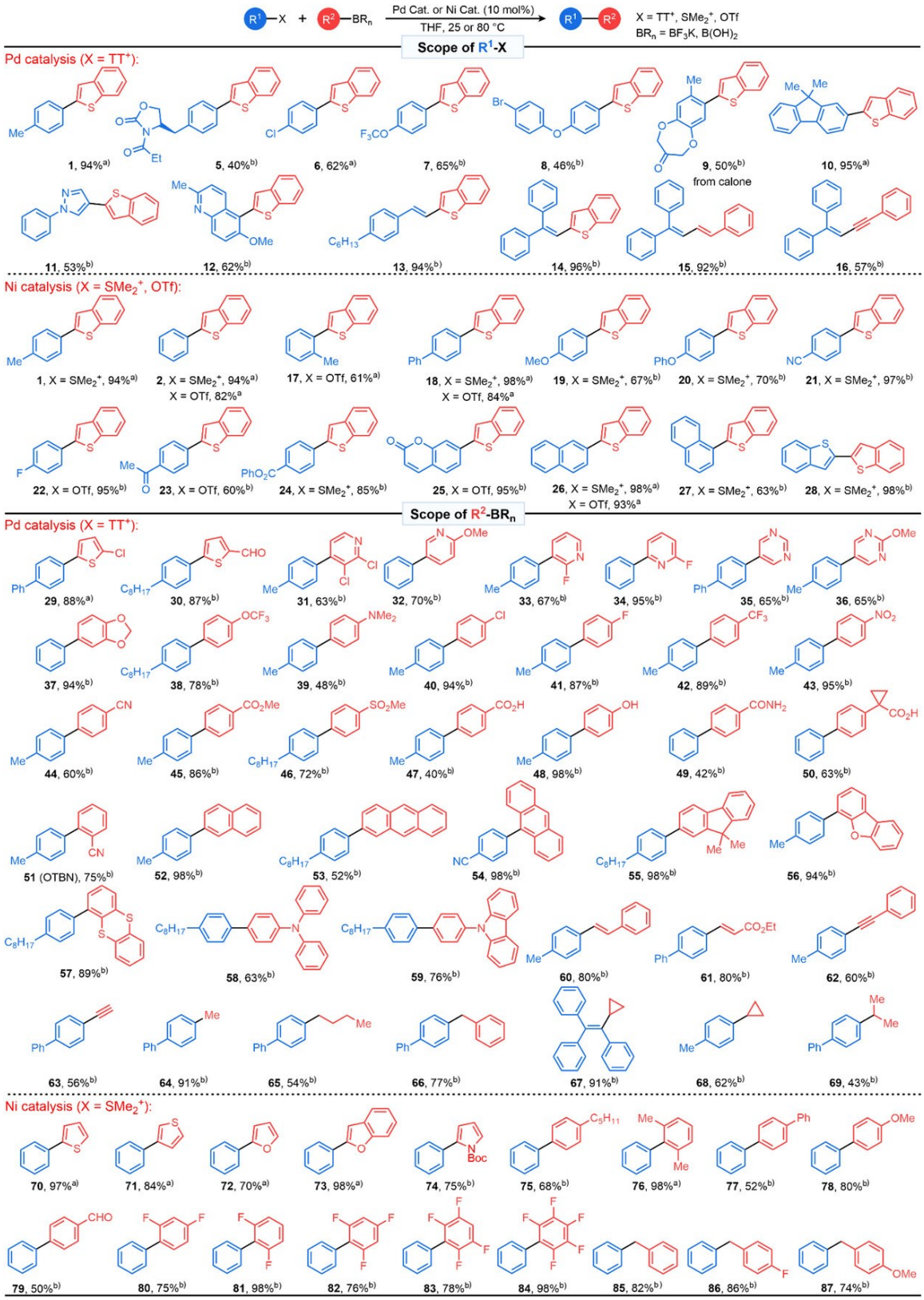
Pd Cat. or Ni Cat. (10 mol%)
THF, 25 or 80 °C
X = TT+, SMe2+, OTf
BRn = BF3K, B(OH)2
Scope of R1-X
Pd catalysis (X = TT+):
1, 94%a)
5, 40%b)
6, 62%a)
7, 65%b)
8, 46%b)
9, 50%b)
from calone
10, 95%a)
11, 53%b)
12, 62%b)
13, 94%b)
14, 96%b)
15, 92%b)
16, 57%b)
Ni catalysis (X = SMe2+, OTf):
1, X = SMe2+, 94%a)
2, X = SMe2+, 94%a)
X = OTf, 82%a
17, X = OTf, 61%a)
18, X = SMe2+, 98%a)
X = OTf, 84%a
19, X = SMe2+, 67%b)
20, X = SMe2+, 70%b)
21, X = SMe2+, 97%b)
22, X = OTf, 95%b)
23, X = OTf, 60%b)
24, X = SMe2+, 85%b)
25, X = OTf, 95%b)
26, X = SMe2+, 98%a)
X = OTf, 93%a
27, X = SMe2+, 63%b)
28, X = SMe2+, 98%b)
Scope of R2-BRn
Pd catalysis (X = TT+):
29, 88%a)
30, 87%b)
31, 63%b)
32, 70%b)
33, 67%b)
34, 95%b)
35, 65%b)
36, 65%b)
37, 94%b)
38, 78%b)
39, 48%b)
40, 94%b)
41, 87%b)
42, 89%b)
43, 95%b)
44, 60%b)
45, 86%b)
46, 72%b)
47, 40%b)
48, 98%b)
49, 42%b)
50, 63%b)
51 (OTBN), 75%b)
52, 98%b)
53, 52%b)
54, 98%b)
55, 98%b)
56, 94%b)
57, 89%b)
58, 63%b)
59, 76%b)
60, 80%b)
61, 80%b)
62, 60%b)
63, 56%b)
64, 91%b)
65, 54%b)
66, 77%b)
67, 91%b)
68, 62%b)
69, 43%b)
Ni catalysis (X = SMe2+):
70, 97%a)
71, 84%a)
72, 70%a)
73, 98%a)
74, 75%b)
75, 68%b)
76, 98%a)
77, 52%b)
78, 80%b)
79, 50%b)
80, 75%b)
81, 98%b)
82, 76%b)
83, 78%b)
84, 98%b)
85, 82%b)
86, 86%b)
87, 74%b)

Figure 46. Substrate scope. Reaction conditions for X = TT^+: R^1-TT^+ (0.5 mmol, 1.0 equiv.), R^2-BR_n (BR_n = $B(OH)_2$ or BF_3K, 1.0 mmol, 2.0 equiv.), $Pd(P^tBu_3)_2$ (0.05 mmol) or $Pd_2(dba)_3$ (0.05 mmol)/$AsPh_3$ (0.10 mmol), THF (5.0 mL), under nitrogen. Reaction conditions for X = SMe_2^+ or OTf: R^1-SMe_2^+ or R^1-OTf (0.5 mmol, 1 equiv.), R^2-BF_3K (1.0 mmol, 2 equiv.), $Ni(PPh_3)_4$ (0.05 mmol), THF (5.0 mL), under nitrogen. [a] 25°C for 6 h. [b] 80°C for 6 h. Isolated yields are shown. Boc, *tert*-butoxycarbonyl.

Subsequently, this reactivity was extended to a range of nucleophiles. First, the heteroatom-containing five- and six-membered aromatic rings with the aldehyde, chloride, fluoride and methoxy groups coupled with aryls TT salts to generate biaryls **29–36** in good to excellent yields. Furthermore, various substituted phenyl potassium trifluoroborates were scrutinized to produce **37–51** in good yields. Notably, the base-sensitive groups substituted phenyl potassium trifluoroborates, such as carboxylic, phenolic, benzamide, produced the target compounds efficiently (**47-50**), revealing the superiority of this method in comparison to traditional base-assisted SMC reaction. Next, a series of fused aryl rings were screened showing good conversion of complex biaryls **52–59**. Meanwhile, the alkenyl- and alkynyl potassium trifluoroborates can be tolerated in the reaction, affording **60–63** in good yields. It is of note, alkylborates underwent a direct cross-coupling reaction to produce products **64–66** (1° alkyl organoboron reagents), **67–69** (2° alkyl organoboron reagents) demonstrated good conversion yields. We speculated cationic intermediates may have faster transmetalation rate than traditional Pd halide intermediates with alkyl organoboron reagents due to the relatively low energy barrier based on the abovementioned DFT calculations, reducing the probability of side reactions and improving the catalytic efficiency of the reaction, largely expanded the scope.[47–49] Finally, we screened the aryl potassium trifluoroborates by coupling with phenyl sulfonium salt under Ni catalyzed condition. All heteroaryl rings, substituted phenyl rings and alkyl borates can react with aryl TT electrophiles,

affording biaryls **70–87** in good to excellent yields. In particular, fluorophenyl substrates (**80–84**), prone to protodeboronation under base condition, underwent cross coupling reactions efficiently, affording the biaryls in good yields, demonstrating the wide substrate scope.[11,12,19] However, several cross-coupling reactions using benzyl derived TT salt or potassium trifluoro(alkyl)borate barely produced any desired products, indicating the limitation of this chemistry.[54]

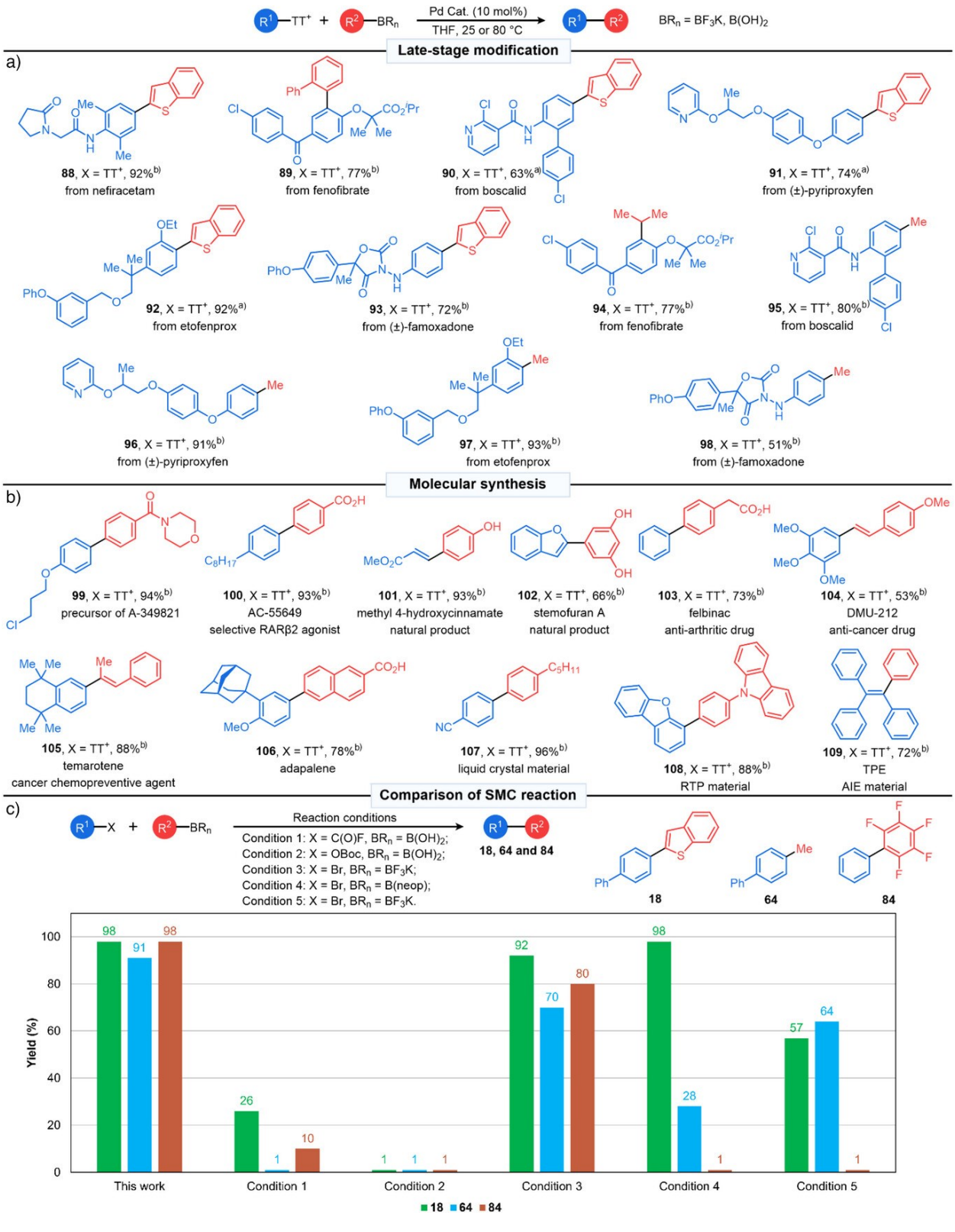
Pd Cat. (10 mol%)
THF, 25 or 80 °C
BRn = BF3K, B(OH)2
Late-stage modification
a)
88, X = TT+, 92%b)
from nefiracetam
89, X = TT+, 77%b)
from fenofibrate
90, X = TT+, 63%a)
from boscalid
91, X = TT+, 74%a)
from (±)-pyriproxyfen
92, X = TT+, 92%a)
from etofenprox
93, X = TT+, 72%b)
from (±)-famoxadone
94, X = TT+, 77%b)
from fenofibrate
95, X = TT+, 80%b)
from boscalid
96, X = TT+, 91%b)
from (±)-pyriproxyfen
97, X = TT+, 93%b)
from etofenprox
98, X = TT+, 51%b)
from (±)-famoxadone
Molecular synthesis
b)
99, X = TT+, 94%b)
precursor of A-349821
100, X = TT+, 93%b)
AC-55649
selective RARβ2 agonist
101, X = TT+, 93%b)
methyl 4-hydroxycinnamate
natural product
102, X = TT+, 66%b)
stemofuran A
natural product
103, X = TT+, 73%b)
felbinac
anti-arthritic drug
104, X = TT+, 53%b)
DMU-212
anti-cancer drug
105, X = TT+, 88%b)
temarotene
cancer chemopreventive agent
106, X = TT+, 78%b)
adapalene
107, X = TT+, 96%b)
liquid crystal material
108, X = TT+, 88%b)
RTP material
109, X = TT+, 72%b)
TPE
AIE material
Comparison of SMC reaction
c)
Reaction conditions
Condition 1: X = C(O)F, BRn = B(OH)2;
Condition 2: X = OBoc, BRn = B(OH)2;
Condition 3: X = Br, BRn = BF3K;
Condition 4: X = Br, BRn = B(neop);
Condition 5: X = Br, BRn = BF3K.
18, 64 and 84
18
64
84
Yield (%)
0
20
40
60
80
100
98
91
98
26
1
10
1
1
1
92
70
80
98
28
1
57
64
1
This work
Condition 1
Condition 2
Condition 3
Condition 4
Condition 5
18
64
84

Figure 47. Synthetic applications and comparison of Suzuki-Miyaura cross-coupling reaction. a) Late-stage modification of agrochemicals, drugs or bioactive molecules. Isolated yields are shown. b) Synthesis of nature products, drugs, bioactive molecules or organic materials. [a)] 25°C for 6 h. [b)] 80°C for 6 h. Isolated yields are shown. c) Comparison between the previous Suzuki-Miyaura reactions and our approach. Yields shown as determined by gas chromatography analysis with anthracene as an internal standard. Neop, neopentyl glycolato.

The robustness of the reaction to various functional groups promotes us to apply this method to the functionalization of various pharmaceuticals (**Figure 47a**). The arylation of commercial medicines occurs efficiently, affording the lipid-lowering drugs (**89**, **90**) and other drugs (**91–93**) in decent to excellent yields. Notably, the magic methyl effect is important in medicinal chemistry, but accessing selective methylation of medicines via derivatization at a late-stage remains a pivotal challenge.[50,51] Here, a series of methyl and isopropyl substituted drugs **94–98** were obtained via $C(sp^2)$–$C(sp^3)$ cross coupling in good to excellent yields. These *ortho*-substituted sterically hindered substitution medicines (**89**, **92**, **97**) are directly synthesized in these base-free conditions, reducing the synthetic steps necessary to prepare such complex compounds. Further capability for a range of diverse synthetic transformations bearing various base sensitive groups and other various functional groups were highlighted (**Figure 47b**) by successful demonstration of bioactive molecules, natural products and functional materials (**100–103**, **107–109**).

To evaluate the synthetic advantages of the SMC reaction, three representative products **18**, **64** and **84** obtained by our method with over 90% yields were selected to compare with the ones synthesized by other established methods (**Figure 47c**). The first two methods (conditions 1 and 2) were performed using the active substrates such as aryl acid fluorides and carbonate as the electrophile under reported base-free SMC conditions.[21,22] However, the target products **18**, **64** and

84 were obtained below 28% yields. Interestingly, the Lewis-acid assisted SMC method (condition 3) produced **18**, **64** and **84** in the yields ranging from 70% to 92%.[27] It is well known that the classic base assisted SMC conditions are the most widely used and robust method.[52,53] However, the condition 4 and 5 demonstrated limited reactivities of methylation and barely tolerated the fluorophenyl groups, resulting in low yield of product **64** (< 64%) and trace amount of product **84**. Therefore, our approach exhibited a high efficiency and broad scope, showcasing their application advantages.

6.5 Conclusion

We have established a base-free SMC reaction of general (pseudo)halide reagents with organoborons, which rendered a wide substrate scope including steric hinderance and base sensitive substrates, exemplified by over 100 compounds. The experimental and theoretical studies revealed a unique EST process, enabled by a stable transition metal cation intermediate. Therefore, this study provides a general and environmentally friendly method to construct C−C bonds with excellent functional group compatibility.

6.6 References

(1) A. Suzuki, *Angew. Chem. Int. Ed.* **2011**, *50*, 6722–6737.

(2) N. Miyaura, A. Suzuki, *Chem. Rev.* **1995**, *95*, 2457–2483.

(3) D. G. Brown, J. Bostrom, *J. Med. Chem.* **2016**, *59*, 4443–4458.

(4) C. Amatore, A. Jutand, G. Le Duc, *Angew. Chem. Int. Ed.* **2012**, *51*, 1379–1382.

(5) A. J. Lennox, G. C. Lloyd-Jones, *Angew. Chem. Int. Ed.* **2013**, *52*, 7362–7370.

(6) X. Wen, W. Xie, Y. Li, X. Ma, Z. Liu, X. Han, K. Wen, F. Zhang, Y. Lin, Q. Shi, A. Peng, H. Huang, *Angew. Chem. Int. Ed.* **2023**, *62*, e202309922.

(7) H. Xiong, Q. Lin, Y. Lu, D. Zheng, Y. Li, S. Wang, W. Xie, C. Li, X. Zhang, Y. Lin, Z.-X. Wang, Q. Shi, T. J. Marks, H. Huang, *Nat. Mater.* **2024**, *23*, 695–702.

(8) Z. Ahmadi, J. S. McIndoe, *Chem. Commun.* **2013**, *49*, 11488.

(9) L. Jedinák, R. Zátopková, H. Zemánková, A. Šustková, P. Cankar, *J. Org. Chem.* **2017**, *82*, 157–169.

(10) P. A. Cox, A. G. Leach, A. D. Campbell, G. C. Lloyd-Jones, *J. Am. Chem. Soc.* **2016**, *138*, 9145–9157.

(11) P. A. Cox, M. Reid, A. G. Leach, A. D. Campbell, E. J. King, G. C. Lloyd-Jones, *J. Am. Chem. Soc.* **2017**, *139*, 13156–13165.

(12) H. L. D. Hayes, R. Wei, M. Assante, K. J. Geogheghan, N. Jin, S. Tomasi, G. Noonan, A. G. Leach, G. C. Lloyd-Jones, *J. Am. Chem. Soc.* **2021**, *143*, 14814–14826.

(13) B. M. Trost, *Science* **1991**, *254*, 1471–1477.

(14) G. A. Molander, B. Biolatto, *J. Org. Chem.* **2003**, *68*, 4302–4314.

(15) E. P. Gillis, M. D. Burke, *J. Am. Chem. Soc.* **2007**, *129*, 6716–6717.

(16) D. W. Robbins, J. F. Hartwig, *Org. Lett.* **2012**, *14*, 4266–4269.

(17) T. Kinzel, Y. Zhang, S. L. Buchwald, *J. Am. Chem. Soc.* **2010**, *132*, 14073–14075.

(18) L. Chen, H. Francis, B. P. Carrow, *ACS Catal.* **2018**, *8*, 2989–2994.

(19) L. Chen, D. R. Sanchez, B. Zhang, B. P. Carrow, *J. Am. Chem. Soc.* **2017**, *139*, 12418–12421.

(20) X. Xie, J. Zhang, X.-Q. Song, W. Li, F. Cao, C. Zhou, H. Zhu, L. Li, *Inorg. Chem.* **2024**, *63*, 2606–2615.

(21) C. A. Malapit, J. R. Bour, C. E. Brigham, M. S. Sanford, *Nature* **2018**, *563*, 100–104.

(22) G. Toupalas, B. Morandi, *Nat. Catal.* **2022**, *5*, 324–331.

(23) L. Guo, W. Srimontree, C. Zhu, B. Maity, X. Liu, L. Cavallo, M. Rueping, *Nat. Commun.* **2019**, *10*, 1957.

(24) N. Lalloo, C. E. Brigham, M. S. Sanford, *Acc. Chem. Res.* **2022**, *55*, 3430–3444.

(25) S. Darses, T. Jeffery, J.-P. Genet, J.-L. Brayer, J.-P. Demoute, *Tetrahedron Lett.* **1996**, *37*, 3857–3860.

(26) I. A. Sanhueza, F. J. R. Klauck, E. Senol, S. T. Keaveney, T. Sperger, F. Schoenebeck, *Angew. Chem. Int. Ed.* **2021**, *60*, 7007–7012.

(27) T. Niwa, Y. Uetake, M. Isoda, T. Takimoto, M. Nakaoka, D. Hashizume, H. Sakurai, T. Hosoya, *Nat. Catal.* **2021**, *4*, 1080–1088.

(28) L. Zhang, Y. Xie, Z. Bai, T. Ritter, *Nat. Synth.* **2024**, *3*, 1490–1497.

(29) W. Li, Y. Chen, R. Yuan, X. Jia, Y. Yao, L. Zhang, *Angew. Chem. Int. Ed.* **2025**, *64*, e202500315.

(30) M. J. G. Sinclair, A. B. Chaplin, *Dalton Trans.* **2022**, *51*, 11617–11619.

(31) C.-C. Li, Á. Adorján, M. Sofiadis, T. Schulte, J. Mateos, M. Rippegarten, T. Ritter, *Angew. Chem. Int. Ed.* **2025**, *64*, e202504012.

(32) W. Li, Y. Chen, R. Yuan, X. Jia, Y. Yao, L. Zhang, *Angew. Chem. Int. Ed.* **2025**, *64*, e202500315.

(33) A. Y. Chan, A. Ghosh, J. T. Yarranton, J. Twilton, J. Jin, D. M. Arias-Rotondo, H. A. Sakai, J. K. McCusker, D. W. C. MacMillan, *Science* **2023**, *382*, 191–197.

(34) F. Berger, M. B. Plutschack, J. Riegger, W. Yu, S. Speicher, M. Ho, N. Frank, T. Ritter, *Nature* **2019**, *567*, 223–228.

(35) D. Zhao, R. Petzold, J. Yan, D. Muri, T. Ritter, *Nature* **2021**, *600*, 444–449.

(36) S. Ni, R. Halder, D. Ahmadli, E. J. Reijerse, J. Cornella, T. Ritter, *Nat. Catal.* **2024**, *7*, 733–741.

(37) C. Amatore, A. Bucaille, A. Fuxa, A. Jutand, G. Meyer, A. Ndedi Ntepe, *Chem. Eur. J.* **2001**, *7*, 2134–2142.

(38) Z. Lian, B. N. Bhawal, P. Yu, B. Morandi, *Science* **2017**, *356*, 1059–1063.

(39) M. Zhang, B.-B. Zhang, Q. Lin, Z. Jiang, J. Zhang, Y. Li, S. Pei, X. Han, H. Xiong, X. Liang, Y. Lin, Z. Wei, F. Zhang, X. Zhang, Z.-X. Wang, Q. Shi, H. Huang, *Angew. Chem. Int. Ed.* **2023**, *62*, e202306307.

(40) Z. Li, Q. Shi, X. Ma, Y. Li, K. Wen, L. Qin, H. Chen, W. Huang, F. Zhang, Y. Lin, T. J. Marks, H. Huang, *Nat. Commun.* **2022**, *13*, 144.

(41) B. Ma, Q. Shi, X. Ma, Y. Li, H. Chen, K. Wen, R. Zhao, F. Zhang, Y. Lin, Z. Wang, H. Huang, *Angew. Chem. Int. Ed.* **2022**, *61*, e202115969.

(42) T. Zhu, L. Jiang, Y. Li, Z. Xie, Z. Li, L. Lv, H. Chen, Z. Zhao, L. Jiang, B. Tang, H. Huang, *Angew. Chem. Int. Ed.* **2019**, *58*, 5044–5048.

(43) J. Srogl, G. D. Allred, L. S. Liebeskind, *J. Am. Chem. Soc.* **1997**, *119*, 12376–12377.

(44) D. Vasu, H. Yorimitsu, A. Osuka, *Synthesis* **2015**, *47*, 3286–3291.

(45) Y. Mutoh, K. Yamamoto, S. Saito, *ACS Catal.* **2020**, *10*, 352–357.

(46) B. Roh, A. O. Farah, B. Kim, T. Feoktistova, F. Moeller, K. D. Kim, P. H.-Y. Cheong, H. G. Lee, *J. Am. Chem. Soc.* **2023**, *145*, 7075–7083.

(47) J. Choi, G. C. Fu, *Science* **2017**, *356*, eaaf7230.

(48) M. K. Bogdos, O. Stepanovic, A. Bismuto, M. G. Luraschi, B. Morandi, *Nat. Synth.* **2022**, *1*, 787–793.

(49) J. C. Tellis, D. N. Primer, G. A. Molander, *Science* **2014**, *345*, 433–436.

(50) S. D. Friis, M. J. Johansson, L. Ackermann, *Nat. Chem.* **2020**, *12*, 511–519.

(51) A. Vasilopoulos, S. W. Krska, S. S. Stahl, *Science* **2021**, *372*, 398–403.

(52) V. M. Kassel, C. M. Hanneman, C. P. Delaney, S. E. Denmark, *J. Am. Chem. Soc.* **2021**, *143*, 13845–13853.

(53) G. A. Molander, B. Canturk, L. E. Kennedy, *J. Org. Chem.* **2009**, *74*, 973–980.

(54) M. Zhang, J.-R. Shan, Y. Xie, L. Wei, H. Xiong, G.-N. Xie, T. Qi, Q. Shi, K. N. Houk, H. Huang, *Angew. Chem. Int. Ed.* **2025**, *64*, e202512496.

Chapter 7: Cobaloxime-Catalysed Regiodivergent Hydrogen Atom Transfer for Alkenyl and Allylic Carbamoylation with Branched Alkenes

7.1 Contributions

This chapter is based on the following published article: Ziyu Jiang, Jing-Ran Shan, Junqi Su, Jia-Nan Mo, Fangyuan Zhang, K. N. Houk, and Jiannan Zhao, "Cobaloxime-Catalysed Regiodivergent Hydrogen Atom Transfer for Alkenyl and Allylic Carbamoylation with Branched Alkenes," *Nat. Commun.* **2026**, *17*, 7764. This work was carried out in collaboration with Prof. Jiannan Zhao and his group at Dalian University of Technology and Westlake University. Ziyu Jiang and I contributed equally to this work and are listed as co-first authors. I designed and carried out all computational studies presented in this work. I also contributed to the writing of the manuscript.

7.2 Abstract

Hydrogen atom transfer (HAT) represents a fundamental reaction in synthetic chemistry, with ongoing innovations aimed at improving its selectivity and efficiency. Leveraging the unique reactivity of cobaloxime, we developed a regioselective HAT process that enables divergent carbamoylation of branched alkenes. Through modulation of the electronic and steric properties of the ligands, this cobalt complex achieves precise discrimination between hydrogen atoms exhibiting minor differences in bond dissociation energies (BDEs), affording vinyl and allylic amides with predictable selectivity. This operationally simple method features a broad substrate scope, excellent functional group tolerance, and is applicable to the late-stage functionalization of

natural products. The synthetic utility of this radical approach is highlighted by the asymmetric total synthesis of a lignan natural product (−)-arctigenin. Experimental and computational studies shed important light on the mechanism and the critical role of the cobaloxime catalyst in regiocontrol.

7.3 Introduction

Hydrogen atom transfer (HAT) is a fundamental reaction involving the concerted transfer of a proton and an electron between two species.[1] It underpins diverse chemical and biological processes, including hydrocarbon combustion, atmospheric chemistry, and enzymatic catalysis. Recent advances in photoredox and electrochemical catalysis have significantly expanded the synthetic applications of HAT-mediated C–H functionalization (**Figure 48a**).[2–6] Homolytic cleavage of C–H bonds provides direct access to carbon-centered radicals that can be intercepted for new bond-forming processes.[7–12] However, achieving high regioselectivity in HAT remains a formidable challenge due to the similar electronic and steric properties of ubiquitous C−H bonds.[13]

Beyond sp^3-hybridized centers, HAT-mediated processes also enable olefinic C–H functionalization.[14–17] Recent studies demonstrate that alkenylation can proceed via radical addition to an alkene, followed by double bond restoration through C–H cleavage at an adjacent carbon atom (**Figure 48b**).[18–23] These one-electron approaches provide a versatile strategy for constructing substituted alkenes, leveraging the high reactivity of radicals with feedstock olefinic acceptors. In this context, Fu and co-workers reported radical alkylation of linear aliphatic alkenes,[22–23] which is less studied in conventional Heck reactions.[24–27] To achieve hydrogen abstraction at a specific position, a directing group was employed, resulting in selective formation of vinyl products (**Figure 48c**). Nevertheless, regioselective functionalization of branched alkenes

remains largely underdeveloped.[28,29] The difficulties arise from competing HAT processes, which generate mixtures of vinyl and allylic products. As depicted in **Figure 48b**, abstraction of the more accessible H_b yields the kinetically favored terminal alkene, while cleavage of the C−H_a bond affords the thermodynamically stable internal isomer. Consequently, developing catalysts capable of distinguishing between H_a and H_b represents a critical objective. Such advancement would enable regiodivergent functionalization of alkenes,[30] delivering either vinyl or allylic products as desired.

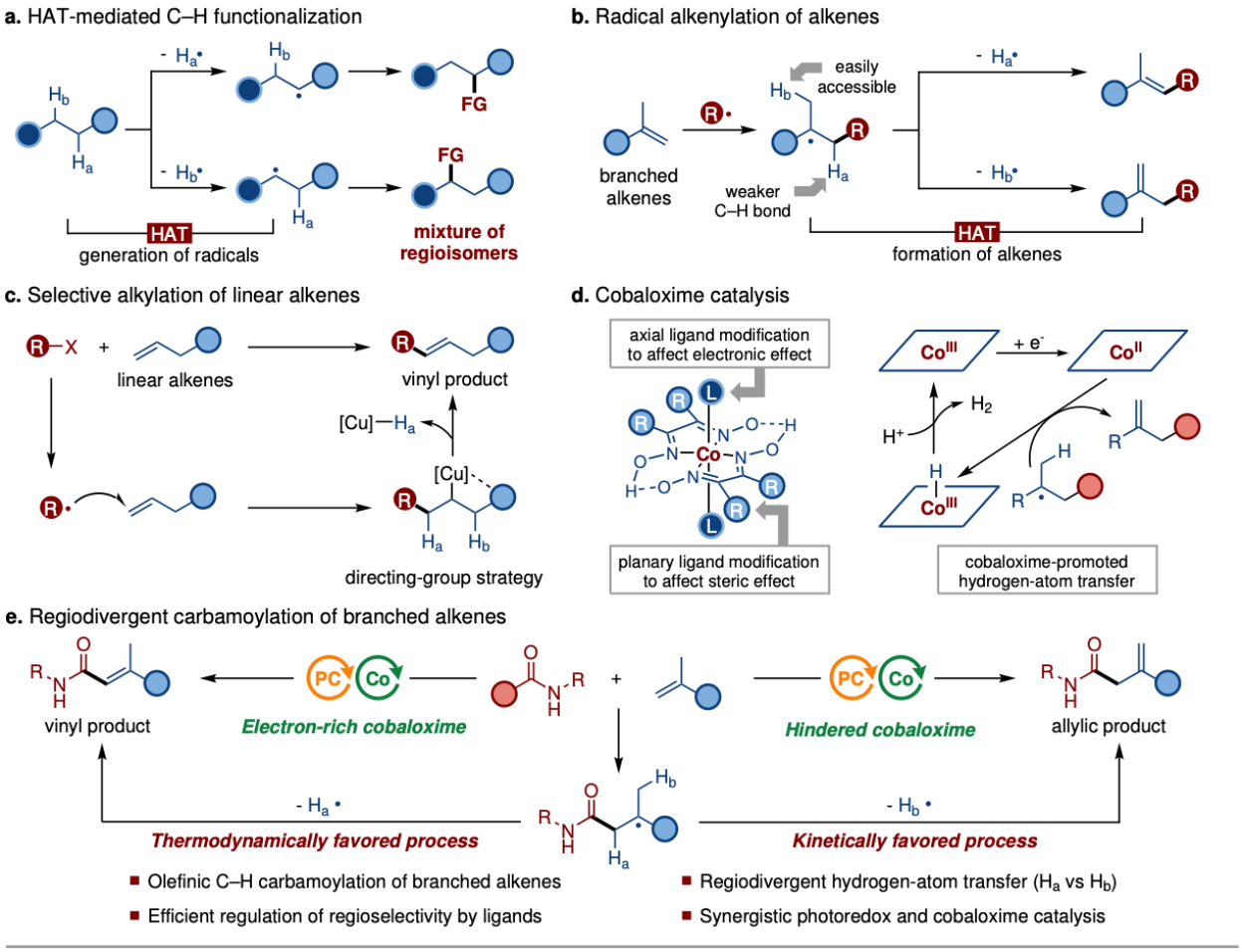

Figure 48. Regioselective functionalization of alkenes via cobaloxime catalysis. a) HAT-mediated C−H functionalization. b) Radical alkenylation and allylation. c) Selective alkylation of linear alkenes. d) Cobaloxime catalysis. e) Regiodivergent carbamoylation of branched alkenes. FG, functional group.

Cobaloxime, originally synthesized to mimic vitamin B12, has been recognized as a highly effective catalyst for hydrogen evolution reactions under mild conditions.[31–34] Recent advancements in photocatalysis have further expanded the applications of these four-coordinated cobalt complexes, leveraging their rich redox chemistry.[35,36] In particular, the planar Co^{II} species can serve as a versatile catalyst for HAT.[37–43] In 2021, Leonori and co-workers integrated halogen-atom transfer (XAT) with photoredox and cobaloxime catalysis to achieve regioselective E2

elimination of unsymmetrical alkyl halides.[39] The initial XAT step generated an alkyl radical, which subsequently interacted with the cobalt catalyst to facilitate the elimination process (**Figure 48d**). Modulation of the steric and electronic properties around the cobalt center provided contra-thermodynamic olefin products, which are typically difficult to access under conventional E2 elimination conditions. Furthermore, the combination of a photocatalyst and cobaloxime offered a solution for radical alkenylations[44–52] with branched alkenes. Lei and co-workers demonstrated that cobaloxime selectively cleaved the less sterically hindered allylic C−H bond adjacent to the carbon-centered radical, which was generated via the addition of aminium radical cations to olefins.[53] This site-selective strategy has since been effectively applied to fluoroalkylation[54–56] and sulfonylation reactions.[57] However, overriding this kinetically favored selectivity to generate internal alkenes remains a significant challenge. Given that the steric and electronic properties of cobaloximes significantly influence their reactivity, we hypothesized that regioselectivity could be modulated through the strategic choice of ligands (**Figure 48e**). Specifically, we postulated that an electron-rich cobaloxime would preferentially abstract the more protic hydrogen (H_a), while a Co catalyst with sterically congested planar ligands would favor HAT at the less hindered site (H_b).

Herein, we report the successful application of this catalyst-controlled strategy to achieve regiodivergent carbamoylation of branched alkenes. The site-selective HAT process provides efficient access for the synthesis of both vinyl and allylic amides. The method exhibits broad substrate scope with excellent regioselectivity, as demonstrated by late-stage functionalization of natural products, the total synthesis of (−)-arctigenin, and other synthetic manipulations.

7.4 Results and Discussion

7.4.1 Reaction Development

Owing to their fundamental role in biological systems and drug discovery, amides are widely applied in both the pharmaceutical industry and in academic research. In this context, photoredox-catalysed carbamoylation reactions have attracted considerable interest from chemists. For example, Melchiorre's group employed an amide-derived dihydropyridine **1** as a carbamoyl radical precursor[58], enabling efficient amide synthesis and peptide modification.[59,60] As illustrated in **Figure 49a**, we propose a dual photoredox/cobalt catalytic system for the regioselective carbamoylation of alkenes to access both vinyl and allylic amides. The catalytic cycle begins with oxidative quenching of the excited photocatalyst (*PC) by cobaloxime, generating a Co^{II} intermediate and $PC^{\bullet+}$. The latter oxidizes 4-carbamoyl-1,4-dihydropyridine **1a**, producing the carbamoyl radical **A** and regenerating the ground state photocatalyst (PC). The carbamoyl radical then adds to the branched alkene **2a**, forming the benzyl radical **B**, which undergoes cobalt-promoted HAT to yield the desired product **3**. Finally, the reaction between Co^{III}–H and a proton release H_2 and complete the cobalt cycle. Based on the analysis of the polar and steric properties of the two hydrogen atoms, we propose that regioselective HAT can be achieved by fine-tuning of the cobaloxime catalyst (**Figure 49b**). Specifically, we hypothesize that an electron-rich Co catalyst favors abstraction of the protic hydrogen (H_a), while steric hindrance shifts selectivity toward the more accessible hydrogen atom (H_b).

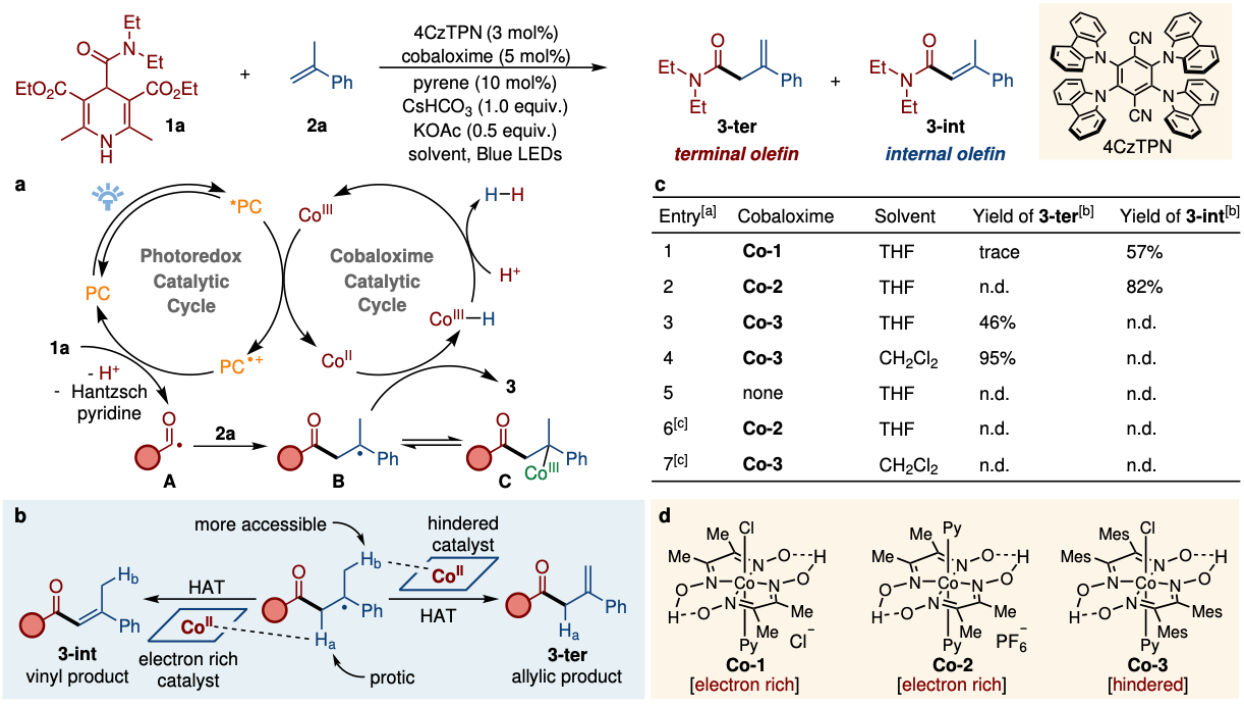

Entry[a]	Cobaloxime	Solvent	Yield of **3-ter**[b]	Yield of **3-int**[b]
1	**Co-1**	THF	trace	57%
2	**Co-2**	THF	n.d.	82%
3	**Co-3**	THF	46%	n.d.
4	**Co-3**	CH_2Cl_2	95%	n.d.
5	none	THF	n.d.	n.d.
6[c]	**Co-2**	THF	n.d.	n.d.
7[c]	**Co-3**	CH_2Cl_2	n.d.	n.d.

Figure 49. Exploration of reaction conditions. a) Proposed mechanism. b) Regiodivergent HAT catalysed by cobaloxime. c) Optimization of reaction conditions. d) Evaluation with various cobaloximes, namely $Co(dmgH)_2PyCl$ (**Co-1**), $[Co(dmgH)_2Py_2]PF_6$ (**Co-2**), $Co(dMesgH)_2PyCl$ (**Co-3**). [a] Substrate **1a** (0.10 mmol), styrene **2a** (4.0 equiv.), 4CzTPN (3 mol%), cobaloxime (5 mol%), pyrene (10 mol%), $CsHCO_3$ (1.0 equiv.), KOAc (0.5 equiv.) in solvent (3.0 mL) under blue light irradiation. [b] Isolated yield. [c] Without 4CzTPN. **ter**, terminal olefin. **int**, internal olefin. n.d., not detected.

The feasibility of this proposal was evaluated by investigating the reaction of 4-carbamoyl-1,4- dihydropyridine **1a** with styrene **2a**, using 4CzTPN as the photocatalyst in THF under blue light irradiation at room temperature (**Figure 49c**). As expected, the electron rich **Co-1** catalyst provided the thermodynamically stable alkene **3-int** in 57% yield, favoring HAT at the protic site (entry 1). The alternation of the axial ligand increased the yield to 82%, while maintaining excellent regioselectivity (entry 2). Furthermore, the sterically hindered cobaloxime **Co-3** completely reversed the regioselectivity, yielding the terminal olefin **3-ter** with > 19:1 r.r. (entry

3). Additionally, switching the solvent to CH_2Cl_2 improved the yield to 95%. Control experiments confirmed that the reaction could not proceed in the absence of cobaloxime or the photocatalyst (entries 5–7).

7.4.2 Substrate Scope

Considering the importance of amides in both the pharmaceutical industry and academic research, we endeavored to expand the applicability of this regiodivergent carbamoylation reaction with various carbamoyl radical precursors. As shown in **Figure 50**, two distinct cobaloxime catalysts facilitated the selective formation of both vinyl and allylic amides. With the sterically hindered Co catalyst (**Co-3**), terminal alkenes **3-ter** to **15-ter** were synthesized with yields ranging from 43% to 95%. The reaction proceeded with **Co-2** provided α,β-unsaturated amides with excellent regioselectivity and stereoselectivity (> 19:1 *E*/*Z*). A range of *N*-alkyl carbamoyl groups were compatible, producing secondary and tertiary amides in moderate to high yields. Notably, amides bearing the sterically hindered adamantyl moiety were synthesized in both catalytic systems (**12-ter** and **12-int**). The reaction also proceeded efficiently with dihydropyridines derived from amino acids, including alanine (**13**), histidine (**14**), and tryptophan (**15**), which were successfully installed into the amide products with complete regiomeric control. Furthermore, the dual catalytic system was also effective for the selective acylation of branched alkenes with 4-acyl-1,4-dihydropyridines (**16** and **17**).

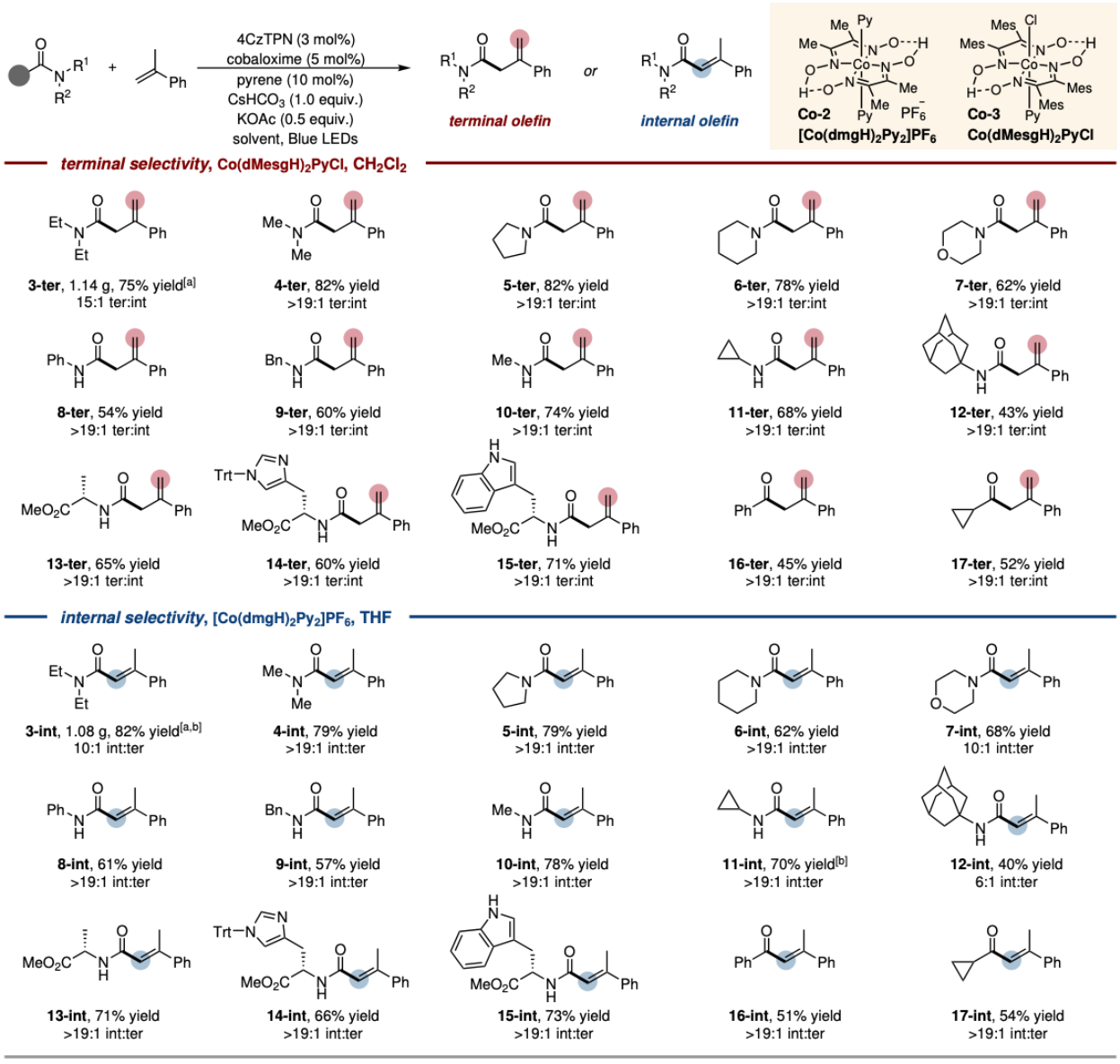

Figure 50. Scope of carbamoyl radical precursors. Reactions generally performed on 0.2 mmol scale at 40°C for 16 h under irradiation by blue LEDs and using dihydropyridines **1** (1.0 equiv.), α-methylstyrene **2a** (4.0 equiv.), $CsHCO_3$ (1.0 equiv.), KOAc (0.5 equiv.) in CH_2Cl_2 or THF (6.0 mL). Isolated product yields. Regiomeric ratios (r.r.) and stereoselectivity (> 19:1 *E*/*Z* for internal alkenes) were determined by ^1H NMR analysis of the mixtures. [a] The reaction was carried out on a gram scale with 7.0 mmol of **2a**. [b] *E*/*Z* = 10:1.

Next, the scope of styrenes was explored (**Figure 51**). A broad range of branched alkenes with different substituents on the aromatic ring were effectively accommodated in both catalytic

systems, yielding both regioisomers with excellent selectivity. The arenes could be substituted with both electron-donating and electron-withdrawing groups, affording the amides in high yields (**18–24**). A variety of functional groups, including trifluoromethyl, cyano, ester, thioether, and naphthalene, were successfully incorporated into the products (**25–29**). Additionally, the transformation proceeded smoothly with substituted thiophenes (**31–32**).

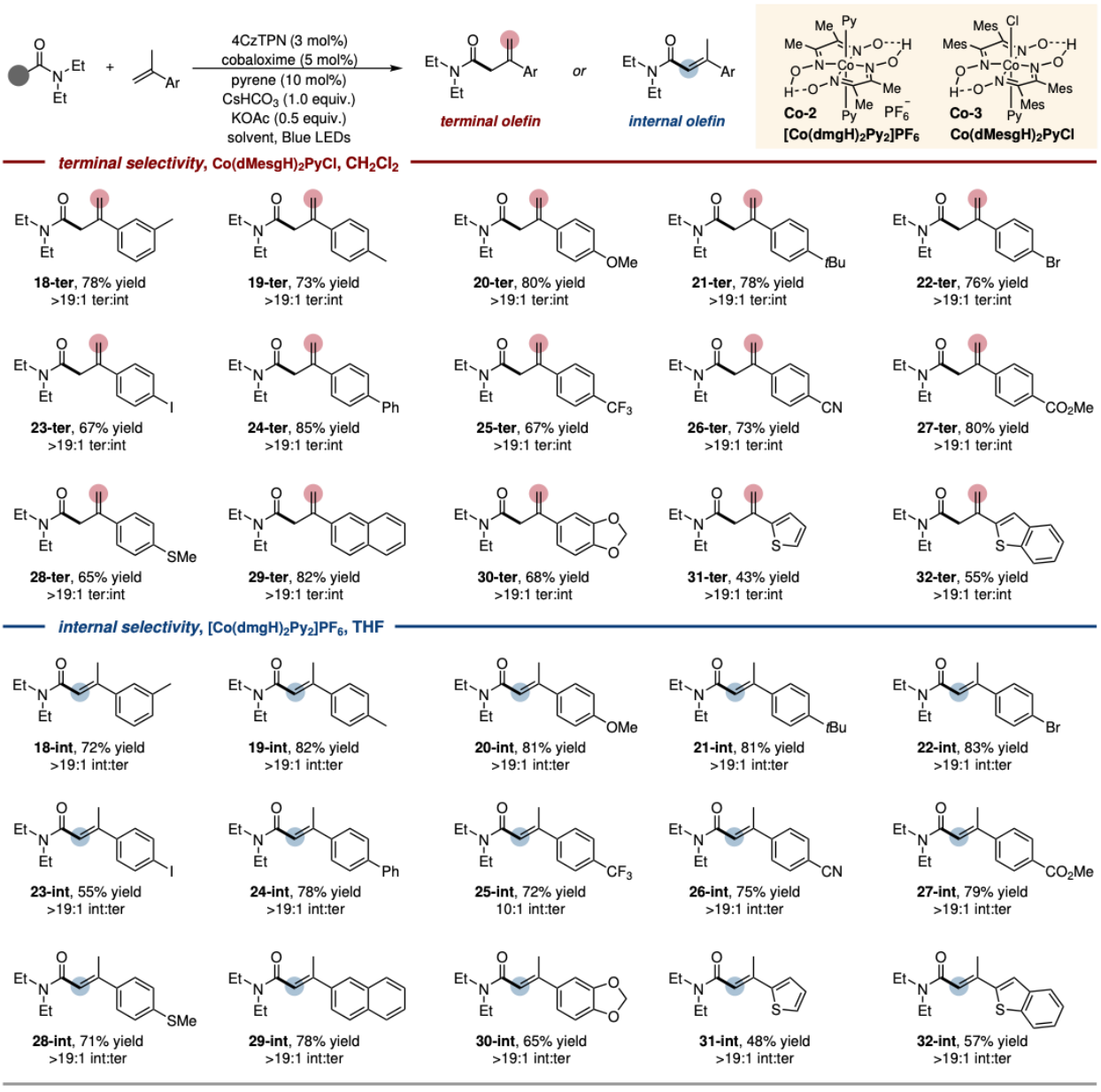

Figure 51. Scope of aromatic alkenes. See **Figure 50** for detailed procedures. Isolated product yields. Regiomeric ratios (r.r.) and stereoselectivity (> 19:1 *E*/*Z* for internal alkenes) were determined by ^{1}H NMR analysis of the mixtures.

Subsequently, we investigated whether the optimized reaction conditions were effective for the regioselective carbamoylation of alternative alkenes (**Figure 52**). Styrenes with ethyl or

propyl substituents at the α-position underwent smooth reactions, yielding the allylic amides **33** and **34** in good yields, respectively. In addition to aromatic alkenes, this carbamoylative method also proved compatible with enol ether and methacrylate (**37** and **38**). Furthermore, natural products and their derivatives successfully participated as coupling partners, including derivatives of eugenol (**39**), (−)-menthol (**41**), (−)-isopulegol (**42**), and andrographolide (**47**). Additionally, this synergistic catalytic system demonstrated excellent compatibility with natural terpenes, producing a range of amide-containing molecules **43–45** with > 19:1 r.r.. Both (−)-*β*-pinene and caryophyllene oxide underwent carbamoylation to the ring-opened products **40** and **46** through the cleavage of the cyclobutane ring, which highlights the radical nature of the reaction. Unfortunately, the reaction with electron-rich cobaloxime **Co-2** failed to transform these alkenes to the vinyl products. Thus, further efforts were made to explore a suitable condition for the isomerization of these allylic amides to its regioisomer. As further illustrated in **Figure 52**, the vinyl amides were successfully afforded in high yields under basic conditions.

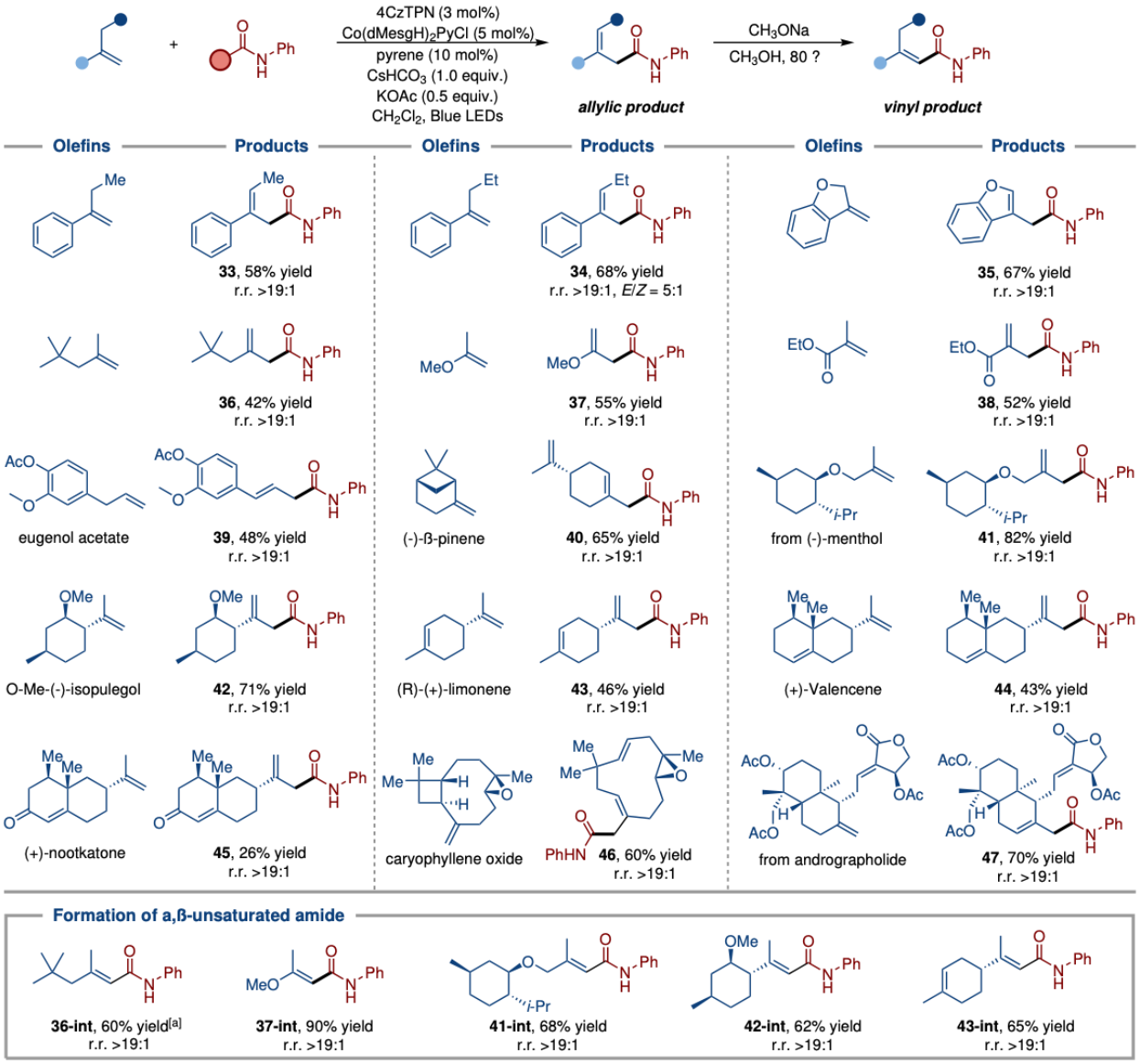

Figure 52. Additional scope of alkenes. Reactions generally performed on 0.2 mmol scale at 40°C for 16 h under irradiation by blue LEDs and using dihydropyridine (1.0 equiv.), alkenes (8.0 equiv.), $CsHCO_3$ (1.0 equiv.), KOAc (0.5 equiv.) in CH_2Cl_2 (4.0 mL). Isolated product yields. Regiomeric ratios (r.r.) were determined by ^1H NMR analysis. [a] E/Z = 10:1.

7.4.3 Synthetic Applications

Derivatizations of the products demonstrated the utility of this cobalt-catalysed transformation for accessing diverse amide-containing molecules (**Figure 53a**). Cyclopropanation of the internal (**3-int**) and terminal (**3-ter**) alkenes afforded amides **48** and **49** in good yields, respectively. Photocatalytic cyclization of the α,β-unsaturated amide **8-int** yielded quinolinone **50**, **61** which was subsequently converted to quinoline-2-thione **51** using Lawesson's reagent. On the other hand, hydroboration of the allylic regioisomer **8-ter**, followed by oxidative work-up, provided γ-hydroxyamide **52**, which underwent cyclization to furnish γ-lactam **53**. The synthetic value of this methodology was further highlighted by its application in the total synthesis of the lignan natural product (−)-arctigenin. As outlined in **Figure 53b**, regioselective carbamoylation of dialkyl-substituted alkene **54** provided allylic product **55** in high yield. Subsequent rhodium-catalysed asymmetric hydroboration of β,γ-unsaturated amide **55** proceed with high regio- and enantioselectivity employing the TADDOL-derived phosphite ligand **L1**.[62] The following oxidation gave γ-hydroxyamide **56**, which was cyclized into γ-lactone **57**. Eventually, (−)-arctigenin **58** was obtained by diastereoselective alkylation of **57** followed by benzyl group removal. The spectroscopic data, including the specific rotation of this obtained sample, completely matched the literature data.[63]

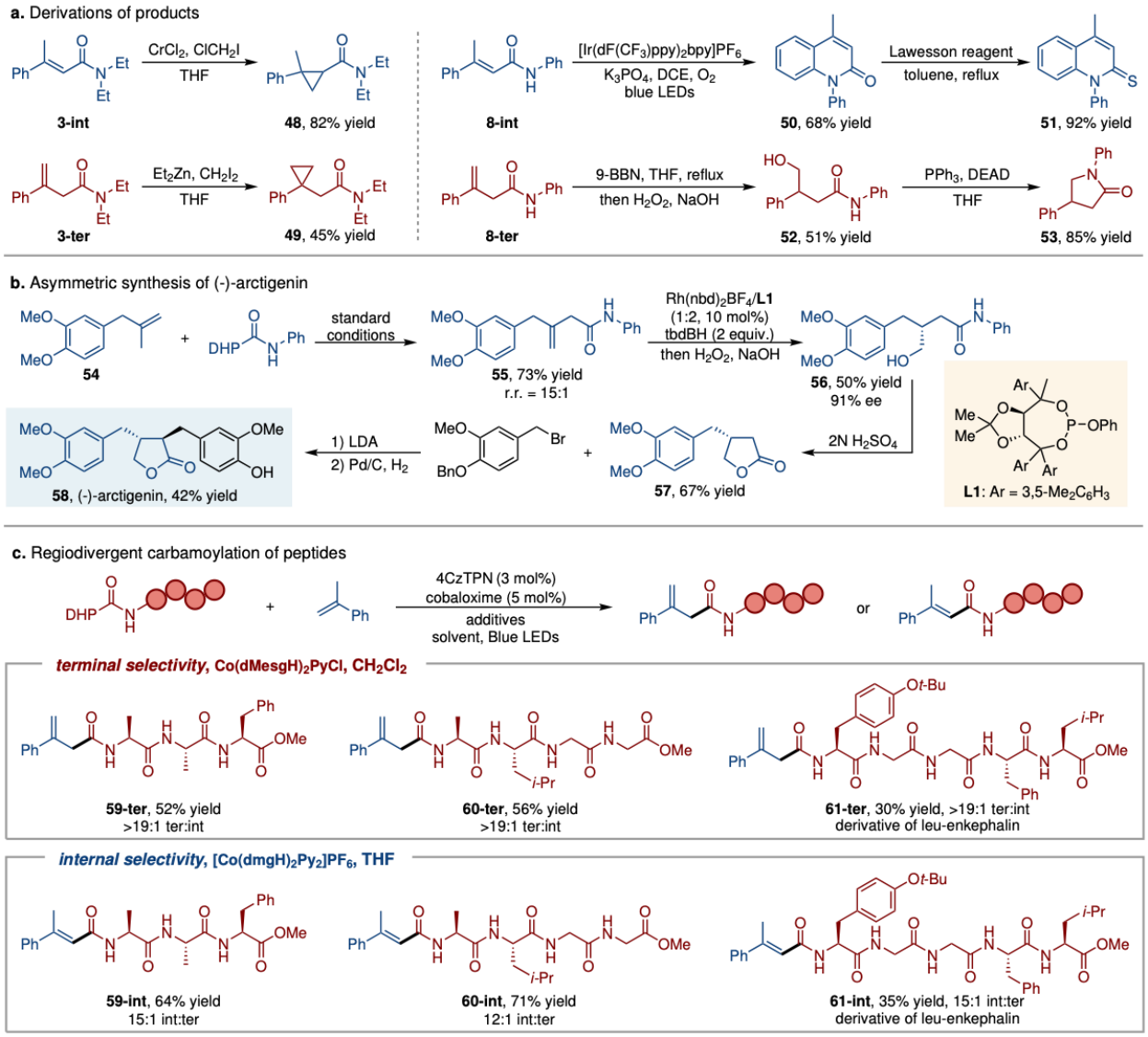

Figure 53. Synthetic applications. a) Derivations of products. b) Asymmetric synthesis of (−)-arctigenin. c) Regiodivergent carbamoylation of peptides.

We next directed our efforts to the regioselective functionalization of peptide *N*-termini (**Figure 53c**), which is a valuable tool for both basic research and the development of new drug candidates.[64] In this context, a series of peptidyl-dihydropyridines were synthesized via late-stage modification with 4-carbamoyl-1,4-dihydropyridines. Encouragingly, the carbamoylation reaction

worked well with peptides containing three to five amino acids, such as the bioactive leu-enkephalin, affording the desired vinyl and allyl products **59–61** with excellent regioselectivity.

7.4.4 Experimental Investigations on the Reaction Pathways

To gain further insight into the catalytic cycle, the mechanism of the carbamoylation reaction was investigated by a radical clock experiment (**Figure 54a**). The cyclopropyl-containing alkene **62** underwent ring opening followed by intramolecular radical addition to afford dihydronaphthalene **63** in good yield. These results strongly support a radical-involved pathway. To monitor hydrogen evolution in the cobaloxime catalytic cycle, the gas phase in the reaction vessel headspace was analyzed by gas chromatography (GC). A 200 μmol-scale reaction produced 60 μmol and 86 μmol of hydrogen in CH_2Cl_2 and THF, respectively (**Figure 54b**). Furthermore, the kinetic isotope effect (KIE) studies were performed using deuterated α-methylstyrene **[D]-2a** (**Figure 54c**). Competitive KIE experiments exhibited k_H/k_D values of 5.7 and 3.3, suggesting that HAT is likely to be the rate-determining step in the catalytic cycle. In addition, the isolated vinyl and allylic products were individually subjected to the optimal reaction conditions (**Figure 54d**). In both cases, no interconversion between the two products was observed, implying that they are formed via regiodivergent pathways.

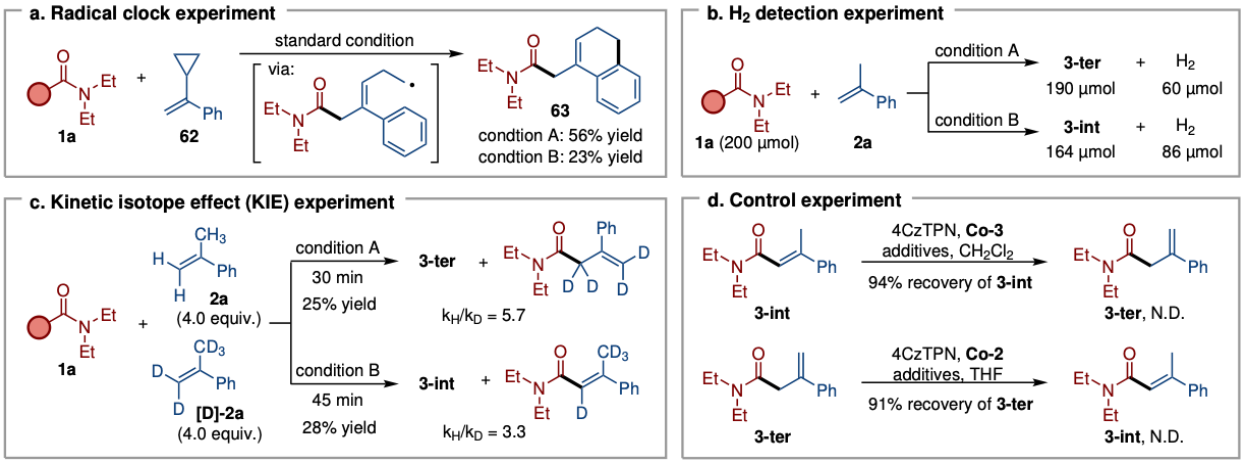

Figure 54. Mechanistic studies. a) Radical clock experiment. b) H_2 detection experiment. c) Kinetic isotope effect (KIE) experiment. d) Control experiment. Reaction conditions A: dihydropyridine **1a** (0.2 mmol), alkene (4.0 equiv.), 4CzTPN (3 mol%), Co(dMesgH)$_2$PyCl (**Co-3**, 5 mol%), pyrene (10 mol%), $CsHCO_3$ (1.0 equiv.), KOAc (0.5 equiv.) in CH_2Cl_2 (3.0 mL) under blue light irradiation. Reaction conditions B: dihydropyridine **1a** (0.2 mmol), alkene (4.0 equiv.), 4CzTPN (3 mol%), $[Co(dmgH)_2Py_2]PF_6$ (**Co-2**, 5 mol%), pyrene (10 mol%), $CsHCO_3$ (1.0 equiv.), KOAc (0.5 equiv.) in THF (3.0 mL) under blue light irradiation.

7.4.5 Computational Studies

To understand how the regioselective hydrogen abstraction by the cobaloxime can be controlled by ligand substituents, density functional theory (DFT) computations were performed on the product-determining hydrogen abstraction steps. Previous DFT studies on related cobaloxime systems have provided important insights into their reactivity and selectivity.[51,65,66] In this work, 4-dimethylcarbamoyl-1,4-dihydropyridine and styrene **2a** were used as the model substrates, with the diethylamino moiety of **1a** simplified to a dimethylamino group. As shown in **Figure 55a**, we first located the transition states **TS1a-Int** and **TS1a-Ter** corresponding to the formation of the internal olefin product **4-int** and the terminal olefin product **4-ter**, respectively, under the catalysis of **Co-2**. In both transition states, the C−H bond at the reactive site is

significantly elongated (C−H bond length: 1.42 Å for **TS1a-Int**; 1.46 Å for **TS1a-Ter**). The C, H and Co atoms are nearly colinear ($\theta_{C\text{-}H\text{-}Co}$: 174.9° for **TS1a-Int**; 172.7° for **TS1a-Ter**), consistent with a typical hydrogen atom transfer (HAT) process. Single-point energy calculations revealed that both transition states exhibit spin-polarized singlet state as the ground state, with $<S^2>$ values of 0.35 and 0.19 for **TS1a-Int** and **TS1a-Ter**, respectively, suggesting partial diradical character. The calculated free energy barriers for **TS1a-Int** and **TS1a-Ter** are 15.4 kcal/mol and 17.0 kcal/mol, respectively, consistent with the experimentally observed regioselectivity (for a complete energy profile, see **Figure 56** and **Figure 57**).

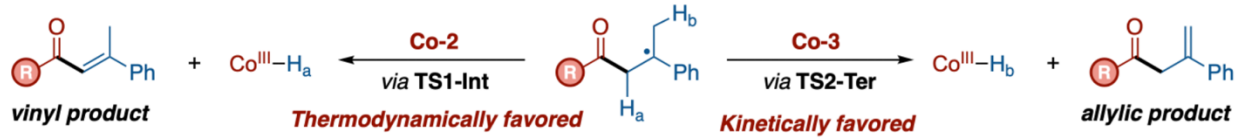

a

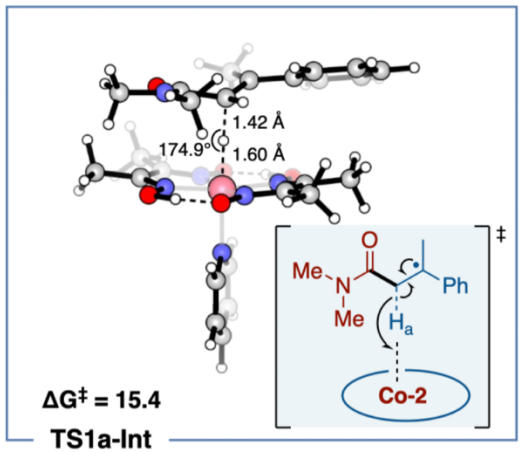

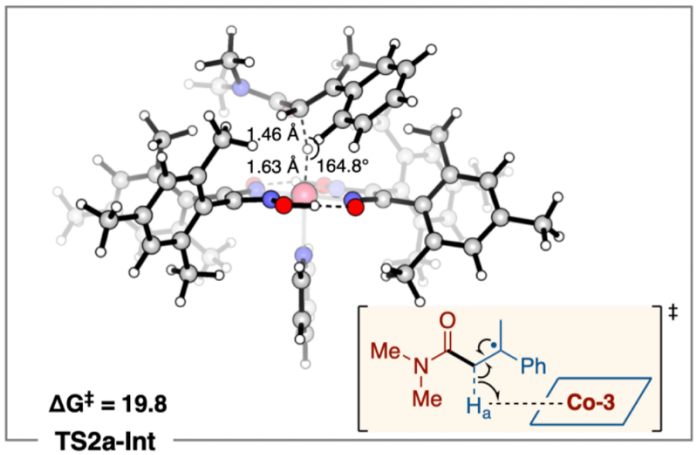

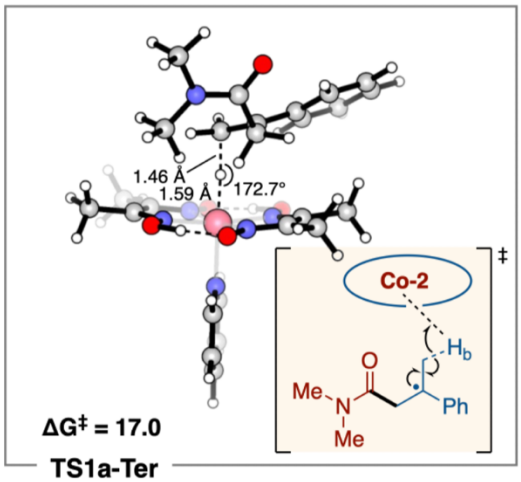

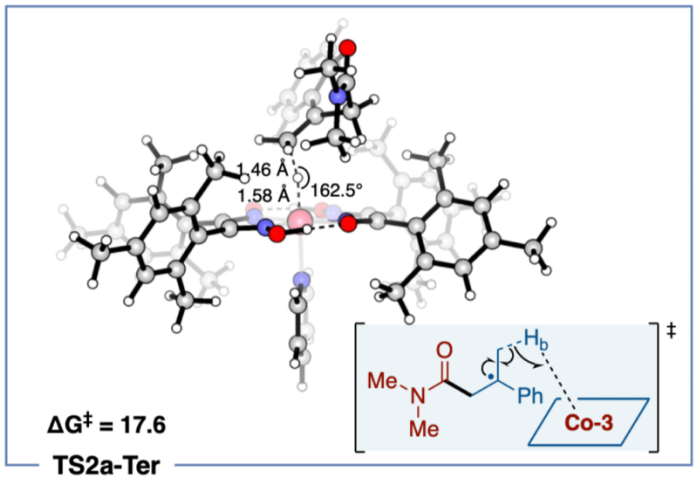

b

R	ΔG‡(TS1-Int)	ΔG‡(TS1-Ter)	ΔG‡(TS2-Int)	ΔG‡(TS2-Ter)
NMe_2	15.4	17.0	19.8	17.6
Me	14.7	16.7	20.8	17.7
Ph	14.4	16.8	18.9	16.4

c

R	BDE of C–H_a (ΔE)	BDE of C–H_b (ΔE)
NMe_2	50.7	54.0
Me	49.5	53.9
Ph	49.9	54.0

d

R	TS1-Int		TS1-Ter		TS2-Int		TS2-Ter	
	$\Delta E_{dis\text{-}sub}$	$\Delta E_{dis\text{-}cat}$	$\Delta E_{dis\text{-}sub}$	$\Delta E_{dis\text{-}cat}$	$\Delta E_{dis\text{-}sub}$	$\Delta E_{dis\text{-}cat}$	$\Delta E_{dis\text{-}sub}$	$\Delta E_{dis\text{-}cat}$
NMe_2	26.8	0.7	27.0	0.7	28.7	2.5	27.4	2.0
Me	25.1	0.6	25.6	0.7	28.3	2.6	26.0	1.5
Ph	26.0	0.8	27.3	0.8	28.2	2.9	27.9	1.7

Figure 55. DFT studies for the origin of regioselectivity. a) Structures and free energy barriers of the competing transition states. b) Differences in free energy barriers. c) Bond dissociation energies (BDE) of the benzyl radical intermediates. d) Distortion energy analysis for the substrate ($\Delta E_{dis\text{-}sub}$) and catalyst ($\Delta E_{dis\text{-}cat}$) fragments. Gibbs free energy calculations were performed at the (u)B3LYP-D3(BJ)/6-311G(d,p) (SDD for Co)/SMD//(u)B3LYP-D3(BJ)/6-31G(d) (SDD for Co) level of theory at 313.15 K with Grimme's entropic correction and Head-Gordon's enthalpic correction. Energies are reported in kcal/mol.

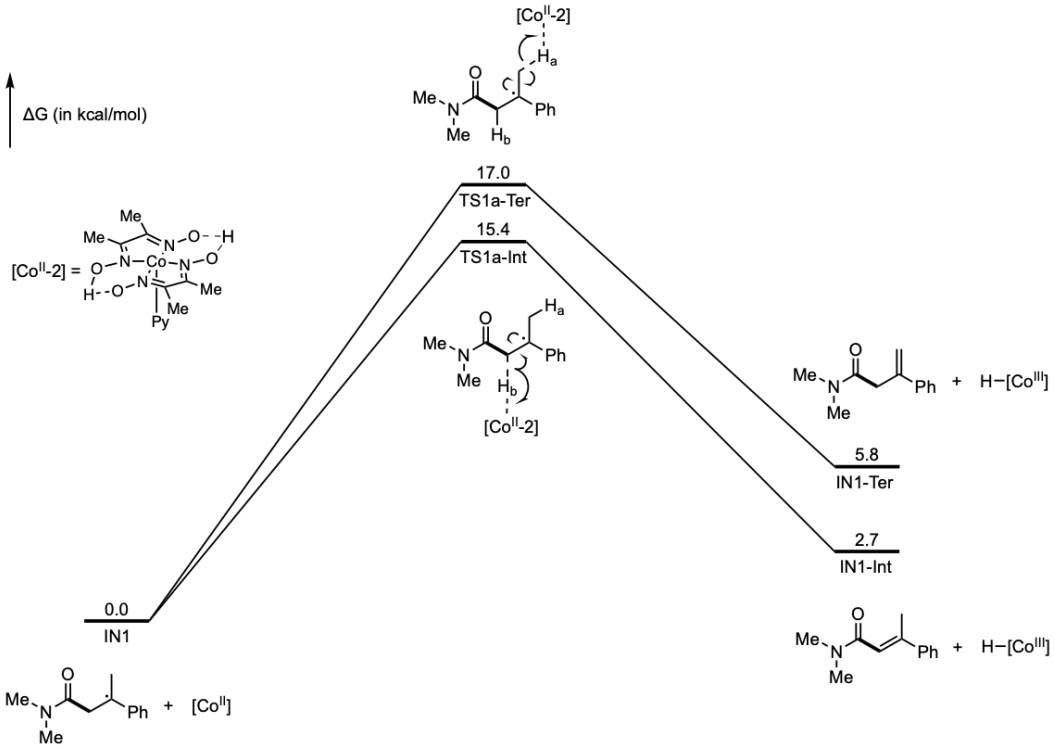

Figure 56. Free energy profile of the reaction on **IN1** (-NMe_2) catalyzed by **Co-2**. Gibbs free energy calculations were performed at the (u)B3LYP-D3(BJ)/6-311G(d,p) (SDD for Co)/SMD//(u)B3LYP-D3(BJ)/6-31G(d) (SDD for Co) level of theory at 313.15 K with Grimme's entropic correction and Head-Gordon's enthalpic correction. Energies are reported in kcal/mol.

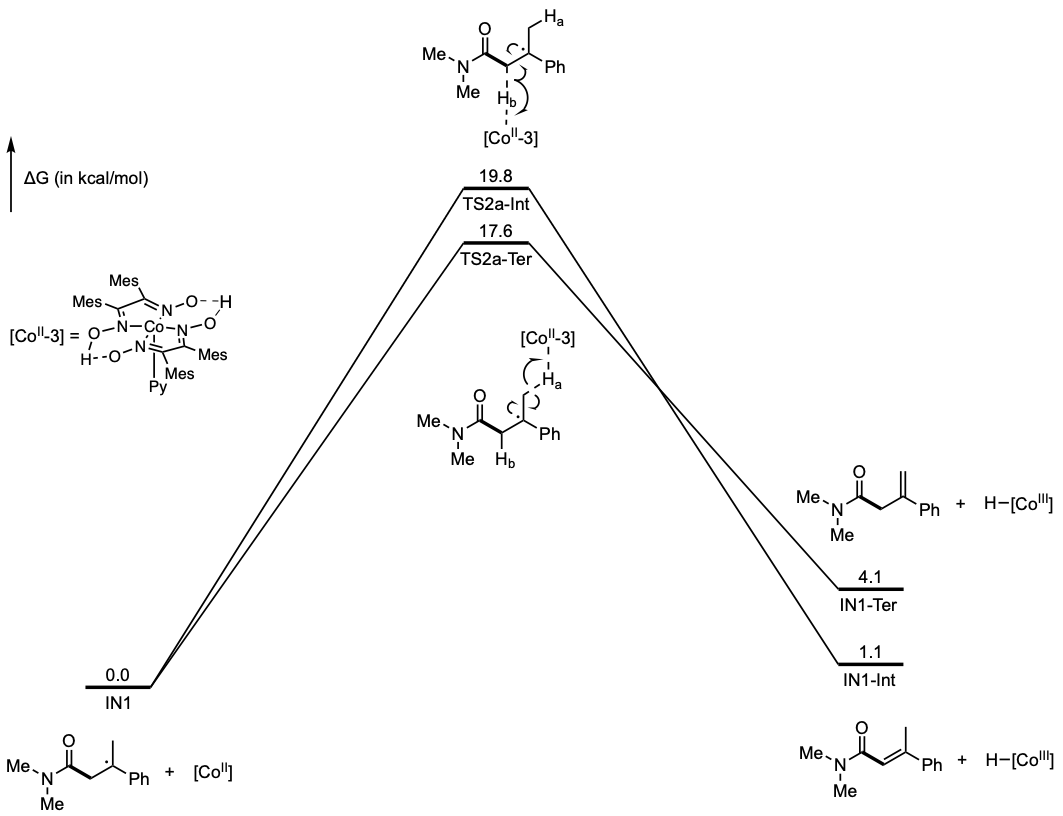

Figure 57. Free energy profile of the reaction on **IN1** (-NMe_2) catalyzed by **Co-3**. Gibbs free energy calculations were performed at the (u)B3LYP-D3(BJ)/6-311G(d,p) (SDD for Co)/SMD//(u)B3LYP-D3(BJ)/6-31G(d) (SDD for Co) level of theory at 313.15 K with Grimme's entropic correction and Head-Gordon's enthalpic correction. Energies are reported in kcal/mol.

For the reaction catalysed by the sterically more hindered **Co-3**, the corresponding transition states **TS2a-Int** and **TS2a-Ter** were also located. Similar to their **Co-2** counterparts, the C−H bond lengths in the **TS2a-Int** and **TS2a-Ter** are significantly elongated. However, the angles between C, H and Co atoms deviate more from a linear alignment ($\theta_{C–H–Co}$: 164.8° for **TS2a-Int**; 162.5° for **TS2a-Ter**), potentially indicating a more congested catalytic center in **Co-3**. Single-point energy calculations show that **TS2a-Int** and **TS2a-Ter** also possess spin-polarized singlet states ($<S^2> = 0.34$ and 0.19, respectively), with their free energy barriers similar to those of **TS1a-**

Int and **TS1a-Ter** (19.8 kcal/mol for **TS2a-Int**; 17.6 kcal/mol for **TS2a-Ter**). Notably, these energy barriers can still be readily overcome at room to moderate temperatures. Interestingly, in contrast to the **Co-2** system, **TS2a-Int** is energetically less favored than **TS2a-Ter** by 2.2 kcal/mol. This reversal in regioselectivity is in line with experimental observations when **Co-3** is employed.

To further explore the role of the cobalt catalyst and substrate architectures in controlling this regioselectivity, we performed calculations on two additional substrates, in which the dimethylamino group (-NMe_2) in the modified **1a** was replaced by a methyl (-Me) and phenyl (-Ph) group, respectively (for a complete energy profile, see **Figure 58**, **Figure 59**, **Figure 60** and **Figure 61**). The calculated free energy barriers for the two competing transition states of each substrate under **Co-2** and **Co-3** catalysis are shown in **Figure 55b**. Overall, the barrier heights are comparable to those of the dimethylamino-substituted substrate. The predicted regioselectivities for both substrates are also consistent with our experimental observations.

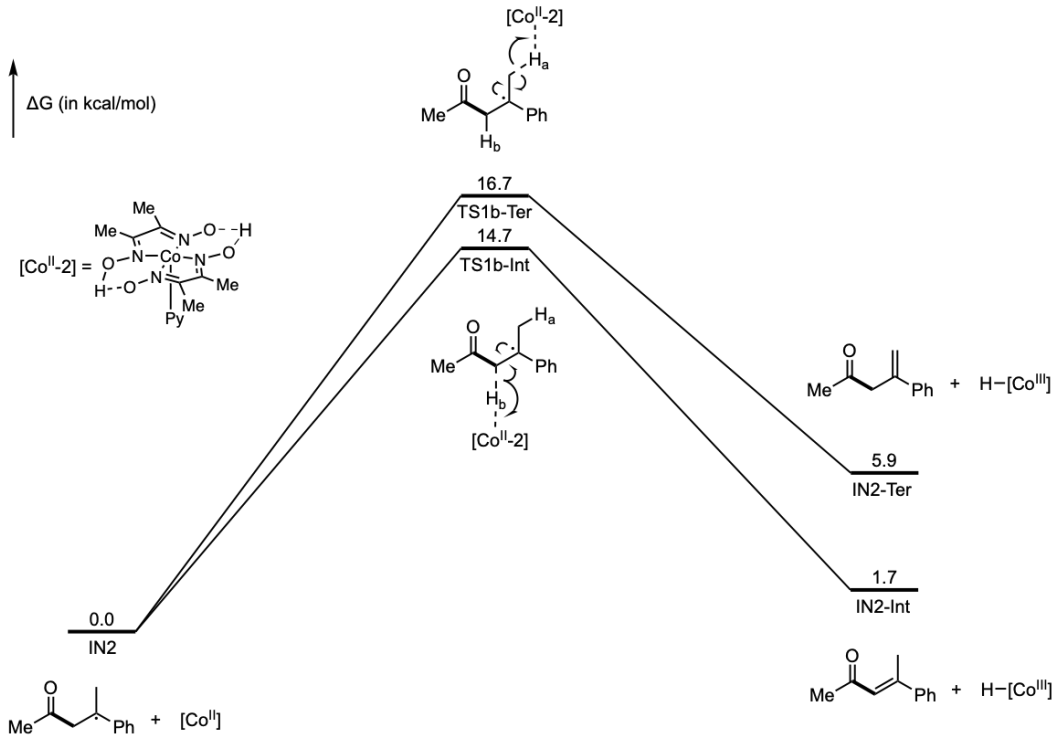

Figure 58. Free energy profile of the reaction on **IN2** (-Me) catalyzed by **Co-2**. Gibbs free energy calculations were performed at the (u)B3LYP-D3(BJ)/6-311G(d,p) (SDD for Co)/SMD//(u)B3LYP-D3(BJ)/6-31G(d) (SDD for Co) level of theory at 313.15 K with Grimme's entropic correction and Head-Gordon's enthalpic correction. Energies are reported in kcal/mol.

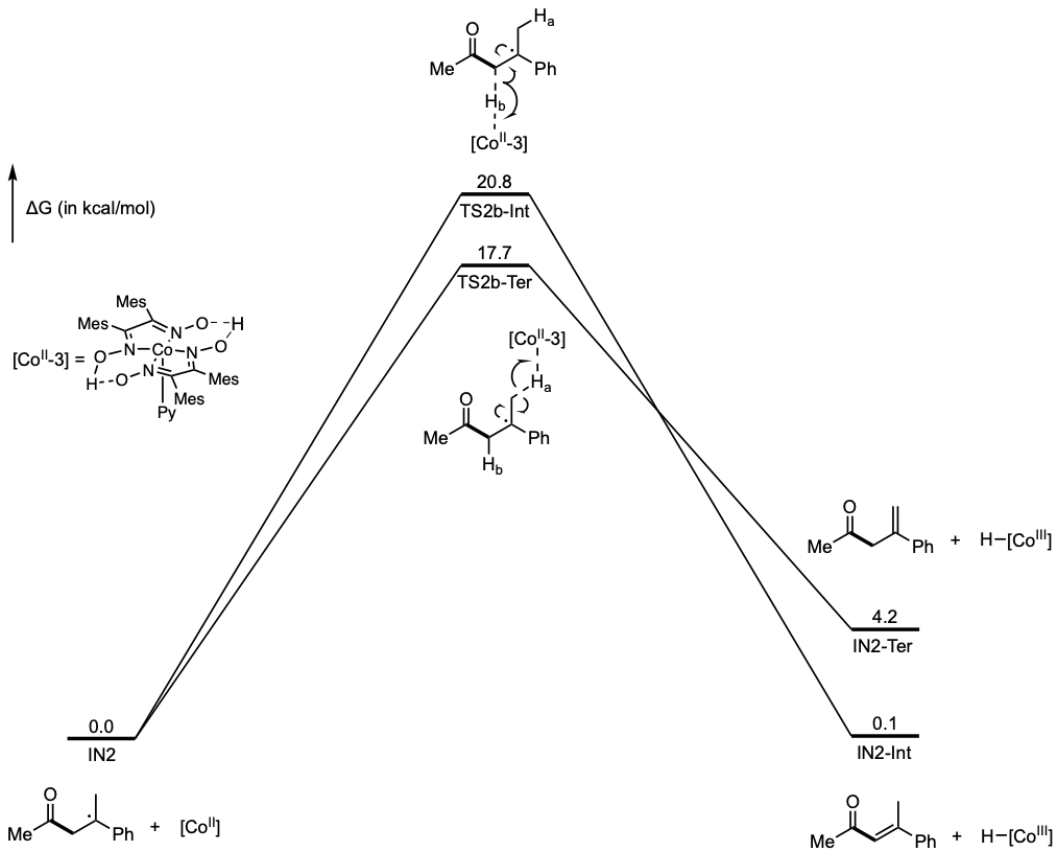

Figure 59. Free energy profile of the reaction on **IN2** (-Me) catalyzed by **Co-3**. Gibbs free energy calculations were performed at the (u)B3LYP-D3(BJ)/6-311G(d,p) (SDD for Co)/SMD//(u)B3LYP-D3(BJ)/6-31G(d) (SDD for Co) level of theory at 313.15 K with Grimme's entropic correction and Head-Gordon's enthalpic correction. Energies are reported in kcal/mol.

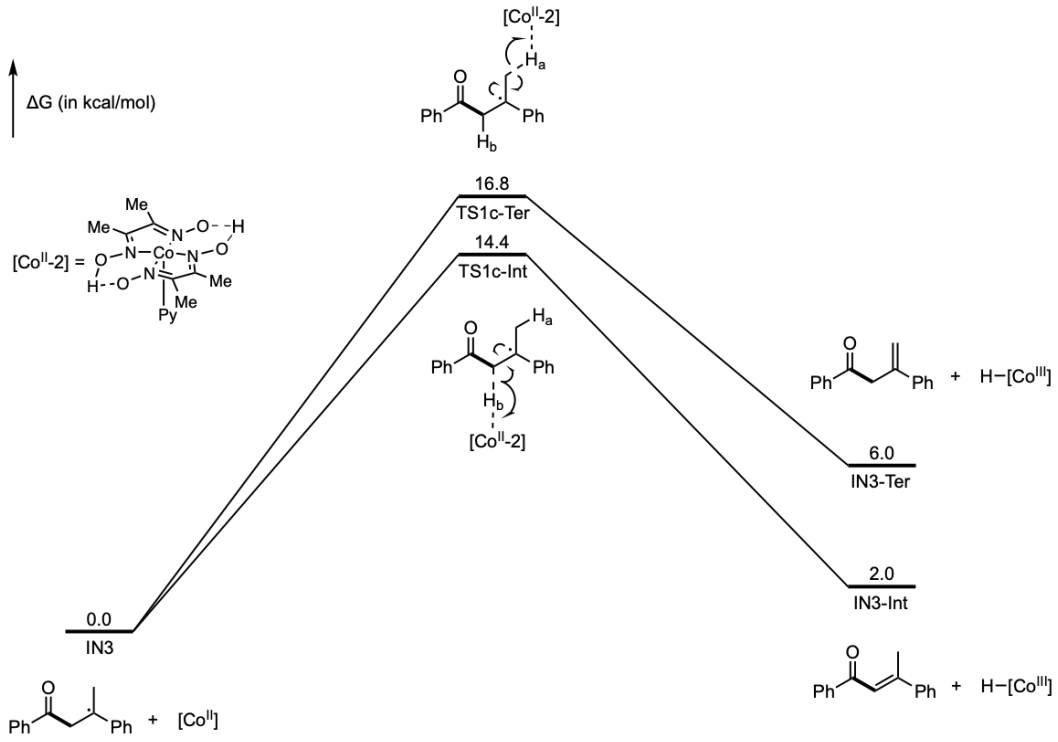

Figure 60. Free energy profile of the reaction on **IN3** (-Ph) catalyzed by **Co-2**. Gibbs free energy calculations were performed at the (u)B3LYP-D3(BJ)/6-311G(d,p) (SDD for Co)/SMD//(u)B3LYP-D3(BJ)/6-31G(d) (SDD for Co) level of theory at 313.15 K with Grimme's entropic correction and Head-Gordon's enthalpic correction. Energies are reported in kcal/mol.

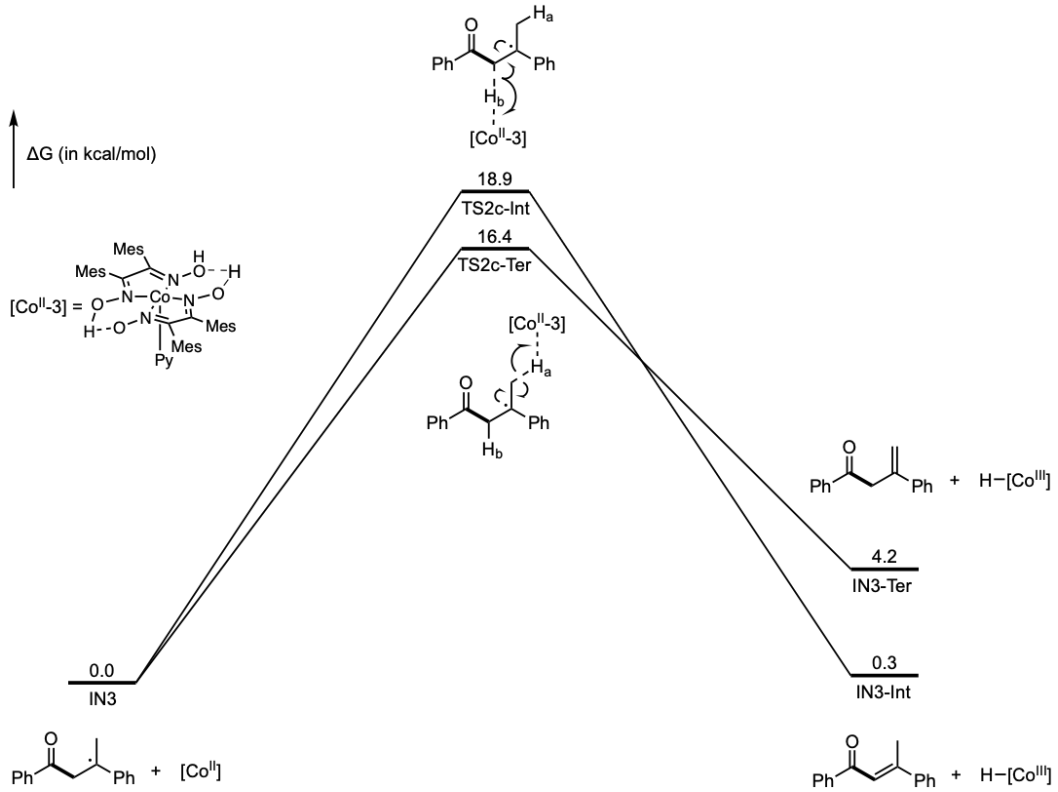

Figure 61. Free energy profile of the reaction on **IN3** (-Ph) catalyzed by **Co-3**. Gibbs free energy calculations were performed at the (u)B3LYP-D3(BJ)/6-311G(d,p) (SDD for Co)/SMD//(u)B3LYP-D3(BJ)/6-31G(d) (SDD for Co) level of theory at 313.15 K with Grimme's entropic correction and Head-Gordon's enthalpic correction. Energies are reported in kcal/mol.

To probe the origin of regioselectivity, we first calculated the C−H bond dissociation energies (BDE) of the benzyl radical intermediates derived from the three substrates. As shown in **Figure 55c**, the C−H_a bond is consistently weaker than the C−H_b bond in all cases, indicating an intrinsic preference for HAT process at C−H_a. This trend agrees with the selectivity observed with **Co-2**. We then performed a distortion energy analysis of the competing transition states (**Figure 55d**). Each transition state was divided into a substrate fragment (sub) and a cobalt catalyst fragment (cat). The distortion energies, $\Delta E_{\text{dis-sub}}$ and $\Delta E_{\text{dis-cat}}$, were defined as the energy differences between their geometries in the transition state and their respective optimized ground

states. For the less hindered **Co-2** (**TS1-Int** and **TS1-Ter** columns; **Figure 55d**), $\Delta E_{\text{dis-cat}}$ is minimal (0.6−0.8 kcal/mol) for both competing transition states, indicating negligible catalyst distortion. The total distortion energy mainly arises from the substrate fragment. In addition, for all three substrates, the $\Delta E_{\text{dis-sub}}$ of the terminal pathway is slightly higher than that of the internal pathway, consistent with the BDE trend and the experimentally observed internal selectivity. In contrast, for the more sterically hindered **Co-3** (**TS2-Int** and **TS2-Ter** columns; **Figure 55d**), steric interactions between the approaching fragments become more pronounced, leading to increased distortion in both components. This is evidenced by the larger $\Delta E_{\text{dis-sub}}$ values as well as an increase of $\Delta E_{\text{dis-cat}}$ to 1.5−2.9 kcal/mol for all transition states. Notably, the increase in substrate distortion $\Delta E_{\text{dis-sub}}$ is more pronounced for the internal transition states, whereas the terminal transition states are comparatively less affected compared to the **Co-2** scenario, thereby shifting the energetic preference to the terminal pathway.

Taken together, these results suggest a mechanistic picture: with the less hindered **Co-2** catalyst, steric interactions between the substrate and the cobalt center are minimal, and HAT occurs preferentially at the intrinsically weaker C−H_a bond, which also leads to the more thermodynamically stable internal product. In contrast, the bulkier **Co-3** catalyst introduces more steric repulsion as the substrate approaches the metal center, requiring greater structural distortion of both fragments in the transition state. Under this condition, the kinetically more accessible C−H_b bond becomes favored, resulting in a reversal of regioselectivity.

7.5 Conclusion

In summary, we developed a regiodivergent carbamoylation reaction of branched alkenes via cobaloxime-catalysed HAT. Central to the success of this strategy is the rational modulation

of the cobalt catalyst, which enables switching between thermodynamically and kinetically favored pathways. The method provides efficient access to both α,β- and β,γ-unsaturated amides and has been applied to the total synthesis of (−)-arctigenin. Experimental and computational investigations elucidate the mechanism and the unique role of the cobaloxime catalyst in promoting HAT. We anticipate that this strategy will facilitate further exploration and development of HAT-mediated C−H functionalization.

7.6 Methods

7.6.1 A General Procedure for the Regioselective Carbamoylation of Alkenes

To an oven-dried reaction tube equipped with a stir bar was added **1** (0.2 mmol, 1.0 equiv.), cobaloxime catalyst (5 mol%), 4CzTPN (3 mol%), pyrene (0.02 mmol, 10 mol%), $CsHCO_3$ (0.2 mmol, 1.0 equiv.), and KOAc (0.1 mmol, 0.5 equiv.). The tube was sealed and purged with nitrogen. Alkene **2** (0.8 mmol, 4.0 equiv.) and solvent (6 mL) were then added. The resulting mixture was stirred and irradiated with blue LEDs at 40°C. Upon completion, the reaction mixture was purified by silica gel column chromatography to afford the desired product.

7.6.2 Density Functional Theory (DFT) Calculations

All calculations were performed using Gaussian 16 program.[67] Geometry optimizations and vibrational frequency analyses for all intermediates and transition states were carried out in the gas phase at the (u)B3LYP-D3(BJ)/6-31G(d) level of theory (u denotes unrestricted calculations), with the SDD effective core potential and corresponding basis set applied to Co atom. Single-point energy calculations were subsequently performed at the (u)B3LYP-D3(BJ)/6-

311G(d,p) level (SDD used for Co atom) with the SMD implicit solvent model. THF (Tetrahydrofuran) and DCM (Dichloromethane) were used as the solvent environments for the intermediates and transition states associated with **Co-2** and **Co-3**, respectively. Gibbs free energies were calculated at 313.15 K with Grimme's entropic correction and Head-Gordon's enthalpic correction applied using Goodvibes program (version 3.2).[68] Additional computational details and the Cartesian coordinates of all calculated structures are provided in the Supporting Information of our published work.[69]

7.7 References

(1) Hynes, J. T., Klinman, J. P., Limbach, H. H. & Schowen, R. L. *Hydrogen-Transfer Reactions*; Wiley-VCH: 2007.

(2) Mayer, J. M. Understanding Hydrogen Atom Transfer: From Bond Strengths to Marcus Theory. *Acc. Chem. Res.* **2011**, 44, 36−46.

(3) Salamone, M. & Bietti, M. Tuning Reactivity and Selectivity in Hydrogen Atom Transfer from Aliphatic C−H Bonds to Alkoxyl Radicals: Role of Structural and Medium Effects. *Acc. Chem. Res.* **2015**, *48*, 2895−2903.

(4) Cao, H., Tang, X., Tang, H., Yuan, Y. & Wu, J. Photoinduced Intermolecular Hydrogen Atom Transfer Reactions in Organic Synthesis. *Chem Catal.* **2021**, *1*, 523−598.

(5) Capaldo, L., Ravelli, D. & Fagnoni, M. Direct Photocatalyzed Hydrogen Atom Transfer (HAT) for Aliphatic C−H Bonds Elaboration. *Chem. Rev.* **2022**, *122*, 1875−1924.

(6) Galeotti, M., Salamone, M. & Bietti, M. Electronic Control over Site-Selectivity in Hydrogen Atom Transfer (HAT) Based C(sp^3)–H Functionalization Promoted by Electrophilic Reagents. *Chem. Soc. Rev.* **2022**, *51*, 2171−2223.

(7) Jeffrey, J. L., Terrett, J. A. & MacMillan, D. W. C. O−H Hydrogen Bonding Promotes H-Atom Transfer from α C−H Bonds for C-Alkylation of Alcohols. *Science* **2015**, *349*, 1532−1536.

(8) Perry, I. B., Brewer, T. F., Sarver, P. J., Schultz, D. M., DiRocco, D. A. & MacMillan, D. W. C. Direct Arylation of Strong Aliphatic C−H Bonds. *Nature* **2018**, *560*, 70−75.

(9) Hu, A., Guo, J.-J., Pan, H. & Zuo, Z. Selective Functionalization of Methane, Ethane, and Higher Alkanes by Cerium Photocatalysis. *Science* **2018**, *361*, 668−672.

(10) Cao, H., Kong, D., Yang, L.-C., Chanmungkalakul, S., Liu, T., Piper, J. L., Peng, Z., Gao, L., Liu, X., Hong, X. & Wu, J. Brønsted Acid-Enhanced Direct Hydrogen Atom Transfer Photocatalysis for Selective Functionalization of Unactivated C(sp^3)–H Bonds. *Nat. Synth.* **2022**, *1*, 794–803.

(11) Hu, X., Cheng-Sánchez, I., Kong, W., Molander, G. A. & Nevado, C. Nickel-Catalysed Enantioselective Alkene Dicarbofunctionalization Enabled by Photochemical Aliphatic C–H Bond Activation. *Nat. Catal.* **2024**, *7*, 655–665.

(12) Wang, M., Huang, Y. & Hu, P. Terminal C(sp^3)–H Borylation through Intermolecular Radical Sampling. *Science* **2024**, *383*, 537–544.

(13) Ruffoni, A., Mykura, R. C., Bietti, M. & Leonori, D. The Interplay of Polar Effects in Controlling the Selectivity of Radical Reactions. *Nat. Synth.* **2022**, *1*, 682–695.

(14) Tang, S., Liu, K., Liu, C. & Lei, A. Olefinic C–H Functionalization through Radical Alkenylation. *Chem. Soc. Rev.* **2015**, *44*, 1070–1082.

(15) Zhang, J., Lu, X., Shen, C., Xu, L., Ding, L. & Zhong, G. Recent Advances in Chelation-Assisted Site- and Stereoselective Alkenyl C–H Functionalization. *Chem. Soc. Rev.* **2021**, *50*, 3263–3314.

(16) Cheung, K. P. S., Sarkar, S. & Gevorgyan, V. Visible Light-Induced Transition Metal Catalysis. *Chem. Rev.* **2022**, *122*, 1543–1625.

(17) Lu, M.-Z., Goh, J., Maraswami, M., Jia, Z., Tian, J.-S. & Loh, T.-P. Recent Advances in Alkenyl sp^2 C−H and C−F Bond Functionalizations: Scope, Mechanism, and Applications. *Chem. Rev.* **2022**, *122*, 17479–17646.

(18) Ikeda, Y., Nakamura, T., Yorimitsu, H. & Oshima, K. Cobalt-Catalyzed Heck-Type Reaction of Alkyl Halides with Styrenes. *J. Am. Chem. Soc.* **2002**, *124*, 6514–6515.

(19) Liu, C., Tang, S., Liu, D., Yuan, J., Zheng, L., Meng, L. & Lei, A. Nickel-Catalyzed Heck-Type Alkenylation of Secondary and Tertiary α-Carbonyl Alkyl Bromides. *Angew. Chem. Int. Ed.* **2012**, *51*, 3638–3641.

(20) McMahon, C. M. & Alexanian, E. J. Palladium-Catalyzed Heck-Type Cross-Couplings of Unactivated Alkyl Iodides. *Angew. Chem. Int. Ed.* **2014**, *53*, 5974–5977.

(21) Wu, X., Riedel, J. & Dong, V. M. Transforming Olefins into γ,δ-Unsaturated Nitriles through Copper Catalysis. *Angew. Chem. Int. Ed.* **2017**, *56*, 11589–11593.

(22) Tang, C., Zhang, R., Zhu, B., Fu, J., Deng, Y., Tian, L., Guan, W. & Bi, X. Directed Copper-Catalyzed Intermolecular Heck-Type Reaction of Unactivated Olefins and Alkyl Halides. *J. Am. Chem. Soc.* **2018**, *140*, 16929–16935.

(23) Zhao, C., Li, Y., Dong, Y., Li, M., Xia, D., Gao, S., Zhang, Q., Liu, Q., Guan, W. & Fu, J. Divergent Regioselective Heck-type Reaction of Unactivated Alkenes and *N*-Fluorosulfonamides. *Nat. Commun.* **2022**, *13*, 6297.

(24) Beletskaya, I. P. & Cheprakov, A. V. The Heck Reaction as a Sharpening Stone of Palladium Catalysis. *Chem. Rev.* **2000**, *100*, 3009–3066.

(25) Delcamp, J. H., Brucks, A. P. & White, C. M. A General and Highly Selective Chelate-Controlled Intermolecular Oxidative Heck Reaction. *J. Am. Chem. Soc.* **2008**, *130*, 11270–11271.

(26) Werner, E. W. & Sigman, M. S. A Highly Selective and General Palladium Catalyst for the Oxidative Heck Reaction of Electronically Nonbiased Olefins. *J. Am. Chem. Soc.* **2010**, *132*, 13981–13983.

(27) Bhoyare, V. W., Sosa Carrizo, E. D., Chintawar, C. C., Gandon, V. & Patil, N. T. Gold-Catalyzed Heck Reaction. *J. Am. Chem. Soc.* **2023**, *145*, 8810–8816.

(28) Liwosz, T. W. & Chemler, S. R. Copper-Catalyzed Oxidative Heck Reactions between Alkyltrifluoroborates and Vinyl Arenes. *Org. Lett.* **2013**, *15*, 3034–3037.

(29) Zou, Y. & Zhou, J. Palladium-Catalyzed Intermolecular Heck Reaction of Alkyl Halides. *Chem. Commun.* **2014**, *50*, 3725–3728.

(30) Nájera, C., Beletskaya, I. P. & Yus, M. Metal-Catalyzed Regiodivergent Organic Reactions. *Chem. Soc. Rev.* **2019**, *48*, 4515–4618.

(31) Dempsey, J. L., Brunschwig, B. S., Winkler, J. R. & Gray, H. B. Hydrogen Evolution Catalyzed by Cobaloximes. *Acc. Chem. Res.* **2009**, *42*, 1995–2004.

(32) Chen, B., Wu, L.-Z. & Tung, C.-H. Photocatalytic Activation of Less Reactive Bonds and Their Functionalization via Hydrogen-Evolution Cross-Couplings. *Acc. Chem. Res.* **2018**, *51*, 2512–2523.

(33) Dam, P., Zuo, K., Azofra, L. M. & El-Sepelgy, O. Biomimetic Photoexcited Cobaloxime Catalysis in Organic Synthesis. *Angew. Chem. Int. Ed.* **2024**, *63*, e202405775.

(34) Mandal, A., Lim, M., Zhang, L., Huang, K.-W. & Dighe, S. U. Synergistic Cobaloxime Catalysis for Photo-Dehydrogenative Transformations. *ACS Catal.* **2025**, *15*, 9976–10004.

(35) Yi, H., Niu, L., Song, C., Li, Y., Dou, B., Singh, A. K. & Lei, A. Photocatalytic Dehydrogenative Cross-Coupling of Alkenes with Alcohols or Azoles without External Oxidant. *Angew. Chem. Int. Ed.* **2017**, *56*, 1120–1124.

(36) Yang, Q., Zhang, L., Ye, C., Luo, S., Wu, L.-Z. & Tung, C.-H. Visible-Light-Promoted Asymmetric Cross-Dehydrogenative Coupling of Tertiary Amines to Ketones by Synergistic Multiple Catalysis. *Angew. Chem. Int. Ed.* **2017**, *56*, 3694–3698.

(37) Sun, X., Chen, J. & Ritter, T. Catalytic Dehydrogenative Decarboxyolefination of Carboxylic Acids. *Nat. Chem.* **2018**, *10*, 1229–1233.

(38) Dighe, S. U., Juliá, F., Luridiana, A., Douglas, J. J. & Leonori, D. A Photochemical Dehydrogenative Strategy for Aniline Synthesis. *Nature* **2020**, *584*, 75−82.

(39) Zhao, H., McMillan, A. J., Constantin, T., Mykura, R. C., Juliá, F. & Leonori, D. Merging Halogen- Atom Transfer (XAT) and Cobalt Catalysis to Override E2-Selectivity in the Elimination of Alkyl Halides: A Mild Route toward contra-Thermodynamic Olefins. *J. Am. Chem. Soc.* **2021**, *143*, 14806–14813.

(40) Yu, W.-L., Ren, Z.-G., Ma, K.-X., Yang, H.-Q., Yang, J.-J., Zheng, H., Wu, W. & Xu, P.-F. Cobalt- Catalyzed Chemoselective Dehydrogenation through Radical Translocation under Visible Light. *Chem. Sci.* **2022**, *13*, 7947−7954.

(41) Huang, H., Luan, X. & Zuo, Z. Cooperative Photoredox and Cobalt-Catalyzed Acceptorless Dehydrogenative Functionalization of Cyclopropylamides towards Allylic N,O-Acyl-Acetal Derivatives. *Angew. Chem. Int. Ed.* **2024**, *63*, e202401579.

(42) Gu, X., Zhang, Y.-A., Zhang, S., Wang, L., Ye, X., Occhialini, G., Barbour, J., Pentelute, B. L. & Wendlandt, A. E. Synthesis of Non-Canonical Amino Acids through Dehydrogenative Tailoring. *Nature* **2024**, *634*, 352−358.

(43) Ying, X., Zhang, Y. & Li, C. Cobalt-Catalyzed Photoelectrochemical Dehydration of Primary Alcohols. *J. Am. Chem. Soc.* **2025**, *147*, 45315–45323.

(44) Cao, H., Jiang, H., Feng, H., Kwan, J. M. C., Liu, X. & Wu, J. Photo-induced Decarboxylative Heck-Type Coupling of Unactivated Aliphatic Acids and Terminal Alkenes in the Absence of Sacrificial Hydrogen Acceptors. *J. Am. Chem. Soc.* **2018**, *140*, 16360–16367.

(45) Liu, W.-Q., Lei, T., Zhou, S., Yang, X.-L., Li, J., Chen, B., Sivaguru, J., Tung, C.-H. & Wu, L.-Z. Cobaloxime Catalysis: Selective Synthesis of Alkenylphosphine Oxides under Visible Light. *J. Am. Chem. Soc.* **2019**, *141*, 13941–13947.

(46) Constantin, T., Zanini, M., Regni, A., Sheikh, N. S., Juliá, F. & Leonori, D. Aminoalkyl Radicals as Halogen-Atom Transfer Agents for Activation of Alkyl and Aryl Halides. *Science* **2020**, *367*, 1021−1026.

(47) Zhou, W., Wu, S. & Melchiorre, P. Tetrachlorophthalimides as Organocatalytic Acceptors for Electron Donor−Acceptor Complex Photoactivation. *J. Am. Chem. Soc.* **2022**, *144*, 8914–8919.

(48) Jia, Z., Zhang, L. & Luo, S. Asymmetric C−H Dehydrogenative Allylic Alkylation by Ternary Photoredox-Cobalt-Chiral Primary Amine Catalysis under Visible Light. *J. Am. Chem. Soc.* **2022**, *144*, 10705–10710.

(49) Prusinowski, A. F., Sise, H. C., Bednar, T. N. & Nagib, D. A. Radical Aza-Heck Cyclization of Imidates via Energy Transfer, Electron Transfer, and Cobalt Catalysis. *ACS Catal.* **2022**, *12*, 4327–4332.

(50) Jia, Z., Cheng, L., Zhang, L. & Luo, S. Asymmetric C–H Dehydrogenative Alkenylation via a Photo-induced Chiral α-Imino Radical Intermediate. *Nat. Commun.* **2024**, *15*, 4044.

(51) Liu, Z., Zhang, L., Luo, S. & Qi, X. Dynamic Hydrogen Bonding Tuned Enantioselectivity Control in Cobaloxime-Chiral Amine Cooperative Catalysis. *Angew. Chem. Int. Ed.* **2025**, *64*, e202506268.

(52) Wei, K., Tang, Y., Chen, X., Zhan, B. & Zhang, X. Stereodivergent Deacylative Mizoroki–Heck Reaction of Unstrained Ketones. *Angew. Chem. Int. Ed.* **2026**, *65*, e18599.

(53) Wang, S., Gao, Y., Liu, Z., Ren, D., Sun, H., Niu, L., Yang, D., Zhao, D., Liang, X., Shi, R., Qi, X. & Lei, A. Site-Selective Amination towards Tertiary Aliphatic Allylamines. *Nat. Catal.* **2022**, *5*, 642–651.

(54) Wang, S., Ren, D., Liu, Z., Yang, D., Wang, P., Gao, Y., Qi, X. & Lei, A. Cobalt-Catalysed Allylic Fluoroalkylation of Terpenes. *Nat. Synth.* **2023**, *2*, 1202–1210.

(55) Zhong, T., Gu, C., Li, Y., Huang, J., Han, J., Zhu, C., Han, J. & Xie, J. Manganese/Cobalt Bimetallic Relay Catalysis for Divergent Dehydrogenative Difluoroalkylation of Alkenes. *Angew. Chem. Int. Ed.* **2023**, *62*, e202310762.

(56) Ren, D., Deng, S., Wang, Y., Ding, W., Wang, P., Yan, J., Wang, S., Yuan, J., Wan, B., Qi, X., Lei, A., Yi, H. Radical Defluoroallylation of Polyfluoroalkyl Compounds with Alkenes via Synergistic Photoredox/Cobalt Catalysis. *Nat. Commun.* **2026**, *17*, 2971.

(57) Ren, D., Wang, Y., Liu, Z., Wang, Y., Ding, W., Yao, F., Qi, X., Lei, A. & Yi, H. Cobaloxime-Catalyzed Radical Allylic C−H Sulfonylation Through Synergistic XAT/HAT Processes. *ACS Catal.* **2025**, *15*, 13127−13135.

(58) Alandini, N., Buzzetti, L., Favi, G., Schulte, T., Candish, L., Collins, K. D. & Melchiorre, P. Amide Synthesis by Nickel/Photoredox-Catalyzed Direct Carbamoylation of (Hetero)Aryl Bromides. *Angew. Chem. Int. Ed.* **2020**, *59*, 5248−5253.

(59) Ye, X.-Y., Wang, G., Jin, Z., Yu, B., Zhang, J., Ren, S. & Chi, Y. R. Direct Formation of Amide- Linked C-Glycosyl Amino Acids and Peptides via Photoredox/Nickel Dual Catalysis. *J. Am. Chem. Soc.* **2024**, *146*, 5502–5510.

(60) Zeng, F.-L., Luo, Y.-X., Chen, J.-N., Jia, Z., Yu, B. & Loh, T.-P. Photocatalytic Carbamoylation to Access Thiocarbonyl Amino Acid/Peptide Derivatives in a Sustainable Solvent. *Green Chem.* **2026**, *28*, 2753−2760.

(61) Moon, Y., Jang, E., Choi, S. & Hong, S. Visible-Light-Photocatalyzed Synthesis of Phenanthridinones and Quinolinones via Direct Oxidative C−H Amidation. *Org. Lett.* **2018**, *20*, 240−243.

(62) Smith, S. M., Hoang, G. L., Pal, R., Khaled, M. O. B., Pelter, L. S. W., Zeng, X. C. & Takacs, J. M. γ-Selective Directed Catalytic Asymmetric Hydroboration of 1,1-Disubstituted Alkenes. *Chem. Commun.* **2012**, *48*, 12180–12182.

(63) Bode, J. W., Doyle, M. P., Protopopova, M. N. & Zhou, Q.-L. Intramolecular Regioselective Insertion into Unactivated Prochiral Carbon–Hydrogen Bonds with Diazoacetates of Primary Alcohols Catalyzed by Chiral Dirhodium(II) Carboxamidates. Highly Enantioselective Total Synthesis of Natural Lignan Lactones. *J. Org. Chem.* **1996**, *61*, 9146–9155.

(64) He, G., Wang, B., Nack, W. A. & Chen, G. Syntheses and Transformations of α-Amino Acids via Palladium-Catalyzed Auxiliary-Directed sp^3 C−H Functionalization. *Acc. Chem. Res.* **2016**, *49*, 635−645.

(65) Corpas, J., Caldora, H. P., Di Tommaso, E. M., Hernandez-Perez, A. C., Turner, O., Azofra, L. M., Ruffoni, A. & Leonori, D. A General Strategy for the Amination of Electron-Rich and Electron-Poor Heteroaromatics by Desaturative Catalysis. *Nat. Catal.* **2024**, *7*, 593–603.

(66) Nyagilo, V. O., Mallojjala, S. C. & Hirschi, J. S. Transition State Analysis of Key Steps in Dual Photoredox-Cobalt Catalyzed Elimination of Alkyl Bromides. *ACS Catal.* **2024**, *14*, 4683–4689.

(67) Frisch, M. J., Trucks, G. W., Schlegel, H. B., Scuseria, G. E., Robb, M. A., Cheeseman, J. R., Scalmani, G., Barone, V., Petersson, G. A., Nakatsuji, H., Li, X., Caricato, M., Marenich, A. V., Bloino, J., Janesko, B. G., Gomperts, R., Mennucci, B., Hratchian, H. P., Ortiz, J. V., Izmaylov, A. F., Sonnenberg, J. L., Williams-Young, D., Ding, F., Lipparini, F., Egidi, F., Goings, J., Peng, B., Petrone, A., Henderson, T., Ranasinghe, D., Zakrzewski, V. G., Gao, J., Rega, N., Zheng, G., Liang, W., Hada, M., Ehara, M., Toyota, K., Fukuda, R., Hasegawa, J., Ishida, M., Nakajima, T., Honda, Y., Kitao, O., Nakai, H., Vreven, T., Throssell, K., Montgomery, J. A., Jr., Peralta, J. E., Ogliaro, F., Bearpark, M. J., Heyd, J. J., Brothers, E. N., Kudin, K. N., Staroverov, V. N., Keith, T. A., Kobayashi, R., Normand, J., Raghavachari, K., Rendell, A. P., Burant, J. C., Iyengar, S. S., Tomasi, J., Cossi, M., Millam, J. M., Klene, M., Adamo, C., Cammi, R., Ochterski, J. W., Martin,

R. L., Morokuma, K., Farkas, O., Foresman, J. B. & Fox, D. J. Gaussian 16, Revision 02C; Gaussian, Inc.: Wallingford CT, 2019.

(68) Luchini, G., Alegre-Requena, J. V., Funes-Ardoiz, I. & Paton, R. S. *F1000Research*, **2020**, *9*, 291.

(69) Jiang, Z., Shan, J.-R., Su, J., Mo, J.-N., Zhang, F., Houk, K. N. & Zhao, J. Cobaloxime-Catalysed Regiodivergent Hydrogen Atom Transfer for Alkenyl and Allylic Carbamoylation with Branched Alkenes. *Nat. Commun.* **2026**, DOI: 10.1038/s41467-026-74595-8.